NEUTRON DIFFRACTION STUDIES OF ICES

A THESIS SUBMITTED TO

THE UNIVERSITY OF LONDON

FOR THE DEGREE OF

DOCTOR OF PHILOSOPHY.

By

Colin Lobban

University College London

April 1998

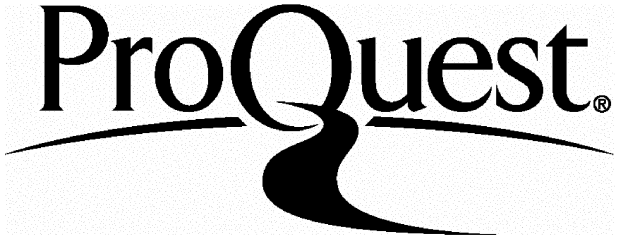

Abstract

This thesis reports on a series of neutron diffraction measurements on ices in the medium-pressure range of the phase diagram in order to address several outstanding issues.

The structure of ice II under its thermodynamic conditions of stability is unknown. Previous studies have used helium gas as the pressurising medium, which is included within the ice structure. Argon gas has been used in this work as the pressure medium, and the detailed structure of ice II is presented and discussed.

Similarly, the structure of ice V under its conditions of stability is established for the first time by this work. For ices III and V, the presence of orientational order is controversial with the results obtained from structural studies on recovered samples differing from conclusions drawn from dielectric and spectroscopic measurements. The results obtained in this work indicate partial ordering of the water molecules which, for ice V, appears to be both temperature and pressure dependant.

Ice IV is a metastable phase of ice that is difficult to form. A structure has been proposed on the basis of samples recovered to ambient pressure at 110 K. This work has successfully prepared ice IV at high temperature and pressure and a structure refinement confirms, for the first time, that the proposed structure is correct.

During studies within the established stability region of ice V, features were observed which could not be identified as any ice or clathrate phase. Further work in this region has successfully formed and retained one such phase. The structure has been solved and the phase identified as a new ice structure. The topology of this phase is unlike that of any known solid water structure, and contains a mixture of seven- and eight-membered rings.

General issues concerning hydrogen-bonding, compressibility and expansivity of these phases are discussed.

Acknowledgements

I would like to thank John Finney and Werner Kuhs for their invaluable help in producing this thesis. For assistance during and after experiments, the instrument scientists are thankfully acknowledged: Mark Adams, Steve Hull, Richard Ibberson and Kevin Knight at ISIS, Alan Hewat and Paolo Radaelli at ILL. Thanks also to Bill Marshall who served as local contact during the experiment on PEARL, and to John Loveday for his help in understanding GSAS. Without the technicians responsible for the high pressure equipment, especially Trevor Cooper and John Dreyer at ISIS, and Louis Melesi at ILL, this work would not have been possible. Finally, thanks to Jennifer for proof reading the thesis.

Contents

List of Tables

List of Figures

Chapter 1

Introduction

1.1 Why ice?

All life on this planet would not survive without the continual presence of water. In man alone, water accounts for around 70% of the body mass. Far from being inert, water is essential for many of the biological mechanisms which keep us alive [4]. The fundamental role of water in nature has led to a massive research effort into studying the physical and chemical properties of this unusual liquid, and although many of the bulk properties of water are known, a description at the molecular level remains incomplete. To this end, many theoretical models have been devised to describe the various properties of water [5], but the difficulty in modelling the hydrogen bond has meant no one model has been adequate in describing its behaviour completely. Water therefore continues to present a problem to scientists who wish to understand water-water and water-solute interactions.

Models of course require experimental data with which to validate their predictions. Water in its solid form, ice, offers an excellent system for testing theoretical

models of the water molecule. In ice, the water molecules are completely hydrogen-bonded and form a regularly repeating structure. Furthermore, ice exists in many different forms in which the water molecules adopt different configurations. The intermolecular forces, which act within the various ice forms, differ in both magnitude and direction. Ices are therefore ideally suited for studies of the water molecule and the hydrogen bond.

As well as providing an excellent system for testing theoretical models of the water molecule, the occurrence of ice in the natural environment means ice is itself of interest to a large number of scientists.

In permafrost regions, ices provide a continuous record of climatic and atmospheric conditions over the last 200,000 years. For example, the isotopic composition of the ice depends mainly upon the temperature of formation [6,7]. The level of greenhouse gases present in the atmosphere can be determined from air bubbles trapped within the ice and reconciled with past climatic changes [8,9]; while the acidity of the ice provides a record of past acidic fallout from volcanic eruptions [10–12].

In the field of meteorology, ice formation plays an important role in cloud development and precipitation [13,14]. In fact, the most common form of cloud seeding, a process used to promote rainfall, involves the release of material, such as AgI, to encourage ice nucleation.

Ice, however, is not always wanted, and there is a great deal of research concerned with preventing its formation. In the field of cryobiology, ice formation is thought to be the most important factor in the damage of cells, tissues and organs when preserved to liquid nitrogen temperatures [15,16]. The formation of ice on aircraft wings, helicopter blades, power lines etc. also presents problems and the development of materials with low ice adhesion is equally important [17,18].

Not only is ice found abundantly on Earth but also on satellites and comets of the solar system [19–21]. Most ices in the solar system are believed to have formed at the same time as the sun. Their study may therefore lead to a better understanding of the conditions under which the solar system was formed [22]. In particular, the identification of different ice phases, thought to occur on some of the larger icy satellites [22–24], may give some idea of the pressures and temperatures involved.

A wide range of investigative methods have been used in the study of ices, e.g. single-crystal and powder diffraction, infrared and Raman spectroscopy, dielectric and thermal conductivity measurements. The work presented in this thesis exploits the use of powder neutron diffraction to examine, for the first time, the structure of some of the high pressure ices within their regions of thermodynamic stability. Their examination under different pressure and temperature conditions provides information on mechanical properties, such as expansivity and compressibility, which may be of further use in examining how the hydrogen bond reacts to changes in pressure and temperature.

Although the intention of this work is not to formulate an alternative model for the water molecule, a significant amount of new information is obtained relating to hydrogen bond geometries in different ice structures and under different conditions of pressure and temperature. These results can now be used to improve upon and validate current water models.

1.2 The water molecule

A water molecule consists of a single oxygen and two hydrogen atoms in a non-linear arrangement, figure 1. The oxygen atom has six outer electrons, two of which it shares

with the electrons of the two hydrogen atoms to form covalent bonds. The remaining four electrons form two lone pairs which repel the electrons of the two O–H bonds resulting in a non-linear molecule.

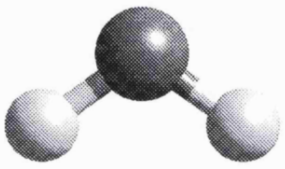

Figure 1: The water molecule.

The geometries of the H_2O and D_2O water molecules in the ground state (non-rotating, non-vibrating), and corrected for zero point motion, are listed in table 1.

	Ground		Zero point	
	Expt.	Theory	Expt.	Theory
O–H	0.9572 Å	0.9584 Å	0.9731 Å	0.9712 Å
O–D	0.9572 Å	0.9584 Å	0.9686 Å	0.9691 Å
H–O–H	104.52°	104.52°	104.70°	104.64°
D–O–D	104.52°	104.52°	104.64°	104.61°

Table 1: The water molecule geometries for H_2O and D_2O in the ground state, and corrected for zero point motion [25]. The experimental bond lengths and angles were determined from spectroscopic data [26].

The larger electronegativity of the oxygen atom, compared to the hydrogen, causes the electron distribution of the two O–H bonds to shift in the direction of the oxygen atom thereby creating a small positive charge on each of the hydrogen atoms. This in turn leads to a permanent dipole moment for the water molecule of 1.855 D [27].

1.3 The hydrogen bond

The hydrogen bond, or more accurately the water hydrogen bond[1], can be thought of as the result of the attraction between the positively charged hydrogen and the negatively charged lone pair electrons. The water molecule has two hydrogen atoms with which to *donate* two hydrogen bonds, and sufficient space around the oxygen atom to allow it to *accept* two hydrogen bonds. The water molecule can therefore bond to four other water molecules with the hydrogen bonds arranged tetrahedrally, figure 2.

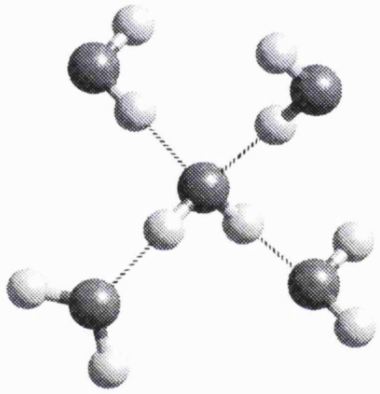

Figure 2: The tetrahedral arrangement of a fully hydrogen-bonded water molecule.

The strength of the hydrogen bond (~20 $kJmol^{-1}$) is intermediate between the weak van der Waals interaction (~1 $kJmol^{-1}$) and the strong covalent bond (~400 $kJmol^{-1}$), and is responsible for many of the anomalous properties of water such as a high melting and boiling point, a high heat capacity and a maximum density in the liquid at 277 K.

[1] In general, the hydrogen bond refers to the attraction between electronegative atoms such as nitrogen, oxygen, fluorine and chlorine, and hydrogen, particularly when the hydrogen atom is bonded directly to an electronegative atom.

1.4 Ice

The water molecules in ice form tetrahedral frameworks with each water molecule hydrogen-bonded to four others. The most familiar form of ice is that formed at temperatures below 273 K at ambient pressure. This is known as ice Ih in which the water molecules arrange to form a series of hexagonal channels, figure 3. However,

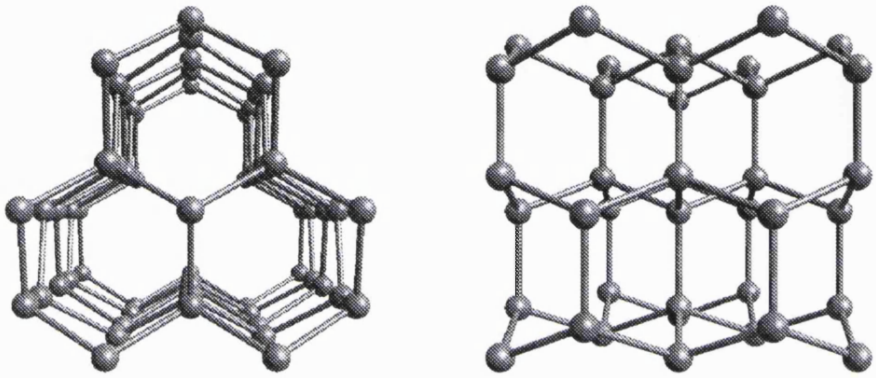

Figure 3: The structure of ice Ih, the common form of ice, as viewed parallel and perpendicular to the hexagonal channels. The open-channelled nature of the structure is responsible for the decrease in density (expansion) upon freezing.

the work of Tammann [28], Bridgman [29–31] and later others [32–36], identified the existence of many more ice structures which form under different conditions of pressure and temperature, figure 4.

As the pressure on the ice structures is increased, the strain on the hydrogen bonds eventually results in breakage with the subsequent water molecule rearrangements forming a different structure of higher density. At pressures less than 6 kbar, the increase in density is accommodated through increased distortion of the tetrahedral framework. At pressures in excess of 6 kbar, the water molecules arrange to form two individual frameworks which interpenetrate each another, for example as in figure 5.

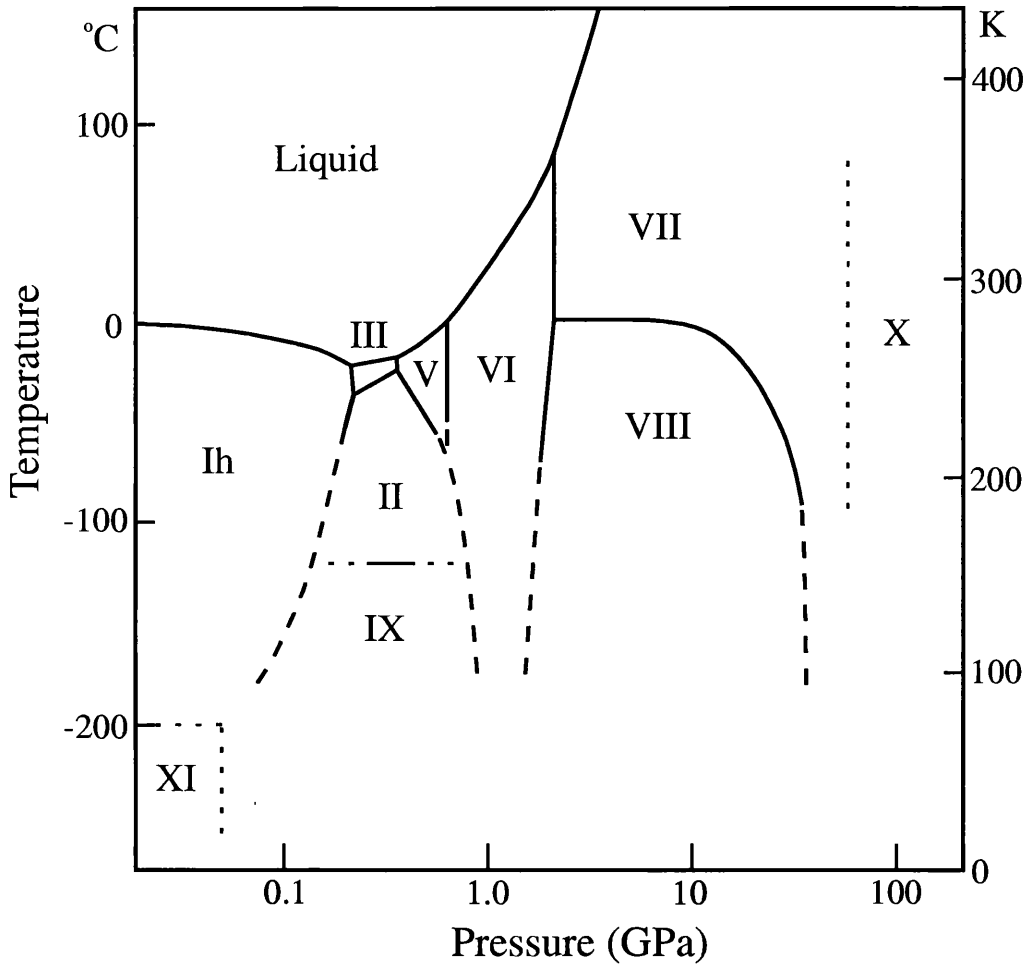

Figure 4: The H_2O phase diagram.

Solid lines represent measured transitions; thick dashed lines, transitions extrapolated to low temperatures; thin dashed lines, predicted transitions. Amorphous ice, which exists in a high and low density form [37,38], ice Ic [39] and ice IV, chapter 7, are not shown. Ices Ic and IV are metastable forms of ice found within the stability regions of ices Ih and V respectively.

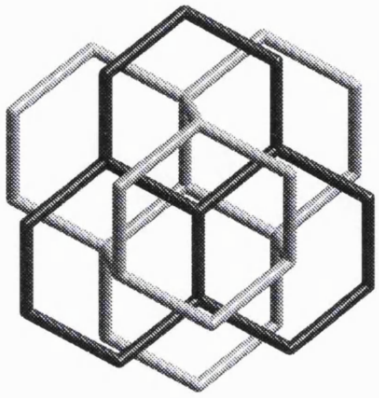

Figure 5: A section of the ice VII structure in which two tetrahedral lattices interpenetrate one another. The two sub-lattices are shaded differently for clarity.

For the large majority of ice structures, the water molecules are orientationally disordered, a state also referred to as proton or hydrogen disorder. A water molecule which is four co-ordinated donates and accepts two hydrogen bonds, figure 2. However, there are six possible ways in which the water molecule can do this, i.e. six possible orientations of the water molecule, all of which are equally viable, figure 6.

In 'disordered' ice structures, all orientations shown in figure 6 occur with equal probability. Since it is not known which orientation is adopted by a particular water molecule, the structure is said to be orientationally disordered, figure 7. In contrast, the water molecules in 'ordered' ice structures have orientations which follow a regular pattern throughout the structure, figure 7.

The structure of ice, as determined by diffraction, chapter 2, is the space-time averaged structure. In disordered ices, the position of a particular water molecule will therefore be the average of all six orientations shown in figure 6. The result of this averaging is a tetrahedral framework of oxygen atoms with not one, but two hydrogen atoms situated across each O—O bond. However, the probability of finding the hydrogen at each site is now only 50%, figure 8. In ordered ices, where the water molecule adopts only one orientation, the probability of finding the hydrogen atom at a particular site is either 0 or 100%. The water molecules in ice can therefore exist,

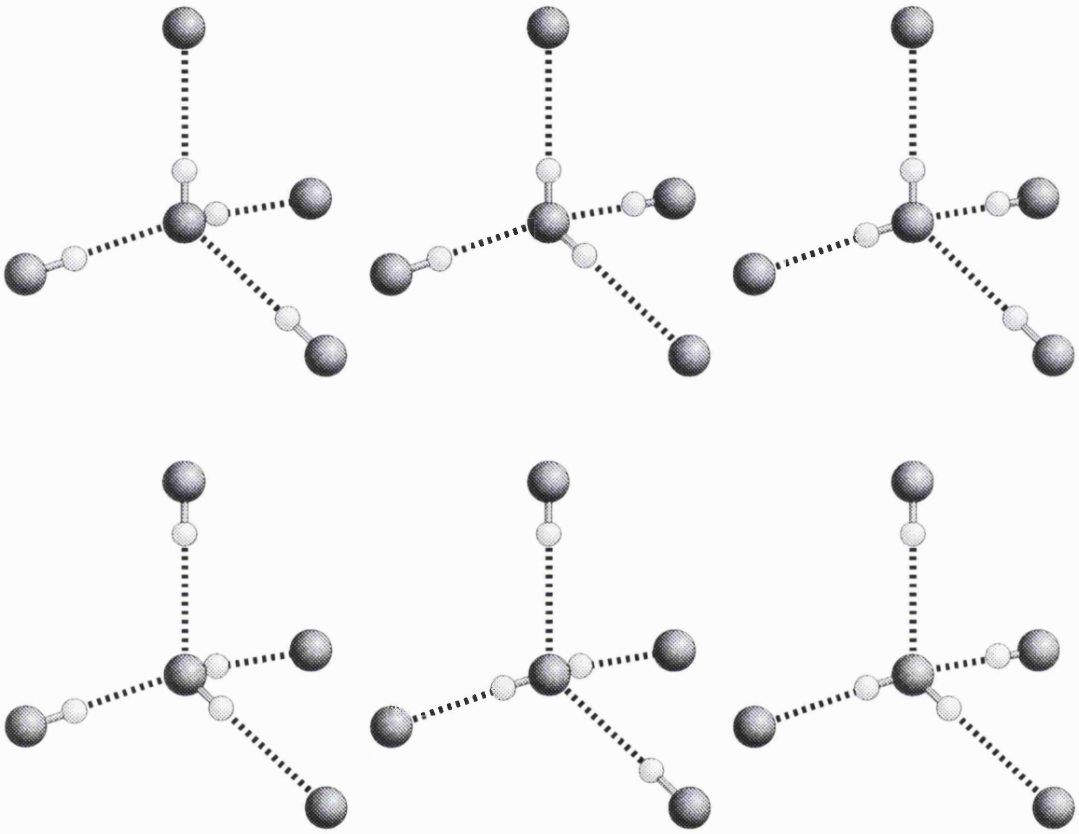

Figure 6: Possible orientations of a water molecule hydrogen-bonded to four neighbouring water molecules. There is an important constraint on the orientation of the water molecule which is that only one hydrogen atom can occupy a bond between neighbouring oxygen atoms [40]. There are therefore six orientations that the water molecule can adopt such that it donates and accepts two hydrogen bonds.

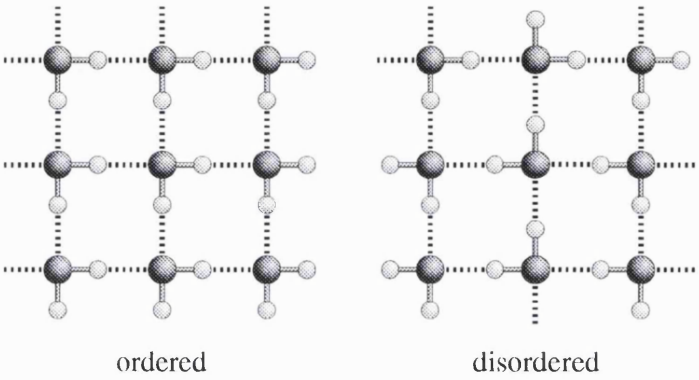

Figure 7: An example ice structure with the orientation of the water molecules ordered and disordered.

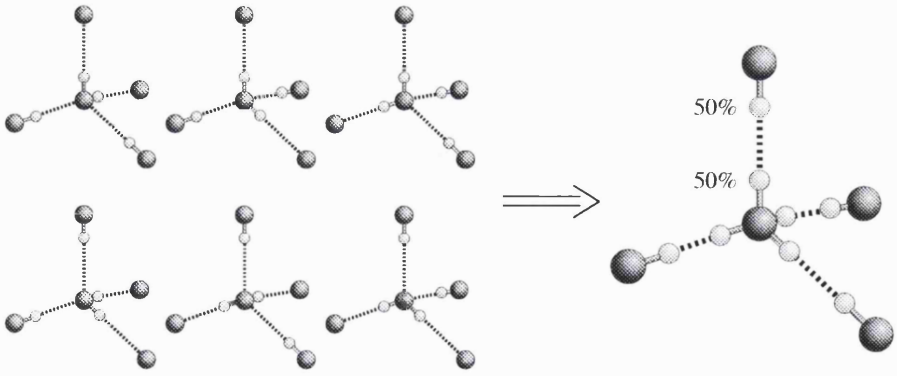

Figure 8: The space-time average structure, as determined by diffraction, is the average of all six possible orientations shown in figure 6. The structure will therefore appear as a tetrahedral network of oxygen atoms with two hydrogen atoms per O—O bond. The probability of finding a hydrogen at each site, however, is only 50%.

in principle, in any orientational state ranging from the fully disordered, 50%, to the fully ordered, 0 or 100%.

1.5 Recovered ices

The structures of the ices examined in this work were all primarily determined from *recovered* samples. This involves preparing the ice at the pressure and temperature conditions under which it is stable. The sample is then lowered into a liquid nitrogen bath where cooling rates of $\sim$15 Ks^{-1} are achieved. Below about 120 K, movement of the water molecules is kinetically hindered and the structure formed at the higher temperatures is ideally retained. The benefits of this are that the pressure can be released to ambient allowing the study of the sample by techniques such as X-ray diffraction and spectroscopy which would otherwise be hampered by the use of a pressure cell. However, it is possible that structural differences might exist between *under pressure* and *recovered* samples upon quenching in liquid nitrogen and releasing the pressure.

1.6 This work

In the work presented in this thesis, the structures of ices II, III, IV and V have been investigated within their thermodynamic regions of stability, figure 4. This involved overcoming problems encountered by others in developing adequate procedures to exert the pressure without otherwise affecting significantly the phase behaviour. Application of this technique in the medium pressure range of the ice phase diagram has allowed many of these phases to be studied by diffraction under their thermodynamic conditions of stability for the first time.

Although ice II has been studied under pressure, the pressurising medium used, helium gas, was found to be included within the ice structure [41]. Chapter 4 presents the unaffected structure of ice II using an alternative pressure medium, argon gas.

The orientation of water molecules in ice III has always been thought to be fully disordered. Yet, until recently the structure of ice III had not been examined under its thermodynamic conditions of stability; the only structural work being on recovered samples which were in fact ice IX [33]. In chapter 5, the structure of ice III under different temperatures and pressures is presented, with particular emphasis on the orientational ordering of the water molecules.

The structure of ice V has likewise never been determined under its conditions of stability. Its structure, under different temperatures and pressures, with particular emphasis on orientational ordering of the water molecules, is presented in chapter 6.

Ice IV is a metastable phase first proposed in the 1930's [30]. Since then it has only been reported by three other research groups in a total of six articles [42–47]. Only once has the structure been suggested, based on samples recovered to ambient pressure [46]. Chapter 7 details the success in forming ice IV, and the structure formed under pressure is presented and discussed.

During this work, a number of unknown phases were formed and are described in chapters 8 and 9. One of these phases has been reproduced and its structure solved from the data collected. The phase is a new form of ice found metastably within the stability region of ice V.

A summary of the results obtained and the conclusions reached, along with suggestions for further work, are given in chapter 10.

Chapter 2

Crystallography and Neutron Diffraction

The science of crystallography has already been addressed by many other authors. The account below offers a simple description of diffraction and its use in the study of crystalline materials as used in the work described in this thesis. The reader is referred to other texts for a fuller description, e.g. [48–52].

2.1 Crystallinity

All solid matter can be described as either crystalline or non-crystalline. The atoms in a crystalline material arrange to form a basic unit, or motif, which repeats periodically in all directions, at least ideally[1]. In a non-crystalline material, there is no periodicity and the atoms adopt an irregular form.

If the periodically repeating motif is represented by a point, then the crystal

[1]In a perfect crystal the motif periodically repeats without change. A real crystal however has imperfections such as dislocations, stacking faults etc.

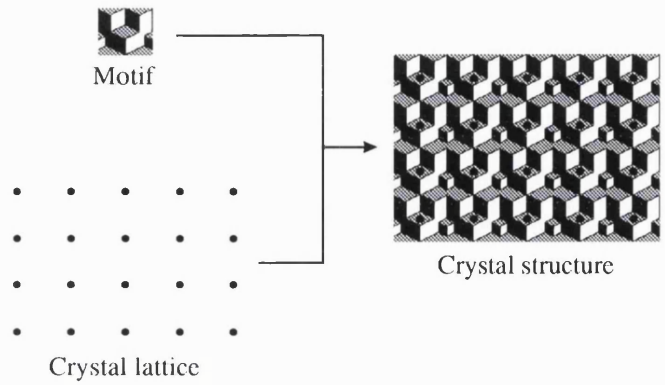

Figure 9: The crystal structure is the convolution of the motif with the crystal lattice.

structure can be represented by a lattice of points, referred to as the *crystal lattice*, figure 9. By joining points within the crystal lattice, a parallelepiped called a *unit cell* is created. The shape and size of the unit cell is chosen to best represent the symmetry of the structure and to simplify mathematical calculations. The unit cell therefore will not always be the smallest and simplest cell available and may often include more than one motif, i.e. more than one lattice point, figure 10. The unit cell can therefore be thought of as the most convenient building-block which when packed side-by-side forms the complete crystal structure.

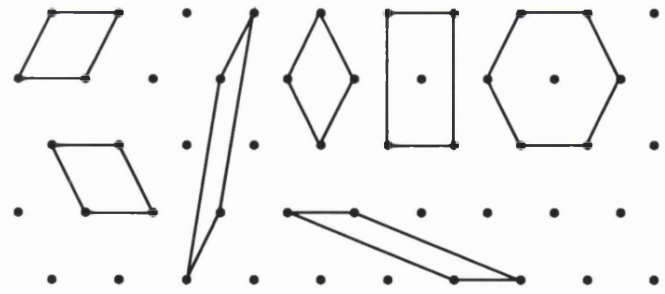

Figure 10: A few examples of possible unit cells, all of which are equally viable in describing the crystal structure.

2.2 Symmetry

The arrangements of atoms within the unit cell are often symmetrically related. For example, the unit cell in figure 11 comprises eight atoms, four of type A and four

of type B. However, there are two mirror planes, perpendicular to the page, about

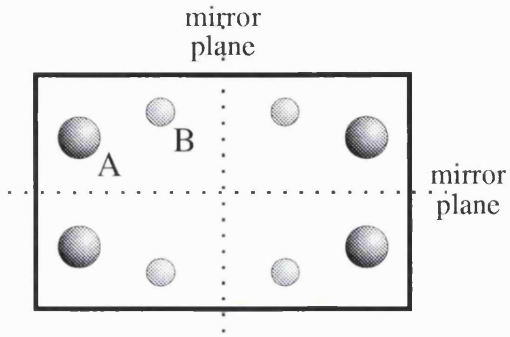

Figure 11: An example unit cell comprising four A-type and four B-type atoms. Two mirror planes exist perpendicular to the page.

which the structure is symmetric. The unit cell, and hence the complete structure, can therefore be described by just two atoms, say those in the upper left quadrant, and two mirror planes. The description of the structure in this manner vastly simplifies the analysis of diffraction data. This is of particular importance for structures in which the unit cell contains a large number atoms. For example, the unit cell of argon hydrate, a compound readily formed throughout this work, comprises around 430 atoms, yet can be described using only twelve. Other forms of symmetry found within crystal structures are inversion centres, rotational and translational symmetry. In addition to the mirror symmetry in figure 11, the unit cell also exhibits two-fold rotational symmetry.

The symmetry elements present within the unit cell are collectively referred to as the *space group symmetry*. The fragment of the unit cell which, when acted upon by the symmetry elements, generates the complete unit cell, is called the *asymmetric unit*. The complete crystal structure can therefore be described solely by the dimensions of the unit cell, the space group symmetry and the contents of the asymmetric unit.

2.3 Diffraction

The diffraction and subsequent interference of waves through a small aperture is a well understood phenomenon [53]. The same principles hold for diffraction of radiation by crystals. Huygens' principle states that *all points along a wavefront can be considered as secondary sources of spherical waves* - an axiom fundamental in the understanding of diffraction. Similarly, any point in a crystal can be thought of as sources of spherical waves. In the diffraction of X-rays, the most common form of radiation used in crystallography, the electromagnetic wave causes an electron in its path to vibrate periodically with the changing electric field. The vibrating electron itself then becomes a source of electromagnetic waves of the same frequency and wavelength as the X-ray. In neutron diffraction, the neutron is captured momentarily by the nucleus of the atom before being re-emitted. Again, the atomic nucleus can be considered as a point source of a spherical waves which result from the emitted neutron.

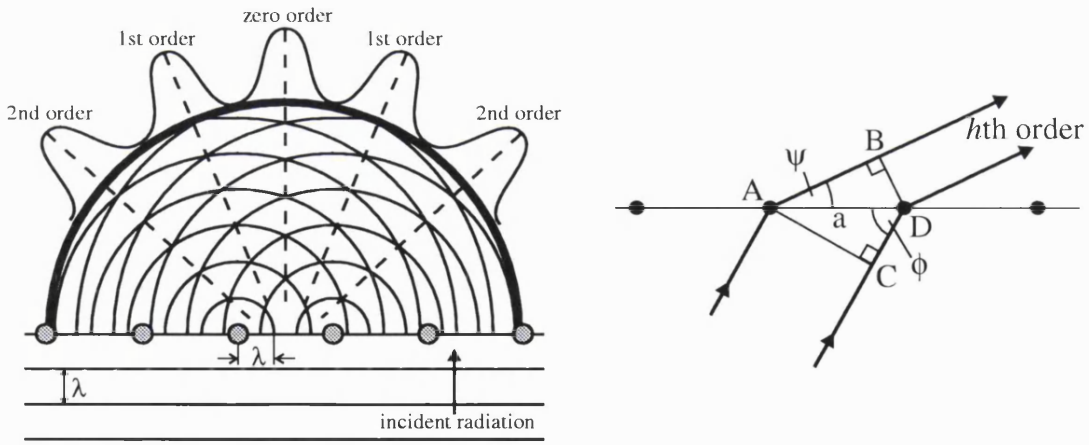

Figure 12: Atoms act as point-like sources of spherical waves which interfere to create bright and dark bands known as diffraction orders (left). If the radiation meets the row of atoms at an angle ϕ, then the hth diffraction order is observed at the angle ψ given by equation 1 (right).

For a line of atoms, all acting as point sources, the spherical waves interfere to

form a series of bright and dark bands, figure 12. If the incident radiation meets the line of atoms at an angle ϕ, then the bright bands, or diffraction orders, are observed at an angle ψ given by the equation:

$$\begin{aligned} AB - CD &= h\lambda \\ a\cos\phi - a\cos\psi_h &= h\lambda \\ \cos\psi_h &= \cos\phi - \frac{h\lambda}{a} \end{aligned} \tag{1}$$

where h is the diffraction order from a row of atoms of separation a, figure 12.

In three dimensions, the incident radiation can impinge upon the row of atoms from any direction which forms the surface of a cone concentric with the row of atoms and of semi-apex angle ϕ, figure 13. Equation 1 is therefore satisfied for all directions that lie on the surface of a cone of semi-apex angle ψ_h, figure 13.

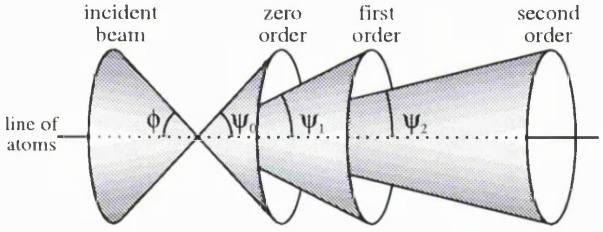

Figure 13: The diffraction cones arising from a line of atoms.

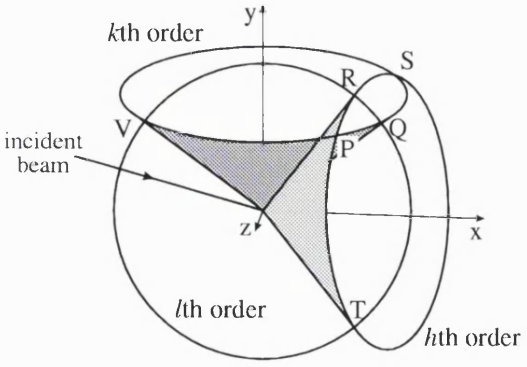

Figure 14: For an array of atoms, the scattered radiation is only in phase when all three cones of the three different axes coincide, i.e. when points P, Q and R meet. Note, the cone of the z axis projects out of the page

For a three-dimensional lattice of atoms there are a series of cones for each of the three different axes. In figure 14, a single diffraction order is shown for each of

the three axes. At the intersection of two cones, points P, Q, R, S, T and V, the scattered radiation from a plane of atoms is in phase. However, the scattering from successive planes is not in phase and diffraction is only observed when all three cones intersect. By varying the angle of the incident beam, the three points P, Q and R can be brought to coincide. When this occurs, every row and hence every atom is scattering in phase and a diffraction spot in the direction of the cone intersection is observed. At this point, all three equations:

$$\begin{aligned} \cos\psi_1 &= \cos\phi_1 - \frac{h\lambda}{a} \\ \cos\psi_2 &= \cos\phi_2 - \frac{k\lambda}{b} \\ \cos\psi_3 &= \cos\phi_3 - \frac{l\lambda}{c} \end{aligned}$$

are satisfied, with the diffraction spot referred to as the hklth order. The equations are known as the *Laue equations* from which it can be shown [48, 54] that all are satisfied for the case:

$$hx + ky + lz = m \tag{2}$$

This is the equation of a plane and implies diffraction is observed only from the constructive interference of a series of planes, where each diffraction spot corresponds to a set of different planes described by equation 2.

This description however is cumbersome, and often crystallographers refer to Bragg's law in describing the diffraction phenomenon from crystals. Although an oversimplification, the Bragg analogy provides a clear and simple interpretation of the features observed in crystalline diffraction.

2.3.1 Bragg's law

Rather than diffraction, Bragg considered the observed phenomenon as planes of atoms *reflecting* the incident radiation, much in the same way that a mirror reflects light, with equal angles of incidence and reflection. The *reflected* radiation from successive planes must be in phase for constructive interference to occur, figure 15.

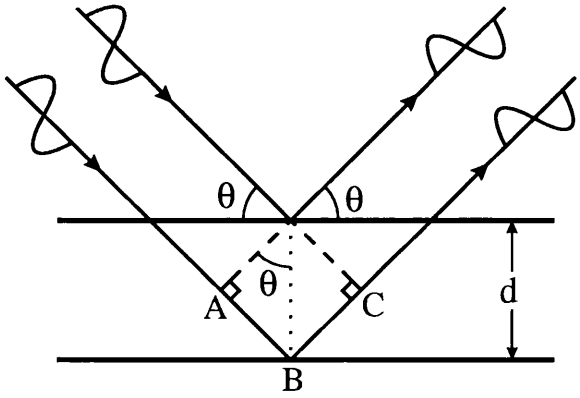

Figure 15: The *reflection* analogy considered by Bragg with equal angles of incidence and reflection. For the two reflected waves to be in phase, the path difference of the two, $AB + BC$, must be an integral number of wavelengths.

The path difference between waves scattered from different planes, $AB + BC$, must be an integral number of wavelengths and hence:

$$\begin{aligned} AB + BC &= n\lambda \\ d\sin\theta + d\sin\theta &= n\lambda \\ 2d\sin\theta &= n\lambda \end{aligned} \tag{3}$$

Equation 3 is referred to as *Bragg's equation* and provides the angle, θ, at which radiation constructively interferes from a series of planes of separation, d, to form a diffraction spot.

Planes defined by equation 2 are characterised by their values of h, k and l. An example of planes with different (hkl) indices are shown in figure 16. Since the

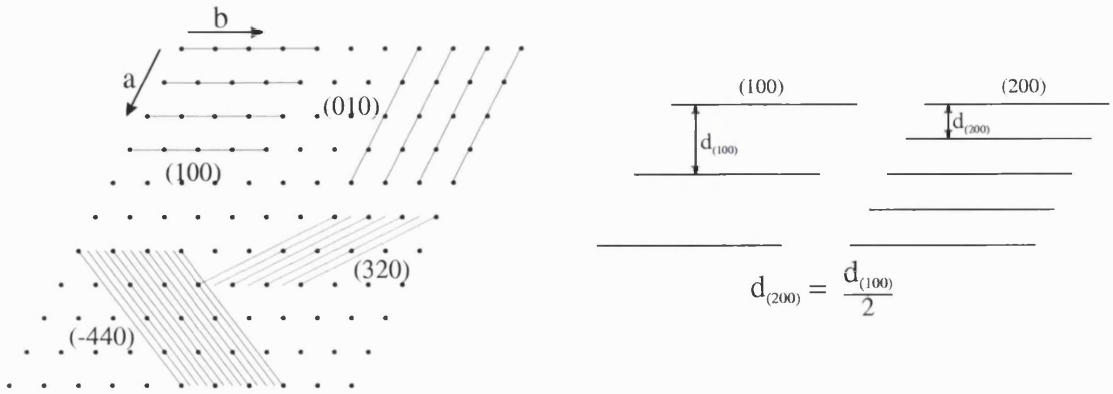

Figure 16: Example planes of different (hkl) indices are shown left. The separation of one set of planes, d, when divided by an integer defines another set of planes as demonstrated right.

separation of a set of planes, d, divided by an integer defines another set of planes, figure 16, the Bragg equation is then:

$$\begin{aligned} 2d \sin\theta &= n\lambda \\ 2d_{(hkl)} \sin\theta &= \lambda \end{aligned} \tag{4}$$

Because of Bragg's analogy with reflection, the diffracted beam is often referred to as a *reflection* with the diffraction arising from the set of (hkl) planes referred to as the (hkl) reflection.

2.4 Intensity

In section 2.3, diffraction was considered for an array of atoms. The same theory applies for an array of unit cells, i.e. where each atom is replaced by a unit cell. Diffraction then arises from the constructive interference of waves from each unit cell. However, the scattered wave from each unit cell is the sum of a number of component waves arising from each individual atom within the unit cell. Each component wave

will have a different phase, and for different atomic elements or isotopes, a different amplitude. The total scattering from the unit cell is therefore the sum of the component waves:

$$\mathbf{F} = \sum_j f_j e^{i\phi_j} \tag{5}$$

where f_j is the amplitude of the scattered wave of phase ϕ_j relative to some origin, figure 17.

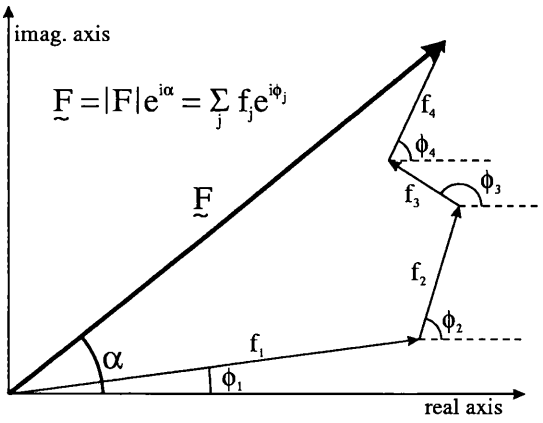

Figure 17: The scattered wave from a unit cell is the summation of a number of component waves. Each component corresponds to the wave scattered from each individual atom within the unit cell. The component waves will differ in phase, and for different elements or isotopes, amplitude.

The phase of each component wave, ϕ_j, is related to the position of the corresponding atom within the unit cell. The difference in phase for atoms on successive planes is 2π, figure 18. An atom at a fraction of the distance between the planes, δ, will have a phase difference of $2\pi\delta$. The position of the atom between the planes, δ, can be expressed in terms of its position within the unit cell. For the simple case of $(h00)$ planes, figure 19, waves scattered from an atom of fractional co-ordinate x

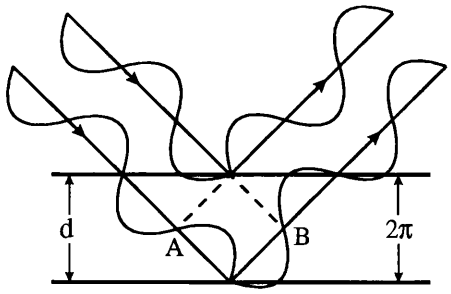

Figure 18: For diffraction to be observed, the scattering from successive planes must satisfy Bragg's equation, eqn. 4. The path difference between waves scattered from successive planes, AB, must therefore be a single wavelength, i.e. a difference in phase of 2π.

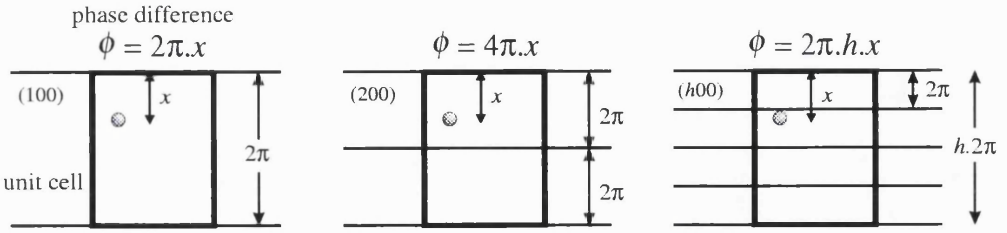

Figure 19: The phase difference between successive planes is 2π. The phase difference across a unit cell is therefore 2π multiplied by the number of planes which pass through the unit cell. For the set of (100) planes, there is only one plane per unit cell, for the (200) there are two and for the (h00) planes there are h. The phase difference for a wave scattered from an atom of fractional co-ordinate x, is therefore $2\pi.h.x$.

will have a phase difference of $2\pi hx$. This is simply extended to the case of three dimension with $2\pi(hx + ky + lz)$ the phase difference between an atom at (0,0,0) and an atom at (x, y, z). The total scattering from the unit cell for a set of (hkl) planes is then:

$$\mathbf{F}_{(hkl)} = \sum_j f_j e^{2\pi i(hx_j + ky_j + lz_j)} \tag{6}$$

where x_j, y_j and z_j are the fractional co-ordinates of atom j within the unit cell.

The intensity of any radiation propagated as a wave is proportional to the square of its amplitude. The intensity of the diffracted beam, I, is therefore proportional to $|\mathbf{F}|^2$. The variation in $\mathbf{F}$ for different (hkl) scattering planes, equation 6, is extremely important and implies the intensity of the different (hkl) reflections is determined by the crystal structure. Conversely, the crystal structure can be determined from the intensities of the different (hkl) reflections.

2.5 Summary

The position at which reflections are observed depends only on the dimensions of the unit cell. The intensity of the reflections depends on the type and arrangement of

atoms within the unit cell. By measuring the diffraction pattern for a crystalline material, i.e. the position and intensity of each reflection, the complete crystal structure can be deduced[2].

2.6 Single crystals and powders

For a single crystal, the diffraction from a set of (hkl) planes creates a single spot, observed in a particular direction. By orienting the crystal, relative to the incident radiation, a spot is found for each set of diffracting planes that satisfies the Bragg equation, $2d_{hkl}\sin\theta = \lambda$. In *powder diffraction* however, the sample consists not of one large, single crystal but of many randomly oriented crystallites. Diffraction from a set of (hkl) planes is no longer observed in a single direction, but in all directions that form the surface of a cone, figure 20. Furthermore, the angle at which the

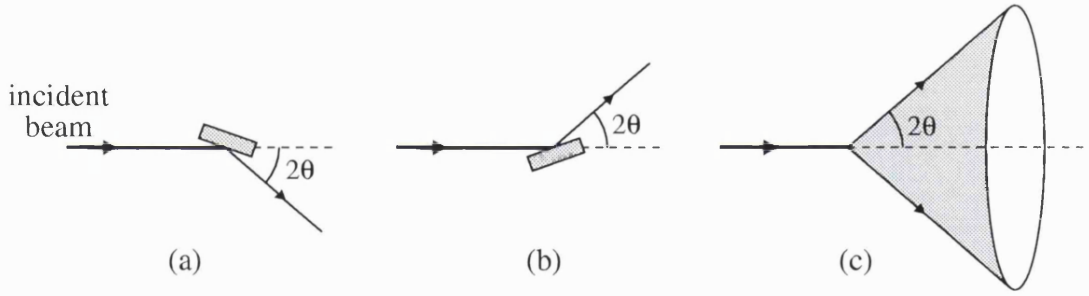

Figure 20: For a particular crystal orientation, diffraction from a set of (hkl) planes is observed in a particular direction (a). If the crystal orientation is changed, diffraction from the same set of planes is observed in a different direction (b). In powder diffraction all crystallites are randomly oriented. The diffraction from a set of (hkl) planes is no longer observed in a single direction, but in all directions which form the surface of a cone with semi-apex angle 2π (c).

[2]The scattered wave from each unit cell has an amplitude $|\mathbf{F}|$ and a phase α, figure 18. The intensities of the different reflections depend only on the amplitude, yet to solve the crystal structure it is necessary to know the phase, equation 6. Fortunately, the majority of this work deals with the refinement of known crystal structures from which the phase can be deduced.

cone is observed is dependent on the interplanar spacing, equation 4. Planes with the same spacing will therefore produce cones of the same semi-apex angle, i.e. diffraction from different planes will overlap. There is therefore a loss of information in going from a single crystal to a powder, from a three-dimensional array of spots to a one dimensional series of circles, figure 21.

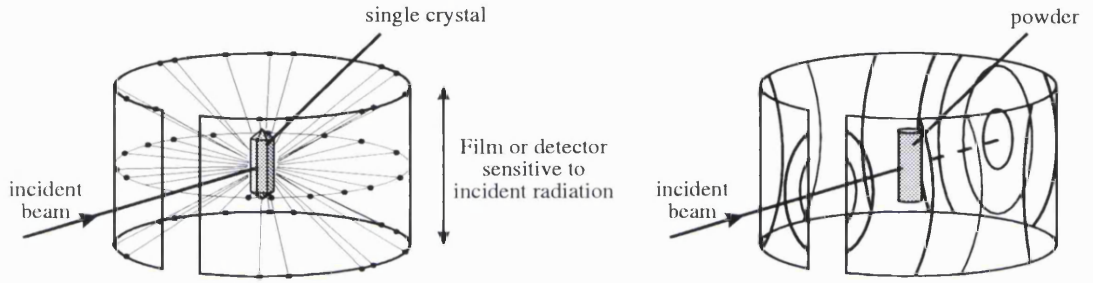

Figure 21: Scattering from a single crystal forms an array of spots, each spot corresponding to a different set of (hkl) planes (left). Scattering from a powder, however, forms a series of circles, each circle corresponding to a different set of interplanar spacings (right).

Ideally, all crystallographic work would be carried out on single crystals. Unfortunately, circumstances make this impossible in all cases. Although single crystals of ice can be formed under pressure by freezing the liquid, it is very difficult to form just the one crystal for the ice structures studied in this work. This does not present a problem if a single crystal can be extracted from the assembly. However, since this work aims to study ices under pressure, the extraction of a single crystal would involve releasing the pressure, thereby destroying the sample. In addition, this work sought to explore the ice phase diagram in some detail. This involved changes in pressure and temperature with transitions from one ice phase to another, all of which would most probably fracture the crystal. For these reasons, the study of ice under pressure was carried out on powdered samples.

Although there is a loss of information in using powders, the increased use and

subsequent improvement of methods used to analyse powder data over the last 20 years has been substantial. With the advances in computing, the use of the Rietveld method in refining crystal structures from powders is now routine.

2.7 Rietveld refinement

In the late 1960's Hugo Rietveld developed a computer-based method for the structural analysis of crystalline compounds from their powder diffraction profiles [55,56]. The algorithm computes the diffraction pattern for an input model and compares it with that observed experimentally. The difference between the observed and calculated diffraction patterns is then minimised in a least-squares refinement by modifying the input model.

The model contains everything that contributes to the diffraction pattern, the most important elements being: the dimensions of the unit cell, the position and thermal motion of atoms, the profile shape of the reflections and the shape of the underlying background, figure 22.

The diffraction profiles are represented in numerical form as a series of steps, with intensity y_i at step i. The residual S is then minimised in a least-squares refinement by changes to the input model:

$$S = \sum_i w_i (y_{io} - y_{ic})^2 \tag{7}$$

where w_i is some weighting factor, e.g. $1/y_{io}$, and y_{io} and y_{ic} are the observed and calculated intensities for step i.

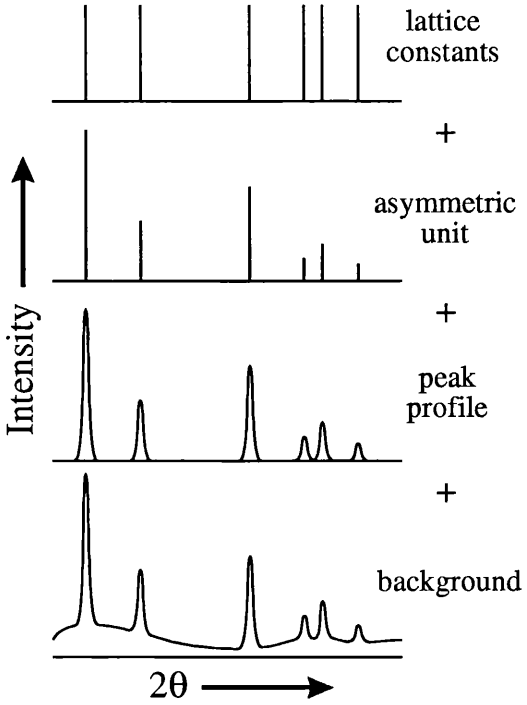

The model used to calculate the diffraction pattern consists essentially of: (a) the lattice constants, or the dimensions of the unit cell, which determines the positions of the reflections; (b) the atoms in the asymmetric unit, their position and thermal motion, which determines the intensity of the reflections; (c) the peak profile which determines the shape of the reflections; and (d) the background.

Figure 22: A calculated diffraction pattern constructed from an input model

2.7.1 Criteria of fit

Changes to the model are made until a point of convergence is reached; this may be regarded as the point at which further changes to the model will lead to no further improvement in the residual. Although no improvement to the residual can be made, this does not imply that a good fit between observed and calculated intensities has been reached. There are a number of criteria used by crystallographers to gauge the quality of fit, for example:

$$R_B = \frac{\sum |I_{ko} - I_{kc}|}{\sum I_{ko}} \qquad \text{Bragg } R\text{-factor}$$

$$R_p = \frac{\sum |y_{io} - y_{ic}|}{\sum y_{io}} \qquad \text{profile } R\text{-factor}$$

$$R_{wp} = \left\{ \frac{\sum w_i (y_{io} - y_{ic})^2}{\sum w_i y_{io}^2} \right\}^{1/2} \qquad \text{weighted profile } R\text{-factor}$$

where I_k is the intensity of the kth Bragg reflection, y_i is the intensity at step i, and w_i is a weighting factor.

Overlapping of reflections is a common feature in powder diffraction and the intensities of the individual peaks, I_{ko}, are therefore rarely observed experimentally. Instead values for I_{ko} are allocated from the total intensity arising from all the overlapping peaks. The values of I_{ko}, and hence the Bragg R-factor, are therefore biased in favour of the model being used. The Bragg R-factor is often used to compare with values obtained in the refinement of single crystal data, where of course reflection overlap is not observed.

The weighted profile R-factor, R_{wp}, is the most meaningful for gauging the progress of the refinement since the numerator is the residual being minimised, equation 7. However, the actual R_{wp} values that are generated are rather useless when comparing with other refined data. This is due largely to the underlying background. The intensity at each step comprises two components, that relating to the Bragg reflection and that from the background:

$$y_i = y_i(Bragg) + y_i(Background)$$

The background, which generally is smoothly varying, is much easier to fit than a series of Bragg peaks. A better fit will therefore be found for diffraction data with a high background.

R_{wp} is also extremely sensitive to factors that do not arise from the structural model. In particular, an additional phase not modelled in the refinement will inflate the value of R_{wp} greatly. If the phase is unknown and cannot therefore be included in the refinement, then the peaks relating to that phase must be excluded from the data. Unfortunately, it is not easy to know which peaks belong to an unknown phase, particular at high angles where overlapping peaks are commonplace. An unknown

phase was found in some of the diffraction data collected in this work.

It is very difficult for someone not involved in the refinement procedure to judge the quality of the fit simply from the R-factors. A visual representation is far more important and immediately demonstrates both the quality of the data and the fit. Therefore, in addition to listing the R_p and R_{wp} factors, the fits arising from the refinement of the data are shown.

2.8 X-rays vs. neutrons

In section 2.3, atoms were considered as point-like sources of radiation. This however is not strictly true. In X-ray diffraction, each electron acts as a source of spherical waves with the same frequency and wavelength as the incident X-ray. Although the electron itself may be regarded as a point-like source, the atom, which has many electrons distributed over a finite size, is not. Scattering from the different electrons within the atom will therefore be out of phase, figure 23. The difference in phase increases with scattering angle causing a drop-off in intensity, figure 23. Neutron diffraction however is much more akin to point-like diffraction. Although the nucleus of an atom has a finite size, the size is insignificant compared to the wavelength of the incident neutron and may be considered as point-like. There is therefore no measurable drop-off in intensity with scattering angle.

At zero scattering angle, the amplitude of the scattered X-ray is proportional to the number of electrons in the atom. For neutrons however, the amplitude depends on the characteristics of the atomic nucleus and does not vary in a systematic way. The X-ray and neutron scattering factors for a variety of atoms are given in table 2. For hydrogen, the small X-ray scattering factor and drop-off in intensity with scattering

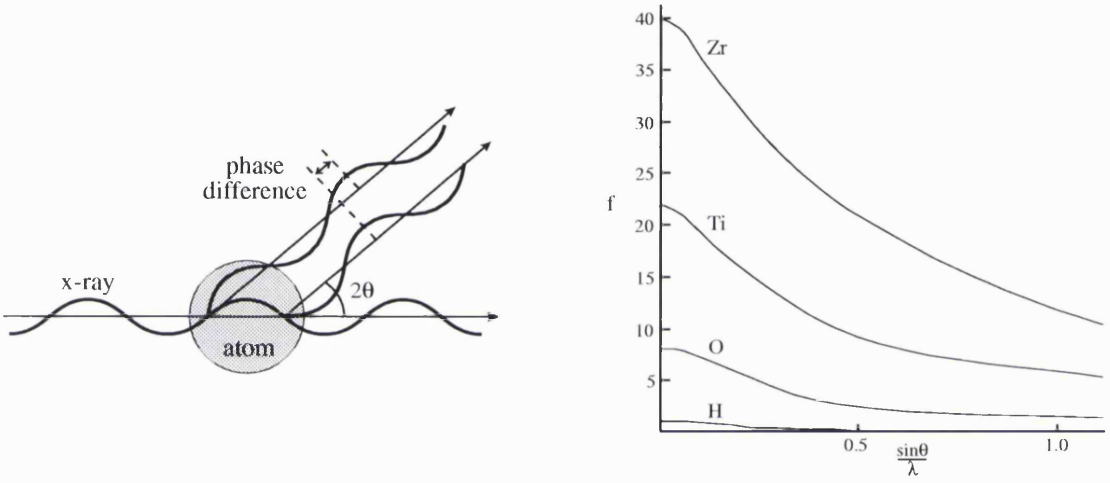

Figure 23: Scattering of X-rays by an atom.
The electrons in an atom each act as point sources of X-rays. Because the electrons are distributed over a distance comparable to the X-ray wavelength, there is a difference in phase for waves from different electrons (left). This leads to destructive interference, causing a decrease in the total scattering intensity from the atom. The phase difference increases with the scattering angle, 2θ, resulting in a drop-off in the intensity with scattering angle (right).

angle makes its identification by X-ray powder diffraction very difficult.

	X-ray f($\theta = 0$)	neutron b(fm)
H	1	-3.74
D	1	6.67
O	8	5.80
Al	13	3.45
Ar	18	1.91
Ti	22	-3.44
Zr	40	7.16
68%Ti 32%Zr	27.8	0.00

Table 2: X-ray and neutrons scattering factors. The negative neutron scattering factors for H and Ti are not unreal, but imply a change in phase of π for the scattered wave. In this way, a mix of elements, such as Ti and Zr, can lead to a zero neutron scattering factor.

All radiation passing through matter is absorbed to some extent and can be described by the equation:

$$I = I_0 e^{-\mu t}$$

where I_0 and I are the intensities of the incident and transmitted radiation respectively, μ is the absorption co-efficient of the material and t is the thickness through which the radiation passes. The crystalline samples in this work were studied under gas pressures of a few thousand atmospheres, requiring a pressure cell of considerable wall thickness. Neglecting the nature of absorption, the absorption co-efficient for X-rays is much greater than that for neutrons. The pressure cells used in this work, whilst transparent to neutrons, absorb X-rays almost completely making it impossible to detect any diffraction from the sample.

For the reasons outlined above, the crystallographic study of ice under pressure is performed using neutron diffraction.

2.9 Neutron production

There are two methods currently used in the production of neutrons of flux suitable for neutron diffraction, fission and spallation, figure 24. In a fission reaction, a thermal neutron is absorbed by a ^{235}U nucleus. The excited nucleus then splits into fission fragments releasing on average 2.5 neutrons, 1.5 of which are required to keep the chain-reaction going. Each fission reaction therefore releases one neutron of typically 2 MeV. In a spallation process, a high energy proton tears through heavy nuclei

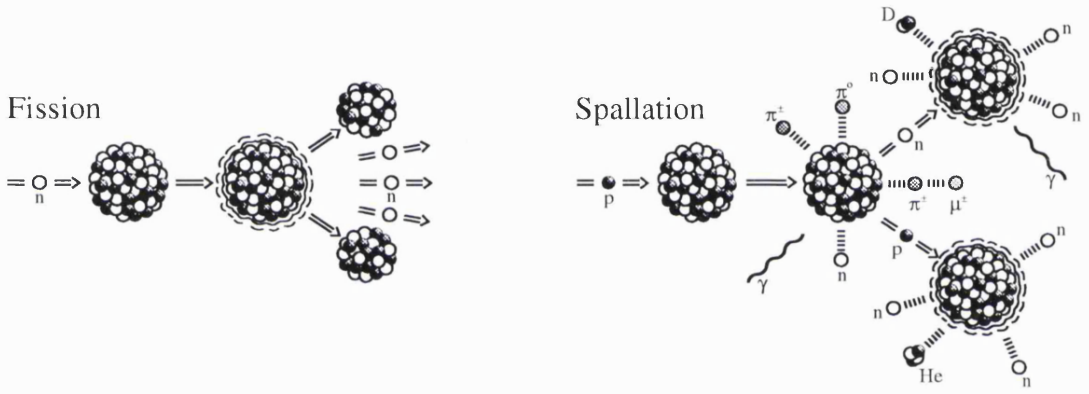

Figure 24: The two different methods commonly used in the production of neutrons of flux and energies suitable for use in the study of condensed matter.

causing the release of a whole range of particles: pions, muons, neutrinos and around 25 neutrons of energies centred around a few MeV. Although the spallation process produces an intense burst of neutrons, the process is usually pulsed as compared to the fission reaction which is continuous.

For diffraction studies, and studies of condensed matter in general, neutrons of ~25 meV in energy are required[3]. The MeV neutrons produced by the fission and

[3]Thermal neutrons, of ~25 meV in energy, have wavelengths comparable to the interatomic spacing in condensed matter; wavelengths necessary for obtaining structural information. The energy also corresponds to typical excitation energies of many solids and liquids.

spallation processes must therefore be slowed down. This is achieved by moderators consisting of light nuclei such as hydrogen or deuterium. As the neutrons pass through the moderator, they are inelastically scattered by the nuclei and are brought into thermal equilibrium with the moderator. In this way, moderators of different temperatures can produce neutrons of different energies. The exiting neutrons are distributed over a range of energies described by a Maxwellian distribution, figure 25.

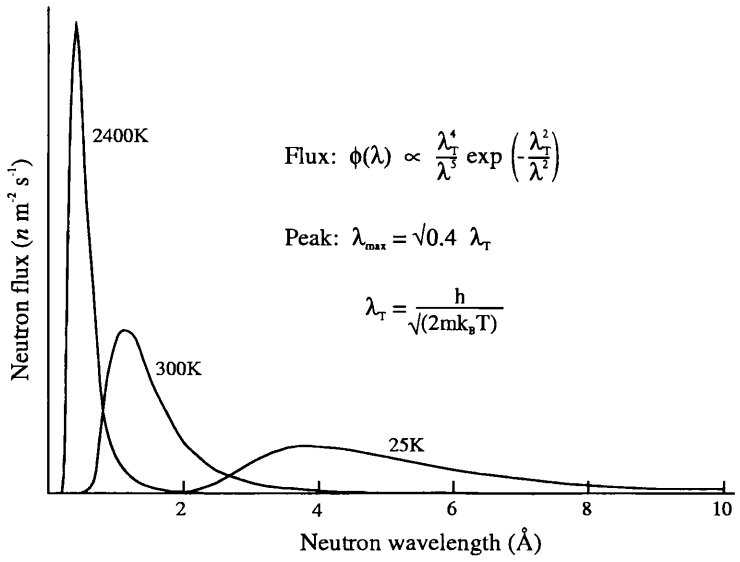

Figure 25: Neutron flux distribution after moderation at different temperatures.

The size of the moderator at pulsed sources is small in comparison to that used at reactor sources; this is to keep the length of the neutron pulse as short as possible. Since the moderator is small, hydrogen is used in preference to deuterium since it has a much larger scattering cross-section, $\sigma_s(\mathrm{H}) = 82$ compared to $\sigma_s(\mathrm{D}) = 8$ barns. The desire for a short pulse length results in some of the neutrons passing through the moderator unaffected. The unmoderated, or "epithermal", neutrons are observed in the wavelength distribution in addition to the Maxwellian distribution, figure 26.

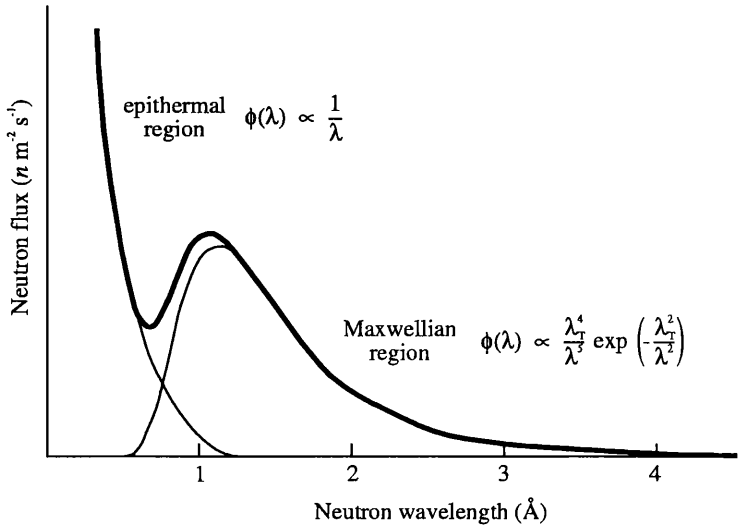

Figure 26: Neutron flux distribution for a pulsed source. The distribution is composed of two components referred to as the epithermal and Maxwellian regions.

2.9.1 ILL

The Institut Laue Langevin in Grenoble, France, operates a reactor source. Several kilograms of highly-enriched uranium are used to produce a continuous supply of neutrons for a period of approximately 50 days. The neutrons are immediately moderated by heavy water at 300 K which surrounds the reactor core, figure 27. Aluminium guides with one end inside the pool of heavy water act as passage for the neutrons to the different instruments. The neutrons moderated by the heavy water have a peak in flux at a wavelength of 1.2 Å. For a flux distribution about a longer wavelength, the neutrons are further cooled by a liquid deuterium moderator at 25 K; an increase in flux at shorter wavelengths is achieved by a graphite moderator at 2400 K, figure 25.

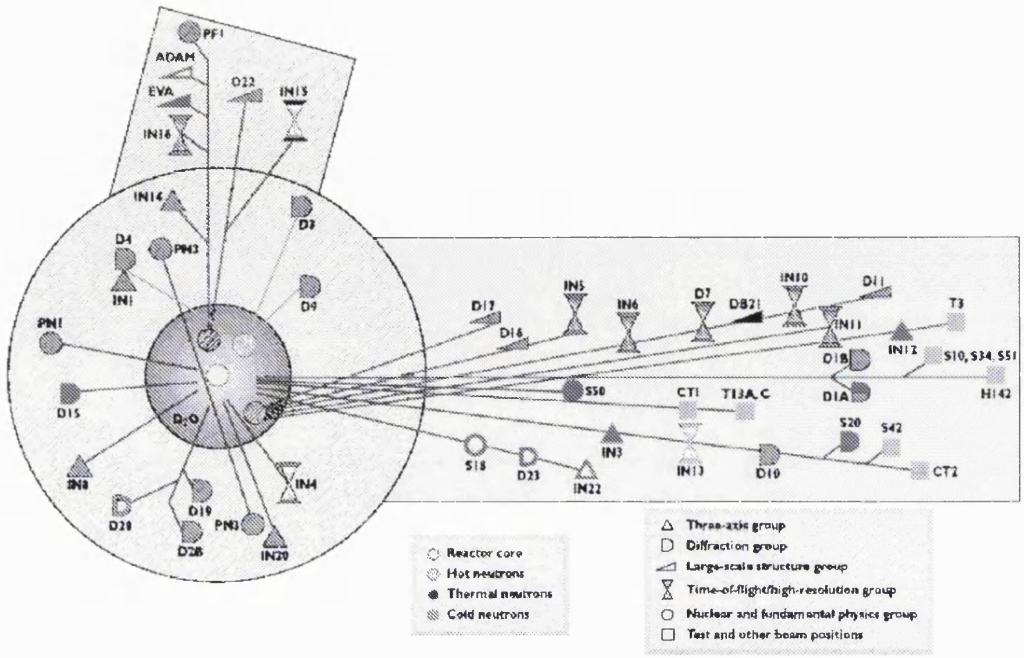

Figure 27: The layout of the ILL in Grenoble, France.
The reactor core is surrounded by a large pool of D_2O which acts to cool the fuel element and thermally moderate the emitted neutrons. A fraction of the moderated neutrons are reflected back towards the core to maintain the fission reaction.

2.9.2 ISIS

The ISIS facility, located near Oxford, England, operates a pulsed, neutron spallation source. The production of protons is achieved by first producing a source of H^- ions which are accelerated to 70 MeV, figure 28. The electrons are then stripped from the ions by use of a thin alumina foil. The remaining protons are accelerated around a synchrotron to energies of 800 MeV (0.84 times the speed of light) before being directed to the target station. The 10^{13} protons ejected by the synchrotron collide with the spallation target, usually depleted uranium or tantalum, with each proton creating around 25 neutrons for uranium and 15 for tantalum. The neutrons are then partially moderated by one of three moderators, water (H_2O, 316 K), liquid methane

(CH_4, 100 K) or liquid hydrogen (H_2, 20 K), before travelling down the guides to the different instruments.

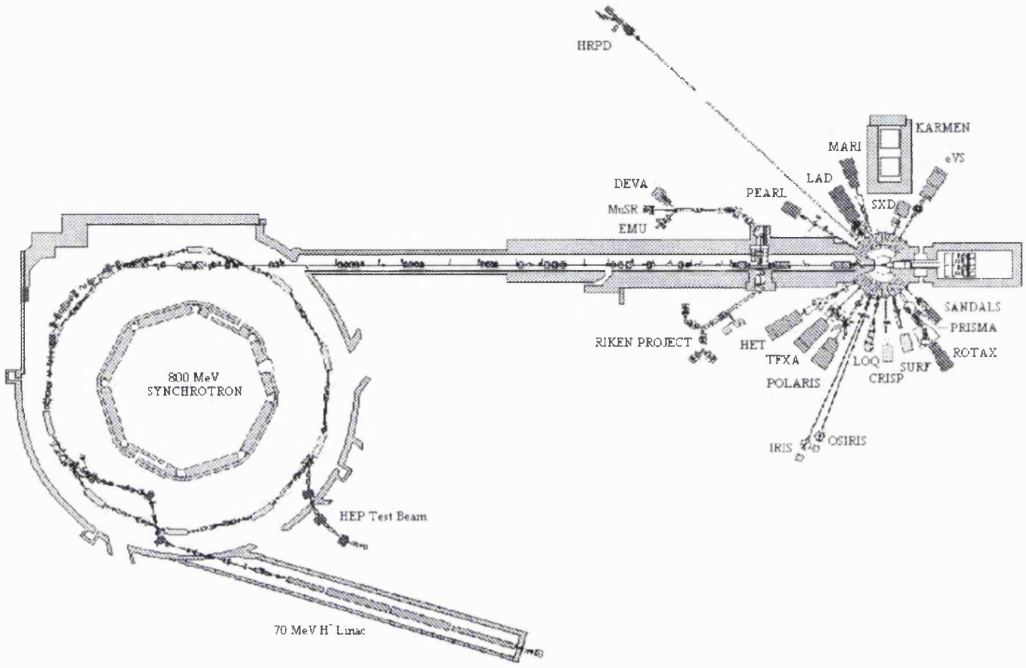

Figure 28: The layout of the ISIS facility near Oxford,UK.

The wavelength of a neutron is determined from its velocity, which is calculated from the time taken to travel from the moderator to the instrument. After a MeV neutron has been created, the time taken for it to reach the moderator is insignificant compared to the time taken for the meV neutron to reach the instrument. The moderator is therefore seen as the point at which neutrons are created, i.e. $t = 0$. If the production of neutrons was continuous it would be impossible to know at what time a particular neutron was created. For this reason, the spallation process at ISIS is pulsed, fifty times per second.

2.10 Angle and energy dispersive diffraction

There are two ways in which neutron diffraction data can be collected: by varying the angle of the detector (angle dispersive) or by varying the wavelength/energy of the incident radiation (energy dispersive).

In angle-dispersive diffraction, not all the available neutrons which exit the moderator are used. Instead, a monochromator, usually a single crystal or crystals, selects only neutrons of a particular wavelength, figure 29. By orienting the monochromator

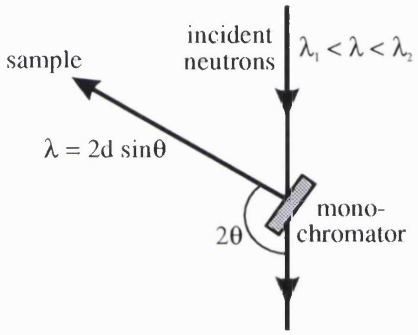

Figure 29: Monochromator used in the wavelength selection of neutrons.

crystal at different angles to the incident beam, while keeping the sample position (i.e. the angle θ) fixed, diffraction occurs for different (hkl) planes. The interplanar spacing will therefore change resulting in similar changes for the wavelength. In this way, different wavelengths can be selected by varying the orientation of the monochromator.

The single wavelength neutrons are then directed at the sample where diffraction according to Bragg's equation, $\lambda = 2d \sin\theta$, is observed. Since λ is fixed, the Bragg reflections corresponding to the different hkl planes are observed at different angles of θ. If a detector covers all angles from θ_{min} to θ_{max} then reflections with interplanar spacing, d, given by equation 8, are observed.

$$\begin{aligned} \lambda &= 2d \sin\theta \\ d &= \frac{\lambda}{2\sin\theta} \end{aligned}$$

since λ is fixed:

$$\frac{\lambda}{2\sin\theta_{min}} < d < \frac{\lambda}{2\sin\theta_{max}} \tag{8}$$

Figures 21 and 30 demonstrate a typical powder diffraction pattern, observed using a two-dimensional detector. For a perfect powder, the intensity around each of the individual rings remains unchanged. The diffraction pattern can therefore be obtained by looking at a small fragment or strip of the complete pattern, figure 30. Linear detectors or one-dimensional detector arrays are therefore generally used in the collection of angle-dispersive data from powders.

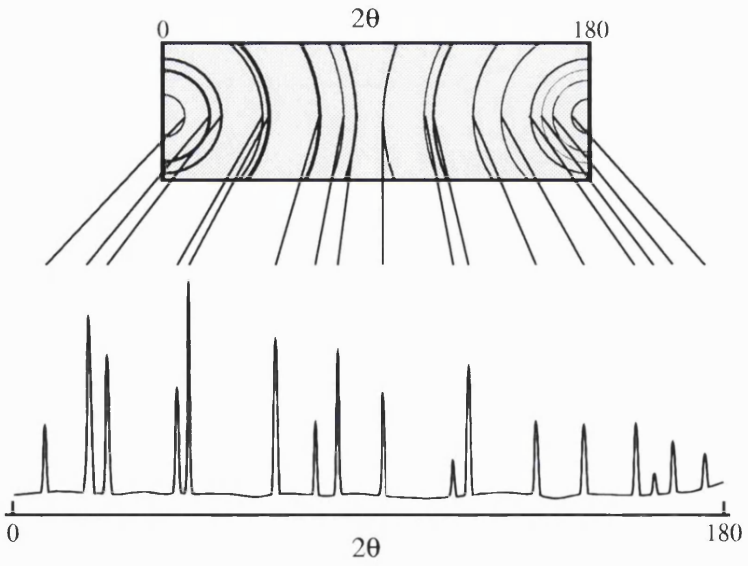

Figure 30: A typical powder pattern recorded using a two-dimensional detector (top) and a one-dimensional detector (bottom).

Rather than extracting a single wavelength from the Maxwellian distribution, figure 25, energy dispersive diffraction makes use of all the available neutrons. A detector positioned at a fixed angle, θ_{det}, will cover all interplanar spacings, d, given by equation 9.

$$\begin{aligned} \lambda &= 2d \sin \theta_{det} \\ d &= \frac{\lambda}{2 \sin \theta_{det}} \end{aligned}$$

since θ_{det} is fixed:

$$\frac{\lambda_{min}}{2 \sin \theta_{det}} < d < \frac{\lambda_{max}}{2 \sin \theta_{det}} \tag{9}$$

where λ_{min} and λ_{max} are the minimum and maximum wavelengths of flux suitable for diffraction. By changing the angle of the detector, θ_{det}, the d-spacing range covered also changes. It is therefore common on energy-dispersive instruments to find many detectors, collectively referred to as a 'bank', at a particular angle, with banks of detectors found at different angles. The diffraction pattern collected on an energy-dispersive instrument differs to that collected on an angle-dispersive instrument with the neutron energy rather than the diffraction angle recorded. Since interplanar spacings, d, are directly proportional to the neutron wavelength, diffraction patterns from energy-dispersive instruments are normally shown as a function of d-spacing.

Chapter 3

Experimental methods

3.1 Sample preparation

3.1.1 The use of D_2O

As discussed in section 2.8, the use of neutrons in the crystallographic study of ices is important for determining the positions of the hydrogen atoms. However, the interaction between neutron and atom differs for the isotopes hydrogen and deuterium. Coherent scattering is responsible for the diffraction features from which structural information is obtained. For hydrogen and deuterium, the coherent neutron scattering lengths are -3.74 and 6.67 fm respectively. The negative coherent scattering length for hydrogen is not unphysical but refers to a change of π in the phase of the scattered neutron. The contrasting scattering lengths for the two isotopes proves extremely useful in locating the position of the hydrogen atoms by H-D substitution, i.e. to repeat the same experiment first with hydrogen and then with deuterium. This technique is of particular use in the study of disordered systems involving hydrogen. For crystalline systems, H-D substitution is not required as the positions of the atoms

are clearly visible as areas of high scattering density in Fourier maps[1]

Hydrogen and deuterium also exhibit incoherent scattering which arises from their nuclear spins. For the same isotope in a crystal structure, the size and parity of the nuclear spin is the same throughout. However, the orientation of the spin varies from atom to atom in a random way. Since the incident neutron itself has spin, the interaction will also differ from atom to atom. This incoherent scattering gives rise to an increase in the recorded background which can obscure structural features arising from the coherent scattering. For hydrogen the incoherent scattering is strong, whereas for deuterium the effect is much weaker, only 3% of that for hydrogen [57]. In single crystal experiments, where the peak-to-background ratio is high, hydrogen is still routinely used. For powders, however, the peak-to-background ratio is much smaller and deuterium is generally used in the study of such systems. In this work, D_2O was used in preference to H_2O for the study of powdered ices.

There are subtle differences in the structure and properties of H_2O and D_2O ices. For example, the melting curves for D_2O ices are as much as 4 K higher than those for H_2O [29, 30]. The lattice constants of H_2O and D_2O ice Ih were examined by Röttger *et al.* [58] using synchrotron radiation over the temperature range 10–265 K. Although the behaviour of the lattice constants for both H_2O and D_2O were very similar, the lattice constants for D_2O ice Ih were larger by a factor of 1.0010(2) at 250 K, decreasing to 1.0003(1) at temperatures below 70 K. The structures of H_2O and D_2O ice Ih were examined by Kuhs and Lehmann [59] at three different temperatures using neutron diffraction. The bond distances for D_2O were slightly

[1]It was shown in equation 6 that the structure factor, $\mathbf{F}_{(hkl)}$, is the Fourier transform of the distribution of scattering density. The distribution of scattering density, $\rho(x, y, z)$, is therefore the Fourier transform of the structure factor, obtained from the intensities of the hkl reflections and the phase α. Two dimensional plots of the density distribution, with the third dimension highlighted by contours, are referred to as Fourier or density maps.

larger that those for H_2O, table 3. The increases in the O–O bond distances for D_2O ice Ih were commensurate with the increases in the lattice constants.

Therefore, it should be noted that while H_2O and D_2O ices are structurally very similar, subtle differences do exist.

	O–H1	O–H2	O–O′	O–O″	H1–O–H2	H2–O–H2	O′–O–O″	O″–O–O″
H_2O	1.009(2)	1.005(1)	2.752(1)	2.752(1)	109.42(14)	109.53(14)	109.37(2)	109.57(2)
D_2O	1.002(1)	1.001(1)	2.755(1)	2.755(1)	109.30(6)	109.65(6)	109.32(1)	109.62(1)

Table 3: The bond distances and angles in H_2O and D_2O ice Ih determined by Kuhs and Lehmann [59] at 123 K.

3.1.2 Ices

Two different methods were adopted in the preparation of the ices. In the first, the pressure cell was loaded with powdered ice Ih prior to any application of pressure. This has the advantage of ensuring a good quality powder. In the second, the pressure cell was loaded with liquid rather than solid D_2O. Having applied the pressure, the temperature was decreased until the liquid froze. Freezing the liquid under such conditions would result in a few large crystals rather than the desired fine powder. It was therefore necessary to include silica wool which assists in forming a good powder by occupying much of the available space, and so prevents the formation of large crystals. Although a good powder is not guaranteed, this approach is necessary when trying to form ices which can only be formed from the liquid, eg. ice IV. The two methods are now described in more detail.

Powdered ice

The deuterium in heavy water will exchange with the hydrogen present as water vapour in the air. To minimise this exchange, the powdered ice was prepared in a glove bag. D_2O was splashed onto the floor of the glove bag and left for several hours prior to sample preparation, the intention being to saturate the air with D_2O. The powdered ice was then prepared by grinding the frozen D_2O with a mortar and pestle. Liquid nitrogen is first poured into the mortar, 1 ml of D_2O (99.9% deuterated) is then slowly dripped into the pool of nitrogen whereupon it immediately freezes to form small droplets of ice. The droplets are then ground using the pestle until finely powdered. This procedure normally takes a few minutes during which time liquid nitrogen is added occasionally to prevent the ice melting.

Once the powdered ice had been prepared it was then carefully loaded into the gas pressure cell. During filling, the cell sits in a small reservoir of liquid nitrogen to maintain sub-zero temperatures. Filling is carried out in small steps, allowing the ice to be compacted been steps; this is done to maximise the amount of sample in the neutron beam. At the same time however, care was taken not to compact the ice too well. Ice Ih grows as flat crystals and severe compression could result in preferred orientation in the (001) direction. As it turned out, none of the samples prepared in this way ever showed signs of preferred orientation and it would have been possible to compress the ice further.

Once loaded, the cell was screwed onto the pressure centrestick and lowered into a helium cryostat. Upon reaching the desired temperature, the gas pressure was increased.

Liquid and silica wool

The preparation using liquid D_2O is much quicker and less tedious than that of powdered ice. The pressure cell was loosely filled with roughly 0.1–0.2 g of silica wool into which ~1.5 ml of liquid D_2O (99.9% deuterated) was distributed throughout using a syringe and needle. The speed with which this could be carried out meant using a glove box to minimise H-D exchange was unnecessary.

The cell was then screwed onto the pressure centrestick and the gas pressure increased. Once at pressure, the sample was lowered into a helium cryostat and cooled to a temperature below the liquid-solid transition curve. A further advantage in preparing ice from the liquid, was that any pressure leaks could be rectified outside the cryostat at room temperature without fear of melting the sample.

3.2 Pressure control

3.2.1 Gas cell

This work required a cell capable of withstanding gas pressures up to 6 kbar, in the temperature range 100–300 K, whilst being transparent to neutrons of typically meV in energy. Ideally the number of Bragg reflections arising from the cell, which only serve to contaminate the data, should be small. The material which best fits the criteria is an alloy of titanium and zirconium. The mechanical properties of the alloy are such that a cell of suitable thickness can be made to withstand such pressures while transparent to the large majority of neutrons. Furthermore, the coherent scattering lengths of titanium and zirconium, table 2, are such that an alloy of 68% Ti and 32% Zr has a total, coherent scattering length of zero. There are therefore no Bragg reflections arising from the cell.

At lower pressures where the mechanical strength required is not as great, aluminium alloys are often used. The total scattering and absorption cross-sections for aluminium are only 19% of that for the TiZr alloy [57]. This increase in transparency facilitates much shorter data collection times. Although the coherent scattering length of aluminium is non-zero, the number of Bragg reflections arising from the cell are small and can be easily excluded from the data profiles.

Two different designs of gas pressure cell were used throughout this work, and although based on the same principle, one clearly performed much better than the other.

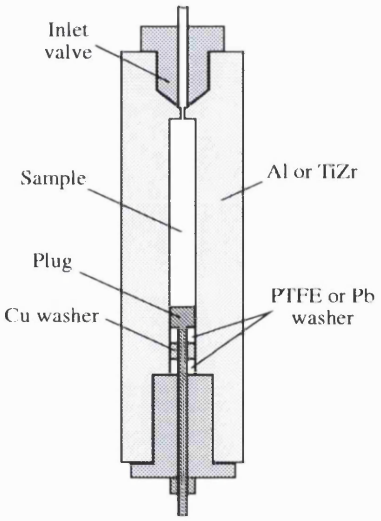

Figure 31: The ISIS gas pressure cell.

The first type of pressure cell is that used by the sample environment team at ISIS, figure 31. It consists of a cylindrical body of either TiZr or Al alloy with two open ends. The top opening provides a small conical aperture for the gas inlet valve. By applying a small amount of torque, the cone of the inlet valve is slightly deformed to form a tight seal. This is generally the tight part of the cell, but because of the small aperture, the sample cannot be loaded from this end. Instead, the sample is loaded from a much larger opening at the bottom of the cell. After loading, a plug

and a couple of washers, collectively known as the Bridgman seal, are screwed into the base of the cell. As the gas pressure is increased, the plug is forced downwards causing the two PTFE or Pb washers to squash, forming a tight seal with the wall of the cell.

The second type of cell is that used at ILL and is based on the original design of Paureau and Vettier [60]. Rather than having two openings in the cell, with two possibilities for leak, the ILL cell has only the one opening. The principles involved in forming a pressure-tight seal are very similar to that used in the ISIS cell. However, rather than having a separate opening for the gas inlet, the gas enters via a capillary which runs inside the plug.

Blockages in the pressure line were frequent when using the ILL pressure cell. This meant that pressure changes throughout the system were sometimes not experienced inside the cell. The blockages were always found to occur close to the point at which the pressure line attaches to the cell. It was therefore thought that the sample may be the cause by blocking the gas inlet valve. As a result, the samples were first loaded into a closed aluminium can which then sat inside the pressure cell. Unfortunately, this did not appear to help and blockages in the pressure line persisted. The blockages were identified by a strain gauge fixed to the pressure cell and cleared by applying heat at the point of juncture between pressure line and cell. Care was always taken to ensure the recorded pressure was that inside the cell. Wherever doubts over the pressure exist, they have been clearly stated as such in this work.

Argon gas was used throughout as the pressure medium for studying the high pressure ices. Although argon forms a gas hydrate in the presence of water, additional work has shown that growth is hindered by remaining at low temperatures [61]. Only by sitting close to the ice melting curve does clathrate growth become considerable.

Even at melting temperatures, the rate of argon clathrate growth was found to be particularly slow in comparison with the rate of growth for other gas hydrates such as xenon or krypton.

3.2.2 Liquid cell

Ideally, investigation of the high pressure ices would be studied using a non-reactive pressure agent. Unfortunately, all gases, which remain gaseous under the conditions required, are known to form gas hydrates[2]. A liquid medium, however, offers a possible alternative. The properties of the liquid must satisfy three important criteria: it must not react with water, remain liquid under the pressure and temperature conditions required, and it must be transparent to neutrons.

An attempt at forming ices III and V using fluorinert proved unsuccessful. The fluid, which had not been tried under such conditions, solidified under the pressures and temperatures required. Since no other liquids appeared suitable, no further attempts were made using the liquid cell.

3.2.3 The compressor and intensifier

Gas pressures up to 6 kbar were produced by the use of a compressor and intensifier. The compressor, which can achieve pressures up to 3 kbar, is analogous to a bicycle pump and tyre. Gas is drawn from the source and forced into a chamber (the tyre), via a one-way valve, by means of a moving piston (the bicycle pump). For pressures greater than 3 kbar, a small fraction of the gas already at 3 kbar is sectioned off. The

[2]It is not known whether hydrogen or neon form gas hydrates. However, the use of hydrogen gas under such pressures clearly carries huge safety problems, while it was feared that neon may form the helium hydrate structure, chapter 4, and prevent the formation of ices III and V.

intensifier then increases the pressure up to 6 kbar by decreasing the volume occupied by the gas. This is done by means of a piston; the piston is slowly driven forwards and backwards to increase and decrease the pressure respectively.

The pressure is recorded by a manganin resistance gauge. Essentially a form of potentiometer, the external pressure on the gauge causes the movement of an internal membrane which then registers a potential difference.

3.3 Temperature control

At both ILL and ISIS, temperatures were controlled by the use of a helium cryostat figure 32. The pressure cell sits in an partly evacuated chamber with only 10 mbar of helium gas. The helium in the chamber is referred to as the exchange gas and acts as a thermal conductor between the pressure cell and the temperature bath. The temperature is crudely controlled by changing the rate of flow of helium gas through the temperature bath. Fine temperature control is achieved through a heater located below the temperature bath. A thermocouple, located at the heat exchanger, is in thermal contact with the sample-chamber wall and is used as the reference temperature of the cryostat. The task of controlling the temperature is fully automated and by varying the power to the heater, the cryostat temperature can be kept within 0.02 K of the desired value. Unfortunately, temperature gradients arise throughout the cryostat as the warmer gas rises and the colder gas sinks. The temperature of the pressure cell, located below the cryostat thermocouple, is often a few degrees colder than that registered. It is therefore essential that the pressure cell also has at least one thermocouple to measure directly the temperature of the cell.

Temperature gradients across the pressure cell still exist, the bottom being slightly

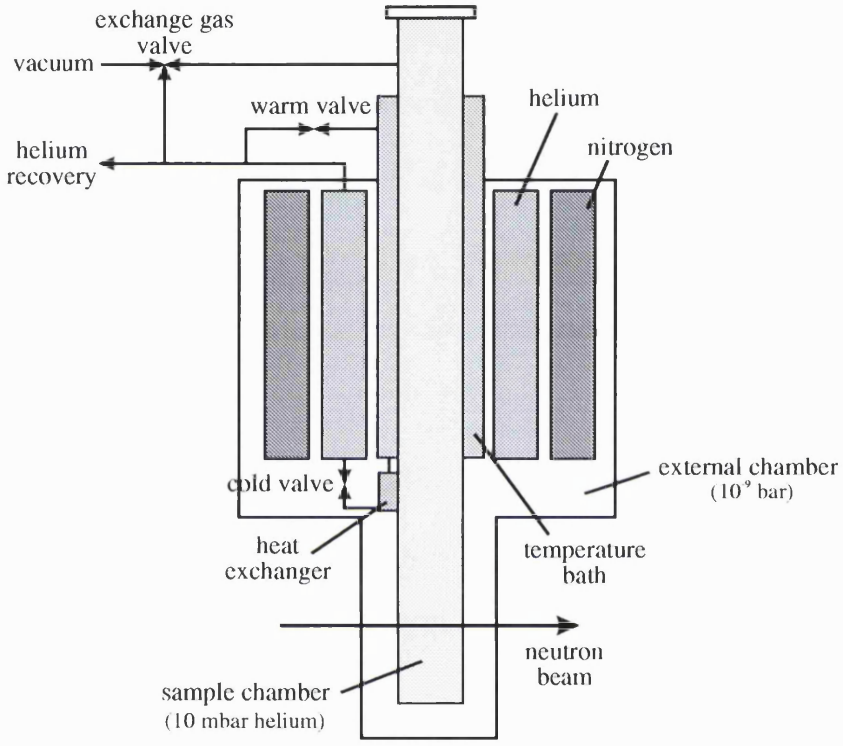

Figure 32: Cross-section of the helium cryostat.
The sample chamber is partly evacuated by means of the exchange gas valve, leaving just 10 mbar helium gas for thermal exchange. The temperature is crudely controlled by opening and closing the warm and cold valves which regulate the flow of helium gas through the temperature bath. A heating coil and thermocouple are located at the heat exchanger for fine control of the cryostat temperature. Warming of the liquid helium is minimised by a surrounding liquid nitrogen chamber. Both are housed inside a chamber evacuated to 10^{-9} bar.

colder than the top, and it is important to highlight here the magnitude of the gradients involved.

The ILL pressure cell had only one temperature sensor located at the top of the cell. The helium flow through the temperature bath was kept low so that the power used in the heating coil was also kept low to minimise the temperature gradients. The difference between the sample and cryostat temperatures was around 3 K. The temperature difference across the sample is expected to be much smaller since it is contained within a metal alloy of much higher thermal conductivity. Although no attempts to establish the size of the temperature gradients were made, they are thought to be less than 1 K [62].

The ISIS pressure cell fortunately had two thermocouples and two heaters, one of each located at the top and bottom of the cell. This not only makes temperature changes much quicker, but temperature gradients are of course eradicated. During one of the many experiments at ISIS, it was not possible to use both cell heaters and the use of only one served to increase the temperature gradient. Both heaters were therefore turned off and a situation similar to that at ILL was established. The temperature difference between the top and bottom of the pressure cell never exceeded 0.5 K.

3.4 Neutron instruments

3.4.1 D1A

D1A [63], figure 33, is a medium-flux, angle-dispersive, powder diffractometer situated 60 m from the nuclear reactor at ILL. Ten germanium crystals select a monochromatic beam of neutrons from the spectrum of energies; the typical wavelengths available are

shown in table 4. The neutrons are then diffracted by the sample and detected by

Ge (hkl)	λ (Å)
117	1.390
335	1.514
115	1.911
113	2.994

Table 4: The available D1A monochromator Bragg planes with corresponding wavelength. The optimum plane in terms of flux is the (115) with a wavelength of 1.911 Å.

ten ^{3}He detectors. Although the instrument resolution is not as good as that found on D2B, the near perfect Gaussian peak shape makes D1A suitable for the study and subsequent refinement of high-symmetry systems. More recently, the number of detectors has increased to twenty five making data collection times shorter, and the monochromator has been improved giving better resolution.

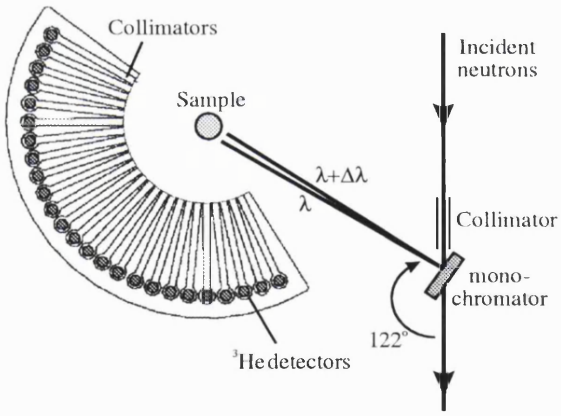

Figure 33: The layout of the D1A diffractometer.

3.4.2 D2B

D2B, like D1A, is also an angle-dispersive powder diffractometer found at ILL [64]. Its design is very similar to that of D1A, figure 33, but is located only 17 m from

the reactor giving a considerable increase in neutron flux. The monochromator is constructed from twenty-eight germanium crystals giving a choice of wavelengths from 1.05 to 3.15 Å, table 5. Better quality germanium crystals and a more sensitive

Ge (hkl)	λ (Å)
557	1.051
337	1.277
551	1.464
335	1.594
331	2.398
113	3.152

Table 5: The available D2B monochromator Bragg planes with corresponding wavelength. The optimum plane in terms of flux is the (335) with a wavelength of 1.594 Å.

positioning system for the detectors result in higher resolution than that found on D1A. The sixty four ^{3}He detectors spaced at 2.5° intervals cover 160° in 2θ also result in much shorter data collection times.

3.4.3 HRPD

The High Resolution Powder Diffractometer (HRPD) at ISIS is the highest resolution neutron powder diffractometer in the world [65]. The resolution is achieved by virtue of the diffractometer's position, some 100 m from the target. This large distance means the relative errors in time and distance travelled by the neutron, ΔT/T and ΔL/L respectively, are very small. Accuracy of the neutron velocity and hence its wavelength lead to similarly small errors in d-spacing. Furthermore, the resolution is effectively constant over the chosen d-spacing range. HRPD is situated on a methane moderator giving it a range of neutron wavelengths between 0.5 and 12 Å with a peak in the neutron flux at 2 Å. However, the long distance travelled by the neutrons

on a pulsed source, where a new batch of neutrons arrives every 1/50th of a second, means problems arise with overlapping neutrons. The overlap can be cured in two ways, although a compromise between the two is normally reached. First, not every pulse is used. Instead, all the neutrons of one pulse are detected before any other pulse is allowed pass. This, however, is time consuming since it involves waiting for the slow, long wavelength neutrons. Second, not all the neutrons in a single pulse are used. If only neutrons of the same velocity are selected from each pulse, then clearly neutrons of one bunch cannot catch-up with another and overlap. Both possibilities involve a reduction in neutron flux and is the price paid for the high resolution. A compromise, which depends on the experimental requirements, typically uses every fifth pulse, with the fragment of the pulse used spanning about 2 Å in wavelength. Two choppers are situated along the neutron guide, the first to select the fragment of the pulse, and the second to select every *nth* pulse, figure 34.

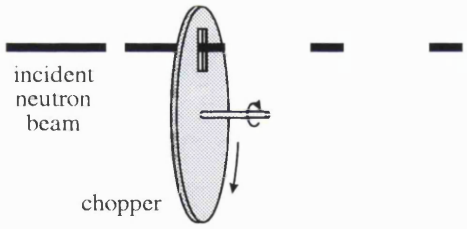

Figure 34: An example of a chopper used in neutron selection.

HRPD has three banks of detectors, two ZnS banks situated at 168° and 90° and one ^{3}He bank situated at 30°. The backscattering (168°) and low-angle (30°) banks were not used in the refinement of the data collected. The large intensity ice reflections are typically in the region 1–4 Å. For this information to be seen in the backscattering bank required incident neutrons of about 8 Å. The flux however decreased quite sharply with very few neutrons at these wavelengths, figure 25. The

additional use of a collimator to eliminate scattering from the cell, section 3.5, further reduced the flux seen by the backscattering bank. The resolution of the low-angle data was very poor and offered no more information than that collected by the 90° bank. The high resolution of HRPD makes the instrument ideal for the study of low-symmetry systems and the structure determination of unknown compounds.

3.4.4 TEB/PEARL

Test beam (TEB) is a very simple instrument used for preliminary investigations. It is located only 13 m from the target and does not require the use of choppers to prevent pulse overlap. Like HRPD, TEB is located on the methane moderator and has a neutron wavelength range of 0.5–12 Å. Originally TEB had only two banks of ^{3}He detectors at 90°. Now the instrument, renamed PEARL, has nine banks of detectors at 90°, each covering 30° around the beam and 15° in 2θ. This large coverage around 2θ (135°) helps in the identification of texture from a poor sample. Furthermore, a small amount of texture may be averaged out by such a large coverage. Because TEB is only 13 m from the target the resolution is poor compared to HRPD, but the neutron flux is much higher. This makes TEB a suitable instrument for probing phase transitions; in particular, the identification of metastable phases with short lifetimes.

3.4.5 POLARIS and IRIS

Other instruments at ISIS which were used in this work are POLARIS and IRIS. The characteristics of POLARIS are similar to those of PEARL: a medium-resolution, high-intensity, powder diffractometer located only 12 m from the target [66]. However, POLARIS uses water rather than methane to moderate the neutrons, resulting in a larger flux at shorter wavelengths. Like PEARL, POLARIS is ideal for the study of

samples with short life-times or small volume. IRIS is analogous to HRPD in its use of choppers [67]. Although IRIS is generally used for quasi- and inelastic scattering, its closer proximity to the target (36 m), and longer wavelength distribution by virtue of the hydrogen moderator, makes the instrument suitable for the study of large scale structures requiring long d-spacing data.

3.5 Collimation of energy dispersive neutrons

The position of detectors used in the collection of energy dispersive data are fixed. This allows the incident and diffracted beams to be collimated at the sample, thereby eliminating scattering from the pressure cell which would otherwise contaminate the diffraction profiles, figure 35. Since this form of cell collimation requires the detectors to be fixed, it cannot be used in the collection of angle-dispersive data. There is, however, an important disadvantage in using this form of collimation. If the diffraction profiles indicate texture within the sample, this can often be removed by rotating the sample through various omega positions. With fixed sample collimation, rotation of the sample is of course impossible.

3.6 Rietveld refinement

3.6.1 GSAS

The General Structure Analysis System (GSAS) [68] was used in the refinement of all data. Although other software packages were investigated, such as FullProf [69], CCSL [70,71] and PROFIL [72], GSAS proved a much more flexible and user-friendly environment in which to analyse the data. Angle-dispersive and energy-dispersive

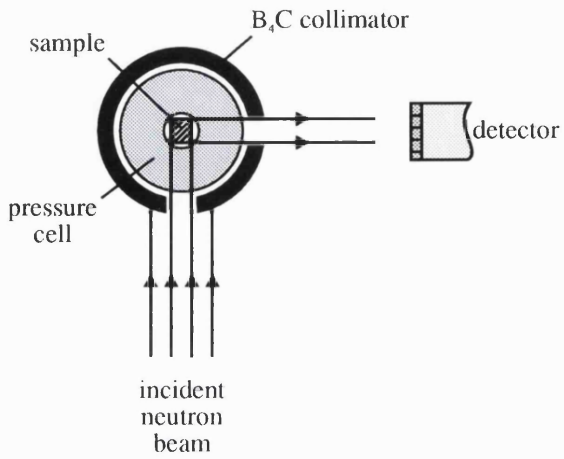

Figure 35: Sample collimation used in energy dispersive data collection to eliminate contamination by the pressure cell. The collimator is made of B_4C which absorbs all neutrons of meV energies. Since only the sample is at the centre, only diffraction from the sample exits and is registered by the detector.

data could both be handled by GSAS, simultaneously if required; many different models for fitting parameters such as the background, peak shape and absorption were available; and parameters could be refined under restraint, a function relied heavily upon in this work

The only drawback in using software written by others is the assumption that all results generated are correct. Fortunately, GSAS has been available to the public since 1985 and has gained much popularity since. The only reports of errors in the software appear to be initial teething problems associated with platform compatibility rather than erroneous results.

Although it would have been advantageous to refine all the data using more than one software package, this would have proven extremely time consuming. At the start of this work, various software packages were used to refine a particular data set. No significant differences were found in the results generated by the different packages.

3.6.2 Criteria for convergence

If the refinement procedure were not controlled in some way, then it would continue indefinitely making smaller and smaller changes to the model being refined. At some point the changes made to each parameter will be smaller than the uncertainty associated with them, section 3.6.9. When this occurs, further changes to the model fail to improve the residual being minimised, equation 7, and the refinement is said to have reached *convergence*. Mathematically, convergence is achieved when

$$\sum_j \left(\frac{\Delta x_j}{\sigma_j}\right)^2 < \varepsilon \tag{10}$$

where Δx_j is the change in parameter x_j, σ_j is the estimated standard deviation associated with parameter x_j, and ε is some fraction. The sensitivity of the refinement is controlled by the value of ε; a large value of ε will cause the refinement to reach convergence quickly while a small value will result in a much slower convergence. If ε is set too small, it is possible that convergence may never be reached. The value of ε used by GSAS was 0.01.

Upon convergence, the refinement is sitting in what is referred to as a *residual minimum*. Further changes to the model at this point will only serve to increase the residual S, equation 7, and hence worsen the fit. If only one parameter is refined, say x, then the residual, S, may vary as in figure 36. If the initial value of x is 0 and the

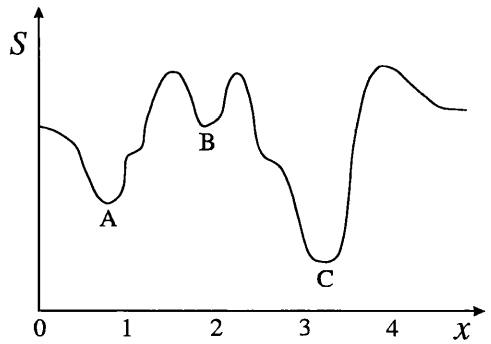

Figure 36: An example of the variation in residual S with parameter x. Points A and B are local minima while point C is the global minimum.

refinement changes x by 0.1 per cycle, then convergence will be reached at $x = 0.8$, point A. However, this is not the lowest possible value of S, i.e. the true residual minimum, which is found at point C. Points A and B are referred to as *local* or *false minima* with point C referred to as the *global minimum.* Naturally, the global minimum is the solution one hopes the refinement will reach. Had the refinement started from a value of $x = 3$, then the global minimum would have been reached without trouble. It is therefore essential that the refinement starts from a point close to C, that is, that the initial model used in the refinement is a reasonable estimate of the true crystal structure.

3.6.3 The initial model

Rietveld refinement is not a form of structure solution [73] and as such an initial structural model must be provided. The correct space group symmetry and a good estimate of the lattice constants and atomic parameters are needed to prevent the refinement from falling into local minima. The required accuracy of the initial model depends on the structure being refined, in particular, the number of atoms in the asymmetric unit. Fortunately, the majority of structures examined in this work had been determined beforehand, albeit at ambient pressure and liquid nitrogen temperatures.

3.6.4 Turn-on sequence

The order in which the parameters are refined can be important for avoiding a divergent refinement and local minima.

The refinement procedure followed in this work consisted of two parts. The first was the stable part of the refinement with the results interpreted graphically rather

than numerically. The background and scale are first refined after which peaks arising from the pressure cell were excluded. The lattice constants and zero-offset were then refined before finally the peak profile. The refinement of all these parameters, with the exception of the peak profile, was extremely robust and the order in which they were refined was not found to be important for locating the global minimum.

The second part of the procedure involved refinement of the atoms themselves, their positions, thermal motions and occupancies. This proved to be the most troublesome part of the refinement and convergence was often sluggish. For this reason, the order in which the parameters were refined was changed to ensure the global minimum had been reached, i.e. the same results were achieved regardless of order.

3.6.5 Instrument calibration

The 'fixed' instrument parameters, wavelength for angle-dispersive data and flight-path length for energy-dispersive data, were obtained through the refinement of data from a silicon standard. The lattice constants of the silicon were known to five decimal places and were kept fixed during the refinement. The instrument parameters were then refined with the resulting figures kept fixed in the subsequent refinement of the ices.

3.6.6 Background modelling

There are a number of sources responsible for the background recorded in a diffraction experiment, the main ones being incoherent scattering, air scattering, thermal diffuse scattering and scattering from non-crystalline components. The background arising from all, with the exception of non-crystalline scattering, can be reliably modelled

using a cosine Fourier series [68]:

$$y_b(Q) = B_1 + \sum_{j=2}^{N} B_j \cos(Q(j-1)) \tag{11}$$

where B_N are the refineable background parameters and Q is the position along the diffraction profile in degrees 2θ. For energy-dispersive data, neutron times are scaled by $180°/\mathrm{T_{max}}$.

The cosine Fourier series is perfectly adequate for describing backgrounds that are generally flat and/or have slowly varying curvature. The series cannot, however, model short period fluctuations such as those arising from non-crystalline matter. Although a background function was available for the treatment of non-crystalline components [74], some knowledge of the compound being modelled was required. Attempts at modelling the background using this function proved unsuccessful.

Fortunately, the backgrounds for all data were generally flat. Data collected at the ILL, and in particular on the D2B diffractometer, did however suffer from a hump at ~28°. To model this feature, the background was first determined manually and subtracted from the diffraction profile. A cosine Fourier series was then used to refine the remaining background.

The background can influence the integrated intensities of the diffraction peaks and hence the structural model. Care was therefore taken when determining the background manually and also in the number of terms used in the cosine Fourier series.

3.6.7 Peak profile modelling

The sources responsible for the peak profiles of neutron diffraction data are now well described [75–77]. The original work of Rietveld [56] was to refine crystal structures from angle-dispersive neutron diffraction data with its near symmetric-Gaussian

shape. Since then, the description of peak profiles for both angle-dispersive and energy-dispersive neutron diffraction, has undergone much development. The profiles used in this work to model the diffraction data are those developed by Howard [78] and Thompson *et al.* [79] for angle-dispersive data and Von Dreele [80] for energy dispersive data.

3.6.8 Absorption modelling

The absorption of neutrons by the pressure cell and sample was modelled according to the description given by Hewat [64], and can be expressed as the product of two factors: a scale factor and a Debye-Waller factor. The Debye-Waller factor means the absorption is directly correlated with the thermal motion of the atoms. For angle-dispersive data (fixed wavelength), the absorption and thermal factors were indistinguishable and could not be refined together. For energy-dispersive data, the absorption was assumed to vary with $1/\lambda$. This variation with wavelength meant that the absorption and thermal factors could be refined simultaneously. For angle-dispersive data, the absorption correction had very little effect on the thermal factors, within the limits of experimental error. For energy-dispersive data, however, the correction was found to be important for achieving thermal factors of the correct magnitude.

3.6.9 Interpretation of the results

In a refinement, parameters are varied to fit the experimental data. The values obtained at the end of the refinement are only an estimate of the parameters being refined. Since the parameters are unknown, the errors (or deviations) in the refined values are also unknown. This uncertainty reflects the lack of exact knowledge of the

values are also unknown. This uncertainty reflects the lack of exact knowledge of the parameters being refined. The uncertainty in the refined value is itself an estimate based on known sources of error (random and systematic). Each fitted parameter therefore has a distribution of possible values with the standard deviation of this distribution referred to as the *estimated standard deviation* (e.s.d.).

The e.s.d. is the minimum possible error arising from random and systematic errors. It does not represent an experimental distribution in a parameter. For example, if the refined position of an atom is $x = 0.3(1)$, it does not imply that the atom position is distributed throughout the crystal structure with mean position $x = 0.3$ and standard deviation 0.1. Instead $x = 0.3$ should be interpreted as the most probable position of the atom, with the e.s.d. a form of confidence factor.

Figure 37 demonstrates the variation of residual S with parameter x for two data sets of different random error. The data set with the smallest error has a better defined residual minimum resulting in a smaller e.s.d.

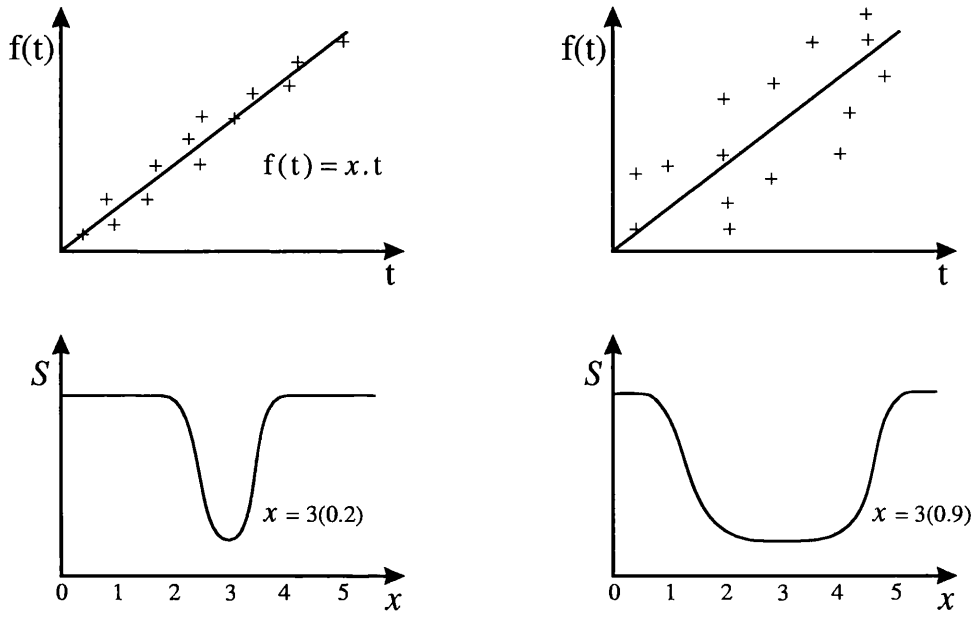

Figure 37: Two data sets of different random error are shown above. The parameter under refinement is the gradient of the line of best fit, x. An example of how the residual S might vary with x is shown beneath. The first data set has a smaller random error resulting in a better defined residual minimum. This in turn leads to a smaller e.s.d. in the estimation of x.

3.6.10 Graphical representation of fit

The profile fits resulting from the Rietveld refinement of all data sets are included in the results. These will demonstrate both the quality of data and the fit resulting from the refinement. The form which these plots take is shown in figure 38.

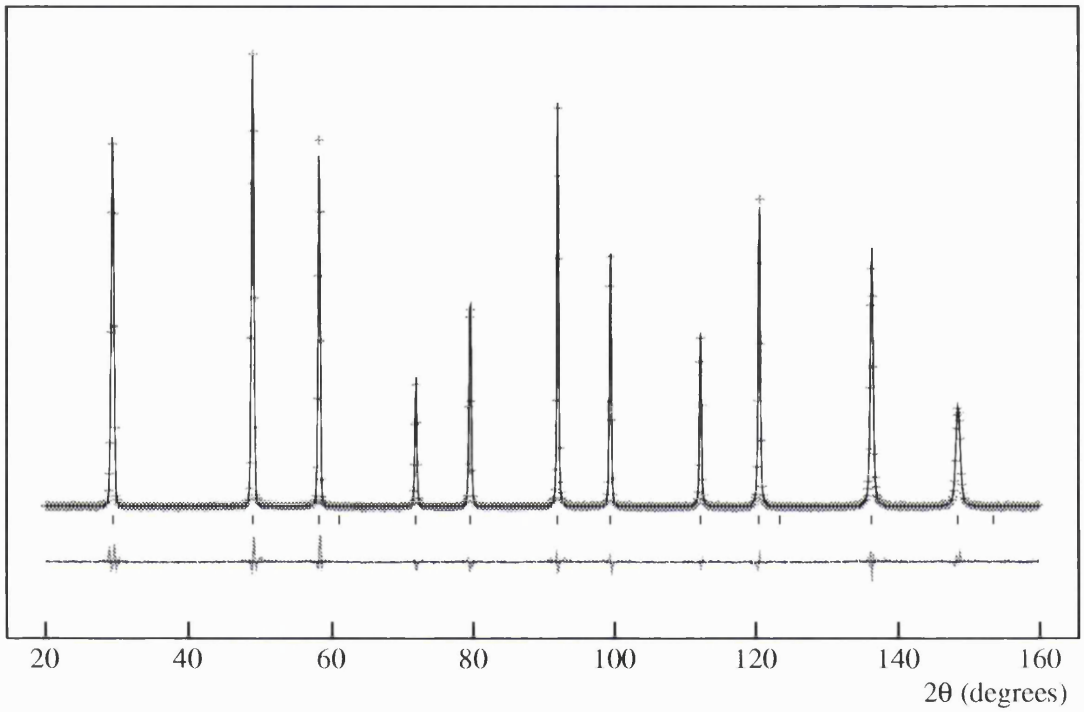

Figure 38: A graphical representation of the fit obtained from the Rietveld refinement of diffraction data. The upper plot represents the observed data (crosses) with the calculated fit (solid line) overlying them. The lower plot represents the difference between observed and calculated intensities. The tick marks between the two plots are the positions of the Bragg reflections.

Chapter 4

Ice II

4.1 Introduction

The structure of ice II was first determined by Kamb [81] in 1964. Although the study was performed using single-crystal, X-ray diffraction, a technique that is relatively insensitive to hydrogen, Kamb was able to determine the positions of the hydrogen atoms through small perturbations in the oxygen positions. In agreement with infrared work by Bertie and Whalley [82], Kamb found the water molecules were orientationally ordered. Neutron diffraction by Finch *et al.* [83] and later Kamb [84] confirmed the proposed ordering scheme.

Although the experiments outlined above were performed at low temperatures and ambient pressure, dielectric work by Wilson *et al.* [85] and entropy measurements by Whalley and Davidson [86] confirmed the existence of orientational order throughout the stability region of ice II.

The structure of ice II is based on a rhombohedral cell, space group $R\bar{3}$, with unit cell dimensions: $a = 7.78$ Å and $\alpha = 113.1°$, or $a_H = 12.92$ and $c_H = 6.23$ Å

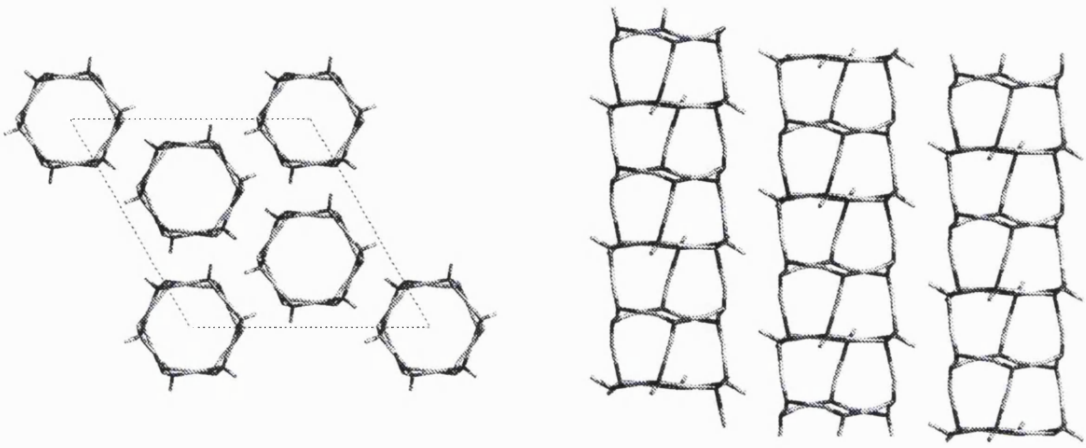

Figure 39: The hexagonal channels of ice II as viewed along (left) and perpendicular to (right) the hexagonal c_H-axis. The bonds between channels have been omitted for clarity.

for the corresponding hexagonal cell. The water molecules bond tetrahedrally to form a lattice of hexagonal channels which run parallel to the c_H-axis, figure 39. Each channel is shifted vertically along the c_H-axis relative to the next allowing the hexagonal rings of different channels to bond laterally. In this way ice II retains an open structure similar to ice Ih whilst having an increased density.

Arnold *et al.* [87] were the first to perform neutron diffraction experiments within the stability region of ice II. Needless to say, they found the water molecules of ice II were orientationally ordered. However, the use of helium gas as a medium for applying the pressure was seen to influence phase boundaries. Arnold *et al.* suggested that helium may be entering the open channels of the ice Ih and ice II structures and thereby stabilising the structures outside their normal region of stability. There was already evidence of helium entering the channels of ice Ih [88] but it was uncertain whether it was occurring in ice II.

Londono *et al.* [41] examined more carefully the effect of helium on the ice phase diagram and found that the helium enters the channels of both ice Ih and ice II in

considerable amounts. Concentrating on ice II, the structure of the helium-affected system was determined by powder neutron diffraction. The helium was found to sit in well defined positions within the c_H-axis channels, figure 40, with the helium content increasing with gas pressure.

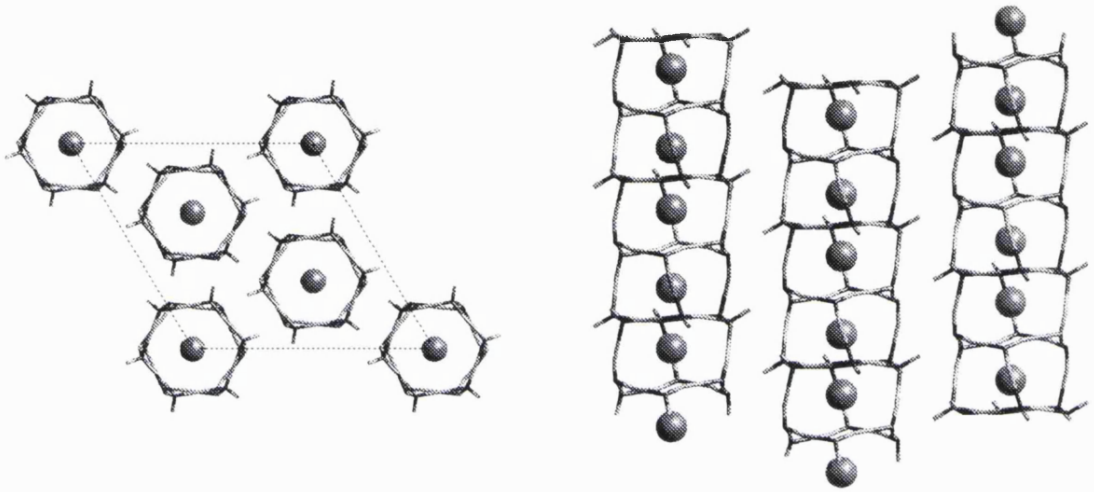

Figure 40: The helium-affected ice II lattice as found by Londono *et al.* [41]. The amount of helium present within the channels was found to increase with pressure. In this figure, the channels are fully occupied to show the definite positions held by the helium atoms.

Although the structural work on ice II appears exhaustive, there has been no diffraction data collected on ice II, under pressure without the use of helium gas, of quality sufficient for structure refinement. Londono *et al.* [41] collected two data sets on the helium-free ice II structure using a clamped cell. Unfortunately the data were very poor and only information on the lattice constants could be obtained[1]. To this end, the detailed structure of "pure" ice II under pressure is still unknown. Neutron diffraction data were therefore collected at several points within the ice II

[1]The lattice constants determined by Londono *et al.* [41] for the helium-free structure were ultimately worthless. The pressure within the clamped cell was unknown and the wavelength used in obtaining the constants proved suspicious [89].

stability region, figure 4. Argon gas was used as the pressurising medium as its size was thought to be too large to enter the c_H-axis channels.

4.2 Experimental procedure

D1A

An aluminium gas pressure cell was loosely filled with silica wool into which ~1.5 ml of D_2O was distributed by use of a syringe and needle. The cell and sample were then lowered into a cryostat located on the diffractometer and cooled to 200 K, thereby freezing the liquid. Inspection of the neutron diffraction data revealed a good ice Ih powder. Argon pressure was then increased to 4.8 kbar resulting in the formation of ice II. Data were collected at 4.8 kbar and 200 K over four different omega positions with a total of 36 hours data collection time.

There was no wavelength calibration data collected at the time of the experiment, and previous data on silicon, collected three months prior to this experiment, were used instead. Unfortunately, the refined lattice constants for ice II and ice III, studied immediately after ice II (chapter 5), were unrealistic using this wavelength. This was evident in the resulting compressibility for ice II and density for ice III. Since data on ice III had been collected on D1A and D2B under the same conditions of temperature and pressure (2.5 kbar and 240 K), the D1A wavelength was refined such that the ice III lattice constants of the D1A data best matched those of the D2B data.

D2B

Roughly 1.0–1.5 g of powdered ice Ih was loaded into an aluminium can which was then placed inside a TiZr gas pressure cell. The sample was cooled to 200 K before

argon pressure was increased to 2.8 kbar. The nature and speed with which the pressure was increased meant that it was impossible to identify the exact pressure at which the ice I–II transition occurred. A brief inspection of the neutron diffraction data showed a transition to ice II had occurred, with a full data set subsequently collected at 2.8 kbar and 200 K over 13 hours. The temperature was then increased to 240 K for a study of ice III, after which the pressure was increased to 4.2 kbar at 250 K. This resulted in a transformation to ice II with a further data set collected at 4.2 kbar and 250 K over 11 hours. Silicon data were collected at the end of the experiment for wavelength calibration.

4.3 Results

Refinement

The initial model used to refine the data was that described by Londono [89] for ice II under helium pressure of 2.9 kbar and at 197 K. The unit cell of ice II is rhombohedral, space group $R\bar{3}$; however, the corresponding hexagonal unit cell was used throughout the refinement. The hexagonal channels, in which the helium atoms are situated, run parallel to the c_H-axis. The role played by helium is therefore best demonstrated using these axes. The asymmetric unit consists of only two water molecules which adopt an orientationally ordered arrangement.

The argon clathrate that formed during data collection was modelled on the structure refined from neutron diffraction data collected at 2.5 and 4.8 kbar [61]. For the ice II data collected at 2.8 and 4.8 kbar, the amount of clathrate present was very small (3 and 11 wt.% respectively) and hence only the lattice constants of the clathrate were refined. However, for the data collected at 4.2 kbar, the clathrate present was

considerable (63 wt.%) and therefore in addition to the lattice constants, the atomic positions of the water molecules were refined. The thermal factors were kept constant. This seems reasonable as the thermal factors for argon clathrate in all refined data sets, from 90 bar to 4.8 kbar, were typically of the same value within the limits of error [61].

Reflections from the aluminium pressure cell were clearly visible in the data collected on D1A and were therefore excluded. Although no reflections from the TiZr cell were visible in the D2B data, peaks from the aluminium can, which served to prevent any sample from blocking the pressure line, were visible and similarly had to be excluded. Background points were required to describe a hump in the D2B data at $\sim 25°$, figure 43, in addition to the mathematical description, section 3.6.6.

The data were refined using GSAS with a typical "turn-on" sequence of parameters described in section 3.6.4. The small number of atoms in the asymmetric unit meant that no initial restraints were required by the refinement. Initially the thermal factors were refined isotropically but were later refined anisotropically.

The profile fits from the refinement of the data are shown in figures 41 to 43. The two sets of ticks represent reflections arising from argon clathrate (upper) and ice II (lower). The structural details arising from the refinement, atomic parameters, bond lengths and angles etc., are listed in tables 6 to 12.

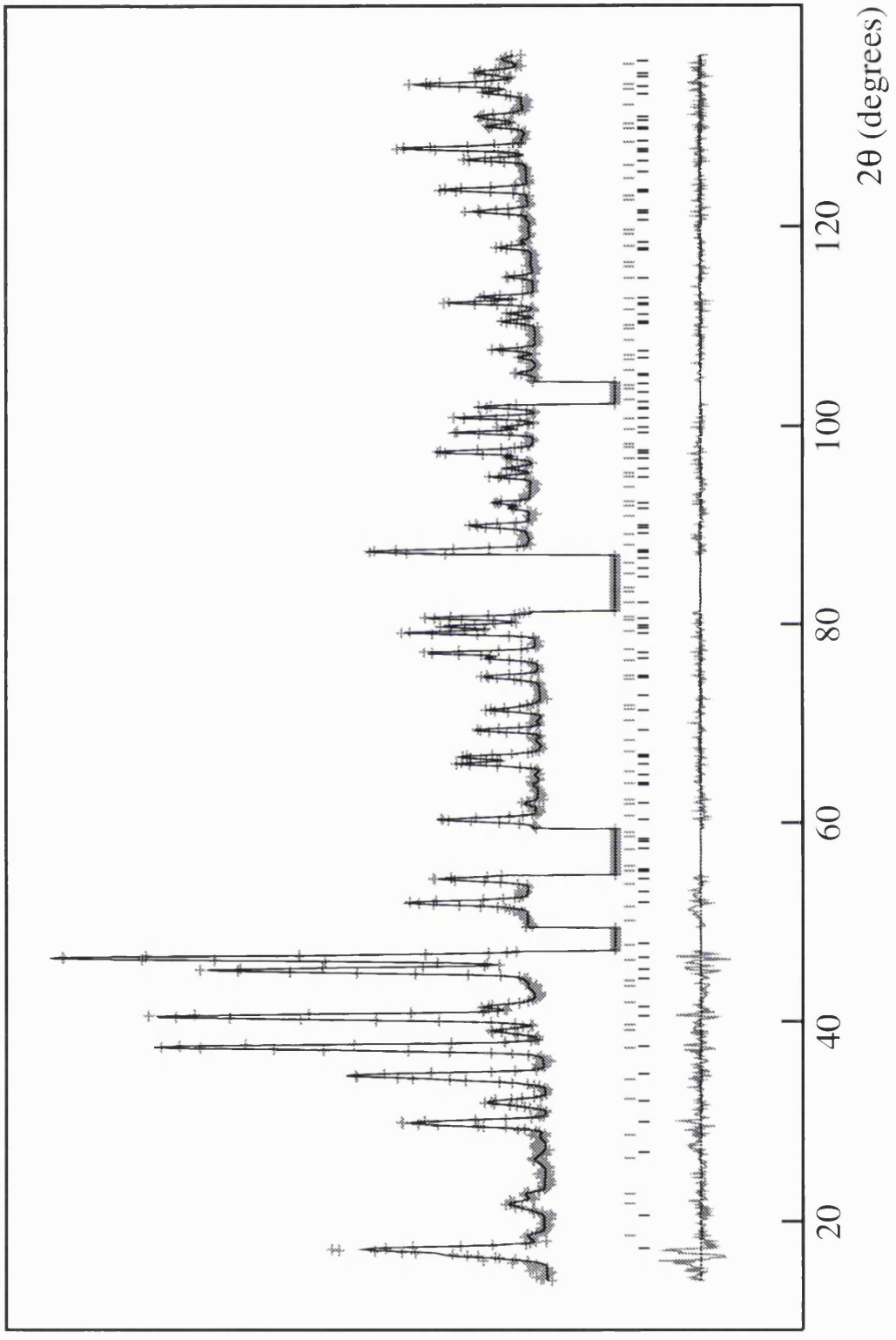

Figure 41: The profile fit for the ice II data collected on D1A at 4.8 kbar and 200 K, $R_p = 0.0302$ and $R_{wp} = 0.0347$. The amount of argon clathrate determined by the refinement was 11 wt.%.

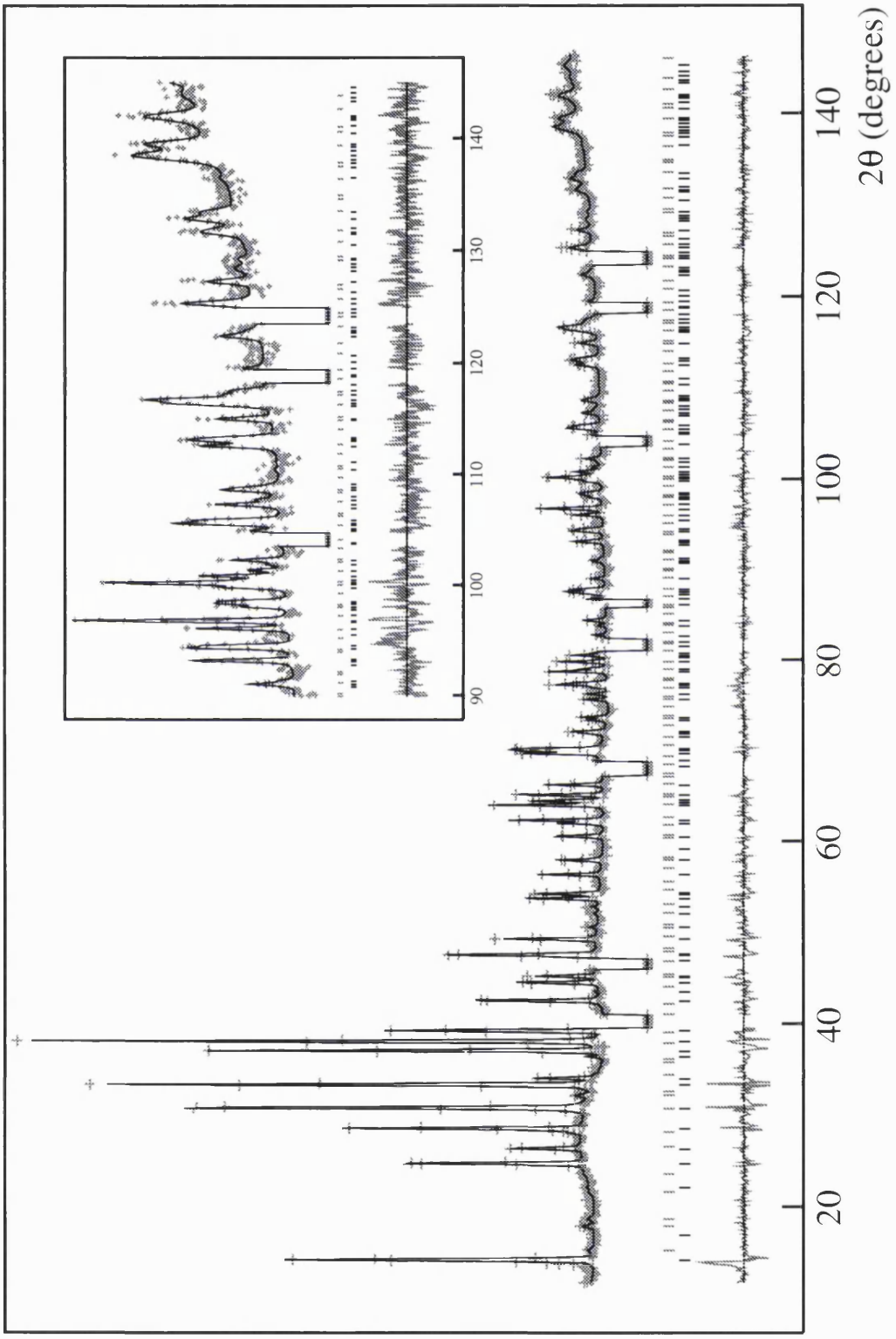

Figure 42: The profile fit for the ice II data collected on D2B at 2.8 kbar and 200 K, $R_p = 0.0122$ and $R_{wp} = 0.0183$. The amount of argon clathrate determined by the refinement was 3 wt.%.

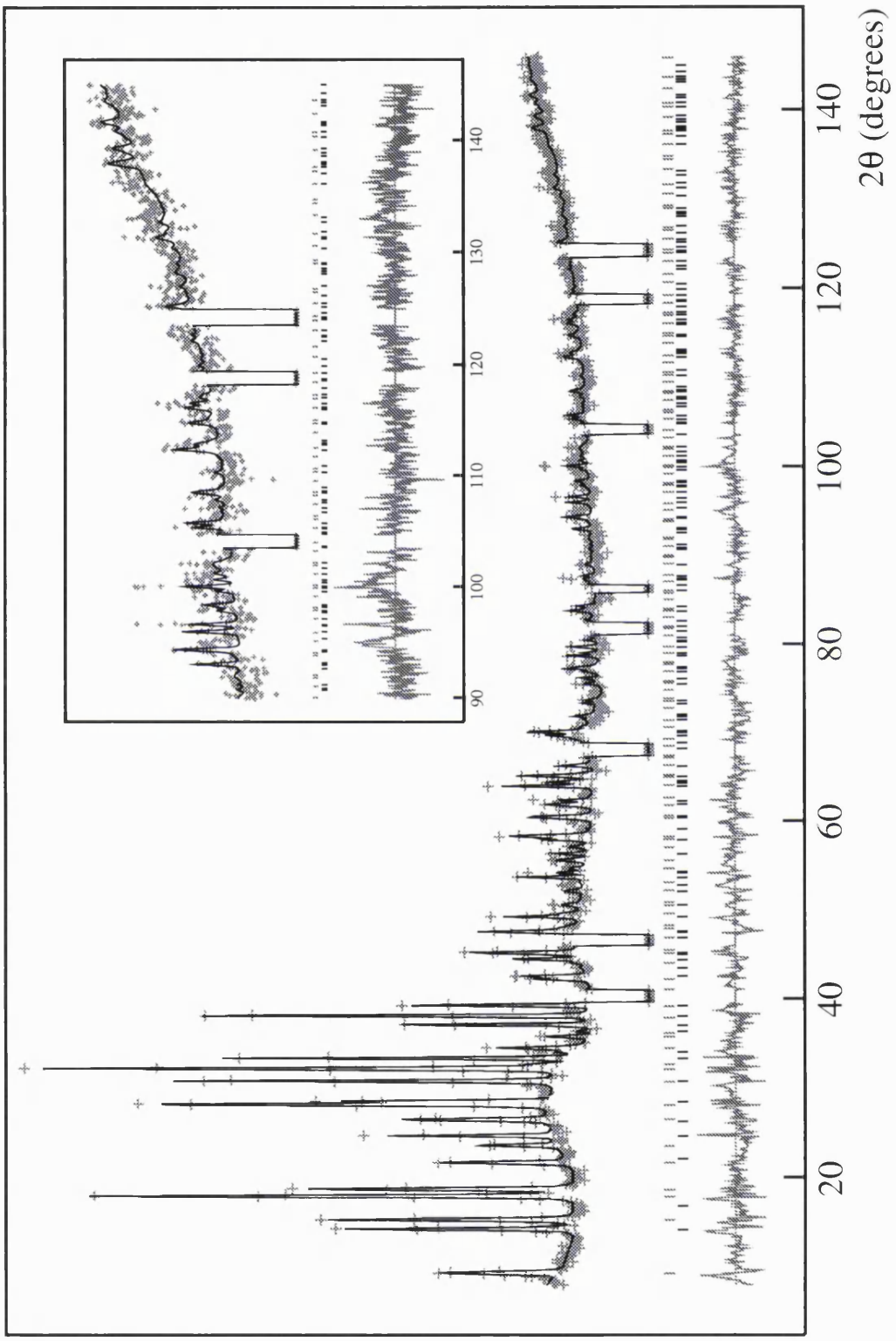

Figure 43: The profile fit for the ice II data collected on D2B at 4.2 kbar and 250 K, $R_p = 0.0132$ and $R_{wp} = 0.0174$. The amount of clathrate determined by the refinement was 63 wt.%.

P(kbar)	T(K)	a_H(Å)	c_H(Å)	c_H/a_H	V(Å^3)	ρ(gcm^{-3})
2.80	200	12.91771(15)	6.22087(12)	0.48158(1)	898.99(2)	1.32995(3)
2.91	*197*	*12.92730(4)*	*6.2143(2)*	*0.48071(2)*	*898.45(3)*	*1.33075(4)*
4.20	250	12.93239(34)	6.22339(35)	0.48123(3)	901.40(6)	1.32639(9)
4.10	*249*	*12.95239(6)*	*6.2057(2)*	*0.47912(2)*	*900.69(3)*	*1.32743(6)*
4.80	200	12.86410(18)	6.18658(12)	0.48092(1)	886.63(2)	1.34849(4)
4.77	*195*	*12.90485(7)*	*6.1790(2)*	*0.47881(2)*	*890.24(3)*	*1.34301(6)*

Table 6: Ice II lattice constants and densities.
Figures in non-italics represent the results of this work for the helium-free structure. Figures in italics are those determined by Londono [89] for the helium-affected structure.

	O(1)	O(2)	D(3)	D(4)	D(5)	D(6)
	0.2223(7)	0.1887(6)	0.1530(6)	0.2216(6)	0.1094(6)	0.2345(5)
x	0.2138(17)	0.1868(13)	0.1581(15)	0.2193(12)	0.1032(14)	0.2413(11)
	0.2215(6)	0.1891(7)	0.1518(6)	0.2220(5)	0.1080(5)	0.2367(4)
	0.1964(7)	0.2286(6)	0.2007(5)	0.2166(6)	0.2148(6)	0.3040(5)
y	0.1965(18)	0.2339(10)	0.1959(11)	0.2079(11)	0.2185(13)	0.3094(15)
	0.1953(6)	0.2300(5)	0.2005(5)	0.2148(6)	0.2148(5)	0.3037(5)
	0.0493(11)	0.4796(14)	-0.0075(13)	0.1972(9)	0.4872(13)	0.5566(12)
z	0.0580(31)	0.4672(28)	-0.0504(31)	0.2143(22)	0.4802(24)	0.5671(36)
	0.0466(13)	0.4816(13)	-0.0071(11)	0.2001(10)	0.4834(10)	0.5574(10)

Table 7: Ice II atomic positions.
The first row of each ordinate represents the atomic positions from the refinement of the data collected on D2B at 2.80 kbar and 200 K; the second row, the data collected on D2B at 4.20 kbar and 250 K; and the third row, the data collected on D1A at 4.8 kbar and 200 K.

	U_{11}	U_{22}	U_{33}	U_{12}	U_{13}	U_{23}
O(1)	0.034(5)	0.037(6)	0.023(4)	0.020(4)	0.003(4)	-0.003(4)
	0.024(5)	0.035(4)	0.030(4)	0.016(3)	-0.001(3)	-0.008(4)
O(2)	0.023(5)	0.023(5)	0.030(4)	0.018(4)	-0.001(4)	-0.011(3)
	0.028(5)	0.024(4)	0.022(4)	0.014(4)	-0.010(5)	-0.016(3)
D(3)	0.044(4)	0.042(4)	0.049(4)	0.019(5)	0.003(5)	0.004(4)
	0.035(4)	0.037(3)	0.045(5)	0.016(3)	0.002(4)	0.007(3)
D(4)	0.053(5)	0.026(4)	0.034(4)	0.023(4)	-0.002(3)	0.008(4)
	0.038(4)	0.029(4)	0.047(5)	0.016(3)	0.001(3)	0.005(5)
D(5)	0.037(4)	0.047(5)	0.031(4)	0.027(5)	-0.005(3)	-0.010(3)
	0.023(3)	0.031(3)	0.035(4)	0.009(3)	-0.008(4)	-0.002(2)
D(6)	0.031(5)	0.035(4)	0.040(4)	0.019(4)	0.006(3)	-0.001(3)
	0.044(4)	0.029(3)	0.029(3)	0.022(3)	0.002(3)	-0.009(3)

Table 8: Ice II anisotropic thermal factors.
The first row for each atom are the thermal factors for the data collected on D2B at 2.8 kbar and 200 K ($D2B_1$); the second row are the thermal factors for the data collected on D1A at 4.8 kbar and 200 K.

	O(1)	O(2)	D(3)	D(4)	D(5)	D(6)
$D2B_1$	0.029(2)	0.020(1)	0.046(1)	0.036(1)	0.037(2)	0.034(1)
$D2B_2$	0.064(5)	0.024(3)	0.088(7)	0.041(4)	0.052(4)	0.081(6)
D1A	0.028(1)	0.026(1)	0.039(1)	0.036(1)	0.033(1)	0.035(1)

Table 9: Ice II isotropic thermal factors.
An anisotropic refinement of the thermal factors for the data collected on D2B at 4.2 kbar and 250 K ($D2B_2$) was not possible, hence the omission of this data set from table 8. An isotropic refinement of the thermal factors was possible, the results of which are detailed in this table. The results of an isotropic thermal refinement for the other two data sets, $D2B_1$ and D1A, are also given for comparison.

	2.80 kbar 200 K	2.91 kbar 197 K	4.80 kbar 200 K	4.77 kbar 195 K
O(1)–D(3)	0.989(8)	*0.982(8)*	0.989(6)	*0.97(1)*
O(1)–D(4)	0.958(8)	*0.973(8)*	0.981(7)	*0.972(8)*
O(2)–D(5)	0.949(8)	*0.967(8)*	0.961(7)	*0.96(1)*
O(2)–D(6)	0.976(7)	*0.983(6)*	0.956(6)	*0.966(7)*
O(1)···D(3)	1.817(10)	*1.825(7)*	1.784(10)	*1.81(1)*
O(2)···D(4)	1.832(9)	*1.830(7)*	1.826(10)	*1.835(9)*
O(2)···D(5)	1.796(7)	*1.805(7)*	1.787(7)	*1.80(1)*
O(1)···D(6)	1.857(9)	*1.830(7)*	1.847(7)	*1.854(8)*
O(1)–O(1)	2.789(9)	*2.787(8)*	2.758(8)	*2.76(1)*
O(1)–O(2)	2.776(10)	*2.786(8)*	2.793(9)	*2.783(9)*
O(1)–O(2)	2.830(9)	*2.809(7)*	2.796(8)	*2.814(9)*
O(2)–O(2)	2.744(7)	*2.768(9)*	2.744(6)	*2.761(9)*

Table 10: Ice II bond lengths.
O(1)–O(1) and O(2)–O(2) are the bond distances found in the puckered and flat hexagonal rings respectively. The two O(1)–O(2) distances are the bond lengths between puckered and flat rings. The first refers to the distance between rings within the same channel and the second refers to the distance between rings across channels. Figures in italics refer to the distances determined by Londono [89] for the helium-affected structure.

	2.80 kbar 200 K	2.91 kbar 197 K	4.80 kbar 200 K	4.77 kbar 195 K
D(3)–O(1)–D(4)	101.3(1.1)	*104.1(7)*	101.4(1.1)	*106.7(9)*
D(5)–O(2)–D(6)	102.8(9)	*106.6(7)*	106.8(8)	*106.6(8)*
O(1)–O(1)–O(1)	115.3(3)	*115.6(2)*	115.7(2)	*115.6(2)*
O(1)–O(1)–O(2)	85.8(6)	*85.0(2)*	86.4(4)	*85.1(3)*
O(1)–O(1)–O(2)	114.8(6)	*114.6(2)*	114.6(3)	*114.7(3)*
O(1)–O(1)–O(2)	125.9(4)	*127.0(3)*	126.7(4)	*127.4(3)*
O(1)–O(1)–O(2)	88.5(4)	*88.3(2)*	87.9(4)	*88.9(3)*
O(2)–O(1)–O(2)	128.9(4)	*128.7(2)*	128.0(4)	*127.4(3)*
O(2)–O(2)–O(2)	119.2(1)	*119.2(2)*	119.3(1)	*119.4(2)*
O(2)–O(2)–O(1)	98.0(8)	*99.0(2)*	98.5(4)	*99.3(3)*
O(2)–O(2)–O(1)	107.2(4)	*106.7(2)*	106.4(5)	*105.4(3)*
O(2)–O(2)–O(1)	125.2(4)	*124.6(2)*	125.8(4)	*125.7(3)*
O(2)–O(2)–O(1)	81.0(4)	*80.7(2)*	80.0(4)	*80.2(3)*
O(1)–O(2)–O(1)	126.9(4)	*126.9(2)*	127.0(2)	*126.7(2)*
O(1)–D(3)···O(1)	166.5(8)	*165.5(6)*	167.6(7)	*165.1(7)*
O(1)–D(4)···O(2)	168.1(9)	*166.7(4)*	168.0(8)	*164.1(5)*
O(2)–D(5)···O(2)	176.3(9)	*173.9(6)*	173.7(7)	*174.8(7)*
O(2)–D(6)···O(1)	174.3(8)	*173.2(6)*	171.4(7)	*171.8(6)*

Table 11: Ice II bond angles
D–O–D are the intramolecular angles; O–O–O and O–D···O, the intermolecular bond angles. Figures in italics refer to the distances determined by Londono [89] for the helium-affected structure.

	2.80 kbar 200 K	2.91 kbar 197 K	4.80 kbar 200 K	4.77 kbar 195 K
Flat ring diameter (Å)	5.464(8)	*5.515(4)*	5.468(7)	*5.506(6)*
Puckered ring diameter (Å)	5.440(9)	*5.446(5)*	5.394(8)	*5.393(8)*

Table 12: Diameters of the hexagonal rings within the ice II structure. Figures in italics are those determined by Londono [89] for the helium-affected structure.

4.4 Discussion

4.4.1 The use of argon

Londono *et al.* [41] found the stability regions for ices Ih and II were increased by the inclusion of helium. Furthermore, ices III and V were never formed from ices Ih or II when helium gas was used. In contrast, no such problems were encountered in these experiments using argon gas. Although time was not spent determining the phase boundaries with any accuracy, phase transitions appeared to occur at pressures and temperatures similar to those found by Bridgman [29]. There is therefore no evidence that argon gas is entering the channels of ice II. The fact that ices III and V could be formed at all, using argon as the pressurising medium, implies ice II is unaffected by its use.

The van der Waals diameters for helium and argon are 2.28 and 3.83 Å respectively [90]. Using the oxygen van der Waals diameter of 2.80 Å [91] for that of a water molecule, the free diameter of the c_H-axis channels is only 2.64 Å at 2.8 kbar. The size of the argon atom is sufficiently large to prevent its inclusion within the ice II structure. Even though the precision of the figures quoted for the diameters

are questionable, particularly that for helium, it should be noted that argon is large enough to form and stabilise the caged clathrate structure [92], whereas helium is not.

4.4.2 Clathrate contamination

The refinement of the 4.2 kbar data set ($D2B_2$) was hampered by the large amount of clathrate present in the sample, figure 44. The clathrate not only contaminated the profile, but also reduced the ice statistics since any increase in clathrate must result in an equivalent decrease in the quantity of ice. The net effect is visible in the refined parameters. The thermal factors for this data set, table 9, which could not be refined anisotropically, are suspiciously high and add serious doubt to the atomic positions. For this reason the bond lengths and angles for this data set were omitted from the tabulation.

4.4.3 The ice II structure

The channels which run parallel to the c_H-axis are constructed from two types of hexagonal ring. The first is built up of type O(1) molecules which form a puckered ring similar to that found in ice Ih [59]. The second is built up of type O(2) molecules which form a much flatter hexagonal ring, figure 45. These rings then stack repeatedly upon each other to form a channel, figure 39.

4.4.4 The effect of helium

On inclusion of helium within the ice II structure, the diameter of the flat ring increases whilst the puckered ring diameter remains largely unchanged, table 12. This

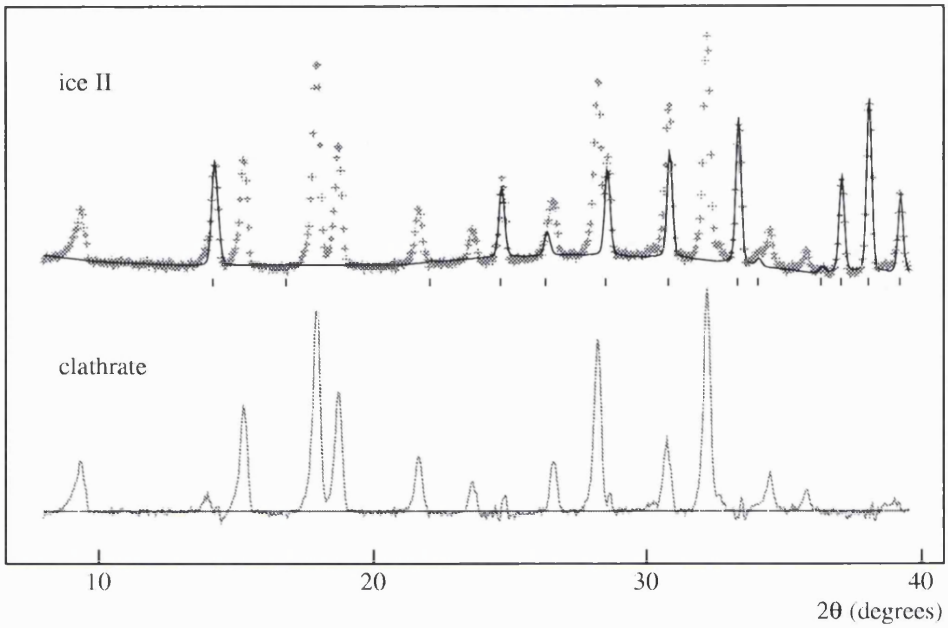

Figure 44: Ratio of ice II to argon clathrate for the 4.2 kbar data set. After refinement of the 4.2 kbar data set, the fraction of argon clathrate was set to zero. In this way the scattering contribution due to the ice (top) and clathrate (bottom) can be separated. The amount of clathrate determined by the refinement was 63 wt.%.

is because the helium is not situated exactly midway between the two rings but sits closer to the flat ring. The water molecules of the puckered ring point up and down the length of the channel with the deuterium atoms forming the vertices of the channel, figure 45. A helium atom midway between the two rings will therefore experience additional repulsion from the deuterium atoms located at the puckered ring and will be repelled from the centre towards the flat ring. This was observed by Londono *et al.* [41] who found the helium atoms to sit at $z = 0.29$, rather than the central position of $z = 0.25$, with the puckered ring located at $z = 0$ and the flat ring at $z = 0.5$.

The effect of the helium is to repel both the water molecules forming the flat

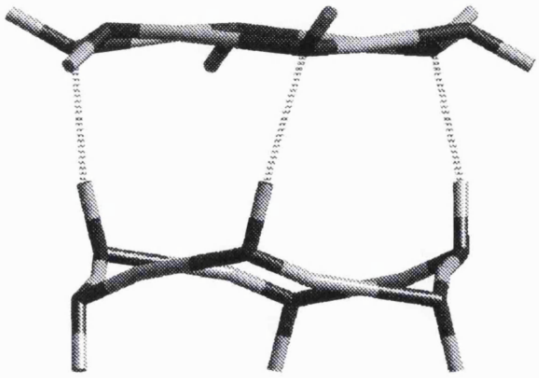

The deuterium atoms of the puckered ring (bottom) are responsible for binding rings above and below together to form a channel. The deuterium atoms of the flat ring (top) are responsible for binding neighbouring channels.

Figure 45: The hexagonal rings found in ice II.

rings and the deuterium atoms forming the vertices of the channels. The expansion of the flat rings upon the inclusion of helium is easily identified by an increase in the O(2)–O(2) bond length, table 10, the distance between neighbouring water molecules within the ring. The repulsion of the deuterium atoms causes their distance from the channel centre to increase from 2.831(6) to 2.845(4) Å at 2.8 kbar, and from 2.811(5) to 2.851(4) Å at 4.8 kbar. In addition, the angle of the hydrogen bond that binds puckered and flat rings together, O(1)–D(4)···O(2), decreases. Unfortunately, since

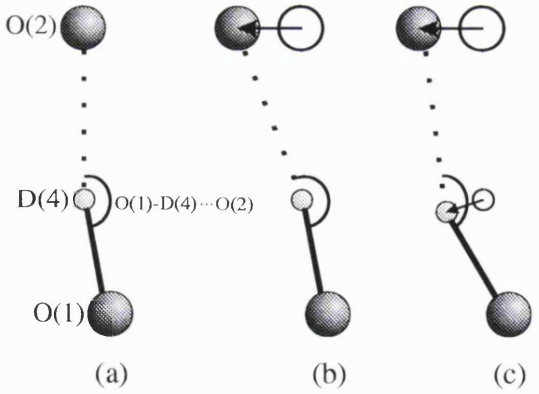

(a) In the helium-free structure the bond angle O(1)–D(4)···O(2) is 168.1°.
(b) The inclusion of helium repels the O(2) atoms within the flat hexagonal ring and should cause the O(1)–D(4)···O(2) bond angle to increase.
(c) Yet the angle actually decreases to 166.7° which is only possible if the deuterium atoms are also repelled.

Figure 46: Interatomic repulsion caused by the inclusion of helium.

O(2), which forms the flat rings, moves due to repulsion, the measurement cannot be easily interpreted. Nevertheless, the angle in the helium-affected structure is smaller, table 11, which is only possible if the deuterium atoms are repelled by the helium,

figure 46.

The increase in diameter of the flat ring upon the inclusion of helium is 0.05 Å at 2.8 kbar and 0.04 Å at 4.8 kbar. If the expansion of the flat rings were translated directly to the lattice constants then an increase in a_H of 0.09 Å at 2.8 kbar, and 0.07 Å at 4.8 kbar, would be expected, figure 47. Yet increases of only 0.01 and 0.04 Å are observed for the respective pressures, table 6. Without a similar expansion in lattice

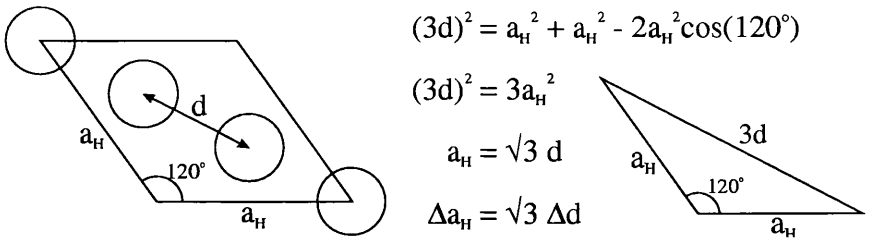

Figure 47: The relation of channel diameter to lattice constant a_H.
There are three c_H-axis channels which span the long diagonal of the ice II unit cell. Any change in the diameter of the channels without change in their separation, Δd, if directly translated to the dimensions of the unit cell, will cause a change $\sqrt{3}\Delta d$ in the lattice constant a_H.

constants, the expansion of the flat rings causes the distance between neighbouring channels to decrease, figure 48. At 2.8 kbar the distance between neighbouring channels decreases from 1.994 to 1.949 Å upon the inclusion of helium, whilst at 4.8 kbar the distance decreases from 1.959 to 1.945 Å.

As crudely illustrated in figure 49, the expansion in width of the channels, upon the inclusion of helium, is accompanied by a shortening of their length. The contraction in length is small and cannot be easily identified by examination of bond lengths or angles. The only visible indicator is the lattice constant c_H which at 2.8 and 4.8 kbar contracts by 0.007 and 0.008 Å respectively, upon the inclusion of helium, table 6.

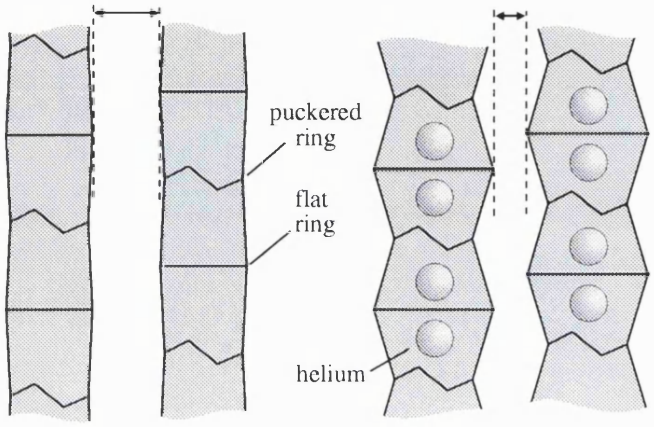

Figure 48: Expansion of the hexagonal rings in ice II upon the inclusion of helium. The figure shows two sets of neighbouring channels, with and without the inclusion of helium. With a relatively small increase in lattice constants, the expansion of the flat hexagonal rings causes neighbouring channels to approach. Bonds between neighbouring channels have been omitted for clarity.

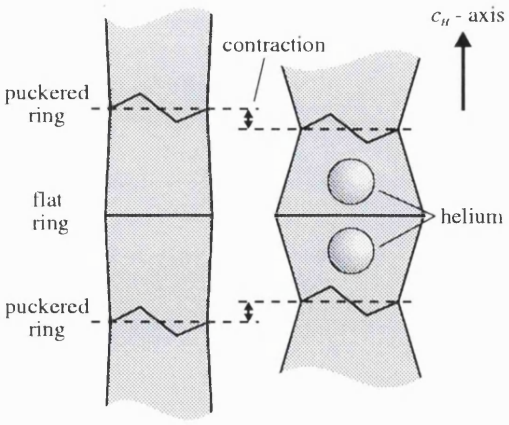

Figure 49: Length contraction of the hexagonal channels upon helium inclusion. The figure does not represent neighbouring channels but rather the same channel with and without helium. The repulsion on helium inclusion causes the channel width to increase and its length to contract.

4.4.5 The effect of pressure

As the pressure is increased from 2.8 to 4.8 kbar, the diameter of the flat hexagonal ring in both the helium-free and helium-affected structures remains largely unchanged, table 12. This is perhaps expected for the helium case where the atoms sitting in the channel oppose the external compression, but seems surprising for the helium-free structure. However, the distance between neighbouring water molecules within the ring, O(2)–O(2), is already short at 2.744 Å, table 10. Any decrease in the diameter of the ring is therefore restricted without some form of large distortion as seen in the puckered rings.

For the helium-free structure, the pressure increase drives neighbouring channels closer together; the separations at 2.8 and 4.8 kbar are 1.994 and 1.959 Å respectively. As the channels approach, possible increases in strain among hydrogen bonds are relieved by a decrease in the diameter of the puckered ring. For example, the bond angle O(2)–O(1)–O(2), already the largest bond angle in the structure, is expected to increase as neighbouring channels approach. Yet the angle actually decreases, table 11, as a result of the decrease in diameter of the puckered ring.

In the helium-affected structure there is no noticeable change in the separation of neighbouring channels upon the increase of pressure. The inclusion of helium within the channels brings about their expansion, causing neighbouring channels to approach. At 2.8 kbar, the separation of channels is only 1.949 Å, smaller that that for the helium-free structure at 4.8 kbar, 1.959 Å. As the helium pressure is increased from 2.8 to 4.8 kbar, any further decrease in the channel separation is structurally resisted.

4.4.6 Compressibility and expansivity

The compressibility and expansivity of a system are defined as:

Compressibility:
$$\kappa(p) = -\frac{1}{V_{p=0}}\left(\frac{\partial V}{\partial p}\right)_T \tag{12}$$

Expansivity:
$$\beta(T) = \frac{1}{V_{T=0}}\left(\frac{\partial V}{\partial T}\right)_p \tag{13}$$

where $V_{p=0}$ and $V_{T=0}$ are the volumes of the system at zero pressure and temperature respectively. These values are not known experimentally and are determined from the volume-pressure and volume-temperature equations at zero pressure and temperature.

The volumes determined in this work are known only for a couple of pressures and temperatures. The derivatives are therefore unknown in detail and are assumed to be constant; this assumption seems reasonable to a first approximation. The compressibility and expansivity are then:

$$\kappa = -\frac{1}{V_{p=0}}\left(\frac{\Delta V}{\Delta p}\right) = -\left(\frac{\Delta p}{V\Delta p - p\Delta V}\right)\left(\frac{\Delta V}{\Delta p}\right) = \frac{\Delta V}{p\Delta V - V\Delta p} \tag{14}$$

$$\beta = \frac{1}{V_{T=0}}\left(\frac{\Delta V}{\Delta T}\right) = \left(\frac{\Delta T}{V\Delta T - T\Delta V}\right)\left(\frac{\Delta V}{\Delta T}\right) = \frac{\Delta V}{V\Delta T - T\Delta V} \tag{15}$$

A figure commonly quoted by authors is the bulk modulus which exists as two forms, the isothermal and the adiabatic bulk modulus. The isothermal bulk modulus relates to the change in volume of a system with pressure, at a fixed temperature, and is simply the reciprocal of the compressibility. The adiabatic bulk modulus is measured without heat flow and is determined by the speed of acoustic waves through the system. For most solids, the isothermal bulk modulus is less than 10% smaller than the adiabatic bulk modulus [93].

The compressibility of ice II, determined from the data at 2.8 and 4.8 kbar, is 6.74(3) $Mbar^{-1}$ at 200 K, which corresponds to an isothermal bulk modulus of 148(1) kbar. This figure is in good agreement with the isothermal bulk modulus found by Gagnon *et al.* [94] for H_2O ice II at 237.5 K, 144 kbar. In contrast, the bulk modulus for the helium-affected structure at 196 K is 206(1) kbar [89]. Naturally, the helium-affected structure has the higher bulk modulus since the helium atoms within the c_H-axis channels will resist any external compression.

Gagnon *et al.* [94] found the density of H_2O ice II could be described by the equation $\rho = 1.1698 + 0.00818p$ over the pressure range 2–4 kbar at 237.5 K, i.e. the volume was found to vary linearly with pressure. Using the volumes determined in this work at 2.8 and 4.8 kbar at 200 K, the volume at 4.2 kbar and 200 K is then 890.34(4) $Å^3$. Using this estimate, and the volume at 4.2 kbar and 250 K, the expansivity of ice II at 4.2 kbar is 261(2) MK^{-1}. For the helium-affected structure, the expansivity at 4.8 kbar is 317(1) MK^{-1}. The higher thermal expansivity for the helium-affected structure must be attributed to changes in the thermal motion of the helium atoms.

4.5 Conclusions

The structure of ice II in the helium-free and helium-affected systems are similar, though different in detail. The helium atoms are situated at well defined positions within the c_H-axis channels. However, the atoms do not sit midway between the two types of hexagonal ring which make up the channels, but sit closer to the flatter rings. Interatomic repulsion, consequent on the inclusion of helium, cause an expansion of the flat rings whilst the puckered rings are left unchanged. This in turn causes the

diameter of the channel to increase and its length to contract. These changes are reflected in the lattice constants with a_H increasing and c_H decreasing on helium inclusion. The expansion of the channels is not translated directly to the a_H lattice constant, but is instead largely accommodated through a decrease in the separation of neighbouring channels.

As the pressure on the helium-free structure is increased, the distance between neighbouring channels decreases. The diameter of the flat ring remains unchanged whilst that of the puckered ring decreases, thereby alleviating increases in hydrogen-bond strain. For the helium-affected structure, the distance between neighbouring channels is already small by virtue of the channel expansion due to helium inclusion. No significant decrease in channel separation is observed upon the increase in helium pressure.

The helium atoms within the channels resist any external compression of the structure, resulting in a smaller compressibility for the helium-affected structure compared to that for the helium-free. The expansivity of the helium-affected structure is greater than that of the helium-free, and is probably due to changes in the thermal motion of the helium atoms.

Although the discussion in this work was concerned with the changes in the ice II structure upon helium inclusion and pressure increase, a comparison should be made between the water molecule geometry found here for ice II under pressure, and that found for ice II recovered to ambient pressure [81,84], and also the free water molecule (monomer and dimer).

Chapter 5

Ice III

5.1 Introduction

The existence of ice III was first discovered by Tammann [28] in 1900. Bridgman [29] soon afterwards confirmed the results of Tammann's work and presented, with greater accuracy and detail, the ice III transition curves. Thermodynamically stable between 240–260 K and 2.2–3.4 kbar, ice III occupies a relatively small region of the ice phase diagram, figure 4.

The structure of ice III was first proposed by McFarlan [95] through the use of X-ray diffraction. Having formed ice III by freezing the liquid at 2.5 kbar, the sample was quenched to 118 K and the pressure released to ambient. The results of his study led McFarlan to conclude that ice III was in fact ionic! Although he found the oxygen atoms retained their four co-ordination, he rejected the idea that the hydrogen bonds were being bent "considerably" from the ideal tetrahedral angle and instead suggested that ice III was built up of protons lying midway between oxygen ions.

The suggestion that the tetrahedral character of hydrogen bonding was being

violated led Kamb and Datta [96] to repeat the work of McFarlan [95]. Their data, in disagreement with those of McFarlan, suggested a structure in which the oxygen atoms "approximately retained" their tetrahedral arrangement. Bertie *et al.* [97] also repeated the work of McFarlan and found their data in agreement with those of Kamb and Datta [96].

Infrared spectra were collected soon afterwards by Bertie and Whalley [82]. The lack of material transparent to a wide range of frequencies whilst capable of withstanding high pressures meant samples were once again recovered. They were however confident that ice III was still present after recovery since no volume changes were recorded other than those associated with cooling and pressure release. The locations of the bands were similar to those found in ice Ih and led them to conclude that ice III is similarly four co-ordinated and fully hydrogen bonded. There was also evidence of non-linear hydrogen bonds which tied in with the tetrahedral arrangement of water molecules since bond bending must be occurring to account for the increase in density of ice III over ice Ih. However, their most important conclusion was that the water molecules within ice III must be orientationally ordered. This was based on the fine structure observed in the stretching and, more importantly, the rotational bands, which was interpreted as water molecule rotations obeying rigorous selection rules.

Wilson *et al.* [85] performed dielectric measurements within the ice III stability region rather than on recovered samples and found well defined dielectric dispersion resulting from rotational relaxation of the water molecules. For an ordered ice structure, the water molecules are frozen into a particular orientation with molecular rotation strongly inhibited. Wilson *et al.* therefore concluded that at high temperatures, the water molecules in ice III are orientationally disordered.

With the orientation of water molecules ordered at low temperatures (infrared) and disordered at high temperatures (dielectrics), work began on locating the order–disorder transition. The first to address the problem were Whalley and Davidson [86]. Using the Clausius–Clapeyron relation, equation 16, the entropic difference of two systems, ΔS, can be determined from the gradient of the phase boundary defining the two, $(\partial p/\partial T)_{equil}$, and the change in volume associated with the transition, ΔV.

$$\left(\frac{\partial p}{\partial T}\right)_{equil} = \frac{\Delta S}{\Delta V} \tag{16}$$

All phases of ice are structurally similar in that the water molecules bond tetrahedrally to four others. In this way, the vibrational entropies of all phases, at approximately the same pressure, are similar. The change in entropy associated with a transition is therefore largely determined by changes in configurational entropy, i.e. changes in the orientational order of the water molecules. Bridgman [29, 30], in measuring the ice phase boundaries and volume changes, found the entropy for ices Ih, III, V and VI to be similar, but very different to ice II, figure 50. Since ices Ih and II were known to be orientationally disordered and ordered respectively, Whalley and Davidson concluded that ices III, V and VI must all be orientationally disordered.

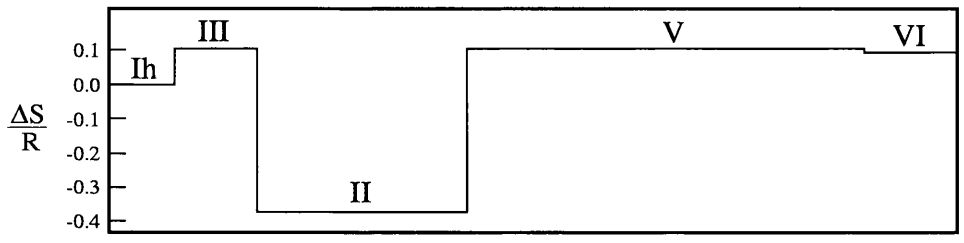

Figure 50: The change in entropy for the various ice phase transitions at 243 K as illustrated by Whalley and Davidson [86] using the data of Bridgman [29, 30].

With the knowledge that an order–disorder transition must be occurring for ice III, Whalley and Davidson then examined carefully the ice Ih–III transition curve.

For two phases of ice with the same orientational order, the change in entropy across the transition will be small, but the change in volume, due to changes in density, will be appreciable. The quantity $\Delta S/\Delta V$ and therefore $(\partial p/\partial T)_{equil}$ will be very small. The transition curve defining the two phases will therefore appear almost vertical, as is indeed observed for the transitions Ih–III and III–V, figure 4. Changes in the ordering of ice III with temperature, without similar changes in ice Ih, should be visible as a curved rather than straight transition line. Whalley and Davidson compared the volume changes measured by Bridgman with those expected if the transition curve were straight. Discrepancies, greatest at 233 K, were attributed to an ordering transition within ice III. They also cite the curved Ih–III line measured by Tammann [28] as further evidence of ordering in this temperature range.

Kell and Whalley [98] remeasured the ice Ih–III line in an attempt to verify the existence of the order–disorder transition. They reported a "nearly straight" transition curve down to 221 K, figure 51, and hence an order–disorder transition could not be occurring above this temperature. They also offered an explanation as to why

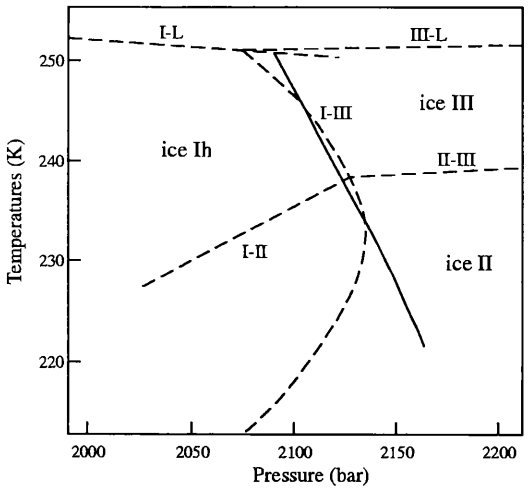

Figure 51: Phase diagram of ice in the Ih–III region. The dashed lines represent the phase transition curves measured by Bridgman [29]. Whalley and Davidson [86] interpreted the curved ice Ih–III transition as an ordering process within ice III. However, Kell and Whalley [98] later remeasured the ice Ih–III transition line and found it to be "nearly straight", solid line.

previous work [28, 29] had suggested a curved transition line. During the transition, ice plugs form which shield the remaining ice from the pressurising medium. Pressure

is then transmitted not by the oil but by the surrounding ice. The elasticity of the ice plug was found to vary with temperature, with equilibrium at "higher" temperatures reached after an hour, whilst at "lower" temperatures equilibrium was only reached after a couple of days. Kell and Whalley believe the transitions measured by Tammann [28] and Bridgman [29] were not in true equilibrium at lower temperatures.

Whalley *et al.* [33] decided to follow the dielectric properties of ice III from the high temperature (250 K) disordered region to the low temperature (110 K) ordered region. They found a gradual ordering transition over the temperature range 205–165 K, with a maximum rate of ordering at 173 K, figure 52. Small volume changes, along with unpublished X-ray studies under pressure, implied the same oxygen framework at high and low temperatures. Whalley *et al.* then proposed positions for the hydrogen atoms of the low temperature phase based on the principle that the new phase, which they called ice IX, had a zero net dipole moment.

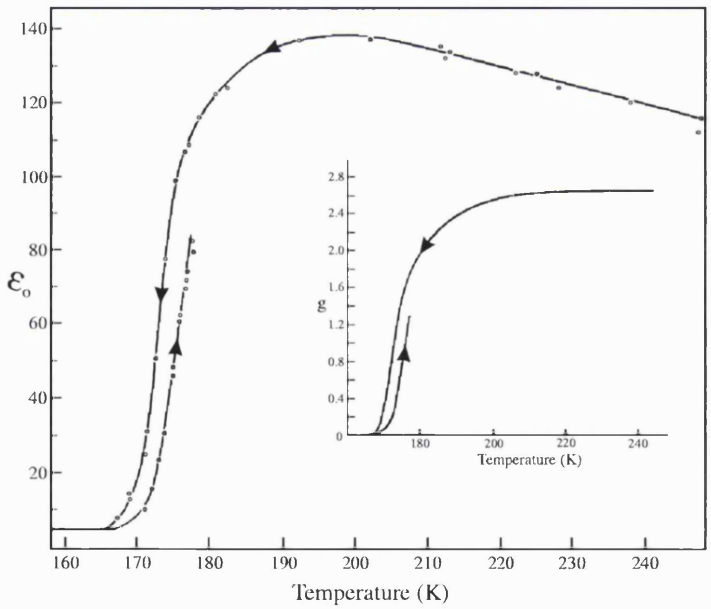

Figure 52: The variation of the limiting, low-frequency dielectric constant for ice III(IX) at 2.3 kbar.

The picture now seemed to be clearing a little. Ice III, thermodynamically stable at temperatures above 240 K, is orientationally disordered with its ordered equivalent, ice IX, stable at temperatures below 165 K.

The first, detailed, crystallographic study of ice IX was performed by Kamb and Prakash [99] on single crystals recovered to ambient pressure at 100 K using X-ray diffraction. The structure is based on a tetragonal unit cell, space group $P4_12_12$, lattice constants: $a = 6.73$, $c = 6.83$ Å, and consists of two crystallographically different water molecules. Molecules of the first type form spirals about 4_1 screw axes and run parallel to the c-axis, figure 53. Molecules of the second type act to bind these spirals together to form a tetrahedrally bonded framework of water molecules, figure 53.

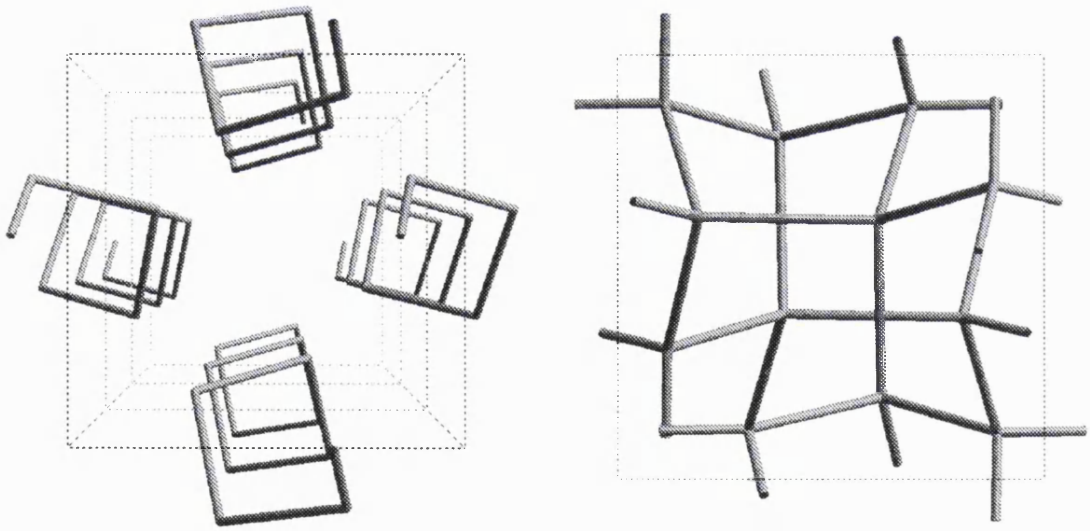

Figure 53: The oxygen framework of ice III(IX). Water molecules of type O(1) form spirals which run parallel to the c-axis (left). Water molecules of type O(2) bind these spirals together to form a tetrahedral framework (right).

The first neutron diffraction work on ice IX was carried out by Rabideau *et al.* [100] on powders recovered to ambient pressure. They found the same oxygen framework as proposed by Kamb and Prakash [99] and hydrogen positions as proposed by Whalley *et al.* [33]. The ordering is such that the water molecules occupy orientations in which the O–O–O angles best match the H–O–H angle of 104.5°. In this way, the degree of hydrogen-bond bending between molecules is minimised.

Arnold *et al.* [87] were the first to study ices III and IX under pressure using powder neutron diffraction. Although the data were not good enough to establish the degree of orientational disorder in ice III, they did find that the diffraction patterns for ice III and IX differed significantly. They too found the ice III–IX transition occurred in the same temperature range observed by Whalley *et al.* [33]. Unfortunately, the transition from ice III to ice IX involves traversing the ice II stability region, figure 4. The instability of ice III with respect to ice II meant that the rate of cooling could be no slower than $\sim$1 Kmin^{-1}. Even at this rate, ice IX was not always obtained. Accurate measurements could not therefore be made during the transition, but the data were sufficient to identify changes in the intensity for the (201) and (221) reflections supporting Whalley *et al.*'s [33] findings that the ordering occurs gradually as a function of temperature.

La Placa *et al.* [101] continued the work on ice IX with neutron diffraction of single crystals, again recovered to ambient pressure. The accuracy of their data allowed identification of a small degree of orientational disorder which they attributed to relaxation times comparable with the rate of cooling. If the ordering of the water molecules is directly related to the static dielectric constant, then the 4% disorder measured by La Placa *et al.* would correspond to a temperature of 168 K. The rotational relaxation time of the water molecules at this temperature, if linearly extrapolated from

values determined by Whalley *et al.* [33], is similar to the rate at which the sample was cooled. It is therefore possible that the rate of cooling "froze" the water molecules at 168 K preventing them from orienting into a fully ordered configuration. La Placa *et al.* suggest that such a small amount of disorder might reasonably go undetected in infrared spectra [82].

Nishibata and Whalley [102] measured the changes in entropy across the ice III–IX transition by a technique referred to as differential calorimetry. With very small volume changes at the transition, it is likely that any entropy change would result from changes in configurational entropy. Using mathematical procedures described by Nagle [2], they calculated the expected entropy change if the water molecules in ices III and IX were fully disordered and ordered respectively. The entropy change determined by experiment, 1.34 $JK^{-1}mol^{-1}$, was only 40% of that expected, 3.37 $JK^{-1}mol^{-1}$. Since there had been no suggestion of any order in ice III, Nishibata and Whalley concluded that the difference must result from partial disorder in ice IX which they estimate at 6–10%. Not only is this larger than that found by La Placa *et al.* [101] but they also dismiss the idea of "frozen-in" disorder for their measurements. Although La Placa *et al.* [101] had quenched their sample at a rate close to 1000 $Kmin^{-1}$, Nishibata and Whalley [102] used variable cooling rates from 0.8 to 2.0 $Kmin^{-1}$ without discerning a difference.

Londono *et al.* [103] continued the work on ices III and IX by studying many different samples, both under pressure and recovered, using powder neutron diffraction. They found the path employed by Arnold *et al.* [87], in which ice III was formed by pressurising ice Ih, led to the formation of ice II in most cases, and instead formed ice III by freezing the liquid at 2.8 kbar. This unfortunately led to a poor powder for ice III and meant the results they obtained were not as conclusive as they had hoped.

Nevertheless, with and without the inclusion of preferred orientation, they found orientational order of around 20%. Concentrating on ice IX, data were collected in an effort to study structural differences arising from different cooling rates. Differences in lattice constants were observed for the same sample when it was quickly quenched to 110 K and when it was cooled at a rate slower than the relaxation times proposed by Whalley *et al.* [33]. Although their data were not of sufficient quality to refine the occupancies of the weakly occupied hydrogen atoms, they attributed the different lattice constants to differences in orientational order.

It is clear that ices III and IX adopt the same oxygen framework; the difference between the two structures is simply one of orientational order.

The structural work on ice IX seems almost complete. The question of whether ice IX can attain full orientational order or whether it possesses residual disorder has not been answered directly. However, in comparing the work carried out so far, a fully ordered structure does appear feasible. La Placa *et al.* [101] found 4% disorder in ice IX when quenched rapidly to 77 K. Londono *et al.* [103] highlighted the need to maintain rates of cooling in line with relaxation times. Differences, attributed to ordering, were found for the same sample when quenched and when cooled in line with relaxation times. Assuming that the quenched sample of Londono had $\sim$4% disorder, then the observed changes in ordering due to slower rates of cooling must have been to a fully, or almost fully, ordered structure. It would therefore appear that complete orientational order is achieved with cooling rates comparable to relaxation times.

The work by Nishibata and Whalley [102], who report a more disordered structure for ice IX based on calculated entropies, can be interpreted in another way. Rather

than their assumption that ice III is fully disordered and hence ice IX partially disordered, the differences in entropy can be explained by a fully ordered ice IX and a partially ordered ice III. Although a modified model by Howe and Whitworth [3] predicts very different entropies, the difference in entropy still cannot be accounted for by a full disorder to order transition.

Unlike ice IX, the structural work on ice III is very limited, the only diffraction work being that of Arnold *et al.* [87] and Londono *et al.* [103]. Although both were able to confirm the oxygen framework as that adopted by ice IX, only Londono *et al.* were able to offer information pertaining to the degree of orientational disorder. Although the sample was textured making results inconclusive, they found that the orientations of the water molecules were partially ordered. The suggestion that ice III may be partially ordered is by no means implausible. The primary mechanism thought to be responsible for orientational ordering is the variation in O–O–O bond angles; the water molecules wish to occupy bond angles which best match the H–O–H angle of 104.5°. In ice III, the O–O–O bond angle of 144° seems particularly unfavourable and may promote ordering even at high temperatures. The "nearly straight" Ih–III transition curve of Kell and Whalley [98] may also be evidence of small changes in ordering with temperature.

In order to determine the ordering scheme adopted by ice III, neutron diffraction data were collected at several points within its stability region. The points were chosen such that variations in structure with temperature and pressure would also be observed.

5.2 Experimental procedure

Samples were prepared in one of two ways as described in section 3.1.2. The data were collected on various instruments at different times, with the conditions under which ice III was formed and studied different for each experiment. Individual descriptions of sample history and conditions under which data were collected are detailed below.

IRIS

Ice III was first prepared during an investigative experiment on IRIS. A TiZr gas pressure cell was loosely filled with silica wool into which ~1.5 ml of D_2O were distributed by syringe and needle. The argon pressure was increased to 5.5 kbar and the temperature gradually decreased. At 260 K, the liquid froze to form ice V. The pressure was then decreased to 3.1 kbar which resulted in the transition to ice III. Data were collected at 3.1 kbar and 260 K over a period of 13 hours.

The detectors of the IRIS instrument were such that no information as to the quality of the powder could be obtained. Only upon refinement of the data could the powder quality be ascertained.

D1A

The experiment on D1A was originally designed to find the ideal conditions for argon clathrate growth. Silica wool and liquid D_2O were loaded into an aluminium gas pressure cell and lowered into a cryostat located on the instrument. The temperature was then decreased at ambient pressure to 240 K which led to the formation of ice Ih. The pressure and temperature were then varied from ambient to 5 kbar and 200 to 260 K in an attempt to establish the best conditions for clathrate growth. At the point prior to forming ice III, the pressure and temperature were 2.5 kbar and 233 K

respectively. The sample was gradually warmed with a transition from ice II to ice III, highlighted by changes in diffraction profiles, at about 240 K. As with the IRIS experiment, the sample had been prepared from the liquid with silica wool. However, by rotating the sample through various omega positions, 0°, 40° and 80°, the quality of the powder could be judged. The peak intensities remained unchanged for the different omega positions indicating a good powder. Data were collected at 2.3 kbar and 240 K over a period of 12 hours at the three omega positions listed.

Göttingen

The work on IRIS and D1A had shown that argon gas could be used as a successful pressure agent for investigations within the ice phase diagram. With this in mind, ices III and V could be examined in a more controlled manner. Before attempting such investigations "on beam", it had to be established that the ices could be formed in a reproducible way. To do this, trial preparations of ice III were performed using the gas pressure system at Universität Göttingen. Although the benefit of neutrons for phase determination was unavailable, abrupt changes in the pressure were equally good in identifying phase transitions. Starting from finely powdered ice Ih, argon pressure was increased over the temperature range 243 to 248 K with abrupt pressure drops recorded on reaching 2.5 kbar. Although inspection of the ice Ih–III transition curve suggests a transition pressure at these temperatures of about 2.2 kbar, an overpressure is required to induce the phase transition. On releasing the pressure, the transition to ice Ih was noted consistently at 2.2 kbar. The pressure equipment was restricted to 3 kbar and hence the preparation of ice V could not to attempted. However, it was now confidently thought that ices III and V could be formed from the powder using argon gas.

D2B

Unfortunately, the preparation of ice III did not prove as simple as that found at Göttingen. The D2B experiment started by following the same recipe but, unlike the preparations at Göttingen, there was no transition to ice III at 2.5 kbar. Instead, the pressure had to be further increased to 2.8 kbar before a transformation occurred. Unfortunately, the transition was not to ice III but to some non-crystalline phase. Puzzled by this, the procedure was repeated at the lower temperature of 244 K. Upon reaching 2.8 kbar there was still no phase transition to ice III and the idea of further pressure increase was rejected for fear of forming the non-crystalline phase. Instead, the same procedure as that followed for the D1A experiment, in which ice III was formed by warming ice II, was adopted. On warming at 2.8 kbar, ice II transformed to ice III in the temperature range 245–250 K. Data were then collected on ice III at the following points: 2.5 kbar and 240 K, 2.5 kbar and 250 K, 3.3 kbar and 250 K, with around 12 hours data collection time for each point. The choice of points was such that structural information as a function of both temperature and pressure was obtained.

Forming ice III from the powder meant there was no need to be concerned about sample quality. Nevertheless, data were collected at various omega positions, -2°, -1°, 0°, 1° and 2°, with no difference recorded in peak intensities.

HRPD

Shortly after the D2B experiment, further data on ice III were collected on HRPD. The study of a different ice III sample on a different instrument would either add credence to conclusions already reached, or highlight discrepancies which might otherwise have been the basis for argument.

Ice III was prepared following the same recipe as before, i.e. through the warming of ice II. The pressure and temperature were set to 3.3 kbar and 250 K and data collected overnight. Inspection of the data the following morning revealed that ice III had been stable at these conditions for only 3 hours, after which it slowly transformed to ice II over a period of 6 hours. Furthermore, the ice II that had formed was textured. The transition to ice II most probably resulted from sitting too close to the ice II–III phase boundary; the texture that resulted however could not be immediately explained. In an attempt to improve the quality of the powder, the sample was cycled through the ice phases Ih, II, III and V, with the knowledge that such phase transitions, with much bond breaking, would help to fracture the crystals. Afterwards, the ice III powder appeared good, at least from the point of view of the detector area. Data were then collected at the slightly lower pressure of 3.0 kbar at 250 K. Not being completely happy with the powder quality, a new sample was prepared. A further data set at 3.0 kbar and 250 K was collected, this time with the knowledge of a good powder. Data collection time for both data sets was about 12 hours.

The different data sets collected on HRPD and D2B have been labelled by subscript for clarity in the discussions that follow.

Data set	p(kbar)	T(K)
$D2B_1$	2.5	240
$D2B_2$	2.5	250
$D2B_3$	3.3	250
$HRPD_1$	3.0	250
$HRPD_2$	3.0	250

Table 13: Labelling of the ice III data collected on D2B and HRPD under different conditions of pressure and temperature. Although both HRPD data sets were collected under identical conditions of pressure and temperature, the $HRPD_1$ data was most likely collected on a textured sample.

5.3 Results

Refinement

The atomic positions of ice III determined by Londono *et al.* [103] were used as the initial model in refining all ice III data. Although Londono *et al.* found evidence for partial ordering, the deuterium atoms at the start of the refinement were populated in a fully disordered manner. In this way, no initial bias was placed on ordering.

Ice III is based on a tetragonal unit cell, space group $P4_12_12$, lattice constants: $a = 6.80$ Å, $c = 6.86$ Å, and comprises twelve water molecules. The asymmetric unit required to describe the complete structure consists of two distinct oxygen and six distinct deuterium atoms. By application of the Bernal-Fowler rules [40], only two parameters are required to describe the orientational ordering of the water molecules, table 14.

$$\begin{aligned}
\text{O(1)–D(3)}\cdots\text{D(7)–O(2)} &\Rightarrow \text{D(3)} + \text{D(7)} = 1 \\
\text{O(1)–D(4)}\cdots\text{D(5)–O(1)} &\Rightarrow \text{D(4)} + \text{D(5)} = 1 \\
\text{O(1)–D(6)}\cdots\text{D(8)–O(2)} &\Rightarrow \text{D(6)} + \text{D(8)} = 1
\end{aligned}$$

The left-hand column represents the hydrogen bonding of neighbouring water molecules. Since there must be one, and only one, deuterium atom per bond, the probability of both deuterium sites being occupied must total 1, as represented in the right-hand column. In addition to this constraint, the sum of the sites around a particular oxygen atom must total 2:

$$\begin{aligned}
\text{D(3)} + \text{D(4)} + \text{D(5)} + \text{D(6)} &= 2 \\
\text{D(7)} + \text{D(7)} + \text{D(8)} + \text{D(8)} &= 2
\end{aligned}$$

From the constraints listed above, the probabilities of all deuterium sites can be represented by just two variables, say α and β:

D(3)			=	α
D(4)			=	β
D(5)	=	1 - D(4)	=	1 - β
D(6)	=	2 - D(3) - D(4) - D(5)	=	1 - α
D(7)	=	1 - D(3)	=	1 - α
D(8)	=	1 - D(6) or 1 - D(7)	=	α

Table 14: The fractional occupancies of the six deuterium atoms in ice III.

The argon clathrate that formed during data collection was modelled on the structure refined from neutron diffraction data collected at 2.5 kbar [61]. Only the lattice constants of the clathrate phase were refined.

There were no visible reflections from the TiZr gas pressure cell in any of the data sets. However, reflections from the aluminium pressure cell in the D1A data, and the aluminium sample can, used to prevent sample from blocking the pressure line, in the D2B data were present and therefore excluded. Background points were required to describe a hump in the D2B data at $\sim 25°$, figure 56, in addition to the mathematical description, section 3.6.6.

It was only possible to refine the IRIS data after the introduction of many restraints. Even so, the thermal factors for the deuterium atoms were lower than those for oxygen, and the ordering parameters were very different to those found for the other data sets. It is not clear whether this is the result of a textured sample or simply the lack of data at short d-spacings. The results arising from the refinement of the IRIS data were therefore not included in the tables below.

The ice III diffraction profiles indicate little intensity for reflections greater than 80°, figure 56. The lack of high angle data in turn led to a troublesome refinement with problems immediately encountered upon refining the thermal factors. Refinement of the HRPD data proved the most problematic with unrealistic thermal factors for the deuterium atoms, table 15. This is almost certainly due to a lack of high angle data, the HRPD data having the smallest coverage in d-spacing, 1.2–3.1 Å as opposed to 0.8–20 Å covered by D2B and 1.0–13 Å covered by D1A. Refinement of the D1A data fared better than the HRPD data, although the thermal factors for atoms D(3) and D(4) were similarly dubious, table 15. The HRPD and D1A data sets were therefore thermally restrained such that all deuterium atoms were refined with the

same thermal factor. The D2B data is a little more difficult to interpret. The thermal factors for atoms D(3) and D(8) are suspiciously low for the $D2B_3$ data set, yet not low enough to discard them as unphysical. A similar behaviour, if somewhat less severe, can also be seen for the $D2B_1$ data set. The deuterium atoms D(3) and D(8) are the weakly occupied positions within the ice III structure. In the fully ordered ice IX structure the occupancies of the two sites are zero. Since there are no apparent structural reasons why these two atoms should have a small thermal motion in comparison with the other deuterium atoms, it would appear the refinement had problems in decorrelating the thermal factor and occupancy for these weakly occupied atoms. The thermal factors for the two atoms were therefore restrained to the same value as their strongly occupied counterparts, i.e. D(3) U_{iso} = D(6) U_{iso} = D(7) U_{iso} = D(8) U_{iso}.

	D(3)	D(4)	D(5)	D(6)	D(7)	D(8)
$D2B_1$	0.048(10)	0.052(11)	0.072(14)	0.068(7)	0.047(6)	0.038(9)
$D2B_2$	0.066(16)	0.052(13)	0.078(14)	0.046(7)	0.063(9)	0.048(15)
$D2B_3$	0.030(16)	0.064(18)	0.074(20)	0.057(9)	0.060(9)	0.031(15)
$HRPD_1$	0.067(13)	0.034(28)	0.105(18)	0.039(15)	0.039(9)	0.042(12)
$HRPD_2$	0.082(13)	0.134(13)	-0.022(41)	0.024(14)	0.039(10)	0.055(14)
D1A	0.098(9)	0.101(11)	0.068(11)	0.053(4)	0.047(4)	0.076(9)

Table 15: The ice III deuterium thermal factors refined free of any restraint.

Since this work aims to probe the deuterium ordering, the uncertainty over the thermal factors would not appear to be an immediate concern. Unfortunately, there is a correlation between the occupancy of the deuterium atoms and their thermal motion. Table 16 details the ordering parameters, α and β, for the D2B data refined free of any thermal restraint and partially restrained with D(3) U_{iso} = D(6) U_{iso} =

D(7) U_{iso} = D(8) U_{iso}.

	Free		Restrained	
	α	β	α	β
$D2B_1$	35(3)	52(4)	37(2)	52(4)
$D2B_2$	35(3)	50(4)	35(2)	53(4)
$D2B_3$	30(3)	51(6)	36(3)	50(5)

Table 16: Ice III population factors, α and β, after a free and restrained thermal refinement of the D2B data. In a restrained refinement the thermal factors for D(3), D(6), D(7) and D(8) were described by one parameter whilst the thermal factors for D(4) and D(5) were refined freely.

The differences in ordering upon the introduction of a thermal restraint are not alarming. The only parameter to vary significantly, although by only 2σ (2*esd), is α for the data set $D2B_3$. This is not surprising since the thermal restraint was introduced to moderate the low D(3) and D(8) thermal factors for the $D2B_3$ data set. Since α corresponds to the occupancy of atoms D(3) and D(8), an increase in their thermal motion will cause an increase in their occupation, i.e. an increase in α. It is encouraging to find that the restraint does not alter the ordering found for the other two data sets. Refinement of the $D2B_3$ data continued with the thermal restraint in place. It should be noted that a free refinement, though thought to be slightly erroneous, leads to an increase in ordering for the α parameter. This finding along with the use of thermal restraints in refining this data set and that collected on HRPD and D1A is further discussed in section 5.4.

The profiles fits from the refinement of the data are shown in figures 54 to 60. The two sets of ticks present in each profile fit, represent reflections arising from the argon clathrate (upper) and ice III (lower). The structural details arising from the refinement, atomic parameters, bond lengths and angles etc., are listed in tables 17 to 24.

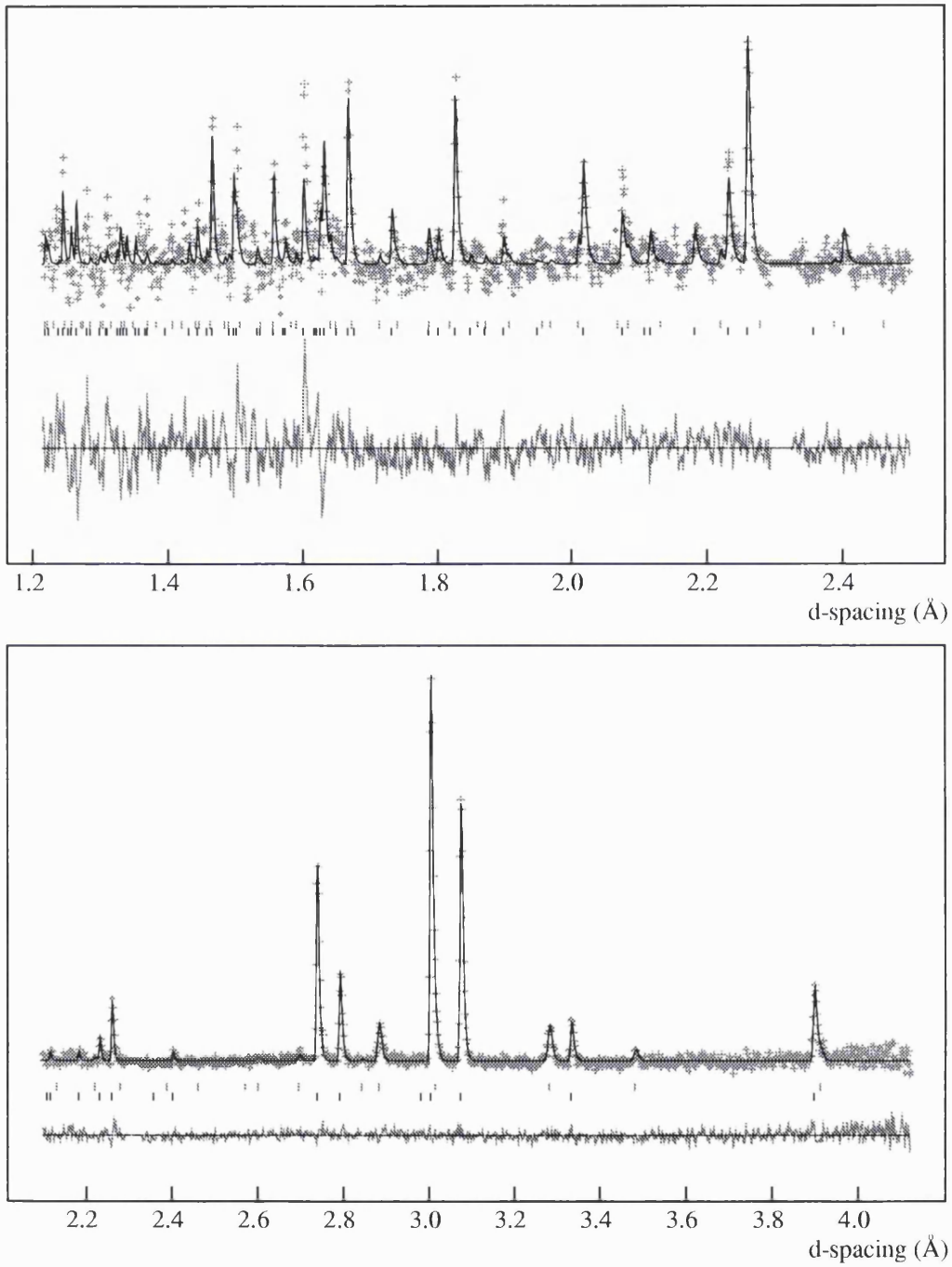

Figure 54: The profile fits for the ice III data collected on IRIS at 3.1 kbar and 260 K, $R_p = 0.0139$ and $R_{wp} = 0.0162$. The amount of argon clathrate determined by the refinement was 18 wt.%.

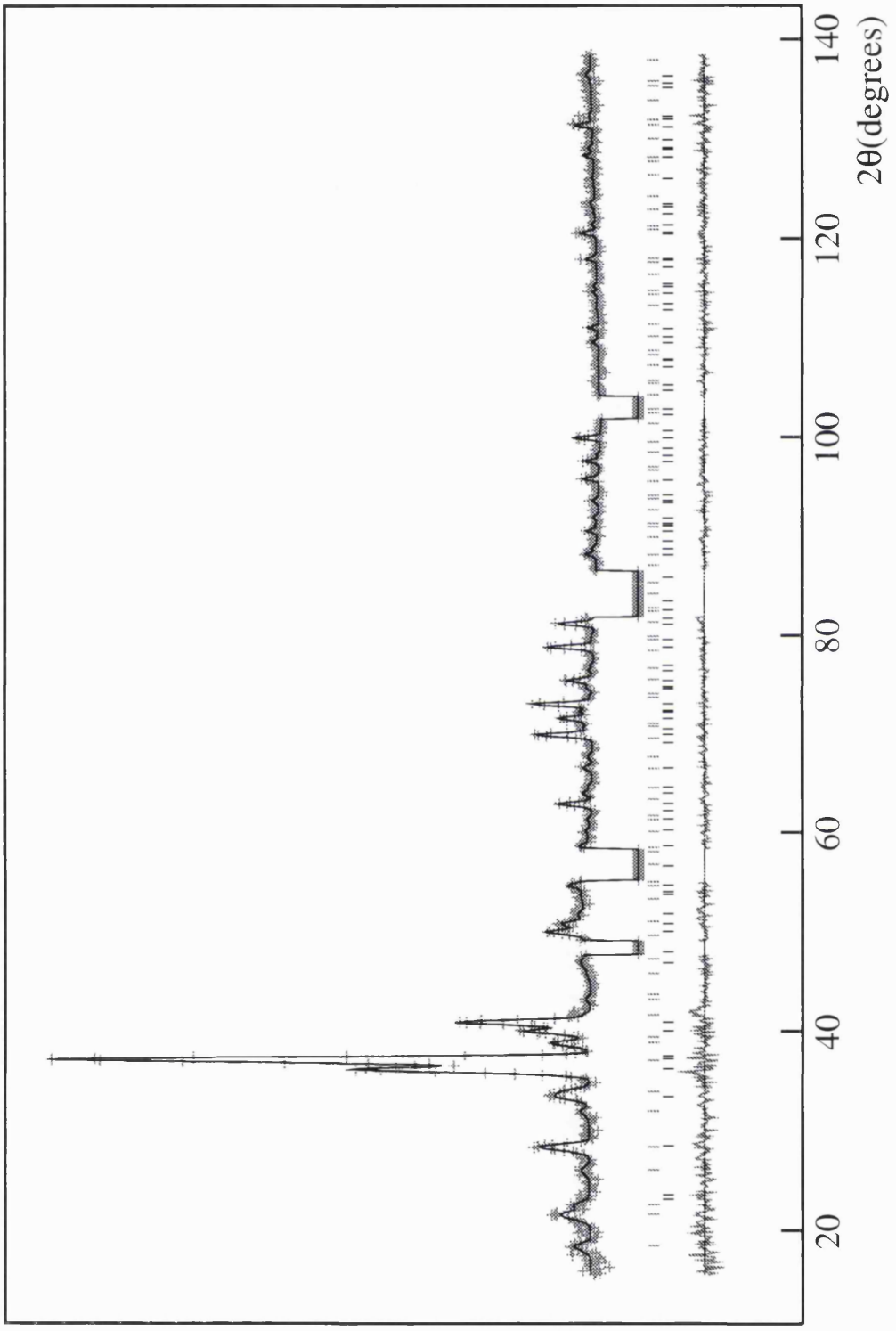

Figure 55: The profile fit for the ice III data collected on D1A at 2.5 kbar and 240 K, $R_p = 0.0450$ and $R_{wp} = 0.0516$. The amount of argon clathrate determined by the refinement was 16 wt.%.

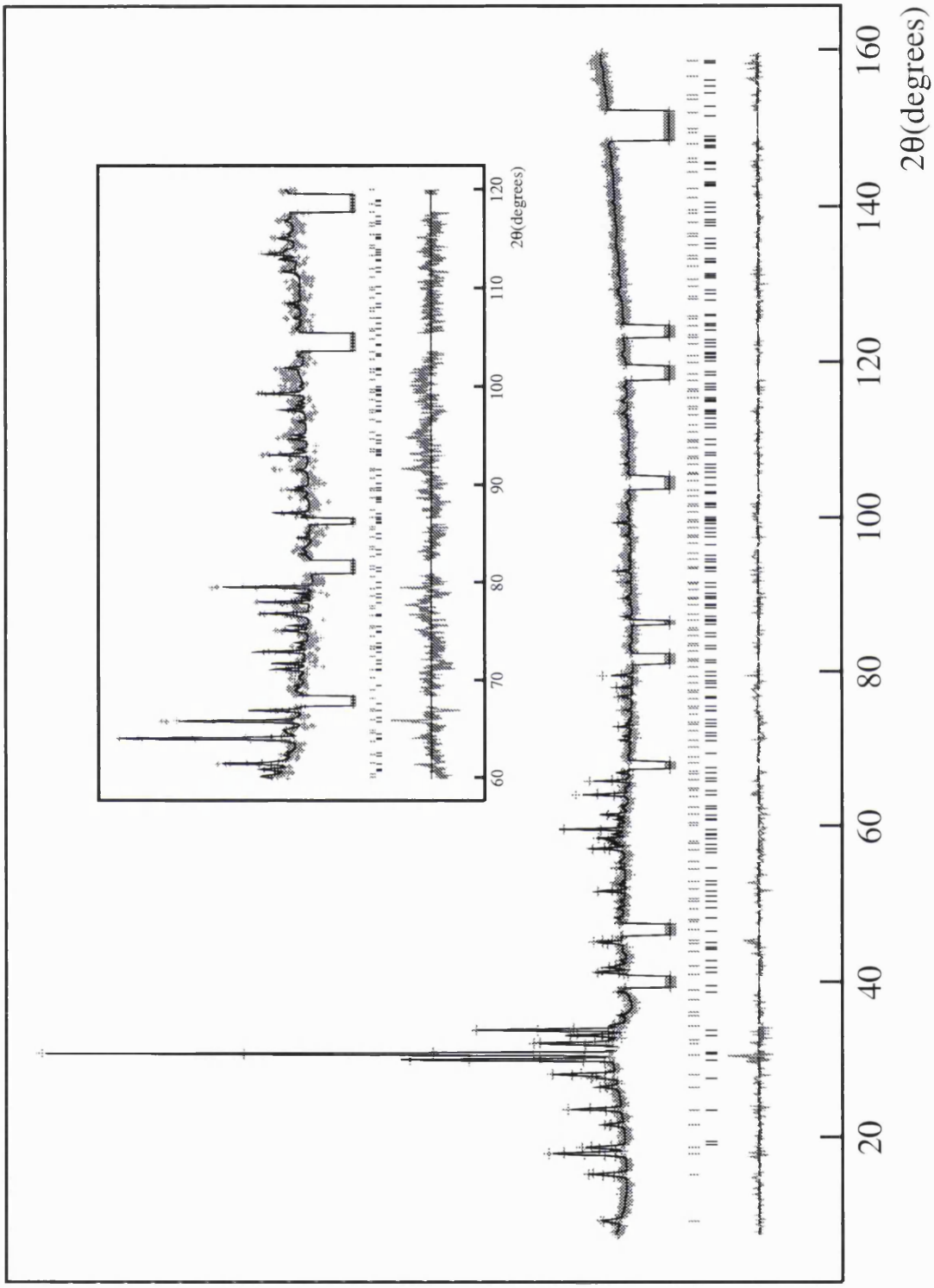

Figure 56: The profile fit for the ice III data collected on D2B at 2.50 kbar and 240 K ($D2B_1$), $R_p = 0.0115$ and $R_{wp} = 0.0156$. The amount of argon clathrate determined by the refinement was 32 wt.%.

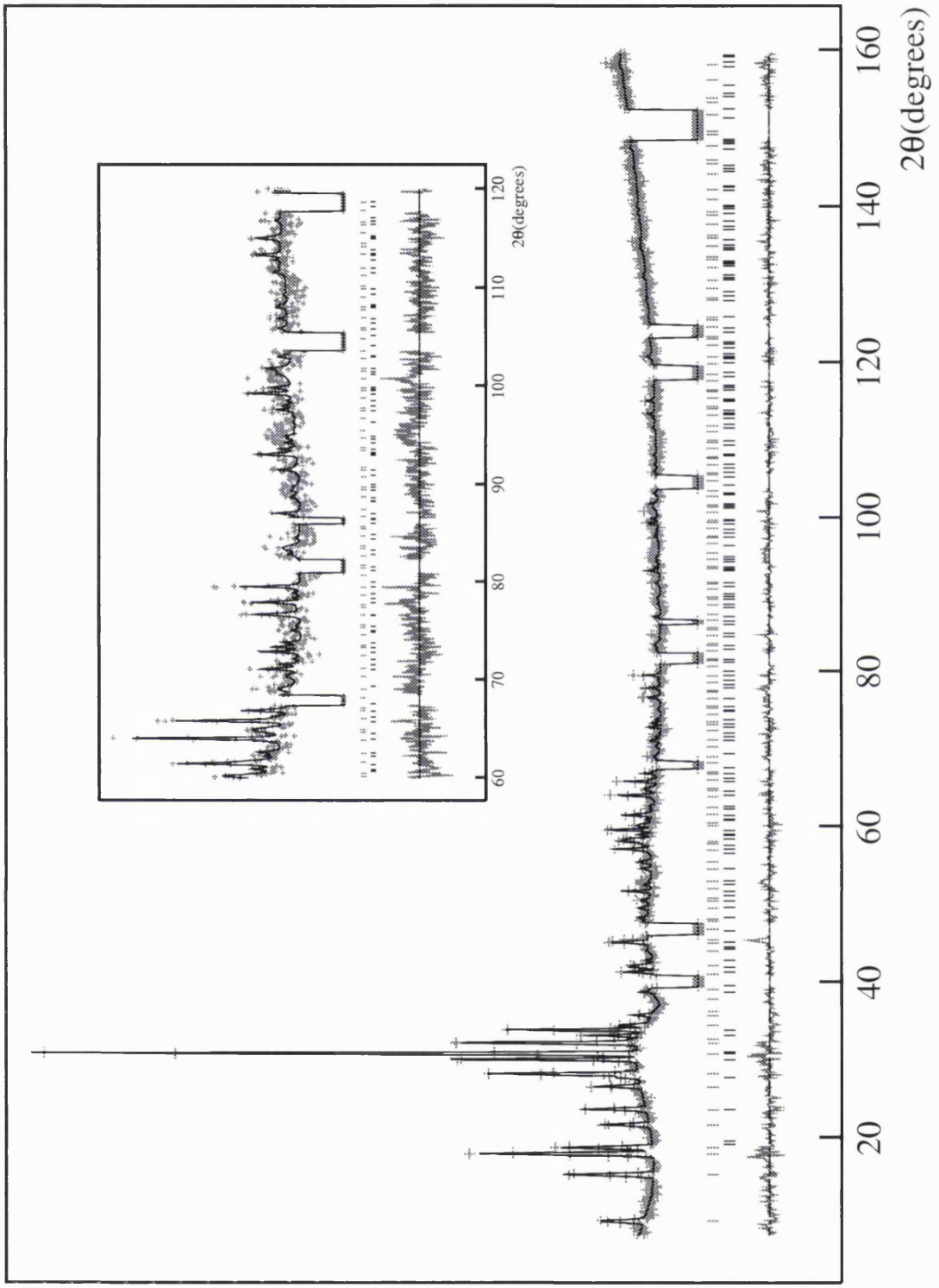

Figure 57: The profile fit for the ice III data collected on D2B at 2.50 kbar and 250 K ($D2B_2$), $R_p = 0.0117$ and $R_{wp} = 0.0156$. The amount of argon clathrate determined by the refinement was 51 wt.%.

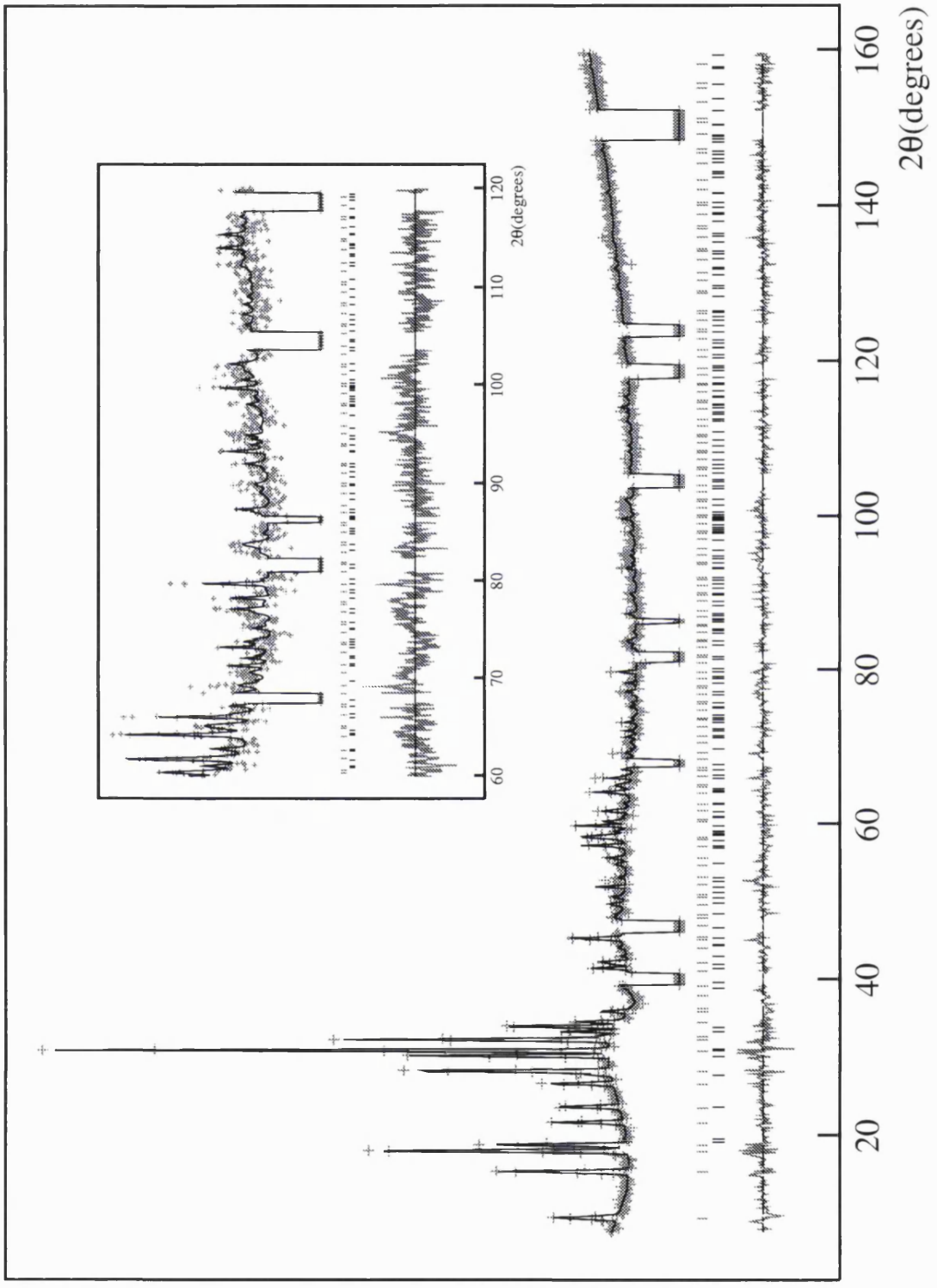

Figure 58: The profile fit for the ice III data collected on D2B at 3.30 kbar and 250 K ($D2B_3$), $R_p = 0.0118$ and $R_{wp} = 0.0159$. The amount of argon clathrate determined by the refinement was 60 wt.%.

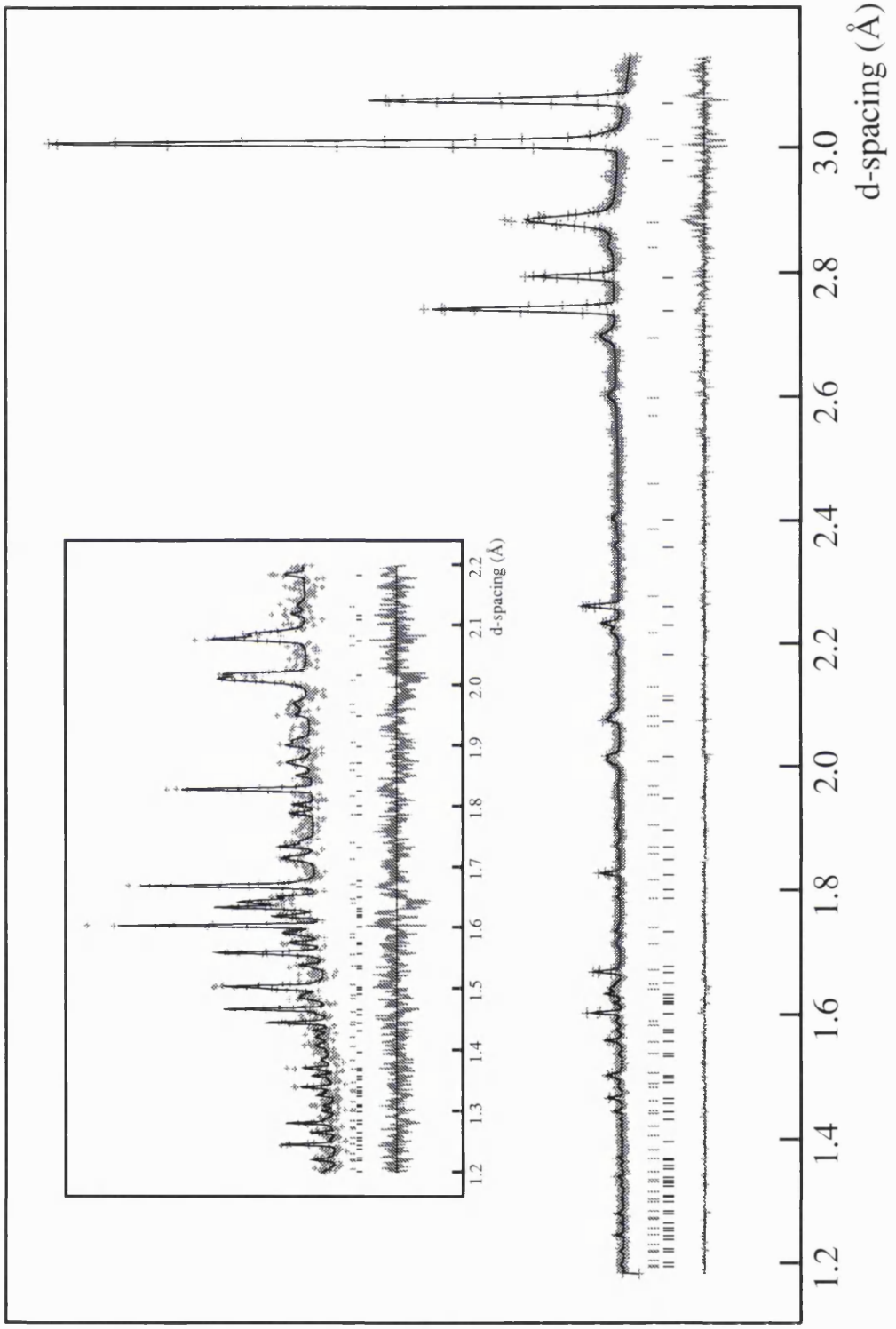

Figure 59: The profile fit for the ice III data collected on HRPD at 3.04 kbar and 250 K ($HRPD_1$), $R_p = 0.0734$ and $R_{wp} = 0.0845$. The amount of argon clathrate determined by the refinement was 36 wt.%.

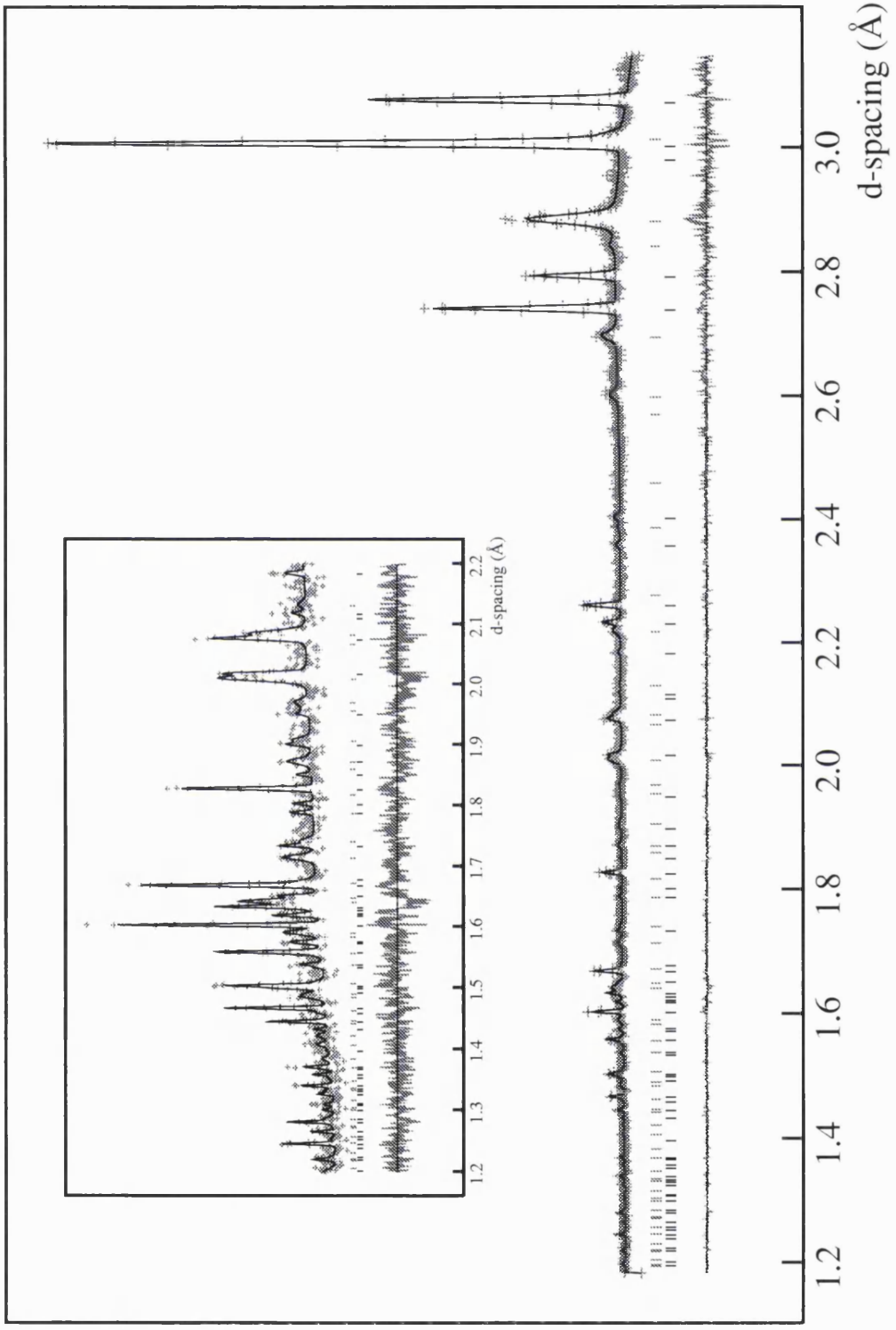

Figure 60: The profile fit for the ice III data collected on HRPD at 3.00 kbar and 250 K ($HRPD_2$), $R_p = 0.0656$ and $R_{wp} = 0.0750$. The amount of argon clathrate determined by the refinement was 47 wt.%.

P(kbar)	T(K)	a(Å)	c(Å)	c/a	V(Å^3)	ρ(gcm^{-3})	Inst.
2.50	240	6.67111(22)	6.96488(40)	1.04404(7)	309.96(2)	1.28576(8)	D1A
2.50	240	6.67596(21)	6.95500(33)	1.04180(6)	309.97(2)	1.28571(8)	$D2B_1$
2.50	250	6.67795(29)	6.96647(46)	1.04320(8)	310.67(3)	1.28283(12)	$D2B_2$
3.30	250	6.66657(36)	6.92482(53)	1.03873(10)	307.76(3)	1.29495(14)	$D2B_3$
3.04	250	6.66935(26)	6.92926(31)	1.03897(6)	308.21(2)	1.29304(9)	$HRPD_1$
3.00	250	6.67092(28)	6.93319(31)	1.03931(6)	308.52(2)	1.29175(10)	$HRPD_2$

Table 17: Ice III lattice constants and densities for the various data sets collected under different conditions of temperature and pressure.

P(kbar)	T(K)	R_{wp}	R_p	α	β	Inst.
2.5	240	0.0516	0.0450	35(1)	49(2)	D1A
2.5	240	0.0156	0.0115	35(2)	52(4)	$D2B_1$
2.5	250	0.0156	0.0117	35(3)	50(4)	$D2B_2$
3.3	250	0.0159	0.0118	36(3)	50(4)	$D2B_3$
3.0	250	0.0845	0.0734	41(3)	47(5)	$HRPD_1$
3.0	250	0.0750	0.0656	36(4)	53(2)	$HRPD_2$

Table 18: Ice III population factors. α and β represent the orientational ordering permitted by the Bernal-Fowler ice rules, table 14. 0 and 100% represent full order, 50% full disorder.

		O(1)	O(2)	D(3)	D(4)	D(5)	D(6)	D(7)	D(8)
D1A		0.116(3)	0.395(3)	0.217(6)	0.141(2)	0.001(6)	0.119(2)	0.298(2)	0.389(4)
$D2B_1$		0.113(3)	0.397(2)	0.239(6)	0.132(3)	-0.004(5)	0.109(3)	0.290(3)	0.383(5)
$D2B_2$	x	0.123(4)	0.398(3)	0.250(9)	0.126(5)	0.004(7)	0.103(3)	0.284(4)	0.382(7)
$D2B_3$		0.113(5)	0.388(4)	0.235(9)	0.133(6)	-0.018(6)	0.101(4)	0.294(4)	0.380(8)
$HRPD_1$		0.121(4)	0.391(3)	0.242(8)	0.129(4)	-0.014(11)	0.122(3)	0.311(5)	0.385(4)
$HRPD_2$		0.126(3)	0.389(4)	0.232(9)	0.121(6)	0.028(8)	0.118(3)	0.297(5)	0.391(5)
D1A		0.309(2)	0.395(3)	0.323(4)	0.402(6)	0.343(4)	0.170(4)	0.357(2)	0.556(7)
$D2B_1$		0.311(3)	0.397(2)	0.321(5)	0.437(4)	0.338(5)	0.182(4)	0.358(2)	0.576(5)
$D2B_2$	y	0.315(4)	0.398(3)	0.319(8)	0.440(4)	0.335(6)	0.184(4)	0.351(3)	0.574(8)
$D2B_3$		0.302(5)	0.388(4)	0.342(6)	0.440(5)	0.322(6)	0.173(5)	0.350(4)	0.562(9)
$HRPD_1$		0.302(3)	0.391(3)	0.314(5)	0.391(11)	0.353(4)	0.177(8)	0.361(4)	0.543(12)
$HRPD_2$		0.309(4)	0.389(4)	0.285(8)	0.414(5)	0.332(5)	0.165(9)	0.353(5)	0.531(2)
D1A		0.288(3)	0	0.191(5)	0.393(5)	0.217(4)	0.303(2)	0.103(3)	-0.014(3)
$D2B_1$		0.287(3)	0	0.195(6)	0.404(4)	0.243(7)	0.318(3)	0.102(3)	-0.037(2)
$D2B_2$	z	0.283(4)	0	0.187(9)	0.401(5)	0.251(9)	0.328(3)	0.100(4)	-0.027(5)
$D2B_3$		0.284(4)	0	0.204(8)	0.394(7)	0.254(9)	0.323(3)	0.107(5)	-0.044(6)
$HRPD_1$		0.288(3)	0	0.183(7)	0.392(11)	0.224(8)	0.299(3)	0.103(5)	-0.037(3)
$HRPD_2$		0.307(4)	0	0.196(9)	0.432(4)	0.238(5)	0.293(3)	0.120(6)	-0.041(4)
D1A		0.071(3)	0.061(3)	0.069(2)	0.069(2)	0.069(2)	0.069(2)	0.069(2)	0.069(2)
$D2B_1$		0.062(3)	0.044(4)	0.048(10)	0.052(11)	0.072(14)	0.068(7)	0.047(6)	0.038(9)
$D2B_2$	U_{iso}	0.062(5)	0.048(6)	0.066(16)	0.052(13)	0.078(14)	0.046(7)	0.063(9)	0.048(15)
$D2B_3$		0.068(6)	0.045(6)	0.050(5)	0.058(14)	0.072(16)	0.050(5)	0.050(5)	0.050(5)
$HRPD_1$		0.062(6)	0.048(5)	0.064(6)	0.064(6)	0.064(6)	0.064(6)	0.064(6)	0.064(6)
$HRPD_2$		0.065(6)	0.044(4)	0.063(5)	0.063(5)	0.063(5)	0.063(5)	0.063(5)	0.063(5)

Table 19: Ice III atomic positions and isotropic thermal factors.

	$D2B_1$	$D2B_2$	$D2B_3$	$HRPD_1$	$HRPD_2$	D1A
O(1)–D(3)	1.05(4)	1.08(6)	1.02(6)	1.09(6)	1.06(6)	0.96(4)
O(1)–D(4)	1.18(4)	1.17(4)	1.20(5)	0.94(9)	1.11(2)	0.97(4)
O(1)–D(5)	0.86(5)	0.84(4)	0.90(5)	1.06(7)	0.83(5)	0.94(4)
O(1)–D(6)	0.89(3)	0.94(3)	0.91(4)	0.84(5)	0.96(6)	0.94(2)
O(2)–D(7)	1.04(2)	1.08(3)	1.01(3)	0.91(4)	1.06(4)	1.00(2)
O(2)–D(8)	1.23(3)	1.20(5)	1.20(6)	1.05(7)	1.00(9)	1.08(3)

Table 20: Ice III O–D bond lengths.

	$D2B_1$	$D2B_2$	$D2B_3$	$HRPD_1$	$HRPD_2$	D1A
O(1)···D(4)	1.54(4)	1.59(5)	1.57(6)	1.89(8)	1.73(4)	1.78(4)
O(1)···D(5)	1.92(6)	1.99(8)	1.99(8)	1.79(7)	1.95(5)	1.81(4)
O(1)···D(7)	1.77(2)	1.69(3)	1.75(3)	1.84(4)	1.75(5)	1.80(2)
O(1)···D(8)	1.57(4)	1.61(6)	1.60(6)	1.73(7)	1.86(9)	1.70(5)
O(2)···D(3)	1.80(5)	1.72(8)	1.77(6)	1.69(6)	1.85(8)	1.85(4)
O(2)···D(6)	1.96(3)	1.98(3)	1.96(3)	1.94(4)	1.87(5)	1.87(2)

Table 21: Ice III O···D bond lengths.

	$D2B_1$	$D2B_2$	$D2B_3$	$HRPD_1$	$HRPD_2$	D1A
O(1)–O(1)	2.713(15)	2.731(21)	2.756(25)	2.795(20)	2.772(27)	2.731(10)
O(1)–O(2)	2.811(18)	2.752(27)	2.754(24)	2.750(20)	2.808(31)	2.795(13)
O(1)–O(2)	2.773(17)	2.794(27)	2.771(28)	2.753(19)	2.832(29)	2.778(19)

Table 22: Ice III O–O bond lengths.

	$D2B_1$	$D2B_2$	$D2B_3$	$HRPD_1$	$HRPD_2$	D1A
D(3)–O(1)–D(4)	107(3)	114(5)	93(5)	115(4)	134(3)	110(3)
D(3)–O(1)–D(5)	120(4)	125(6)	127(6)	109(3)	97(4)	101(3)
D(3)–O(1)–D(6)	104(3)	110(5)	118(4)	98(2)	78(4)	99(2)
D(4)–O(1)–D(5)	101(3)	95(4)	98(4)	99(3)	108(5)	113(2)
D(4)–O(1)–D(6)	121(2)	116(3)	124(4)	124(3)	135(3)	123(3)
D(5)–O(1)–D(6)	105(4)	96(5)	97(5)	111(4)	95(4)	108(3)
D(7)–O(2)–D(7)	97(3)	91(4)	103(5)	101(5)	111(4)	101(4)
D(7)–O(2)–D(8)	110(2)	109(3)	114(3)	113(2)	117(3)	107(2)
D(7)–O(2)–D(8)	121(1)	125(2)	114(2)	112(2)	109(2)	125(1)
D(8)–O(2)–D(8)	101(3)	101(5)	99(5)	97(4)	93(5)	94(4)

Table 23: Ice III D–O–D bond angles.

	$D2B_1$	$D2B_2$	$D2B_3$	$HRPD_1$	$HRPD_2$	D1A
O(1)–O(1)–O(1)	114.3(3)	114.0(4)	112.6(4)	112.9(4)	113.0(5)	114.0(2)
O(1)–O(1)–O(2)	100.1(8)	101.7(1.2)	99.0(1.4)	99.4(9)	103.4(1.1)	100.5(9)
O(1)–O(1)–O(2)	143.6(6)	144.3(7)	143.4(1.1)	145.4(9)	148.2(5)	144.0(6)
O(1)–O(1)–O(2)	90.5(3)	90.9(4)	90.5(4)	90.5(4)	88.4(5)	90.2(4)
O(1)–O(1)–O(2)	96.2(1.1)	93.4(1.4)	98.5(2.0)	95.9(1.5)	92.3(1.0)	96.0(1.0)
O(2)–O(1)–O(2)	99.0(6)	100.2(9)	98.5(9)	99.5(8)	95.9(1.0)	98.8(8)
O(1)–O(2)–O(1)	126.9(7)	126.4(1.0)	127.1(1.2)	125.1(1.0)	120.2(8)	126.2(9)
O(1)–O(2)–O(1)	104.6(4)	103.1(6)	105.5(8)	105.4(5)	105.8(4)	104.7(4)
O(1)–O(2)–O(1)	103.1(8)	104.1(1.3)	103.5(1.3)	104.1(1.1)	109.8(1.5)	104.0(1.3)
O(1)–O(2)–O(1)	93.4(1.1)	96.3(6)	90.7(2.0)	93.7(1.7)	95.1(1.2)	93.4(1.1)

Table 24: Ice III O–O–O bond angles.

5.4 Discussion

5.4.1 Texture

As already noted in section 5.3, the results obtained from the refinement of the IRIS data were highly suspicious. The small number of detectors on the IRIS instrument meant the area sampled around the diffraction rings was small. Information on powder quality could not therefore be gained by inspection of the individual detectors. Whether the results obtained are an artefact of a textured sample, or poor data statistics at short d-spacings, remains uncertain. The results were therefore omitted from the tables above.

It was always suspected that the sample, from which the $HRPD_1$ data were collected, was textured. Prior to collecting the data set $HRPD_1$, the sample, which quite clearly suffered from textured, was cycled through the ice phases Ih, II, III and V in attempt to improve the powder quality. After two such cycles, there was no apparent texture in the ice III diffraction pattern and data were collected. Inspection of the individual detectors indicated no change in intensities for the large reflections at ~2.9 Å. However, there were only four large ice reflections from which the quality of the powder was judged. Differences in intensities for the small reflections were impossible to identify by inspection of the individual detectors due to poor statistics. After data collection, ices II and V were again formed through changes in temperature and pressure. The data from both phases indicated that the texture had not been fully removed from the sample. Although only 6° around the diffraction rings was sampled by the detectors, the data were nevertheless refined. Unsurprisingly, the bond lengths and ordering parameters for the $HRPD_1$ data appear anomalous in comparison with results from the other data. Although included in the tables above, the results arising

from the refinement of the $HRPD_1$ data must be disregarded.

5.4.2 Phase transitions

Experiments at Göttingen had shown that phase transitions, thought to be ice Ih–III transitions, occur at 2.5 kbar and 248 K on pressure increase, and at 2.2 kbar and 248 K on pressure decrease. Although phase identification was not possible, the pressures at which the transitions were observed strongly indicate that the Ih–III and III–Ih transitions were observed[1]. However, the experiment on D2B, which followed the same procedures, found a non-crystalline phase upon pressurising ice Ih, the cause of which remains uncertain. The point at which the non-crystalline phase formed, 2.8 kbar and 248 K, is close to the extended ice Ih melting line and it may simply be that the ice melted. A sub-cooling of 11 K, i.e. a temperature of 245 K, has been noted [103] as necessary for the formation of ice III from the liquid which would explain why ice III did not immediately form from the melt. Alternatively, the non-crystalline phase may be some form of amorphous argon hydrate. In ice Ih, the water molecules all form six-membered rings. However, ice III comprises mostly five-membered rings with some seven- and eight-membered rings; there are no six-membered rings. The transition from ice Ih to ice III must therefore involve the breaking of many hydrogen bonds. It is possible that as the ice Ih bonds break, the argon atoms squeeze their way into the structure preventing the water molecules from rearranging to form ice III. What remains is an amorphous mess consisting of water and argon. However, ice II is similar in structure to ice Ih and hence the same behaviour might therefore be expected for the transitions II–III and II–V, yet

[1] Although the ice Ih–III transition occurred at 2.5 kbar, with the established equilibrium line at 2.2 kbar, overpressure has been recorded by others [87,89] as being necessary to induce the formation of ice III from ice Ih.

no amorphous transitions were observed. The argument for melting ice Ih therefore seems more likely.

During the experiment carried out on HRPD, ice III transformed over a period of 6 hours to ice II at 3.3 kbar and 250 K. The slow rate of transition suggests that the pressure and temperature conditions were very close to the ice II–III transition line, but just inside the ice II stability region. This is contrary to the current D_2O phase diagram which suggests that the transition should occur some 2 K lower. The ice II that resulted was highly textured. The formation of texture from a good powder would suggest that the ice III is first melting, before freezing to form ice II. This seems feasible with the temperatures involved. The slow rate of transition would allow the melt to form large drops before freezing to form large crystallites.

A similar behaviour was observed by Arnold *et al.* [87] when attempting the formation of ice III from ice Ih. Using helium gas, the pressure was increased incrementally at 249 K in a manner similar to that followed in the D2B experiment. At 2.35, 2.41 and 2.62 kbar, only ice Ih was observed; however, at 2.75 kbar the sample transformed to textured ice II. At the slightly colder temperature of 243 K, ice III formed momentarily before transforming once again to textured ice II. The formation of texture led Arnold *et al.* to suggest that an unstable liquid had formed. Unfortunately, there were no reports of the times involved. Although the use of helium would have been responsible for the difficulty in forming ice III, it cannot explain the transformation of good to poor powder.

5.4.3 The use of thermal restraints

The nature of the ice III diffraction profiles, with the reflections at high angles low in intensity, meant that the refinement of the deuterium thermal factors was difficult.

Only for the D2B data, for which the d-spacing coverage was greatest, was it possible to refine the thermal factors freely. Although restraining the thermal factors for the HRPD and D1A data was by no means ideal, it is certain that the values obtained after a free refinement were erroneous, table 15. Unfortunately, there is a correlation between the occupancy of the deuterium atoms and their thermal motion: an increase in thermal motion leads to an increase in occupation.

The β ordering parameter corresponds to the occupancy of deuterium atoms D(4) and D(5) only. For all D2B data, in which the thermal factors were refined free of any restraints, the thermal factors for D(5) were found to be greater than those for D(4), table 19. Yet for the HRPD and D1A data, the thermal factors for the two atoms were constrained to the same value. This is most probably the cause for a β occupancy slightly greater than 50% for the data set $HRPD_2$, table 18. When the same thermal restraint was used to refine the $D2B_2$ data set, β increased from 50 to 55%.

A free thermal refinement of the $D2B_3$ data led to suspiciously low thermal factors for the atoms D(3) and D(8), table 15. Not only were the thermal factors for these two atoms lower than those of the other deuterium atoms, but they were also lower than those of the more massive oxygen atoms. Although ice III is positionally disordered, section 5.4.4, and therefore a variation in thermal factors is not unexpected, the thermal factors for these two atoms seem rather too low. There are two possible explanations as to why low thermal factors were obtained for this data set. First, the two atoms of concern are weakly occupied and it may simply be that the refinement had trouble decorrelating the thermal motion and occupancy for this data set; there are also indications of low thermal factors for these atoms in the refinement of the $D2B_1$ data. Second, the amount of argon clathrate is largest for the $D2B_3$ data,

figure 58. This not only contaminates the ice data, but an increase in clathrate must also be accompanied by a decrease in the amount ice III. The thermal factors for the two atoms were therefore partially restrained as described in section 5.3. The effect of the restraint on the ordering parameters is also discussed in section 5.3.

5.4.4 Positional disorder

The geometry of the water molecule in ice is not thought to differ much from that found in the vapour, O–D = 0.97 Å and D–O–D = 104.5°. However, the bond lengths and angles determined by crystallography are often very different for ices in which the water molecules are orientationally disordered. There are six possible orientations that a water molecule can adopt, figure 6. The positions of atoms determined by crystallography are the space-time average of all six orientations. However, the position of the water molecule for each of the six orientations may differ. Local displacements from the crystallographic mean lead to artificial bond lengths and angles, figure 61.

The O–D bond lengths, table 20, and D–O–D bond angles, table 23, found in this work reflect the positional disorder present in ice III. To try and determine the nature of the disorder by crystallographic means alone is difficult. In the case of ice III the picture is too complicated to attempt a full explanation. The short and long O–D bond lengths most probably arise as a result of disorder similar to that in figure 61.

There are two likely mechanisms responsible for displacing the water molecules from their crystallographic mean, both of which are discussed in detail in section 5.4.5. First, the water molecules move to better accommodate the O–O–O bond angles and thereby decrease the strain on the O–D$\cdots$O hydrogen bonds, figure 61. Second, the water molecules experience intermolecular interactions, both attractive and repulsive,

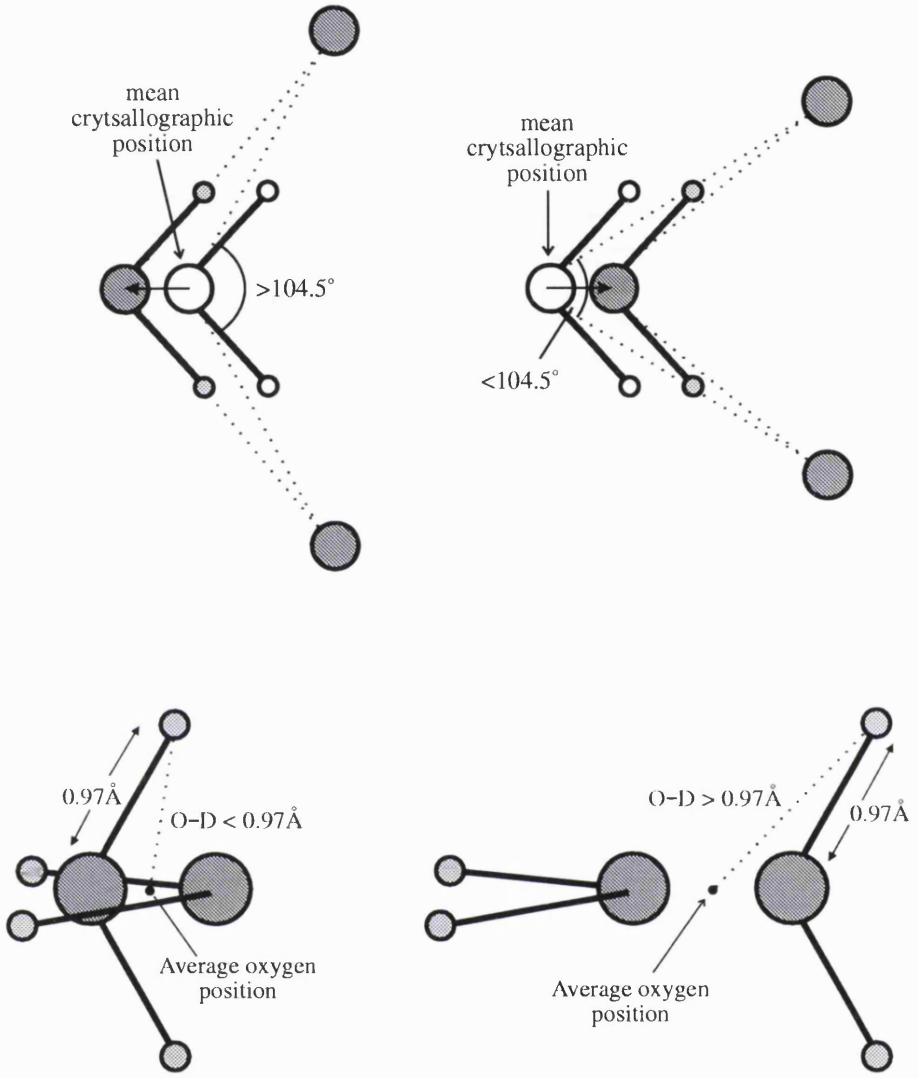

Figure 61: Positional disorder arises from water molecules which move from their crystallographic mean positions. One source of this shift in water molecule position is related to hydrogen-bond strain. A water molecule in a particular orientation will move such that the O–O–O bond angle approaches 104.5°, thus decreasing the bending strain on the O–D···O hydrogen bonds. Two examples are shown above for orientations in which the crystallographic O–O–O bond angle is greater and smaller than 104.5°. Shifts from the crystallographic positions lead to artificial bond lengths and angles. Again, two examples are shown which lead to O–D bond lengths greater and smaller than 0.97 Å. An O–D bond length greater than 0.97 Å is observed for ice Ih [59], while an O–D bond length shorter than 0.97 Å is observed for ice VII [104,105].

from the surrounding non-bonded water molecules. If the positional disorder were attributed solely to the accommodation of bond angles then it might have been possible to explain the origins of the disorder and interpret the O–D bond lengths. Unfortunately, the introduction of atomic interactions makes the task extremely difficult. There are simply too many atoms within close proximity acting with different forces in many different directions.

The positional disorder for water molecules of type O(1) appears to be greater than that for molecules of type O(2). The higher thermal factor for the atom O(1), table 19, implies that its displacement from the crystallographic mean is greater than that for O(2). This may in part be attributed to the O–O–O bond angles, where the deviation from the ideal angle of 104.5° is greater in those occupied by molecules of type O(1), table 24.

5.4.5 Orientational disorder

As with positional disorder, discussed in section 5.4.4, there are two likely mechanisms responsible for the orientational ordering of water molecules in ice.

The first is related to hydrogen-bond strain. In ice, the water molecules are arranged tetrahedrally with each water molecule donating two hydrogen bonds to two neighbouring water molecules, figure 61. The O–O–O bond angle into which the water molecule donates the two hydrogen bonds, is referred to as the *donor angle.* Unless the donor angle is 104.5°, the D–O–D bond angle, the hydrogen bonds between water molecules will be bent. The larger the deviation from 104.5°, the larger the amount of bond bending. Since it is impossible to have tetrahedral co-ordination with all four angles at 104.5°, all hydrogen bonds in ice are bent to some degree. To relieve the bending strain on the hydrogen bonds, the water molecule may move

from its mean position, figure 61. This movement in turn leads to positional disorder and artificial bond lengths and angles. The water molecule can also be selective as to which neighbouring water molecules it chooses to donate its two hydrogen bonds. Each water molecule can adopt one of six possible orientations, figure 6. The different orientations may have different O–O–O bond angles and will therefore result in different amounts of hydrogen-bond bending. The energy required by the water molecule to occupy each of the different orientations will therefore also differ. This leads to partial ordering of the water molecules, with some orientations more favourable, and therefore more occupied, than others.

The second mechanism which can influence orientational ordering is related to non-bonded interactions. Each water molecule experiences forces, both attractive and repulsive, from the surrounding, non-bonded water molecules. A water molecule which adopts a particular orientation may experience forces from surrounding water molecules which cause the molecule to shift from its mean position. This then introduces a further source of positional disorder. In addition, non-bonded interactions may be responsible for influencing the orientations adopted by water molecules. For example, the occupation of one orientation might deter another because it would involve short, repulsive D$\cdots$D distances.

The results of the refinements clearly indicate partial ordering of water molecule orientations within ice III, table 18. Ignoring the erroneous $HRPD_1$ data, section 5.4.1, the ordering found is consistent for all data sets with occupancies of 35% and 50% for α and β respectively. The question that now arises is what are its origins? Can the partial order be explained purely by the variation in O–O–O bond angles or are non-bonded interactions also important?

The variation in O–O–O bond angles for ice III is huge, figure 62 and table 24.

Partial ordering of the water molecules might therefore be expected. However, it may be that at the temperatures involved (>240 K), the water molecules have sufficient energy to occupy all orientations without bias. Only as the temperature, and therefore the energy of the water molecules, is decreased, is ordering and the subsequent transition to ice IX then observed.

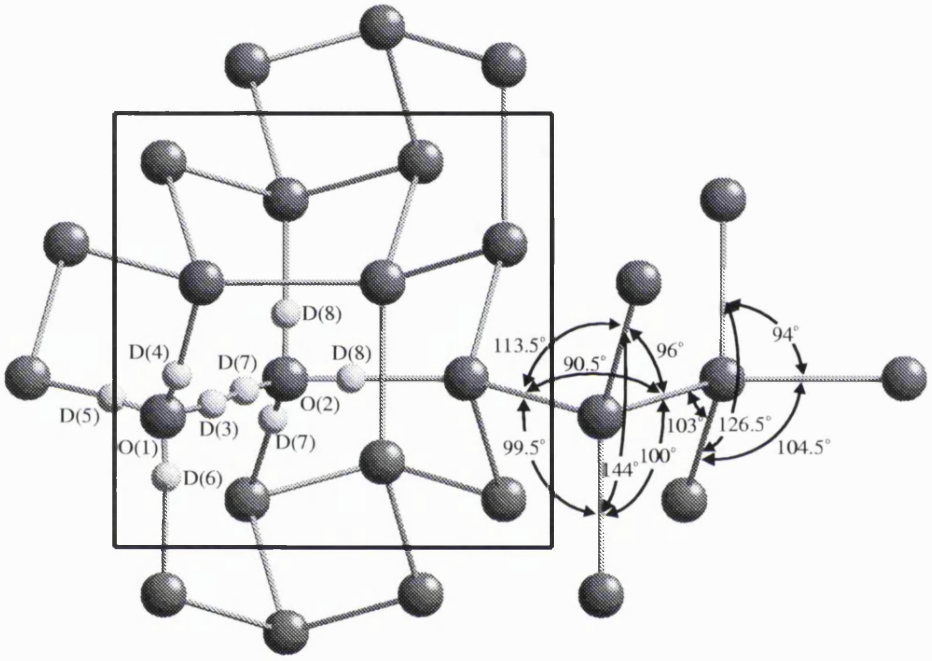

Figure 62: The ice III structure viewed along the *c*-axis. Only deuterium atoms of the asymmetric unit are shown for clarity.

The orientational possibilities, and the O–O–O bond angles involved, are considered for the two crystallographically different water molecules. The possible orientations available to water molecule of type O(1), figure 63, are considered first. The donor angle in configuration 1 deviates by only 9° from the D–O–D angle of 104.5° and is not therefore considered unfavourable. Since the orientation affects both β and $(1 - \beta)$, its occupation, regardless of frequency, will lead to a β value of 50%. Configuration 6 is similar to configuration 1 in that the deviation in the donor angle

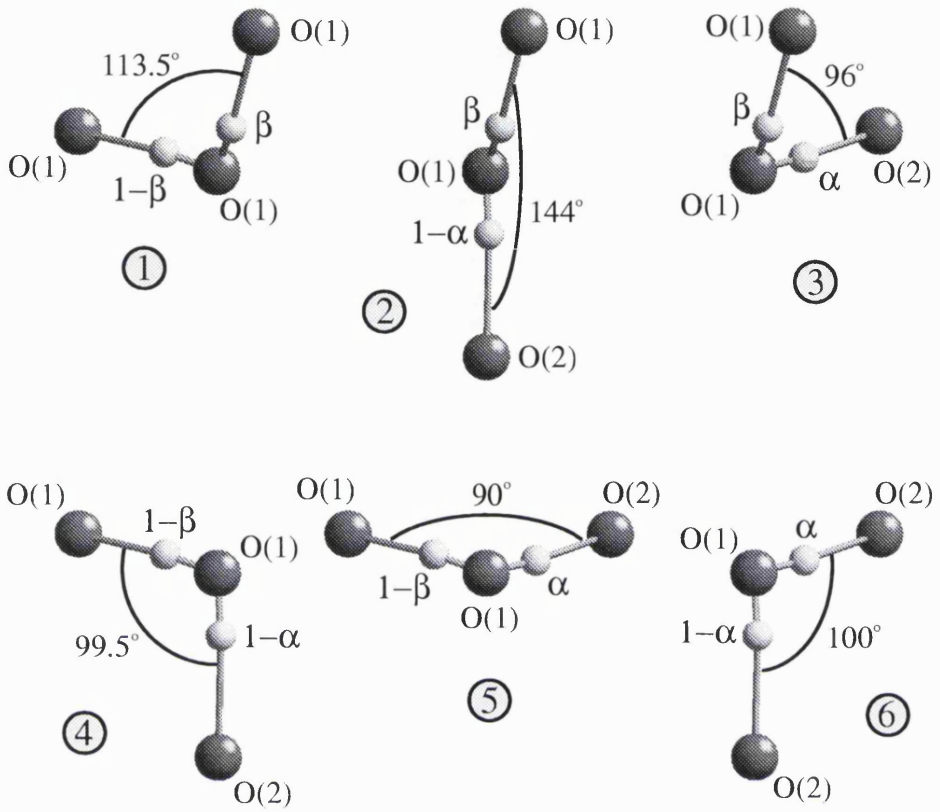

Figure 63: The six different orientations which water molecules of type O(1) can adopt.

from the ideal is small, only 5°, and that its occupation affects both α and $(1-\alpha)$. The orientation is therefore not considered unfavourable and will result in an α value of 50%. Configurations 3 and 4 are very much alike in that both have similar donor-angle deviations from the ideal, 8.5° and 5° respectively. However, configuration 3 affects the ordering parameters α and β, whereas configuration 4 affects $(1-\alpha)$ and $(1-\beta)$. If configuration 4 occurs more frequently than configuration 3, by virtue of the slightly smaller bond-angle deviation, then both α and β would be slightly less than 50%. But since the donor angles are similar, it is reasonable to assume that both configurations occur with equal probability. If this is so, then the ordering

parameters α and β remain unchanged at 50%. Configurations 2 and 5 influence the ordering parameters in a similar way to configurations 3 and 4, but have very different donor-angle deviations from 104.5°. The donor angle of configuration 2 is the largest found in any ice structure and has a massive 39.5° deviation from the ideal. Configuration 5, however, has a rather more moderate donor-angle deviation of 14°. It is clear that configuration 2 is less favourable in terms of hydrogen-bond bending than its counterpart configuration 5, and should occur less frequently. This will result in an increase in α and an equivalent decrease in β from the nominal 50%.

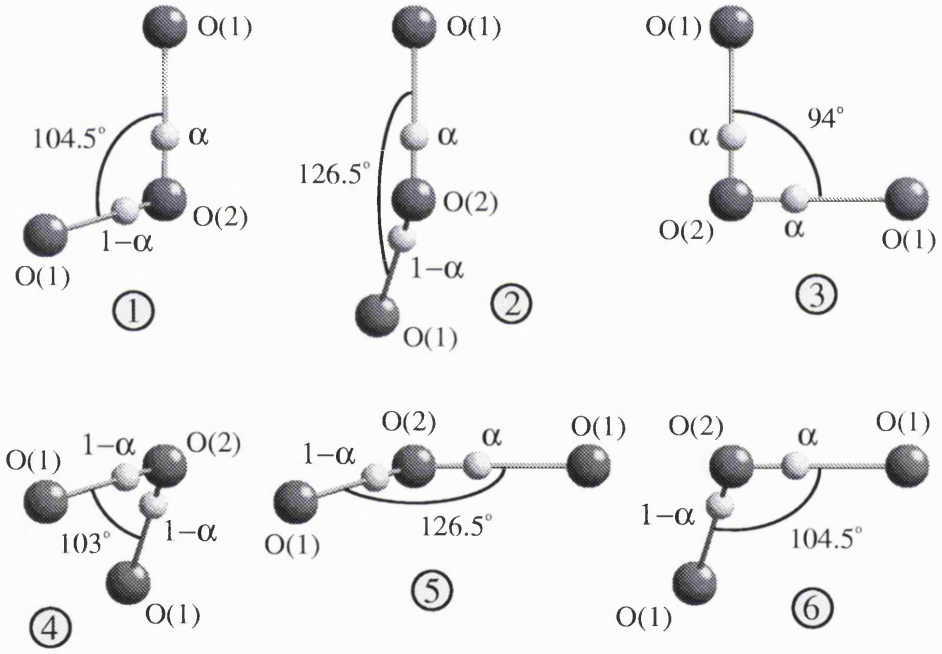

Figure 64: The six different orientations which water molecules of type O(2) can adopt.

The possible orientations available to water molecules of type O(2), figure 64, are now considered. Configurations 1 and 6, and, 2 and 5, are equivalent by symmetry. In addition, they all involve α and $(1-\alpha)$. Regardless of any bias these orientations might have, the α ordering parameter remains unchanged at 50%. Only configurations 3

and 4 have any bearing on the value of α. The donor-angle deviation for configuration 3, 10.5°, is larger than that for configuration 4, 1.5°. More frequent occupation of configuration 4 would result in a decrease in α.

In summary, the donor angles for water molecules of type O(1) suggest an increase in α and an equivalent decrease in β from the nominal 50%. The donor angles for water molecules of type O(2), on the other hand, suggest a decrease in α. The difference in donor-angle deviation for O(1) configurations 2 and 5 is larger, 25.5°, than the difference for O(2) configurations 3 and 4, 9°. The increase in α arising from water molecules O(1) is therefore expected to be larger than the decrease arising from water molecules O(2). The ordering parameters expected are therefore: α slightly greater than 50% and β less than 50%.

However, the observed ordering parameters are $\alpha = 35\%$ and $\beta = 50\%$. A β occupancy of 50% can only be accounted for if the O(1) configurations 2 and 5 occur with equal probability. If this is so, then α is also unaffected by O(1) water molecule orientations. A decrease in α is therefore expected from the O(2) configurations 3 and 4. This is indeed what is observed. However, things do not end there. If the difference in donor-angle deviation for O(1) configurations 2 and 5 does not result in favouritism, then why should the smaller difference for O(2) configurations 3 and 4? Of course, it is possible that O(1) configurations 2 and 5 do not occur at all because the donor angles for both configurations are highly unfavourable. This seems unlikely since one of the two donor angles in ordered ice II is 88°. Clearly, the argument has now reached speculation. What can be said however, is that the ordering cannot be simply explained in terms of favourable and unfavourable donor angles. It would therefore appear that non-bonded interactions play an important role in the ordering process.

In ice II, the water molecules are all orientationally ordered. However, the water molecules do not occupy the orientations with the least amount of bond bending [81,84]. Rather than occupying sites with donor angles 99° and 115°, the water molecules occupy sites with donor angles 88° and 99°. The ordering process in ice II is therefore not solely controlled by the desire for linear hydrogen bonds. Although the water molecules in ice IX occupy sites of least bond strain, the water molecules are not symmetrically oriented with respect to the donor angles which they occupy [101], a feature also found in ice II. The amount of hydrogen-bond bending is therefore increased unnecessarily. This points to strong influences other than that of bond strain on the orientation of the water molecules. The mechanism responsible is most likely non-bonded, interatomic interactions. In particular, deuterium–deuterium interactions may cause one orientation to deter another.

The ordering determined in this work, $\alpha = 35(3)\%$, $\beta = 50(4)\%$, differs from that found by Londono *et al.* [103], $\alpha = 33(7)\%$, $\beta = 41(1)\%$. There are several reasons why this may be the case, the most likely being texture. Londono *et al.* found that their ice III sample was textured and, in refining the data, chose a single axis of preferred orientation which led to the biggest improvement in fit. However, texture is a different phenomenon to that of preferred orientation and cannot be easily modelled. From the experience gained in this work in forming ice from the liquid, one axis of preferred orientation has never been sufficient to describe the texture. The texture is in fact more akin to graininess than it is to preferred orientation and an attempt to identify the many different axes of preferred orientation is hopeless. It therefore seems unlikely that the single axis found by Londono *et al.*, by means of trial and error, is a true description of the texture.

The difference in the order parameters may also be attributed to restraints placed

on the refinement. Londono *et al.* fixed three of the five deuterium thermal factors which, as observed in this work, are partly correlated to the deuterium occupancies. More important, however, is the use of bond-length restraints. Londono *et al.* refined the atomic positions with an O–D bond-length restraint of 0.97(5) Å. The use of the same restraint to refine the data collected in this work had a small but significant effect on the occupancies, table 25.

	Free		O–D = 0.97(5)	
	α	β	α	β
$D2B_1$	35(2)	54(2)	34(2)	47(2)
$D2B_2$	35(3)	55(3)	31(2)	47(3)
$D2B_3$	34(3)	50(4)	32(2)	44(3)
$HRPD_2$	36(4)	53(2)	37(2)	48(2)
D1A	35(1)	48(2)	35(1)	49(2)

Table 25: Ice III population factors, α and β, upon refining the atomic positions free of any restraint and with an O–D bond-length restraint of 0.97(5) Å. The D2B data were refined with the same thermal restraint as that used to refine the HRPD and D1A for a fair comparison, hence the slight difference in ordering to that listed in table 18 for a free thermal refinement.

As already noted, positional disorder within ice III means that variations in the O–D bond lengths from the vapour value of 0.97 Å are expected. The use of bond-length restraints is therefore not ideal. Nevertheless, one still expects bond lengths of around 0.97 Å. For example, an O–D bond length of 2.0 Å would certainly be interpreted as unphysical, but what about a bond length of 1.2 Å? The O–D bond lengths obtained in this work could be seen as unrealistic, varying from 0.83 to 1.23 Å, table 20. However, there is a trend in the bond lengths for different data sets which adds some weight to the results obtained.

If the bond lengths do require restraining, then by how much? Londono *et al.* used the restraint 0.97(5) Å based on the bond lengths determined by La Placa *et al.* for ice IX. However, ice IX is essentially ordered and the positional disorder will therefore be small. The restraint may therefore be too constrictive for the more disordered ice III structure. Table 26 demonstrates the effect of bond-length restraints on the ordering parameters for varying degrees of restraint. As the error on the restraint was decreased, i.e. as the restraint was more enforced, the orientational ordering of the water molecules was increased.

O–D	α	β
0.97(1)	31(2)	42(2)
0.97(2)	31(2)	43(2)
0.97(3)	31(2)	44(2)
0.97(4)	31(2)	46(3)
0.97(5)	31(2)	47(3)
free	35(3)	54(3)

Table 26: Ice III population factors, α and β, upon refining the $D2B_2$ data. The data were refined with O–D bond-length restraints of varying strength.

The use of bond-length restraints did not lead to a different ice III structure, which would have implied that the refinement was in a false minimum. Instead, the restraint merely prevented the deuterium atoms from attaining their desired positions. The different data sets behaved differently on restraining, supporting the idea that bond-length restraints are unsuitable. Whilst the amount of orientational order for the D2B data increased as the strength of the restraint was increased, table 26, the ordering remained largely unchanged for the HRPD and D1A data.

The uncertainty surrounding the O–D bond lengths could be clarified by examining the oxygen frameworks of ices III and IX. The water molecule orientations in ice IX are almost fully ordered. There should, therefore, be little positional disorder

within ice IX. By comparing the positions of the oxygen atoms in ices III and IX, the local shift of the water molecules in ice III can be estimated. From this, the expected O–D distances can be determined and compared with those observed in this work. Since ice IX is stable only at temperatures below 165 K, such a comparison would have to ignore temperature-dependent shifts of the fractional co-ordinates. However, the shifts in bond length from 0.97 Å are as much as 0.2 Å, table 20, which is certainly more than the relative shifts in atomic positions expected from temperature changes [59].

There were no measurable changes in the ordering upon changes in pressure and temperature. This is not surprising since if the changes were any larger, one would have expected to observe them dielectrically [33, 85] and/or spectroscopically [106]. Small changes with temperature would also explain why an 'almost' straight, rather than a perfectly straight, ice Ih–III transition line was measured by Kell and Whalley [98].

The points chosen for study were such that a large fraction of the ice III stability region was covered while remaining safely within the established transition lines. Partial ordering was found for all points suggesting the water molecules of ice III are partially ordered throughout the entire stability field.

5.4.6 Entropy considerations

Nishibata and Whalley [102] recorded a change in entropy of 1.34 ± 0.29 $JK^{-1}mol^{-1}$ for the transition ice III–IX. However, the figure was only 40% of that expected, 3.37 $JK^{-1}mol^{-1}$, if ice III were fully disordered and ice IX fully ordered. Since dielectric measurements gave no indication of partial order within ice III [33,85], Nishibata

and Whalley concluded that ice IX must be partially disordered. Using the configurational statistics described by Nagle [2], the measured entropy change corresponded to 7.5% of the hydrogen atoms in ice IX occupying disordered sites. With the partial ordering found in this work for ice III, the recorded transition entropy corresponds to partial disorder of 6% within ice IX. If it is assumed that $\alpha = 0.7\beta$, the ratio found in this work, the work of La Placa *et al.* [101] and Londono *et al.* [103], then the transition entropy corresponds to $\alpha = 5.5\%$ and $\beta = 8\%$ for ice IX, figure 65.

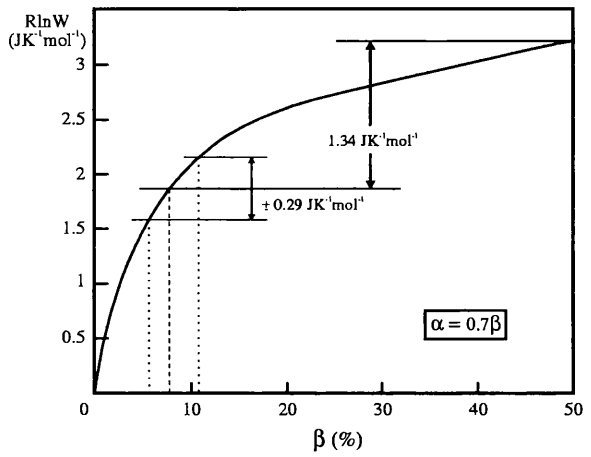

Figure 65: The variation in configurational entropy as a function of the orientational ordering using the configurational statistics described by Nagle [2]. The figure represents a special case with $\alpha = 0.7\beta$. Using the partial ordering found in this work for ice III ($\alpha = 35\%$, $\beta = 50\%$), the ice III–IX transition entropy recorded by Nishibata and Whalley [102] corresponds to partial disorder of 6% within ice IX, with $\alpha = 5.5\%$ and $\beta = 8\%$.

However, Howe and Whitworth [3] have since shown that the calculations of Nagle were incorrect and derived an alternative model, which Nagle himself agreed is the more correct. Unfortunately, the publication only listed the workings for the simple case of one ordering parameter, i.e. $\alpha = \beta$. With 20% ($\alpha = \beta = 40\%$) of the water molecules in ice III orientationally ordered, the transition entropy measured by Nishibata and Whalley [102] corresponds to a massive 36% ($\alpha = \beta = 18\%$) disorder within ice IX, figure 66. This is much larger than the disorder found by La Placa *et al.*, $\alpha = 3.4(7)\%$ and $\beta = 5.1(9)\%$, and Londono *et al.*, $\alpha = 2.9(3)\%$ and $\beta = 5.6(4)$ through neutron diffraction. The only conclusion one can reach is that the

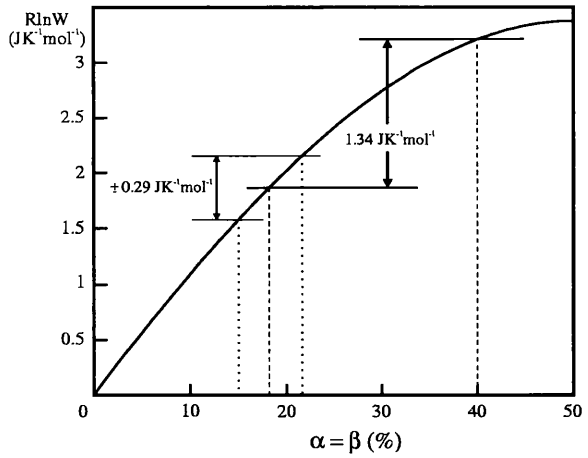

Figure 66: The variation in configurational entropy as a function of the orientational ordering using the configurational statistics described by Howe and Whitworth [3]. Using the partial ordering found in this work for ice III ($\alpha = \beta = 40\%$), the recorded ice III–IX transition entropy corresponds to partial disorder of 36% within ice IX, with $\alpha = \beta = 18\%$.

entropy measured by Nishibata and Whalley is in some way erroneous. Unfortunately, it is not immediately evident why.

5.4.7 Compressibility and expansivity

The compressibility and expansivity of ice III were calculated using only the refined D2B lattice constants, table 17. In this way, systematic errors associated with measuring the temperature, pressure and wavelength were removed.

The compressibility of ice III, determined from the D2B data at 2.5 and 3.3 kbar, is 11.4(2) $Mbar^{-1}$ at 250 K, which corresponds to an isothermal bulk modulus of 88(2) kbar. This figure is in agreement with the isothermal bulk modulus determined by Gagnon *et al.* [94] at 237.5 K, 96.0 kbar, and the adiabatic bulk moduli determined by Tulk *et al.* [107] at 253 K, 92.7 kbar, and by Shaw [93] at 248 K, 85 kbar. The adiabatic moduli were determined by acoustic velocity measurements by Brillouin spectroscopy on single crystals (Tulk *et al.*) and by ultrasonics on powders (Shaw) for H_2O ice III. The isothermal bulk modulus found by Gagnon *et al.* was determined by measuring the volume change of powdered H_2O ice III as a function of pressure.

The expansivity of ice III, determined from the D2B data at 240 and 250 K,

is 239(12) MK^{-1} at 2.5 kbar. The compressibilities and expansivities of all the ice structures examined in this work are discussed in section 9.6.8.

The change in the c/a ratio with pressure and temperature, table 17, immediately indicates anisotropic compressibility and expansivity. The linear compressibilities and expansivities in the *ab*- and *c*-axis directions are 2.12(12) and 7.34(17) $Mbar^{-1}$, and 30(8) and 172(12) MK^{-1} respectively. Since no change in orientational ordering was observed with temperature or pressure, these figures imply that the freedom of movement of the water molecules in the *c*-axis direction is greater than that in the *ab*-axis direction. An examination of the structure indicates a possible reason why changes with temperature and pressure are greater in the *c*-axis direction. Water molecules of type O(1) form spirals which run parallel to the *c*-axis, while water molecules of type O(2) act to bind four neighbouring spirals together. In this way, the spirals can be though of as springs, with compression and thermal expansion of the structure easiest along the axis of the springs, i.e. along the *c*-axis.

5.5 Conclusions

This study has found the water molecule orientations in ice III are partially ordered, confirming the earlier findings of Londono *et al.* [103]. There were no noticeable changes in the amount of order with changes in pressure and temperature, which suggests that partial order exists throughout the established stability region of ice III. The amount of order found in this work is slightly less than that suggested by Londono *et al.* This is thought to be due to texture present within the sample studied by Londono *et al.*

Although the water molecules in the fully ordered structure (ice IX) occupy the

orientations with the least amount of hydrogen-bond bending, the partial order found in ice III cannot be explained by orientations which are unfavourable in terms of bond bending. The ordering process is not, therefore, driven solely by the desire for linear hydrogen bonds. Non-bonded, interatomic interactions are thought to be important, as are the O–D···O···D–O acceptor angles. Further examination of the ice III structure, using the data collected in this work, may be of help in trying to establish what interatomic interactions (D···D and O···D) are responsible for the observed partial order.

There is some doubt surrounding the positions of the deuterium atoms, the doubt arising from the credibility of the O–D bond lengths. By comparing the oxygen frameworks of ices III (disordered) and IX (ordered), the degree of positional disorder within ice III can be estimated. From this, the expected O–D bond lengths can be determined and compared with those observed.

The ice III structure exhibits strong anisotropic compressibility and expansivity. This may be due to the spirals formed by water molecules of type O(1) which run parallel to the *c*-axis. These spirals may be thought of as springs, with compression and thermal expansion of the structure easiest along the axis of the springs.

During the work on ice III, unexpected phase transitions were observed. In particular, pressure increase on ice Ih did not lead to the formation of ice III as expected, but to a non-crystalline phase at 2.8 kbar and 248 K. Although the transition was most probably the melting of ice Ih, an amorphous solid cannot be ruled out.

The results obtained in this work were not as well defined as one had hoped; the thermal factors were refined isotropically and were restrained for some data sets. However, it is doubtful that further work on powders will improve matters. This is due mainly to the nature of the ice III diffraction profiles with reflections of suitable

absent at high scattering angles, angles necessary for the accurate determination of the thermal motions and occupancies of the atoms. Further work on single crystals may, however, prove fruitful. In particular, diffuse scattering could possibly identify the causes of positional and orientational disorder found in this work; information which can only be discerned by examining the local environment of the water molecules.

Chapter 6

Ice V

6.1 Introduction

Ice V was first discovered by Tammann [28] in 1900 and was confirmed soon afterwards by Bridgman [29]. The thermodynamic stability region of ice V extends roughly 210–270 K and 3.5–6.0 kbar, figure 4. Though slightly larger than that of ice III, the stability region of ice V is still small in comparison to other ices.

Bertie and Whalley [82] examined ice V, quenched to liquid nitrogen temperatures and recovered to ambient pressure, by infrared spectroscopy and concluded that the water molecules were four co-ordinated and fully hydrogen bonded. The lack of fine structure in the stretching and rotational bands, together with their rather large widths, figure 67, led them to conclude that the structure consists of many crystallographically different O-H$\cdots$O bonds. Such a scenario is possible for a unit cell large in size and/or low in symmetry, or if the hydrogen atoms within ice V were positionally disordered. Either or both could be occurring and could not be distinguished by their work.

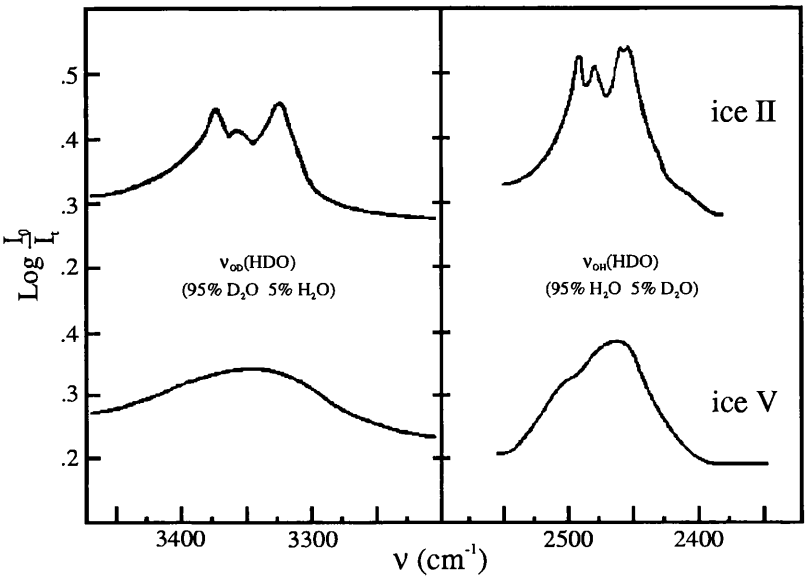

Figure 67: The stretching (ν_{OH} and ν_{OD}) bands for ice II and ice V as measured by Bertie and Whalley [82]. The fine structure observed for ice II, yet absent for ice V, arises from ordered orientations of the water molecules.

Dielectric measurements by Wilson *et al.* [85], this time within the stability region of ice V, also implied four co-ordination and full hydrogen bonding. Moreover, dielectric dispersion, attributed to rotational relaxation of the water molecules, led them to conclude that the water molecules in ice V are orientationally disordered.

Changes in entropy associated with phase transitions were interpreted by Whalley and Davidson [86] as further evidence for an orientationally disordered ice V. Bridgman had determined the change in entropy for the ice transitions, Ih–III, III–II, II–V and V–VI, using the Clausius-Clapeyron relation, equation 16, and found the entropies for ices Ih, III, V and VI were similar yet very different to ice II, figure 50. Since ices Ih and II were known to be orientationally disordered and ordered respectively, Whalley and Davidson concluded that ices III, V and VI must all be orientationally disordered.

The structure of ice V was first determined by Kamb *et al.* [108] from X-ray diffraction data collected on single crystals recovered to ambient pressure. Although diffraction data had been collected in the past [97, 109], they were not of sufficient quality for structure analysis.

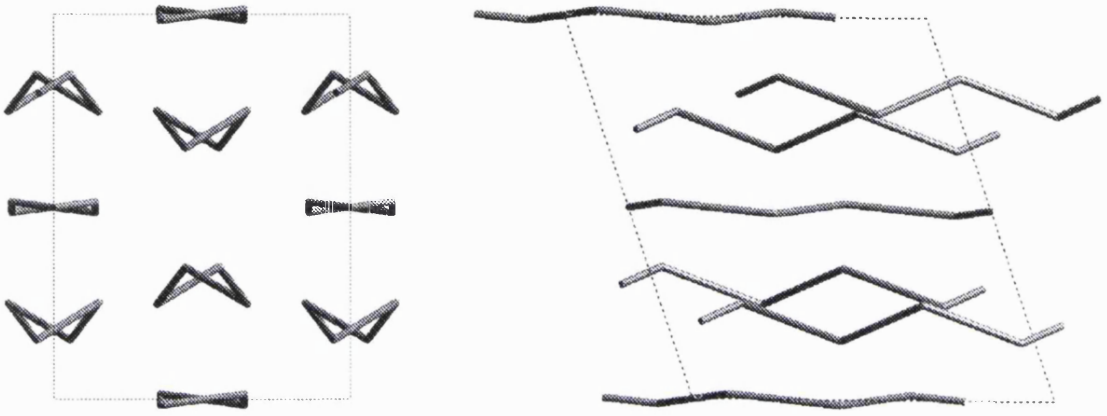

Figure 68: Water molecules of type O(2), O(3) and O(4) form zigzag chains which run parallel to the a-axis, viewed parallel (left) and perpendicular (right) to the a-axis. The chain of type O(4) is the flatter of the two chains seen at $z = 0$ and $z = 0.5$.

Ice V adopts a complicated structure in comparison to the other ice phases and cannot be easily visualised. The crystallographic unit cell is monoclinic, space group $A2/a$, lattice constants: $a = 9.22$, $b = 7.54$, $c = 10.35$ Å, $\beta = 109.2°$, and comprises twenty eight water molecules, four of which are required to describe the structure completely. The structure, best described by Kamb *et al.* [108], consists of zigzag chains of water molecules running parallel to the a-axis, figure 68. Of the four molecules required to describe the structure, molecules of type O(2) and O(3) form one chain whilst molecules of type O(4) form the other. The chains bond together to form layers, figure 69, with adjacent layers bound together by molecules of type O(1).

Although Kamb *et al.* [108] were able to determine the oxygen framework, the use of X-rays meant that the hydrogen atoms could not be located. In ice III, the

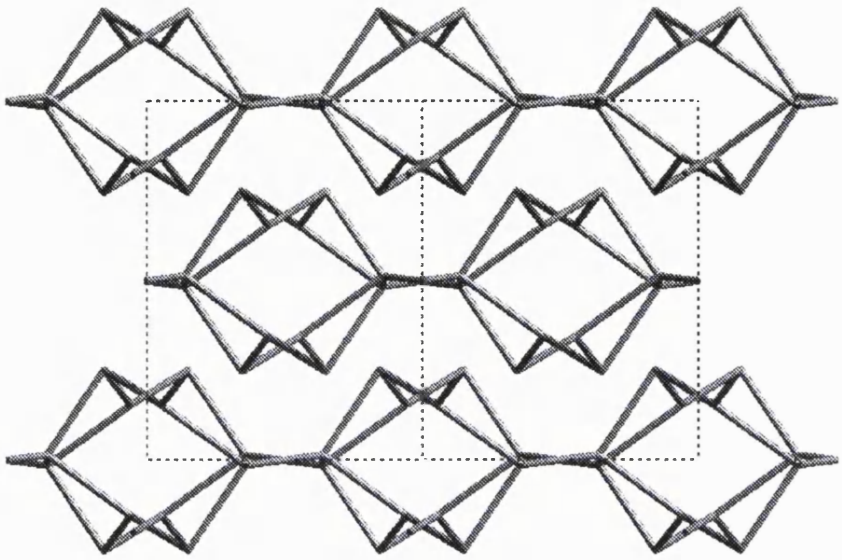

Figure 69: Chains bond together to form a layered structure viewed here parallel to the a-axis.

water molecules can adopt orientations which range from full disorder to full order without change in symmetry; this is not the case for ice V. The symmetry proposed, $A2/a$, does not permit full orientational order of the water molecules; it is however possible under a slightly degraded symmetry, Aa. Unfortunately, the distinction between $A2/a$ and Aa cannot be made by examination of the diffraction data; the reflection conditions for the two space groups are the same. Kamb *et al.* then turned to the infrared spectra of Bertie and Whalley [82], from which Bertie and Whalley had concluded that ice V consists of many non-identical O-H$\cdots$O bonds. Of course with the structure now known, they were in a position to determine the number of such bonds. An ordered structure would consist of only 14 non-identical O-H$\cdots$O bonds which, they believed, would appear as fine structure in the stretching bands. This was not the case, leaving Kamb *et al.* to conclude that a disordered structure, with 126 non-identical O-H$\cdots$O bonds, must exist.

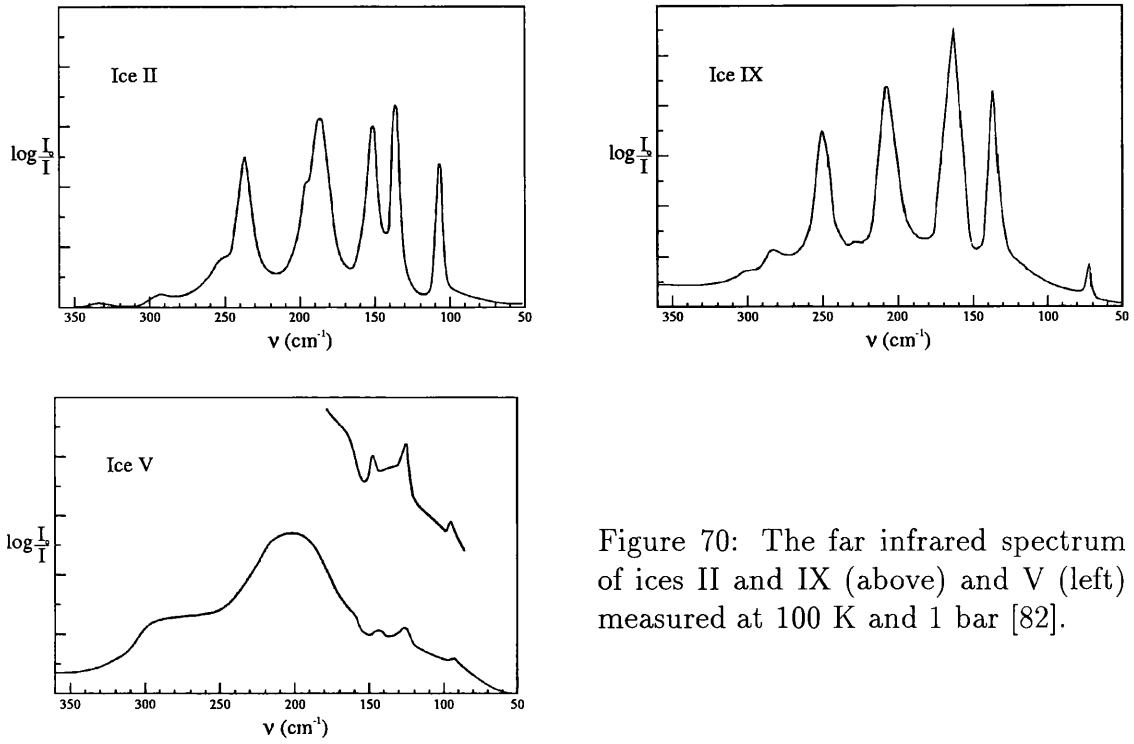

Figure 70: The far infrared spectrum of ices II and IX (above) and V (left) measured at 100 K and 1 bar [82].

Further infrared work by Bertie *et al.* [110], this time in the far infrared frequency range, again found the lack of resolution in the translational bands indicative of many vibrations, as opposed to the spectra of orientationally ordered ices II and IX, figure 70. Although possibly spurious, fine structure in the frequency range 150–195 cm^{-1}, they explain, might be evidence of ordered vibrations, figure 70. However, such information is difficult to obtain purely from translational vibrations.

Hamilton *et al.* [1] were the first to study ice V using neutron diffraction. Collecting data on single crystals, again recovered to ambient pressure, they confirmed the structure of ice V as that proposed by Kamb *et al.* [108]. In addition, the use of neutrons enabled them to determine, for the first time, the position and occupancy of the deuterium atoms. They found that ice V was neither fully disordered nor fully ordered, but instead, the deuterium atoms occupied positions with differing

probabilities, table 27. As already noted, the space group $A2/a$ does not permit full

D(5)	66	D(12)	9
D(6)	38	D(13)	41
D(7)	39	D(14)	94
D(8)	7	D(15)	50
D(9)	49	D(16)	50
D(10)	86	D(17)	61
D(11)	59	D(18)	44

Table 27: The partial order found by Hamilton *et al.* [1] for the deuterium atoms of ice V. 50% occupancy corresponds to full disorder for that site, 0 and 100% full order.

orientational order whereas Aa does. The partial ordering found could be described as three possible fully-ordered schemes under the space group Aa. However, when tested, all three models were in poor agreement with the diffraction data. In trying to understand why full order was not occurring, as in ice IX, they suggest that perhaps the order–disorder transition occurs at such a low temperature that relaxation times are preventing the transition from completing. They base this argument on the dielectric work of Wilson *et al.* [85] which, when extrapolated, predicts relaxation times of several hours at 150 K.

Until the work of Hamilton *et al.*, the general belief was that ice V was fully disordered. Now that ice V was found to be partially ordered, work began investigating the order–disorder transition.

An abstract submitted by Kamb and La Placa [111] reports that ice V undergoes a reversible order–disorder transition in the temperature range 105–130 K. Collecting neutron diffraction data on single crystals recovered to ambient pressure, they attributed changes in symmetry from $P2_1/a$ to $A2/a$ to an order–disorder transition. Unfortunately, they have never published their findings.

Handa *et al.* [112] confirmed the existence of the order–disorder transition proposed by Kamb and La Placa [111], although not necessarily with a change in space group. Heat capacities were recorded as samples, recovered to ambient pressure, were warmed from 77 K. They found that an endothermic transition occurred over the temperature range 106–132 K, thought to be the reorientation of water molecules from an ordered to disordered state. With the identification of the order–disorder transition, they then studied the effect of annealing[1] on the transition. Samples were annealed for various times at 110 K before being cooled to 77 K. Each sample was then warmed through the transition with an increase in the transition entropy, and therefore the amount of order, found for longer annealing times. With the amount of order observed to increase with annealing time, Handa *et al.* then repeated the process using KOH[2] doped ice V. After 30 hours annealing of the doped sample, the entropy change across the transition was more than double that of the 60 hour annealed undoped sample.

The transition entropy for the undoped sample after 60 hours annealing was 0.84 $Jmol^{-1}K^{-1}$. Using the model described by Nagle [2], Handa *et al.* estimated a transition entropy of 0.8 $Jmol^{-1}K^{-1}$ for the partial order found by Hamilton *et al.* [1]. This would suggest that the amount of order present in the 60 hour annealed sample is comparable to that found by Hamilton *et al.* The transition entropy of the doped samples implies a much higher degree of ordering. Nevertheless, the amount of order required to account of the transition entropy is possible under the A2/a space group. In this sense, the work of Handa *et al.* was unable to confirm the change in symmetry

[1]The term *annealing* is used with reference to the removal of disorder. Annealing at 110 K for three hours simply means maintaining the temperature at 110 K for a period of three hours with the aim of removing disorder.

[2]Doping of ice structures by impurities such as KOH, HF and HCl, is thought to introduce various kinds of lattice defects which accelerate the rate of water molecule reorientation.

suggested by Kamb and La Placa [111].

Raman spectra by Sukarova *et al.* [113,114] also indicate an ordering process, this time under pressure. They collected spectra at 83 and 251 K, and found the lattice vibration bands were better resolved at 83 K, figure 71. Similar behaviour was found

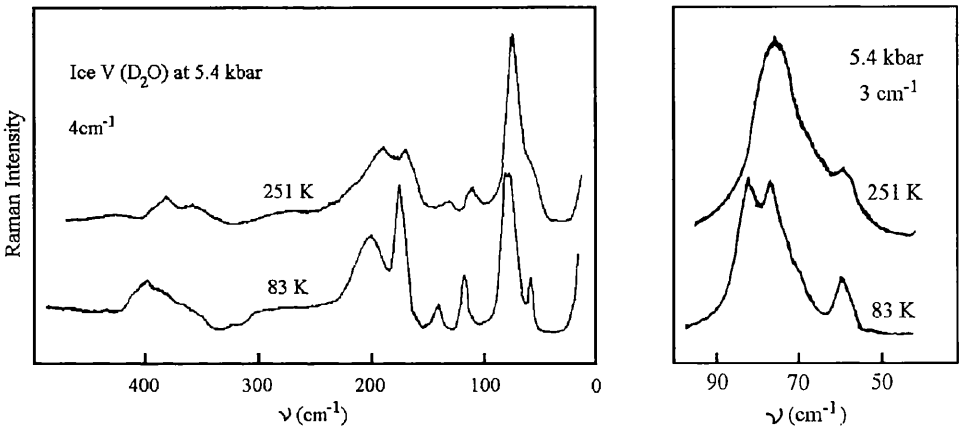

Figure 71: The ice V Raman spectra measured by Sukarova *et al.* [114] at 83 and 251 K in the region of rotational and translational vibrations.

for the Raman spectra of ice III(IX) [106,113], suggesting orientational order at 83 K approaching that of ice IX. Spectra were not collected at any other temperatures and hence no information concerning the order as a function of temperature is available. Although features in the spectra indicated increased orientational order, there was no evidence of a change in symmetry required for full orientational order.

From the work described above it is apparent that ice V is still not well understood. To summarise, ice V is orientationally disordered at high temperatures but undergoes a transition between 105–130 K to an ordered, though not necessarily fully ordered, state. From reading the literature, it is apparent that most researchers have adopted the view that ice exists in a either an orientationally ordered or disordered state; anything in between has been regarded as unstable. Kamb *et al.* [108] concluded

that ice V, at liquid nitrogen temperatures, is orientationally disordered since full order would be visible in the infrared spectra measured by Bertie and Whalley [82]; they ignored, however, the possibility of partial order. Even the partial order found by Hamilton *et al.* [1] has been explained as a 'frozen in' intermediary to full order.

The notion that ice V is fully disordered at high temperatures is certainly debatable. The dielectric work by Wilson *et al.* [85] suggest orientational disorder based on the rotational relaxation of water molecules. This implies water molecules are reorienting in a number of directions and do not follow strict selection rules expected for full order. However, such behaviour would also be seen under a partial ordering scheme where all orientations are possible, but simply that some are more probable than others. The conclusions drawn by Whalley and Davidson [86] that ice V is disordered at high temperatures were once again founded on the principle of either full order or disorder. They reached their conclusions after comparing the change in entropy for the transitions III–V and V–VI. Again, partial order could be missed through such comparisons, particularly if ices III and VI also exhibit partial order. The work by Sukarova *et al.* [113,114] indicated differences in order at high and low temperature. Certainly any partial order would be temperature dependent, but their work cannot determine the degree of order at either temperature.

The remainder of the work has been carried out at liquid nitrogen temperatures, with samples recovered to ambient pressure. Although partial order has been reported by all, the amount is suspected to be different for all cases. The reasons for this have been highlighted by Handa *et al.* [112]. They found that the water molecules are kinetically hindered at low temperatures, reflected in relaxation times. The amount of orientational order is therefore seriously affected by rates of cooling.

What seems clear about the work carried out so far is the existence of an ordering

transition between 105–130 K. None of the work indicates the degree of order below or above the transition and only the work by Hamilton *et al.* [1] suggests the amount of order at some point within the transition. Handa *et al.* [112], after annealing for sixty hours, recorded a change in entropy of 0.8 $Jmol^{-1}K^{-1}$ for the transition. The partial order found by Hamilton *et al.* would result in a similar entropy change if ice V were fully disordered above the transition. It seems at least unlikely that Hamilton *et al.* would have annealed their sample for 60 hours prior to data collection. One must therefore assume that ordering in the 60 hour sample is greater than that found by Hamilton *et al.* since annealing assists in the ordering process. If the amount of order below the transition is greater, the only way to account for an entropy change of 0.8 $Jmol^{-1}K^{-1}$ is if partial order exists above the transition.

This work aims to clarify the question of orientational order within ice V. Neutron diffraction data were collected at several points within the stability field to determine the existence of partial order, and if any, its variation with temperature and pressure.

6.2 Experimental procedure

Samples were prepared using the two approaches described in section 3.1.2. As with ice III, the data on ice V were collected on various instruments at different times, with the conditions under which ice V was formed different for each experiment. An individual description of sample history and conditions under which data were collected are detailed below.

IRIS

Ice V was first prepared during an investigative experiment on IRIS. The experiment was originally designed to look at argon clathrate, but in fact led to the formation of several high pressure phases of ice, including a phase yet to be identified, chapter 8.

A TiZr gas pressure cell was loaded with silica wool and liquid D_2O, the argon pressure increased to 5.5 kbar and the temperature gradually decreased. At 260 K, the liquid froze to form ice V. Rather than immediately collecting data on ice V, the pressure was decreased to 3.1 kbar which resulted in the transition to ice III. Data were collected on ice III before the pressure was then increased to 5.0 kbar, which resulted in the reformation of ice V. Data were eventually collected on ice V at 4.8 kbar and 260 K over a period of 12 hours.

The detectors on the IRIS instrument were such that no information on the quality of the powder could not be obtained. Only upon refinement of the data could the quality of the powder be ascertained. However the V–III and III–V transitions would have assisted in forming a good powder.

POLARIS

During the IRIS experiment, an unknown phase formed at 5.4 kbar and 263 K. Unfortunately, the data collected were insufficient for structure solution. The intention of the POLARIS experiment was to try and reproduce the phase with the hope of gathering low d-spacing data to assist in structure solution.

A TiZr gas pressure cell was loaded with silica wool and liquid D_2O, the argon pressure increased to 5.5 kbar and the temperature gradually decreased. At 261 K, the liquid froze but, unfortunately, the phase formed was not the desired phase but ice V. Data were nevertheless collected on ice V at 4.9 kbar and 258 K, with roughly

fourteen hours data collection time.

Inspection of the individual POLARIS detectors indicated that the ice V sample was textured. The detectors covered a sufficiently large area around the diffraction rings that the data, although textured, may be fine as a result of averaging. Refinement of the data was therefore attempted.

HRPD

The experiments on IRIS and POLARIS had shown that ice V could be prepared from the liquid using argon gas as the pressure medium. Later, experiments at Göttingen and at ILL, section 5.2, had shown that ice III could be successfully prepared from the powder, again using argon gas. The intention of the HRPD experiment was to collect good quality powder data on ice V.

A TiZr cell was loaded with powdered ice Ih and lowered into the cryostat located on the instrument. The temperature was then decreased to 235 K before the pressure was increased to 4.3 kbar. Inspection of the data indicated ice V had formed. The pressure increase was carried out as one quick step in order to form a tight pressure seal. The pressure at which the ice Ih–II and II–V transitions occurred was therefore unknown. Data were collected at 250 K and 4.0 kbar, 250 K and 5.0 kbar, and 237 K and 5.0 kbar. These points were chosen such that structural information as a function of both temperature and pressure could be obtained. With the loss of beam throughout the experiment, the time spent at each point (and the time during which the beam was on) were: 24(15), 17(13) and 15(11) hours for the three points listed respectively. The time spent at each data point meant clathrate formation was considerable and was decomposed between points by releasing the pressure to a few bar and warming to 260 K.

PEARL

The experiment on PEARL proved very productive, with ice IV formed for the first time under its conditions of stability, and the formation of a new phase of ice, labelled in this work as the blue phase, chapter 9.

The preparation of the sample leading up to data collection on ice V is detailed elsewhere, section 9.2. After data on the blue phase had been collected, the temperature was decreased to induce the formation of ice V, this would then provide an indication of the density of the new phase. The transition from the blue phase to ice V occurred at 4.65 kbar and 245 K. The rate of cooling was fairly rapid, 1 $Kmin^{-1}$, and this temperature should not be interpreted as the phase boundary. Data on ice V were collected at 4.81 kbar and 245 K. Since ice V was not the phase of interest, only 3 hours were spent on data collection for lattice constant information.

6.3 Results

Refinement

The initial model used in the refinement of all ice V data was based on the single crystal results of Hamilton *et al.* [1]. Their data, collected at 110 K, indicate strong partial order of the deuterium atoms. Since this work aims to establish the degree of orientational order within ice V, no initial bias was placed on the occupancies of the deuterium atoms. The initial model therefore comprised the atomic positions described by Hamilton *et al.* with the deuterium atoms populated in a fully disordered way.

Ice V is based on a monoclinic unit cell, space group $A2/a$, lattice constants: $a = 9.22$, $b = 7.54$, $c = 10.35$ Å, $\beta = 109.2°$, and comprises twenty eight water molecules.

The asymmetric unit consists of four distinct oxygen and fourteen distinct deuterium atoms. The deuterium occupancies, by virtue of the Bernal-Fowler rules [40], can be described by just four variables[3], α, β, γ and δ, table 28. Oxygen atoms of the type O(4) are bound to one another across two-fold axes and symmetry centres. For this reason the two deuterium atoms D(16) and D(18) are constrained to fully disordered occupancies of 50%.

The argon clathrate that formed during data collection was modelled on the structure refined from neutron diffraction data collected at 4.8 kbar [61]. Only the lattice constants of the clathrate phase were refined.

No reflections from the TiZr pressure cell were observed and the background was adequately modelled by a simple cosine Fourier series, section 3.6.6.

After refinement of the background, scale, lattice constants and peak shape, there were features in the data not adequately described by the current models. Peaks, clearly visible at 2.90 and 3.09 Å and perhaps at 3.02, 2.54 and 2.36 Å, figure 72, could not be explained as ice V nor argon clathrate. Various other ice phases were included in the refinement in an attempt to identify the additional phase. Unfortunately, this proved unsuccessful and the peaks had to be excluded from the data. This was not ideal since the peak at 2.9 Å shouldered a strong ice V reflection.

After the initial refinement cycles, attention turned to the atomic parameters. There were three parameters associated with each atom under refinement: the atomic position, the thermal factor and the occupancy. The refinement of all these parameters, seventy six in all, when unrestrained, led to unrealistic bond lengths and thermal factors. To guide the refinement towards the global rather than a local minimum, the O–D bond lengths were restrained to a distance of 0.97(2) Å and the thermal factors

[3]The ordering can actually be described by only three variables since $\alpha + \beta + \gamma + \delta = 200\%$.

D(5) ···D(7) D(6) ···D(11)	D(5) + D(6)	= 1	D(5) = 1 - D(7) D(6) = 1 - D(5) = D(7)	1 − α α
D(7) ···D(5) D(8) ···D(14) D(9) ···D(15) D(10) ···D(12)	D(7) + D(8) + D(9) + D(10)	= 2		α β γ δ
D(11) ···D(6) D(12) ···D(10) D(13) ···D(17) D(14) ···D(8)	D(11) + D(12) + D(13) + D(14)	= 2	D(11) = 1 - D(6) = 1 - D(7) D(12) = 1 - D(10) D(13) = 1 - D(17) = 1 - D(9) D(14) = 1 - D(8)	1 − α 1 − δ 1 − γ 1 − β
D(15) ···D(9) D(16) ···D(16) D(17) ···D(13) D(18) ···D(18)	D(15) + D(16) + D(17) + D(18)	= 2	D(15) = 1 - D(9) D(16) = 1 - D(16) = 0.5 D(17) = 1 - D(15) = D(9) D(18) = 1 - D(18) = 0.5	1 − γ 0.5 γ 0.5

Table 28: The ice V deuterium occupancies, as represented by the four variables: α, β, γ and δ. The first column represents the deuterium atoms of concern and the deuterium atom which shares the same O–O bond. In accordance with the Bernal-Fowler rules, each O–O bond must be occupied by a single deuterium atom. The occupancy for the two atoms across each bond must therefore total one. The second column represents the total occupancy around each oxygen atom. A water molecule of course consists of one oxygen and two deuterium atoms. The occupancy of the deuterium atoms surrounding each oxygen atom must therefore total two (atoms D(5) and D(6) are repeated by symmetry). By a process of elimination, third column, all deuterium occupancies can be represented by the occupancies of atoms D(7), D(8), D(9) and D(10), which are represented by α, β, γ and δ, fourth column.

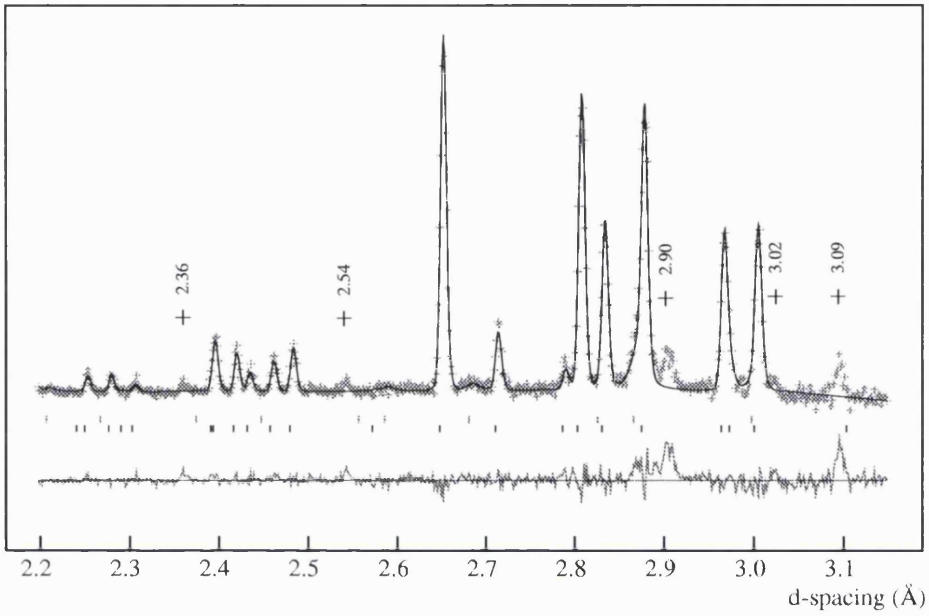

Figure 72: Reflections arising from an unknown phase which were visible in all ice V data collected on HRPD.

were restrained to the same value for each atom type. The occupancies were of course already restrained in accordance with the Bernal-Fowler rules.

Once the restrained refinement had reached convergence, a criterion outlined in section 3.6.2, the easing and removal of the restraints was attempted.

Removal of the O–D bond-length restraint did not improve the R-factors and the refinement took several orders of magnitude longer in time, than a restrained refinement, to reach a point of convergence. The O–D restraint was therefore retained but was further relaxed to 0.97(3) Å. Any further relaxation only served to hamper the refinement.

Likewise, there were problems in trying to remove the thermal restraints. For the data collected at 254 K, a refinement free of any thermal restraint led to unrealistic thermal factors for many of the deuterium atoms. However, a free thermal refinement

was possible for the data collected at 237 K. The reason for this is most probably due to low contamination by additional phases. For the data collected at 237 K, the degree of argon clathrate and unidentified phase was negligible in comparison to the data collected at the warmer temperature of 254 K. Upon removal of the thermal restraint for the data collected at 237 K, the refinement converged quickly with the thermal factors differing little from their previous values.

One may argue that by restraining the thermal factors, the refinement may have fallen into a local minimum. Removal of the restraint at such a late stage would therefore be of no help in pulling the refinement out of such minima. Such an argument is valid and at no time, prior to the end, could the thermal factor restraint be removed. However, in defence, the refinement of ices II (chapter 4), III (chapter 5), the blue phase (chapter 9) and argon and krypton clathrate [61] have shown that the thermal factors for each atom type differ by only small amounts. In the case of ice III, the difference in thermal factors for a free and restrained thermal refinement was significant for certain data sets, but this was attributed to poor data at high angles. Nevertheless, if the thermal restraint was removed at the end of the refinement, the thermal factors returned to their non-restrained values, i.e. refining freely from the beginning, or refining just at the end made no difference.

Table 29 demonstrates the effect of thermal restraints on the deuterium occupancies for the data collected at 237 K. In a refinement free of any thermal restraint, the weakly occupied deuterium atoms D(8) and D(12) had comparatively small thermal factors. The thermal factors for these weakly occupied positions were therefore constrained to be the same value as their strongly occupied counterparts, D(14) and D(10) respectively. The implications are that the occupancies do not change, within the limits of error, upon the relaxing of the thermal restraint. This is encouraging

for the two data sets at 254 K where free refinement of the thermal factors was not possible.

	Restrained		Free		Partially restrained	
	occ.(%)	U_{iso}	occ.(%)	U_{iso}	occ.(%)	U_{iso}
D(5)	57.2(1.5)	0.046(3)	56.7(1.4)	0.043(11)	56.5(1.4)	0.041(10)
D(6)	42.8(1.5)	0.046(3)	43.3(1.4)	0.050(15)	43.5(1.4)	0.053(15)
D(7)	42.8(1.5)	0.046(3)	43.3(1.4)	0.042(12)	43.5(1.4)	0.040(11)
D(8)	29.8(1.6)	0.046(3)	29.6(1.5)	0.028(16)	30.1(1.5)	0.042(9)
D(9)	49.5(1.2)	0.046(3)	49.3(1.2)	0.034(12)	49.2(1.2)	0.034(11)
D(10)	77.9(2.0)	0.046(3)	77.8(1.7)	0.043(7)	77.2(1.8)	0.042(7)
D(11)	57.2(1.5)	0.046(3)	56.7(1.4)	0.046(9)	56.5(1.4)	0.045(9)
D(12)	22.1(2.0)	0.046(3)	22.2(1.7)	0.025(20)	22.8(1.8)	0.042(7)
D(13)	50.5(1.2)	0.046(3)	50.7(1.2)	0.040(11)	50.8(1.2)	0.041(11)
D(14)	70.2(1.6)	0.046(3)	70.4(1.5)	0.041(9)	69.9(1.5)	0.042(9)
D(15)	50.5(1.2)	0.046(3)	50.7(1.2)	0.056(13)	50.8(1.2)	0.057(13)
D(16)	50	0.046(3)	50	0.062(14)	50	0.063(14)
D(17)	49.5(1.2)	0.046(3)	49.3(1.2)	0.049(12)	49.2(1.2)	0.051(12)
D(18)	50	0.046(3)	50	0.040(14)	50	0.042(14)

Table 29: The effect of thermal factor restraints on the deuterium occupancies for the HRPD data collected at 237 K. The first column represents a refinement in which the deuterium thermal factors were restrained to the same value for all. In the second column, the thermal factors were refined free of any restraint. And in the third column, the thermal factors were partially restrained such that the weakly occupied atoms D(8) and D(12) had the same thermal factors as their strongly occupied counterparts D(14) and D(10) respectively.

The sample prepared on PEARL was textured and only data required for the refinement of the lattice constants were collected. Nevertheless, it was still possible to refine the structure and the occupancy of the deuterium atoms. The increased order found for this data, over that for the HRPD data, must be an artefact of the texture. Although the ordering cannot therefore be trusted, the figures were included in the results to demonstrate the same pattern of ordering. Increased order was also found for the data collected on IRIS. Although no information on the degree of texture was available for this sample, the data collected on ice III data were insufficient for structure refinement. It is not certain whether this is due to texture or simply poor statistics at low d-spacings. The IRIS data must therefore be treated with scepticism.

The profiles fits from the refinement of the data are shown in figures 73 to 78. The two sets of ticks present in each profile fit, represent reflections arising from the argon clathrate (upper) and ice V (lower). Excluded regions are not attributed to reflections from the pressure cell but from an unidentified phase. The structural details arising from the refinement, atomic parameters, bond lengths and angles etc., are listed in tables 30 to 38. The different data sets collected on HRPD have been labelled by subscript for clarity.

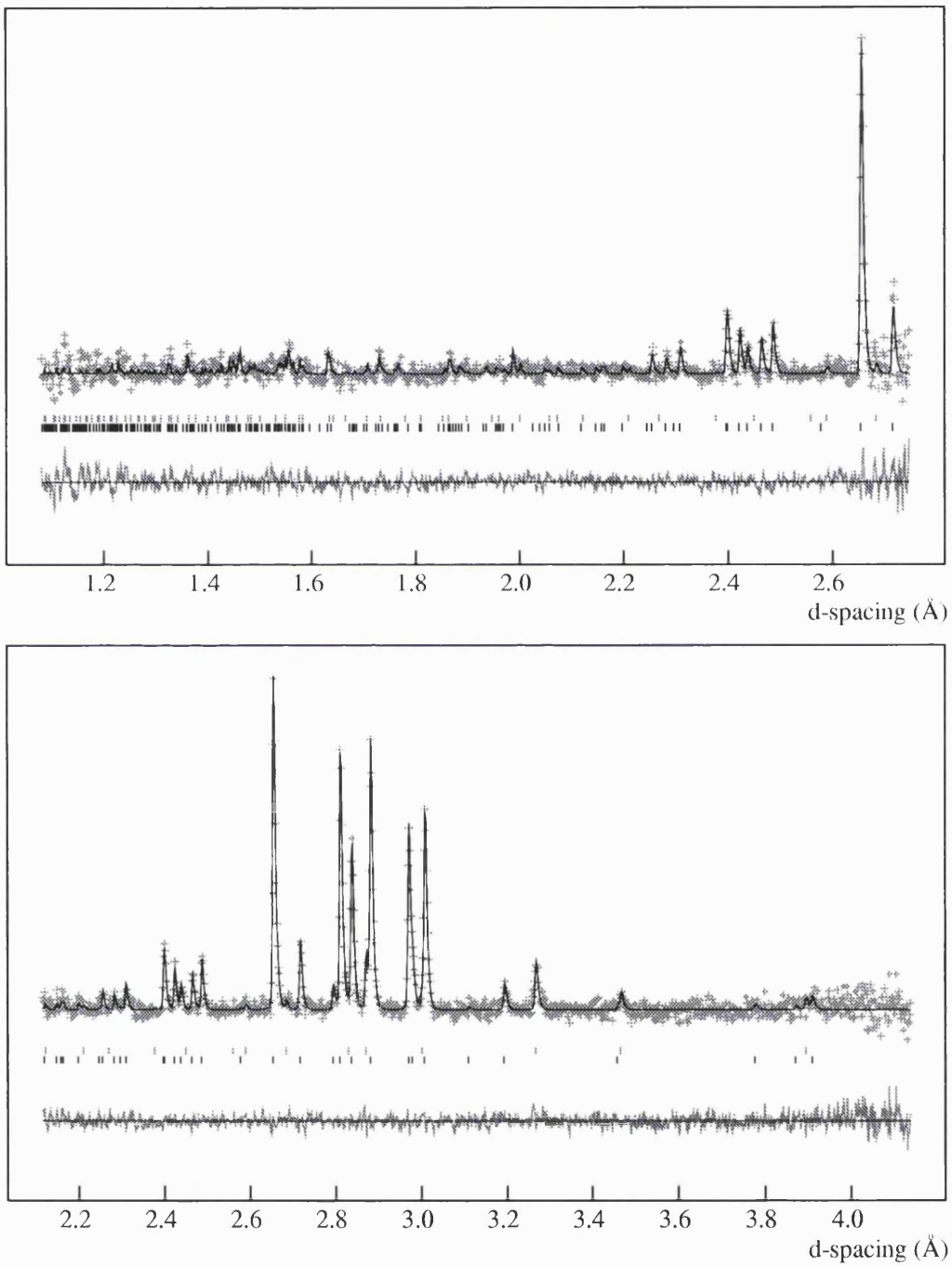

Figure 73: The profile fits for the ice V data collected on IRIS at 4.80 kbar and 260 K, $R_p = 0.0177$ and $R_{wp} = 0.0179$. The amount of argon clathrate determined by the refinement was 12 wt.%.

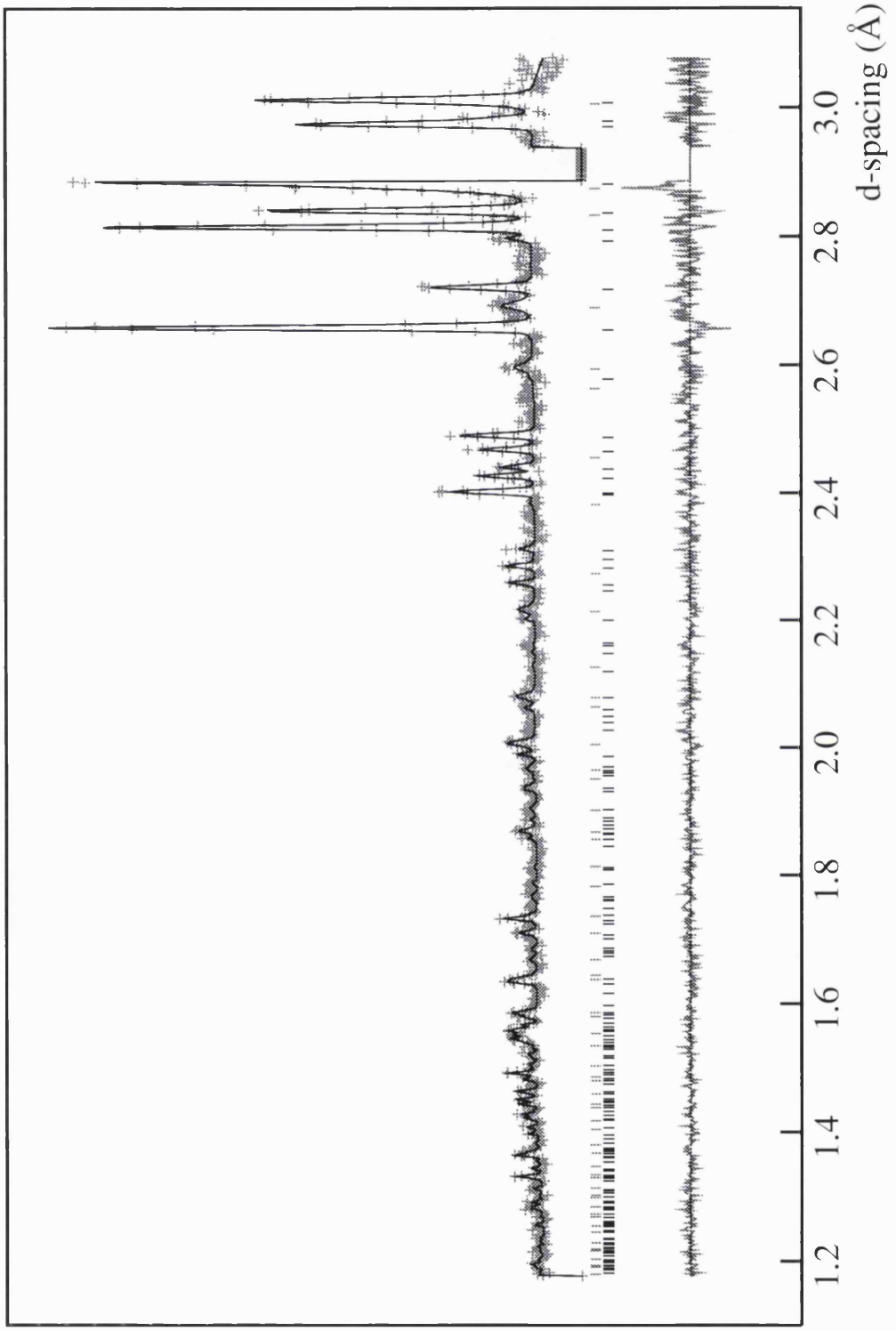

Figure 74: The profile fit for the ice V data collected on HRPD at 4.00 kbar and 254 K ($HRPD_1$), $R_p = 0.0724$ and $R_{wp} = 0.0790$. The amount of argon clathrate determined by the refinement was 45 wt.%.

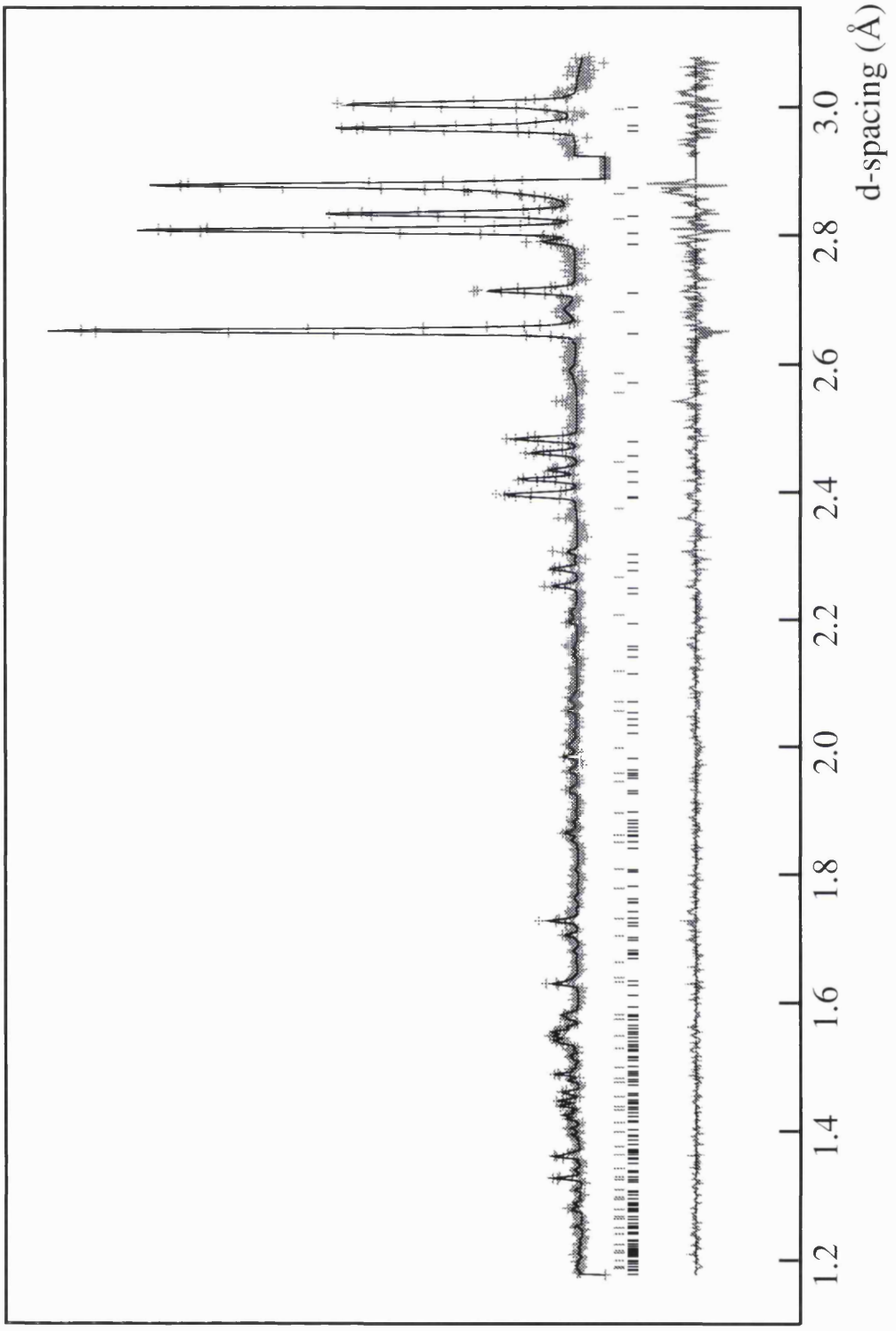

Figure 75: The profile fit for the ice V data collected on HRPD at 5.00 kbar and 254 K ($HRPD_2$), $R_p = 0.0625$ and $R_{wp} = 0.0665$. The amount of argon clathrate determined by the refinement was 28 wt.%.

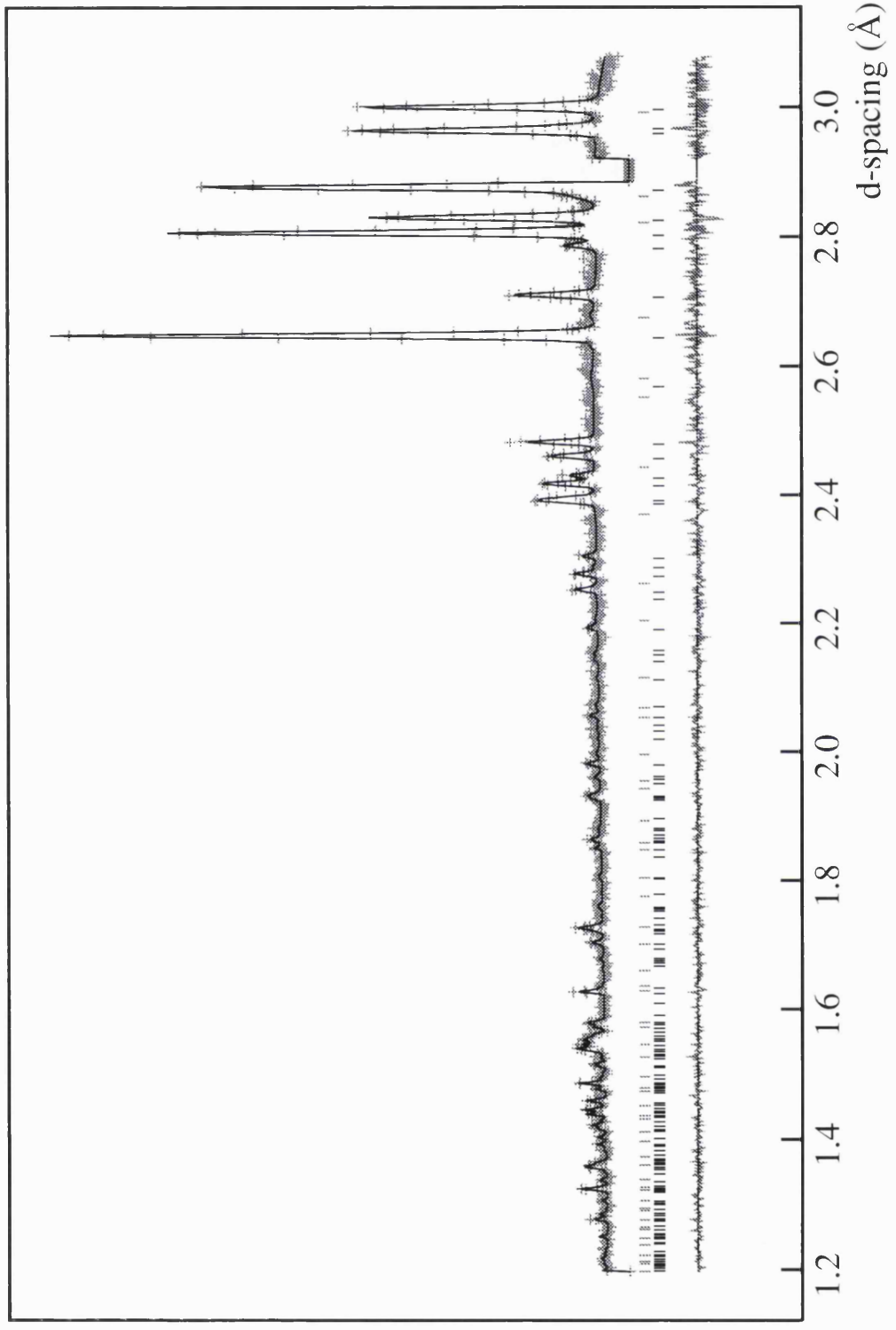

Figure 76: The profile fit for the ice V data collected on HRPD at 5.00 kbar and 237 K ($HRPD_3$), $R_p = 0.0641$ and $R_{wp} = 0.0791$. The amount of argon clathrate determined by the refinement was 9 wt.%.

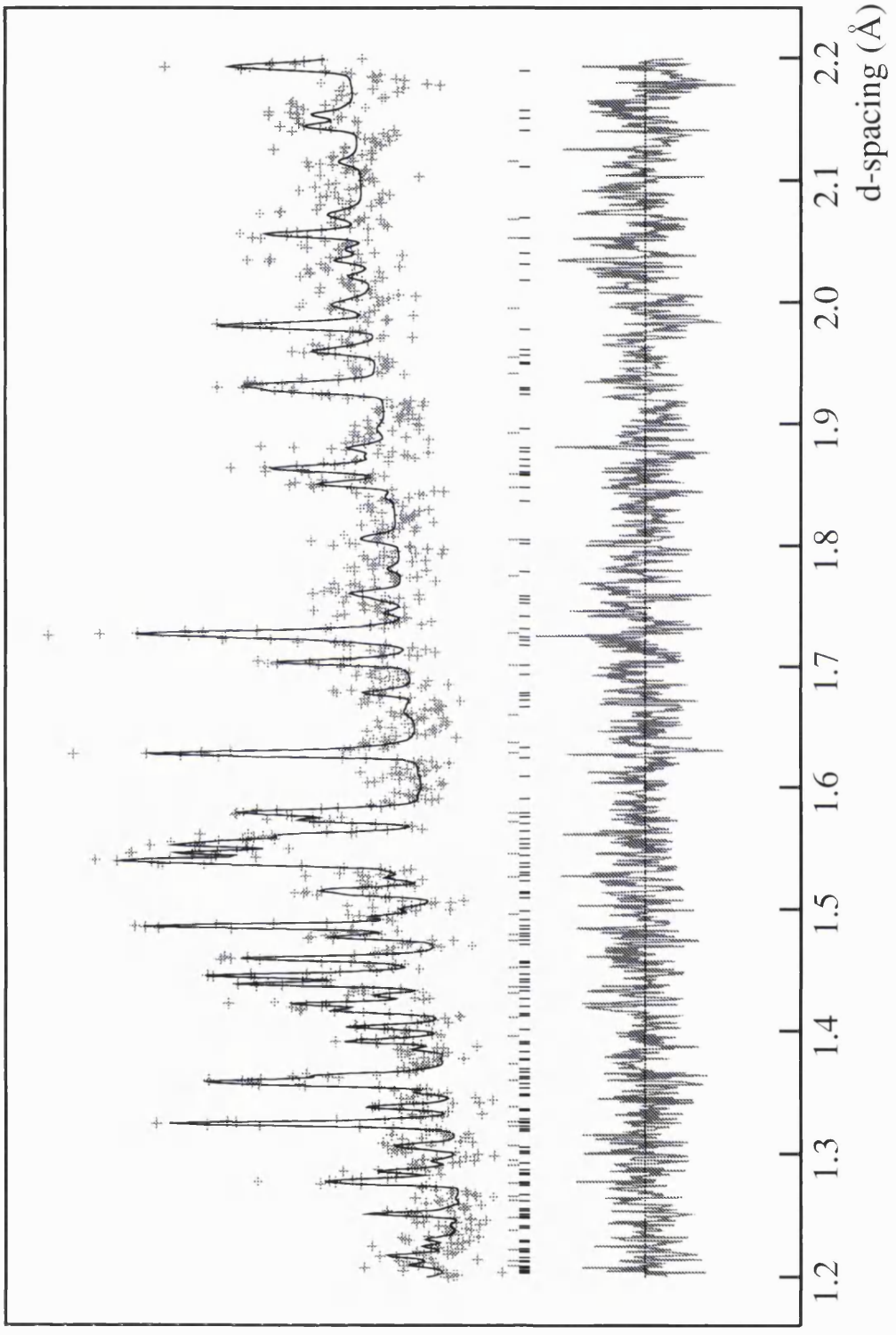

Figure 77: The profile fit for the ice V data collected on HRPD at 5.00 kbar and 237 K ($HRPD_3$) in the 1.2–2.2 Å region.

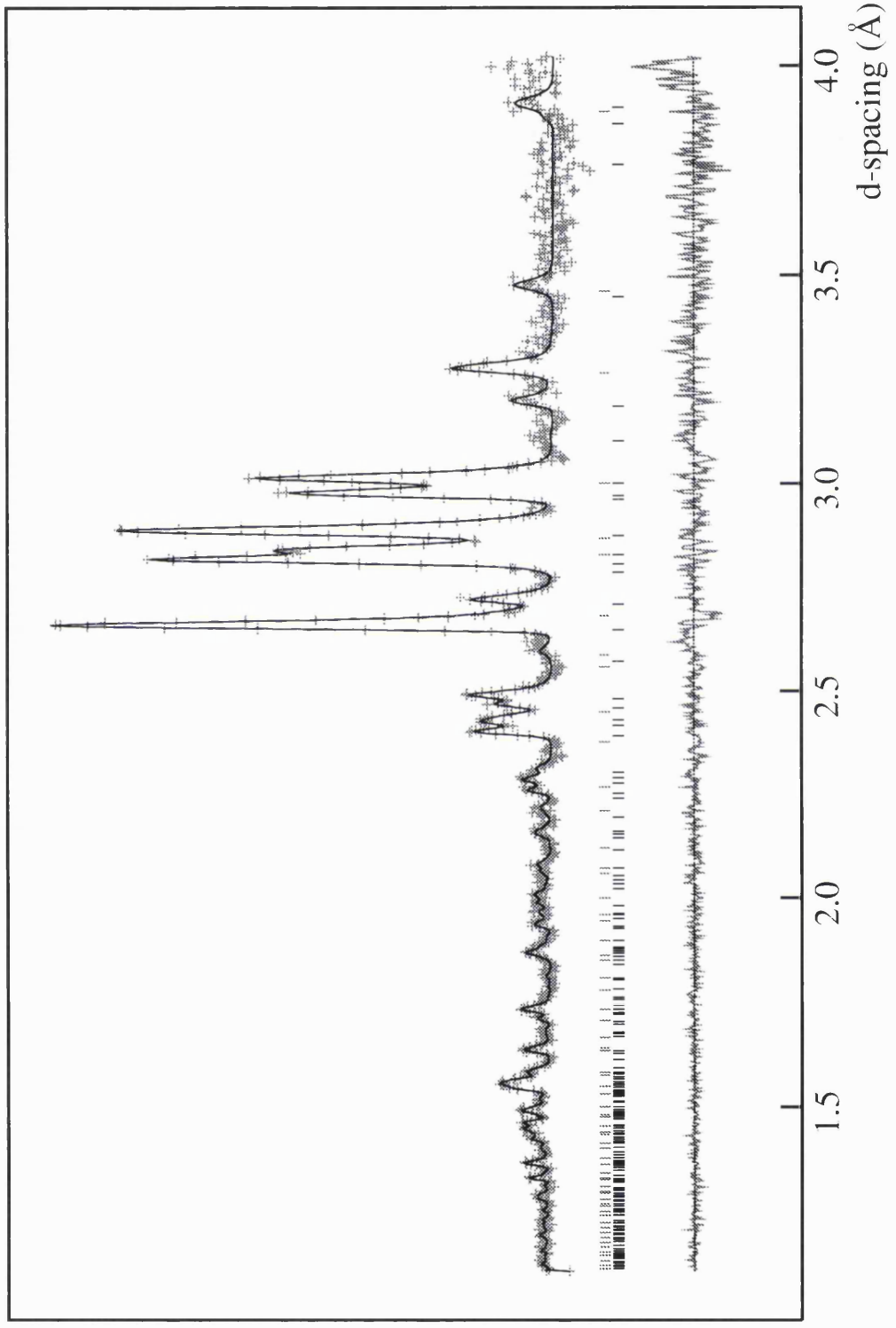

Figure 78: The profile fit for the ice V data collected on PEARL at 4.81 kbar and 245 K, $R_p = 0.0097$ and $R_{wp} = 0.0066$. The amount of argon clathrate determined by the refinement was 20 wt.%.

P(kbar)	T(K)	a(Å)	b(Å)	c(Å)	β	V(Å^3)	ρ(gcm^{-3})	Inst.
4.43	260	9.08513(13)	7.55293(14)	10.25015(14)	109.0616(13)	664.79(2)	1.39881(4)	IRIS
4.0	254	9.09800(32)	7.56201(39)	10.26524(44)	109.0770(42)	667.45(5)	1.39322(11)	$HRPD_1$
5.0	254	9.07444(24)	7.54348(29)	10.23728(30)	109.0675(27)	662.32(4)	1.40402(8)	$HRPD_2$
5.0	237	9.07039(16)	7.52714(20)	10.22730(21)	109.1134(18)	659.77(3)	1.40947(4)	$HRPD_3$
4.81	245	9.0769(6)	7.5392(7)	10.2382(7)	109.090(6)	662.09(9)	1.4045(2)	PEARL

Table 30: Ice V lattice constants and densities.

P(kbar)	T(K)	R_{wp}	R_p	α	β	γ	δ	Inst.
4.43	260	0.0179	0.0177	44.9(2.8)	29.8(3.0)	43.7(2.6)	81.6(3.1)	IRIS
4.0	254	0.0790	0.0724	48.1(1.8)	30.6(2.0)	48.7(1.7)	72.6(2.3)	$HRPD_1$
5.0	254	0.0665	0.0625	47.0(1.6)	29.9(1.6)	48.5(1.2)	74.6(1.8)	$HRPD_2$
5.0	237	0.0791	0.0641	43.5(1.5)	29.9(1.6)	50.2(1.2)	76.4(1.9)	$HRPD_3$
4.81	245	0.0066	0.0097	44.5(1.6)	22.4(1.6)	53.4(1.4)	79.8(2.1)	PEARL

Table 31: The ice V order parameters.

	x	y	z	U_{iso}
O(1)	0.25	-0.192(5)	0	0.0210(32)
	0.25	-0.178(4)	0	0.0259(25)
	0.25	-0.173(4)	0	0.0245(24)
O(2)	0.465(4)	0.056(3)	0.148(3)	0.0210(32)
	0.457(3)	0.051(3)	0.148(2)	0.0259(25)
	0.461(3)	0.054(3)	0.151(2)	0.0245(24)
O(3)	0.283(3)	-0.348(4)	0.253(3)	0.0210(32)
	0.281(3)	-0.344(3)	0.246(3)	0.0259(25)
	0.283(3)	-0.344(3)	0.249(2)	0.0245(24)
O(4)	0.401(3)	0.355(3)	-0.027(3)	0.0210(32)
	0.410(3)	0.362(3)	-0.020(2)	0.0259(25)
	0.406(2)	0.363(2)	-0.019(2)	0.0245(24)
D(5)	0.339(4)	-0.115(4)	0.049(4)	0.0410(34)
	0.339(4)	-0.102(3)	0.052(3)	0.0421(26)
	0.344(3)	-0.104(3)	0.055(3)	0.0443(29)
D(6)	0.244(5)	-0.269(4)	0.075(4)	0.0410(34)
	0.242(4)	-0.264(3)	0.070(4)	0.0421(26)
	0.248(4)	-0.260(3)	0.071(4)	0.0443(29)
D(7)	0.392(4)	-0.029(5)	0.090(4)	0.0410(34)
	0.390(4)	-0.031(4)	0.082(3)	0.0421(26)
	0.387(4)	-0.021(5)	0.081(3)	0.0443(29)
D(8)	0.402(6)	0.051(7)	0.207(5)	0.0410(34)
	0.405(5)	0.078(6)	0.214(4)	0.0421(26)
	0.394(5)	0.082(6)	0.204(4)	0.0443(29)
D(9)	0.459(4)	0.157(4)	0.084(3)	0.0410(34)
	0.463(3)	0.159(4)	0.098(3)	0.0421(26)
	0.463(3)	0.160(32)	0.099(3)	0.0443(29)

Table continued overleaf.

	x	y	z	U_{iso}
D(10)	0.561(4)	0.012(3)	0.212(3)	0.0410(34)
	0.560(3)	0.009(3)	0.206(3)	0.0421(26)
	0.563(2)	0.006(3)	0.203(3)	0.0443(29)
D(11)	0.244(4)	-0.289(5)	0.164(4)	0.0410(34)
	0.251(4)	-0.29(4)	0.157(3)	0.0421(26)
	0.249(4)	-0.288(3)	0.155(3)	0.0443(29)
D(12)	0.367(6)	-0.432(8)	0.292(7)	0.0410(34)
	0.357(6)	-0.439(6)	0.283(6)	0.0421(26)
	0.349(8)	-0.451(7)	0.263(8)	0.0443(29)
D(13)	0.311(4)	-0.248(5)	0.320(4)	0.0410(34)
	0.318(3)	-0.262(5)	0.324(3)	0.0421(26)
	0.317(4)	-0.253(4)	0.318(3)	0.0443(29)
D(14)	0.178(3)	-0.380(3)	0.255(2)	0.0410(34)
	0.182(3)	-0.383(3)	0.258(2)	0.0421(26)
	0.183(3)	-0.383(3)	0.256(2)	0.0443(29)
D(15)	0.440(4)	0.275(5)	0.052(4)	0.0410(34)
	0.437(3)	0.265(4)	0.045(3)	0.0421(26)
	0.439(3)	0.268(4)	0.050(3)	0.0443(29)
D(16)	0.314(3)	0.385(4)	0.001(4)	0.0410(34)
	0.318(3)	0.384(3)	-0.002(3)	0.0421(26)
	0.307(3)	0.390(3)	-0.005(3)	0.0443(29)
D(17)	0.382(5)	0.286(5)	-0.109(4)	0.0410(34)
	0.374(4)	0.305(4)	-0.110(3)	0.0421(26)
	0.372(4)	0.293(5)	-0.104(3)	0.0443(29)
D(18)	0.469(4)	0.456(4)	0.011(4)	0.0410(34)
	0.473(4)	0.468(4)	0.010(4)	0.0421(26)
	0.476(4)	0.463(4)	0.006(4)	0.0443(29)

Table 32: The ice V atomic positions and isotropic thermal factors obtained from the refinement of the HRPD data. For each atom, the first row corresponds to the 4.0 kbar and 254 K data ($HRPD_1$); the second, 5.0 kbar and 254 K ($HRPD_2$); the third, 5.0 kbar and 237 K ($HRPD_3$).

	$HRPD_1$	$HRPD_2$	$HRPD_3$
O(1)–D(5)	0.994(17)	0.996(13)	0.997(13)
O(1)–D(6)	0.984(18)	0.979(14)	0.986(14)
O(2)–D(7)	0.973(23)	0.965(18)	0.986(19)
O(2)–D(8)	0.968(27)	0.959(21)	0.960(21)
O(2)–D(9)	0.995(23)	0.975(18)	0.960(18)
O(2)–D(10)	0.963(20)	0.988(15)	0.967(16)
O(3)–D(11)	0.974(24)	0.968(18)	1.005(17)
O(3)–D(12)	0.978(28)	0.981(21)	0.984(21)
O(3)–D(13)	1.000(22)	0.972(18)	0.960(18)
O(3)–D(14)	0.986(20)	0.985(15)	0.974(15)
O(4)–D(15)	0.981(23)	0.963(18)	0.978(13)
O(4)–D(16)	0.944(20)	0.936(15)	0.979(16)
O(4)–D(17)	0.965(24)	0.967(19)	0.971(19)
O(4)–D(18)	0.978(22)	0.974(17)	0.968(17)

Table 33: Ice V O–D bond lengths.

	$HRPD_1$	$HRPD_2$	$HRPD_3$
O(1)···D(7)	1.81(4)	1.69(3)	1.69(3)
O(1)···D(11)	1.85(3)	1.80(3)	1.81(3)
O(2)···D(5)	1.80(4)	1.65(3)	1.69(3)
O(2)···D(12)	1.72(5)	1.82(4)	1.83(5)
O(2)···D(14)	1.95(3)	1.89(3)	1.91(2)
O(2)···D(15)	1.90(4)	1.91(3)	1.89(3)
O(3)···D(6)	1.84(4)	1.83(3)	1.86(3)
O(3)···D(8)	2.01(5)	1.95(4)	1.90(3)
O(3)···D(10)	1.83(4)	1.85(3)	1.81(3)
O(3)···D(17)	1.73(5)	1.83(3)	1.79(3)
O(4)···D(9)	1.85(4)	1.91(3)	1.91(3)
O(4)···D(13)	1.71(4)	1.81(3)	1.81(3)
O(4)···D(16)	2.07(5)	2.15(4)	2.03(4)
O(4)···D(18)	1.83(5)	1.65(4)	1.67(3)

Table 34: Ice V O···D bond lengths.

	$HRPD_1$	$HRPD_2$	$HRPD_3$	mean	Kamb
O(1)–O(2)	2.78(4)	2.64(3)	2.65(3)	2.69(3)	2.766
O(1)–O(3)	2.78(3)	2.74(2)	2.78(2)	2.77(2)	2.782
O(2)–O(3)	2.86(4)	2.82(3)	2.83(3)	2.84(3)	2.798
O(2)–O(3$''$)	2.69(4)	2.76(3)	2.72(2)	2.72(3)	2.781
O(2)–O(4)	2.83(4)	2.86(3)	2.85(3)	2.85(3)	2.820
O(3)–O(4′)	2.66(4)	2.77(3)	2.75(3)	2.73(3)	2.819
O(4)–O(4′)	2.97(6)	3.07(4)	2.98(4)	3.01(5)	2.867
O(4)–O(4″)	2.78(5)	2.60(4)	2.63(4)	2.67(4)	2.766

Table 35: Ice V O–O bond lengths for the three data sets, their mean, and the lengths found by Kamb *et al.* for ice V recovered to ambient pressure at 120 K.

	$HRPD_1$	$HRPD_2$	$HRPD_3$
O(1)···O(2)	3.56(3)	3.59(2)	3.56(2)
O(1)···O(4)	3.34(3)	3.33(2)	3.38(3)
O(2)···O(2)	3.40(5)	3.43(4)	3.48(4)
O(2)···O(2)	3.55(5)	3.58(4)	3.51(4)
O(2)···O(3)	3.52(4)	3.55(3)	3.51(4)
O(3)···O(4)	3.27(3)	3.27(3)	3.27(2)

Table 36: Ice V O···O non-bonded distances.

	$HRPD_1$	$HRPD_2$	$HRPD_3$
$<(\delta\theta)^2>^{1/2}$	18.18	18.46	18.23

Table 37: The total r.m.s of the O–O–O bond-angle deviations from the ideal tetrahedral angle of 109.5° (see table 38).

	$HRPD_1$	$HRPD_2$	$HRPD_3$
O(2)-O(1)-O(2′)	95.0(1.8)	97.9(1.5)	100.0(1.5)
O(2)-O(1)-O(3′)	129.6(0.8)	131.8(0.7)	132.2(0.7)
O(2)-O(1)-O(3″)	86.3(0.8)	86.0(0.6)	85.6(0.6)
O(2′)-O(1)-O(3′)	86.3(0.8)	86.0(0.6)	85.6(0.6)
O(2′)-O(1)-O(3″)	129.6(0.8)	131.8(0.7)	132.2(0.7)
O(3′)-O(1)-O(3″)	129.9(1.7)	125.9(1.3)	124.8(1.3)
$<(\delta\theta)^2>^{1/2}$	20.46	20.42	20.40
O(1)-O(2)-O(3)	82.5(1.0)	85.3(0.7)	83.3(0.7)
O(1)-O(2)-O(3$'^{v}$)	100.0(1.2)	102.4(1.0)	102.2(1.1)
O(1)-O(2)-O(4)	103.5(1.3)	104.8(1.0)	102.6(0.9)
O(3)-O(2)-O(3$'^{v}$)	133.4(1.3)	132.7(1.0)	134.1(1.0)
O(3)-O(2)-O(4)	89.8(1.1)	91.1(0.8)	89.8(0.9)
O(3$'^{v}$)-O(2)-O(4)	133.0(1.5)	129.8(1.1)	131.5(1.1)
$<(\delta\theta)^2>^{1/2}$	19.86	18.01	19.43
O(1′)-O(3)-O(2)	125.9(1.2)	128.3(0.9)	126.5(0.9)
O(1′)-O(3)-O(2″)	114.8(1.0)	115.7(0.7)	115.8(0.7)
O(1′)-O(3)-O(4′)	116.3(1.2)	115.3(0.9)	114.8(0.8)
O(2)-O(3)-O(2″)	112.9(1.2)	111.0(0.9)	112.3(0.9)
O(2)-O(3)-O(4′)	89.4(1.1)	89.3(0.8)	89.3(0.8)
O(2″)-O(3)-O(4′)	87.5(1.3)	84.8(0.9)	87.1(1.1)
$<(\delta\theta)^2>^{1/2}$	14.39	15.52	14.57
O(2)-O(4)-O(3‴)	91.0(1.2)	89.9(1.0)	90.4(0.8)
O(2)-O(4)-O(4′)	84.1(1.1)	83.0(0.8)	84.5(0.9)
O(2)-O(4)-O(4″)	121.4(1.6)	127.0(1.2)	125.0(1.3)
O(3‴)-O(4)-O(4′)	90.9(1.6)	87.9(0.8)	88.8(0.9)
O(3)-O(4)-O(4″)	132.8(1.9)	130.8(1.6)	129.4(1.6)
O(4′)-O(4)-O(4″)	123.1(1.3)	123.5(9)	125.4(0.9)
$<(\delta\theta)^2>^{1/2}$	19.16	20.45	19.61

Table 38: Ice V O–O–O bond angles grouped for each oxygen atom. The r.m.s. bond angle deviations from the ideal tetrahedral angle of 109.5° are also given for each oxygen atom.

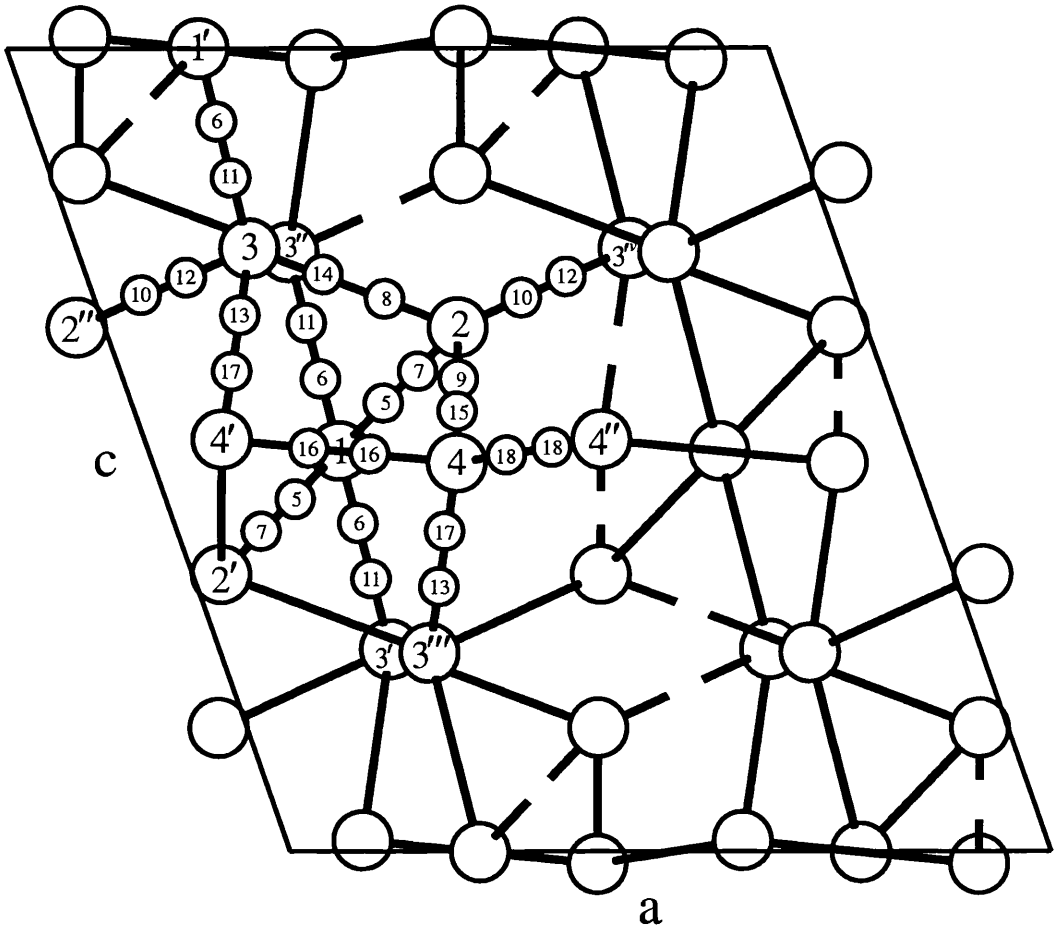

Figure 79: The structure of ice V viewed along the b-axis. The oxygen atoms of the unit cell are shown as large circles with some of the deuterium atoms shown as small circles. The atoms are labelled according to table 32.

6.4 Discussion

6.4.1 Additional phase

The additional peaks present in the HRPD data could not be identified as any known phase of ice or argon hydrate. Previous diffraction studies by Kamb *et al.* (X-ray) [108] and Hamilton *et al.* (neutron) [1] were performed at liquid nitrogen temperatures and ambient pressure. This work represents the first diffraction data collected on ice V at high temperature and pressure, i.e. within the established stability region of ice V. The additional peaks might therefore be an indication of a different structure to that reported. The space group adopted by ice V, $A2/a$, permits a large range of ordering possibilities, from full disorder to almost full order. Since the amount of order at high temperatures is expected to be smaller than that at low temperatures, and hence smaller than that found by Hamilton *et al.* at 110 K, the additional peaks cannot be explained by different orientational order. If the additional peaks were attributed to ice V, then they must be occurring, not as a result of a different ordering scheme, but because ice V adopts a subtly different structure. Fortunately, the additional peaks were later found in diffraction data collected on ice IV. The peaks are therefore the result of a different, as yet unidentified, phase which is further discussed in section 7.4.2.

6.4.2 The use of O–D restraints

As discussed in sections 5.4.4 and 5.4.5, ices in which the water molecules are orientationally disordered also exhibit positional disorder. This positional disorder, when examined crystallographically, can often lead to apparent bond lengths and angles which differ from those in the vapour. The use of O–D bond-length restraints is

therefore not ideal in the refinement of a disordered ice such as ice V. Unfortunately, their use was unavoidable.

After the refinement of ices III, IV and the blue phase, several of the O–D bond lengths were found to be very different from 0.97 Å. When restrained, although the bond lengths approached 0.97 Å, they were still recognisably different. For example, ice III when refined free of any bond-length restraint had two very striking bond lengths of 0.84 and 1.20 Å. After refining with a bond restraint of 0.97(3), the same as that used in refining the ice V data, the bonds lengths were 0.93 and 1.04 Å respectively. Similar behaviour may be occurring in ice V, with short and long bond lengths found for O(4)–D(16) and O(1)–D(5) respectively, table 33.

Fortunately, the ordering was not as sensitive to bond-length restraints as in the case of ice III, table 26. The order parameters obtained after refining the $HRPD_1$ data with an O–D bond-length restraint of different strengths are listed in table 39. Although the consequence of bond-length restraints has been listed for one data set only, ice V at 4.0 kbar and 254 K, the effects were similar, if not smaller, for the other two HRPD data sets.

O–D	α	β	γ	δ
0.97(1)	48.3(1.7)	30.9(1.9)	48.4(1.5)	72.4(2.2)
0.97(2)	48.3(1.8)	30.8(1.9)	48.5(1.6)	72.4(2.3)
0.97(3)	48.1(1.8)	30.6(2.0)	48.7(1.7)	72.6(2.3)
0.97(4)	47.9(1.9)	30.4(2.0)	48.9(1.8)	72.8(2.3)
0.97(5)	47.7(2.0)	30.2(2.0)	49.1(1.9)	73.0(2.4)

Table 39: Ice V order parameters after refining the $HRPD_1$ data with O–D bond-length restraints of varying strength.

6.4.3 The ice V structure

The structure of ice V recovered to ambient pressure, determined by Kamb *et al.* [108] and later confirmed by Hamilton *et al.* [1], is established by this work as the structure formed at high pressure. Although the oxygen framework for recovered ice V is similar to that found in this work for ice V under pressure, there are significant differences. The O–O distances in the recovered structure were found to cluster around 2.80 Å with the exception of one "conspicuously long" bond at 2.87 Å. No such behaviour is found in the ice V structure under pressure. The O–O bond lengths all differ greatly, with two distances shorter than 2.7 Å, while the "conspicuously long" bond in this work was found to be 3.01 Å.

The long O(4)–O(4′) bond distance arises from the four-membered rings present within ice V. In three dimensions, the sum of the angles around a quadrangle is at a maximum when the nodes of the quadrangle lie in the same plane, i.e. when the quadrangle is flat. When this occurs, the angles total 360°, each angle at a mean of 90°. The average O–O–O bond angle around the four-membered rings is therefore 90° maximum, figure 80, yet the D–O–D angle of the water molecule is 104.5°. The bending of the hydrogen bonds which results, causes the distance between bonding water molecules to increase, figure 80, thereby reducing the strain. Not surprisingly, the four-membered rings are almost flat such that the maximum 360° is utilised, with each of the four angles approximately 90°, table 38.

The O–O bond lengths around the four-membered rings are the largest of all the ice V bonds, table 35. Only the bond distance O(3)–O(4′) seems to be of normal length. However, lengthening of this bond appears prohibited by non-bonded interactions, figure 81. The short, non-bonded distance between atoms O(3) and O(4), 3.27 Å, is not much longer than the O(1)–O(1′) bond found in ice IV, 3.08 Å. It therefore

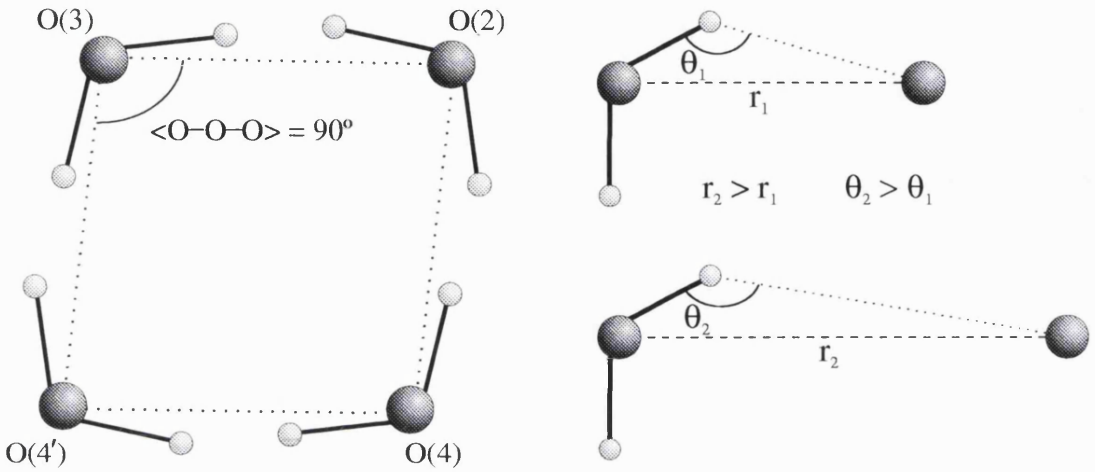

Figure 80: The four-membered rings found in ice V, for which the average O–O–O bond angle is 90° maximum. The size of the bond angles creates a large bending strain on the hydrogen bonds between neighbouring water molecules. The strain is relieved by an increase in the separation of the water molecules.

seems reasonable to assume that lengthening of the O(3)–O(4′) bond is prevented by repulsion.

Lengthening of the bonds around the four-membered rings is also responsible for the short O(1)–O(2) and O(4)–O(4″) distances. As the O(4)–O(4′) bond within the four-membered rings increases, the distance between neighbouring rings, O(4)···O(4″), decreases, figure 82. Similarly, the expansion of the O(4)–O(4′) bond causes the non-contact distance O(1)···O(4) to decrease. This repels the O(1) water molecule in the direction of O(2) resulting in a short O(1)–O(2) bond length.

The large number of distinct deuterium atoms, all of which exhibit positional disorder, and the use of bond-length restraints, unfortunately make any useful interpretation of the O–D bond lengths and D–O–D bond angles impossible.

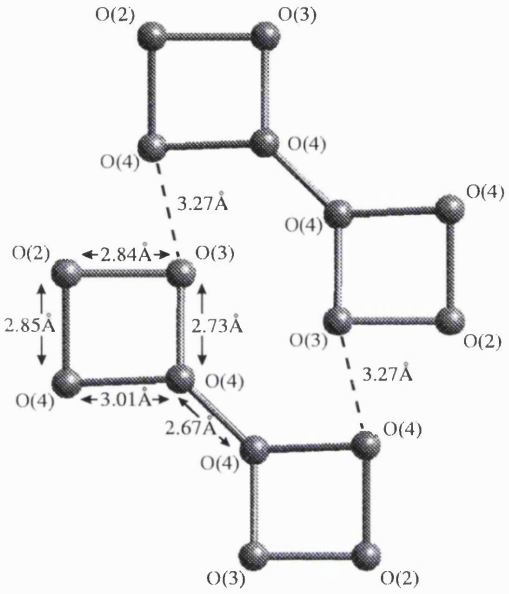

Figure 81: Increase in the O(3)–O(4′) bond length is prohibited by the short, repulsive O(3)···O(4) contact. All atoms shown lie approximately within the same plane.

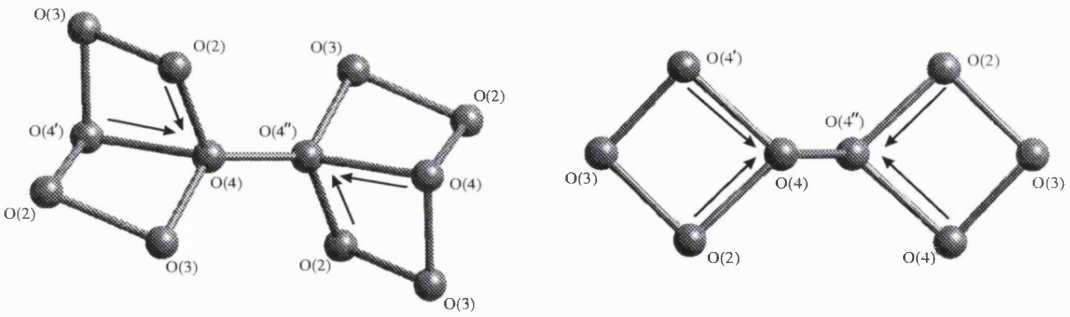

Figure 82: A few of the four-membered rings found in ice V. The lengthening of the O(2)–O(4) and O(4)–O(4′) bonds within the rings, causes the bond between neighbouring rings, O(4)–O(4″), to decrease.

6.4.4 Comparisons with spectroscopy

Dielectric measurements [85] and Raman spectroscopy [113–115] represent the only work carried out on ice V under its thermodynamic conditions of stability. The bond lengths obtained in this work can be used to estimate the uncoupled O–D stretching frequencies, which can then be compared to those observed spectroscopically. Berglund [116] derived a relation between the O–D stretching frequency and the O–D and O–O distances from data on deuterated solids, equations 17 and 18.

$$\nu_{OD} = \nu^0_{OD} - e^{11.156-(3.02 r_{O-D})} \quad (17)$$

$$\nu_{OD} = \nu^0_{OD} - e^{16.009-(3.73 r_{O-O})} \quad (18)$$

where $\nu^0_{OD} = 2727 cm^{-1}$, r_{O-D} and r_{O-O} are the O–D and O–O bond lengths respectively.

The use of bond length restraints in refining the ice V structure prevents the use of O–D distances. However, an estimate of the stretching frequencies can be made from the O–O distances. Table 40 lists the uncoupled O–D stretching frequencies which correspond to the average O–O distances listed in table 35.

O–O (Å)	ν_{OD} (cm^{-1})	O–O (Å)	ν_{OD} (cm^{-1})
2.69	2333	2.85	2510
2.77	2435	2.73	2388
2.84	2502	3.01	2608
2.72	2375	2.66	2287

Table 40: Ice V mean O–O bond lengths and the corresponding ν_{OD} stretching frequencies.

The eight different O–O distances correspond to eight different bands within the infrared and Raman spectra. Positional disorder, which arises from orientational

disorder, results in a small spread of values for each particular O–O bond distance. This in turn leads to broad bands in the spectra. As the water molecules within the structure begin to adopt ordered orientations, the degree of positional disorder decreases and the bands should begin to sharpen. However, as can be seen in figures 67 and 83, there does not appear to be any fine structure in the ice V spectra, infrared and Raman, at low (< 120 K) temperatures. This finding left Sukarova *et al.* [115] to reconsider their earlier conclusion that, at low temperatures, the ordering in ice V approached that of ice IX. Instead, ice V now retained an "appreciable amount of disorder" at low temperatures.

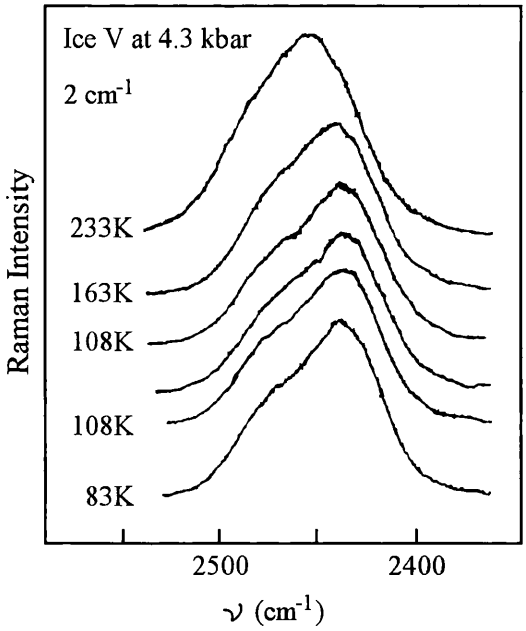

Figure 83: The Raman spectra of KOH doped ice V at 4.3 kbar measured by Sukarova *et al.* [115] over the temperature range 83–233 K.

Ices II and IX, in which the water molecules adopt ordered configurations, exhibit fine structure in both their infrared [82,110] and Raman [106,113,117] spectra. However, unlike ice V which has eight distinct O–O bonds, ices II and IX have only four

and three distinct O–O bonds respectively. For ice V, it may be that fine structure is difficult to resolve in amongst eight overlapping bands. The amount of disorder present at both high and low temperatures is therefore difficult to estimate from spectroscopic data.

The most troubling aspect of the spectroscopic data, however, is the location of the different stretching bands. The frequencies estimated from the O–O distances, table 40, differ from those observed spectroscopically. In particular, the bands attributed to the one long and two short O–O bonds do not appear in the spectra at all.

Bond bending will increase the stretch frequencies, which might account for the bands corresponding to the two short O–O bonds which will shift upwards in frequency. However, the long O(4)–O(4′) distance, which occurs within the four-membered rings, is also strained with O–O–O bond angles of 90°. This should result in a similar shift upwards in frequency, yet no features are observed in the spectra at frequencies greater than 2550 cm^{-1}. Kamb *et al.* [108] and Hamilton *et al.* [1] also recorded a long O(4)–O(4′) bond length at ambient pressure, which similarly cannot be seen in the spectra at high or ambient pressure.

The description offered by Berglund is based on data at ambient pressure, mainly on hydrates with more or less isolated hydrogen bonds; the description does not appear to hold for the high pressure ices. Nelmes *et al.* [118] and Besson *et al.* [119] similarly found that changes in the ice VIII O–D stretch frequency did not translate to changes in the O–D bond length according to empirical relationships.

6.4.5 Orientational disorder

Ice V is partially ordered, with the degree of order across some bonds being particularly strong, table 31. The pattern of ordering is similar to that found by Hamilton *et al.* [1] at the much colder temperature of 110 K, table 41.

	237 K	110 K		237 K	110 K
D(5)	56.5	60	D(12)	23.6	11
D(6)	43.5	40	D(13)	49.8	44
D(7)	43.5	40	D(14)	70.1	85
D(8)	29.9	15	D(15)	49.8	44
D(9)	50.2	56	D(16)	50.0	50
D(10)	76.4	89	D(17)	50.2	56
D(11)	56.5	60	D(18)	50.0	50

Table 41: The deuterium occupancies (%) determined by this work at 5 kbar and 237 K, and by Hamilton *et al.* [1] at ambient pressure and 110 K. Hamilton *et al.* refined the deuterium occupancies free of any restraint, table 27. However, in doing so, the occupancies do not satisfy the Bernal-Fowler rules. An approximation of the partial order found by Hamilton *et al.* which satisfies the Bernal-Fowler rules is given in this table.

The factors responsible for the partial order cannot be easily identified for such a complicated structure. Ice V possesses a large number of O–O–O bond angles which differ greatly from the D–O–D bond angle of 104.5°. Competition between orientations makes the task of understanding ordering difficult. For example, the water molecule of type O(2) has two O–O–O donor angles which are much more favourable in terms of bond strain than the rest, O(1)–O(2)–O(3^{iv}) and O(1)–O(2)–O(4), table 38 and figure 79. The occupation of only these orientations will lead to order parameters: $\alpha = 100\%$, $\beta = 0\%$ and $\gamma = \delta = 50\%$. However, the donor

angles for water molecules of type O(1) would suggest order parameters: $\alpha = 0\%$ and $\beta = 100\%$. There is therefore competition as to what the ordering should be. There are four crystallographically different water molecules, each with six possible orientations. It is therefore difficult to try and explain the ordering in terms of the O–O–O bond angles for the twenty six orientations. The ordering is not governed solely by which orientation is the more favourable: (a) or (b)?, but rather if (a) is chosen then what are the following choices and are these choices more, or less, favourable than if (b) had been chosen. This eventually lead to a huge number of permutations, making any justification of the partial order in terms of the bond angles impossible.

It is highly unlikely that the observed order is purely related to O–O–O bond angles. For ices II and III, there are other factors, most probably non-bonded interactions, responsible for the observed order. Since ice V is more dense than both ices II and III, it seems reasonable to assume that non-bonded interactions will also have an important influence on the ordering of water molecules within ice V.

Although the detailed origins of the partial order cannot be identified, something can be said about the changes in the amount with pressure and temperature. Each water molecule at a particular site within the ice structure can adopt one of six possible orientations, figure 6. Each orientation involves the occupation of a different O–O–O bond angle and therefore a different amount of bond bending between neighbouring water molecules. The different orientations will each have a different occupation energy. A water molecule will require more energy to occupy an orientation for which the O–O–O bond angle is 140°, than for one in which the angle is 104.5°. As the temperature is decreased, the total energy of the system decreases and the average energy of the individual water molecules also decreases. The occupation of orientations with large bond-strain will therefore decrease with temperature. Of course, all

water molecules do not have exactly the same energy, but have a range of energies described by a Boltzmann distribution. The orientations of the water molecules do not therefore go directly from a state of disorder to order. Instead, the process is gradual with temperature as the average energy of the water molecules decreases. On cooling ice V from 254 to 237 K, the partial order increased, table 31. This, along with the larger amount of order found by Hamilton *et al.* at 110 K, suggests that the order does indeed increase gradually as the temperature is decreased.

The change in orientational order with pressure is of a different nature to that of temperature and can be attributed to two effects. First, the increase in pressure further distorts the ice structure. As the water framework of any ice structure is compressed, the hydrogen bonds linking water molecules bend under strain and eventually break. For ice V, the increase in hydrogen bond strain with pressure is visible by the increase in bond angle distortion, table 37. As the hydrogen bond strain increases, the energy required for occupation of the different orientations increases. The situation is similar to that upon temperature decrease: the energy of the water molecules relative to that required for occupation decreases.

Second, as the pressure is increased the density of the ice naturally increases. The fraction of space occupied by each water molecule therefore decreases, and non-bonded interactions become increasingly important.

6.4.6 Entropy considerations

Handa *et al.* [112] found an endothermic transition over the temperature range 106–132 K, thought to be the reorientation of water molecules from an ordered to disordered state. After annealing at 110 K for a period of sixty hours, they measured a change in entropy of 0.84 $Jmol^{-1}K^{-1}$ for the transition. After doping the sample with

KOH to assist in the ordering process, the transition entropy rose to 1.9 $Jmol^{-1}K^{-1}$.

This work has shown that ice V is partially ordered above the transition and not fully disordered as was thought. The transition entropy measured by Handa *et al.* clearly arises from further ordering of the water molecules. The question that remains is whether a change in space group is required to account for the measured entropy change. Of the fourteen crystallographically different deuterium atoms, only two determine the space group. Any change in the ordering of these two atoms, from their nominal values of 50%, will cause a change in symmetry. Since the change need only be subtle, it would prove impossible to detect entropically.

If the individual order parameters at 254 and 237 K are each extrapolated linearly, then the ordering at 130 K might be: $\alpha = 21.5\%$, $\beta = 29.9\%$, $\gamma = 60.9\%$ and $\delta = 87.7\%$. If this is the assumed order above the transition recorded by Handa *et al.*, then the transition entropy of 1.9 $Jmol^{-1}K^{-1}$ could be accounted for, without a change in space group, if the order below the transition were: $\alpha = 1\%$, $\beta = 2.5\%$, $\gamma = 97\%$ and $\delta = 99.5\%$; the figures were obtained using the statistical methods described by Nagle [2]. This amount of orientational order would be surprising to find without the other two deuterium atoms, D(16) and D(18), ordering in some way. The calculations of Nagle, therefore, suggest a change in space group is needed to account for the entropy change measured by Handa *et al.*

Howe and Whitworth [3] found a flaw in the model described by Nagle which over estimates the entropy, particularly for nearly ordered systems. Unfortunately, the model proposed by Howe and Whitworth details the configurational entropy for an ice structure with one ordering parameter only. If the order found in this work is represented by a single parameter, and again linearly extrapolated to 130 K, then 39.0% of the deuterium atoms will occupy ordered sites. The transition entropy

of 1.9 $Jmol^{-1}K^{-1}$ would then correspond to 84.2% of deuterium atoms occupying ordered sites below the transition. If the two deuterium sites which determine the symmetry are fixed at 50%, then the 84.2% order corresponds to: $\alpha = 1\%$, $\beta = 1\%$, $\gamma = 99\%$ and $\delta = 99\%$. Again, it seems unlikely that the two deuterium atoms which determine the symmetry should remain disordered while all other deuterium atoms adopt almost fully ordered configurations. The workings of Howe and Whitworth, like those of Nagle, also suggest a change in space group is needed to account for the measured entropy change.

In the above discussion, the amount of order was assumed to increase linearly with decrease in temperature. However, in many second-order phase transitions the variation in ordering parameter with temperature is non-linear. Non-linear behaviour is also expected for the orientational ordering of water molecules in ice. As the temperature approaches T_c, the temperature at which full order is achieved, ordering of the water molecules becomes increasingly difficult. For example, the last water molecule to order may require some 10^{22} other water molecules to reorient before it can do so. The linear approximation used above is most likely an underestimate of the amount of ordering at 130 K temperatures. This is because the approximation predicts a negative temperature for complete order, i.e. $T_c < 0$ K. The amount of order at 130 K, i.e. above the transition, is probably greater than that estimated and hence the amount of order below the transition must also be greater. The case for a change in space group still holds.

6.4.7 Transition curves

Bridgman examined the ice III–V and V–VI transitions over a range of pressures and temperatures and found that the equilibrium curves defining the transitions were

straight. The Clausius-Clapeyron relation, equation 16, states that the gradient of the equilibrium curve is proportional to the entropic difference between the two phases. Since the amount of orientational order for ice V is sensitive to temperature, the gradient of the equilibrium curves, III–V and V–VI, should also change with temperature. However, the difference in the orientational order for the two temperatures, 254 and 237 K, corresponds to a change in entropy of only 0.03 $Jmol^{-1}$, i.e. 0.0018 $Jmol^{-1}K^{-1}$, regardless of whether the statistics of Nagle [2] or Howe and Whitworth [3] are used. The average change in volume for the transition ice III–V was 0.98 cm^3mol^{-1} [29]. From this, the change in gradient of the equilibrium curve is 0.02 $barK^{-1}$. This is of course too small to be measured experimentally and hence a straight equilibrium curve is recorded. For the ice V–VI transition, the change in volume is slightly smaller, 0.69 cm^3mol^{-1} [29], but a similarly small change in gradient is expected 0.03 $barK^{-1}$.

6.4.8 Compressibility and expansivity

The compressibility and expansivity of ice V were estimated from the lattice constants from the refined HRPD data only. In this way, systematic errors arising from temperature, pressure and wavelength calibration were removed.

The compressibility of ice V, determined from the data at 4.0 and 5.0 kbar, is 7.46(9) $Mbar^{-1}$ at 254 K, which corresponds to an isothermal bulk modulus of 134(2) kbar. This figure is in agreement with the isothermal bulk modulus determined by Gagnon *et al.* [94] at 237.5 K, 138.6 kbar, and the adiabatic bulk moduli determined by Tulk *et al.* [107] at 238 K, 143 kbar, and by Shaw [93] at 248 K, 132 kbar. The adiabatic moduli were determined by acoustic velocity measurements by Brillouin spectroscopy on single crystals (Tulk *et al.*) and by ultrasonics on powders (Shaw) for H_2O ice V. The isothermal bulk modulus (Gagnon *et al.*) was determined

by measuring the volume change of powdered H_2O ice V as a function of pressure.

The expansivity of ice V, determined from the data at 237 and 254 K, is 240(5) MK^{-1} at 5.0 kbar. The compressibilities and expansivities of all the ice structures examined in this work are discussed in section 9.6.8.

6.5 Conclusions

This work has studied for the first time the crystalline structure of ice V within its thermodynamic region of stability. The results conclusively show that the water molecules adopt partially ordered orientations. Such findings differ from current views which assume the water molecules are fully disordered at high temperatures [85,115], and only begin to order at temperatures of around 120 K [1,112]. Although the ice structure under pressure is similar to that at ambient pressure [1,108], significant differences in the oxygen frameworks exist.

The orientational order of the water molecules increases with both increase in pressure and decrease in temperature. With the order found by Hamilton *et al.* [1] of a similar nature, the ordering appears to be gradual with temperature. The variation in order with temperature is small, which accounts for the straight ice III–V and V–VI transition curves measured by piston-in-cylinder experiments.

Although this work can offer no information on the structure of ice V at low temperatures, it seems unlikely that the transition entropy measured by Handa *et al.* [112], at 120 K, can be attributed to further order under the same space group. With the space group determined by Hamilton *et al.* [1] at 110 K the same as that determined by this work at 254 K, it would appear that KOH doping is needed to assist in the ordering necessary for a symmetry change. Although a change in symmetry is

suggested by the entropy measured by Handa *et al.*, it is not known whether the space group after the transition is $P2_1/a$, as suggested by Kamb and La Placa [111], or a small degradation in the current space group to Aa. At the time of writing, neutron powder diffraction data have been collected on ice V at 5 kbar and 234–100 K. Initial analysis indicates no change in space group over this temperature range.

The behaviour of ice V at low temperature remains unknown. Data collected recently at low temperature should address some of the outstanding questions. If, as is initially indicated, there is no change in space group, then the order achieved as a function of temperature will be of interest and may highlight the onset of an ordering transition, such as that found by Handa *et al.* [112]. The dielectric work of Wilson *et al.* [85] predicts water molecule relaxation times of several hours at 150 K. With any ordering transition most likely below this temperature, further work with the use of KOH to assist in the ordering process will also be of interest.

Chapter 7

Ice IV

7.1 Introduction

Ice IV was first postulated by Bridgman in 1912 [29] when he twice found ice at 5 kbar to melt at a higher temperature than the established melting curve for ice VI. He later confirmed the existence of ice IV using D_2O [30], which was found to form ice IV more readily than H_2O. Starting from ice VI, ice IV was formed on decreasing the pressure to a point close to the extended ice VI melting curve, figure 84. Bridgman measured several points on the ice IV melting curve, together with a couple of points on the ice IV–VI transition curve, and found that ice IV exists completely within the stability region of ice V. He also found ice IV to be unstable relative to ice V since once ice V had formed, ice IV could not be recovered. The difficulty in forming ice IV and its instability with respect to ice V soon became apparent with subsequent work by others [85, 108, 120] failing to find the metastable phase.

There were no further reports of ice IV until 1967 when Evans [42] outlined the use of organic compounds as nucleators for the high pressure ices. Starting from the

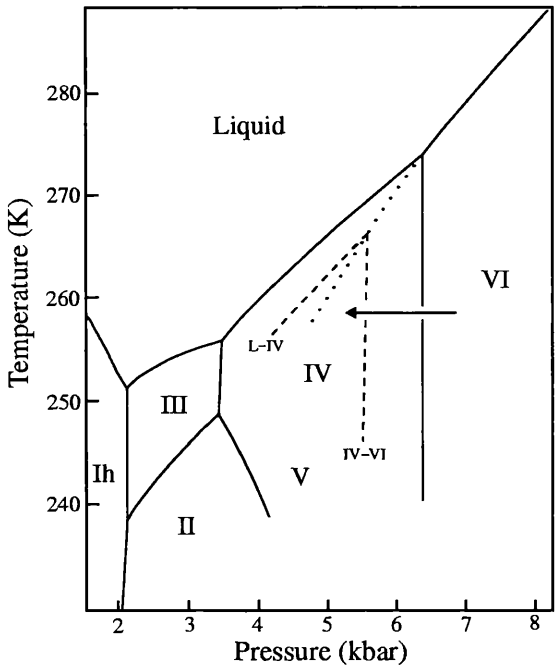

Phase transition curves measured by Bridgman [29, 30] and later Nishibata [45]. Solid lines represent stable transitions; dashed lines, metastable ice IV transitions; dotted line, the extended liquid–VI transition. Ice IV was formed from ice VI by decreasing the pressure at 259 K, as indicated by the arrow. The existence of ice IV was suspected when the sample was found to melt at a higher temperature than the extended liquid–VI curve.

Figure 84: The ice phase diagram in the region of ice IV.

liquid, Evans found several compounds which assisted in the formation of ice IV upon freezing. As a result, Evans was able to determine several points on the ice IV melting curve and found his work to be in "substantial agreement" with that of Bridgman [30].

The nucleators proposed by Evans [42] now offered a way of forming ice IV from the liquid and Engelhardt and Whalley [43] soon exploited their use. Using a similar experimental set-up to that of Evans, Engelhardt and Whalley identified phase transitions through abrupt changes in sample temperature. In this way they were able to determine the melting curves for both H_2O and D_2O ice IV. Again, the D_2O ice IV melting curve was in good agreement with that of Bridgman. However, there was poor agreement in the location of the liquid–IV–VI triple point, which differed by 200 bar and 2.2 K. The cause of the discrepancy was unknown.

Several of the samples prepared by Engelhardt and Whalley [43] were then quenched to 110 K and recovered to ambient pressure. They were confident that ice IV had been recovered successfully since no thermal effects were recorded to suggest

a phase transition. Infrared spectra were then collected in the region of the O–H stretching and rotational frequencies [44]. The location of the bands implied that the water molecules, as in all other ices, were four co-ordinated and fully hydrogen bonded. The lack of fine structure in the stretching and rotational bands, figure 85, was interpreted as evidence for orientational disorder. In defence of this conclusion, Engelhardt and Whalley cited the change in entropy associated with the ice IV–VI transition, 0.04 $Jmol^{-1}K^{-1}$, measured by Bridgman [30]. The small transition entropy implied the configurational entropies of ices IV and VI were similar. Since the water molecules in ice VI were established by diffraction [81], dielectric measurements [85] and infrared spectroscopy [121] as orientationally disordered, the water molecules in ice IV must also be disordered.

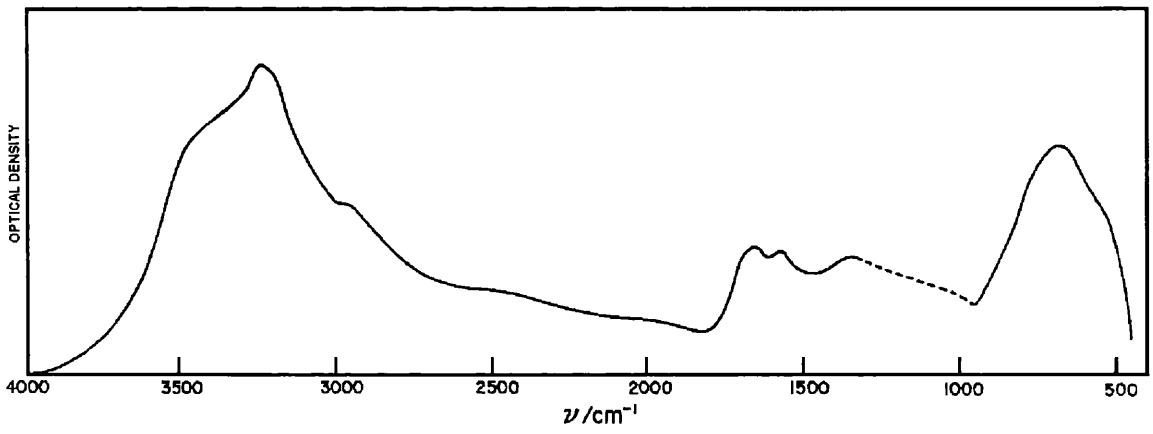

Figure 85: Infrared spectrum of ice IV.
The lack of fine structure in the O–H stretching band, centred at 3235 cm^{-1}, and the rotational band, centred at 680 cm^{-1}, led Engelhardt and Whalley to conclude that the water molecules in ice IV were orientationally disordered.

At around the same time as the work of Engelhardt and Whalley, Nishibata [45] also reported the formation of ice IV, this time without the use of nucleants. In the same way as reported by Bridgman [30], Nishibata formed ice IV from ice VI

by decreasing the pressure. Although the formation of ice IV occurred for a small region only, between 258.4–259.4 K and 5.00–5.35 kbar, it remained stable beyond this once formation had reached completion. Using dielectric properties to record phase transformations, Nishibata measured several points on the ice IV melting curve along with points on the ice IV–VI curve.

The structure of ice IV in its recovered form was finally determined by Engelhardt and Kamb [46,47] from powder and single crystal X-ray diffraction data collected on the recovered samples of Engelhardt and Whalley [43].

The crystallographic structure is based upon a rhombohedral unit cell, space group $R\bar{3}c$, lattice constants: $a = 7.60$ Å and $\alpha = 70.1°$, or $a_H = 8.74$ and $c_H = 17.05$ Å for the corresponding hexagonal cell. The unit cell comprises twelve water molecules, only two of which are required to describe the structure completely. The first occupies a general position and forms hexagonal rings similar to those found in ices Ih and II. These rings arrange to form planes which stack upon one another, figure 86. The

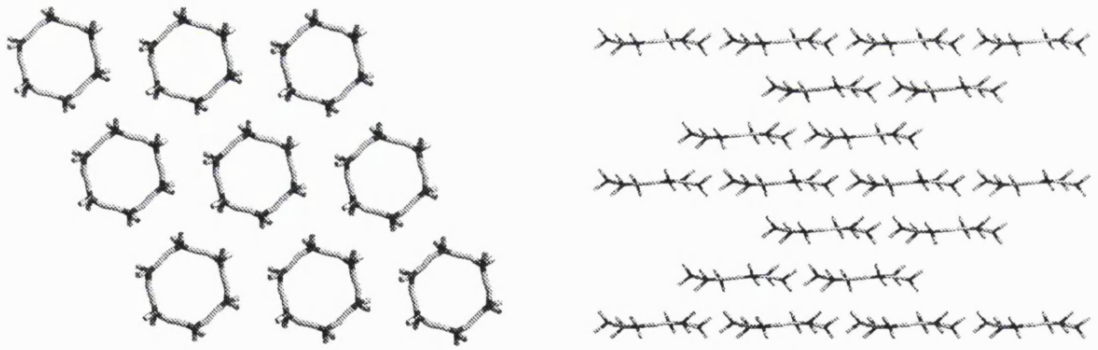

Figure 86: Water molecules of one type form hexagonal rings in a planar arrangement (left). The planes then stack upon one another (right). The bonds between planes have been omitted for clarity.

rings within a particular plane do not bond directly to one another but instead bond to the next nearest rings in the planes immediately above and below, figure 87. Water

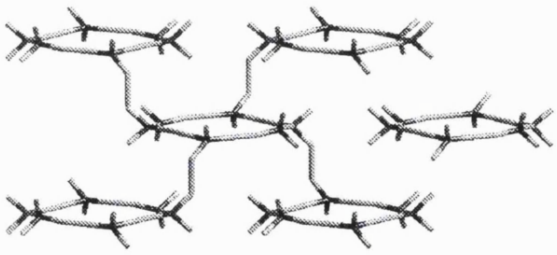

Figure 87: Rings within a particular plane do not bond directly to one another but instead bond to the next nearest rings in the planes immediately above and below.

molecules of the second type occupy special positions on the $\bar{3}$ symmetry axis and sit just above and below the centre of each ring. As a consequence, the hydrogen bond binding these two molecules passes through the centre of the ring. These water molecules then serve to bind every second plane together, figure 88.

Figure 88: Water molecules of type II passing through the centre of the hexagonal rings.

The symmetry of ice IV is such that full orientational order of the water molecules is not possible. Complete disorder at such low temperatures (< 130 K) is uncommon, with ices Ih and Ic being the only other phases to exhibit such behaviour. Engelhardt and Kamb [47] believe such disorder may be attributed to the O–O–O bond angles. All such angles in ice IV, they explain, differ by similar amounts from the H–O–H bond angle of 104.5°. There are no bond angles close to 104.5° which would favour H–O–H occupation, nor are there any bond angles hugely different from 104.5° which would deter H–O–H occupation.

The difficulty in forming ice IV has clearly hampered research, indeed the work outlined above represents the current sum of published material on ice IV. Only four parties appear to have been successful in forming ice IV. Two achieved this by decreasing the pressure on ice VI, the other two by freezing the liquid with the use of nucleants. Although there is a general agreement as to the location of the ice IV melting curve, the errors involved were large and there appear to be some discrepancies in the results. It is possible that the nucleants used by Evans [42] and Engelhardt and Whalley [43] are influencing phase stability. However, even here there are problems: for the same nucleant, Evans found ice IV stable over the pressure range 3.2–4.0 kbar whilst Engelhardt and Whalley found ice IV stable over 4.2–5.9 kbar.

Organic nucleants are successful in forming the desired ice structure by acting as centres around which water molecules aggregate. Nucleants which differ in size and shape cause the water molecules to aggregate differently; hence, different nucleants are successful in forming different ice structures. There is no evidence from the literature to suggest that the 'ice IV' formed by Engelhardt and Whalley, using nucleants, is the same as that formed by Bridgman.

To accurately establish the stability region of ice IV without the use of nucleators is certainly warranted. However, a more realistic target would be to try and form ice IV without the use of nucleants and if successful, to confirm or otherwise that the structure formed is the same as that proposed by Engelhardt and Whalley. Ideally, this would be carried out under the conditions of stability outlined for ice IV; although Engelhardt and Whalley found no thermal effects on quenching, this does not completely rule out a phase transition or some modification of structure.

It would be senseless to pursue this line of research indefinitely since, even with nucleants, Engelhardt and Whalley achieved inconsistent results. Only 10% of trials

resulted in the successful formation of ice IV; they never managed to form H_2O ice IV without the use of nucleants, and were successful on only a few occasions with D_2O.

The question of orientational ordering is not an immediate concern. Full order is not permitted by symmetry and there is no evidence from spectroscopic data to suggest otherwise. The use of neutrons will, however, highlight any symmetry violations that may have gone undetected by X-rays.

7.2 Experimental procedure

From the work detailed above, two routes appeared successful in the formation of ice IV. The first involved the release of pressure on ice VI, requiring initial pressures in excess of 6.5 kbar. Although easily possible with anvil cells, such pressures were not possible with the gas cells available. The second route involved freezing the liquid with the use of organic nucleants, which boasted a 10% success rate. With no report of ice IV ever being formed from ice V, the only route possible was through freezing the liquid.

Since formation was attempted from the liquid, silica wool was required such that when the liquid froze, a good powder was formed. The silica wool, unlike the inorganic nucleants, was solid and insoluble. It assists in forming a good powder by occupying much of the available space, and so prevents the formation of large crystals. The use of silica wool is not thought to be necessary for the formation of ice IV, nor is it thought to modify the structure.

PEARL

A TiZr gas pressure cell was filled with of silica wool into which 1.5 ml of D_2O was distributed by use of a syringe and needle. Argon pressure was increased to 5.8 kbar at room temperature and the cell lowered into a cryostat located on the diffractometer. The temperature was then decreased at a rate of 0.3 $Kmin^{-1}$ to 268 K. It should be noted that whilst the temperature sensors located on the outside of the cell registered a rate of 0.3 $Kmin^{-1}$, the sample inside the cell would have experienced some lag. Once at 268 K, the pressure which had fallen due to cooling was topped back up to 5.8 kbar. Cooling then resumed at the rate of 0.3 $Kmin^{-1}$ from 268 to 260 K. Immediately upon reaching 260 K, a phase transition occurred identified by a drop in pressure from 5.75 to 5.05 kbar. For reasons already stated, it is doubtful that the sample temperature was 260 K at the time of transition.

Inspection of the data revealed that the phase formed was ice IV with the individual detectors indicating a good powder. A full data set was collected over 14 hours at 5.05 kbar and 260 K to solve the detailed structure. The pressure was then decreased in steps with data, sufficient for lattice constant refinement, collected at 4.8, 4.5 and 4.2 kbar at 260 K. This then provides an indication of the compressibility of ice IV at this temperature.

On decreasing the pressure to 3.9 kbar, the sample began to melt. This was visible through an increase in pressure due to changes in sample volume (water is less dense than ice IV) and the appearance of a water hump in the diffraction profiles. As the sample melted the pressure continued to rise, finally settling at 4.16 kbar. At this point, the water and ice IV are in equilibrium and the pressure and temperature are at a point on the liquid–IV equilibrium curve. A further data set, again sufficient for lattice constants, was collected at this pressure.

Ideally data would also have been collected at various temperatures to obtain expansivity information but unfortunately there was insufficient time to warm/cool the sample, wait for temperature equilibration and collect data.

Prior to the above success at forming ice IV, attempts were also made at the lower pressures of 5.0 and 5.5 kbar. Freezing at 5.0 kbar resulted in the formation of ice V and is discussed in chapter 6. However, the freezing at 5.5 kbar resulted in a completely new phase of ice. This was a very important find and is further discussed in chapter 9.

7.3 Results

Refinement

The structure of ice IV proposed by Engelhardt and Whalley was used as the initial model in refining the data. The unit cell of ice IV is rhombohedral, space group $R\bar{3}c$, lattice constants: $a = 7.60$ Å, $\alpha = 70.1°$. However, the corresponding hexagonal unit cell, lattice constants: $a_H = 8.74$ and $c_H = 17.05$ Å, was used throughout the refinement as this provided an easier axis for observing structural effects upon compression. The asymmetric unit consists of eight atoms: two oxygen and six deuterium. The symmetry of ice IV permits ordering of the deuterium atoms across one bond type only. The occupancies for all deuterium atoms were therefore fixed initially at 50%.

The argon clathrate that formed during data collection was modelled on the structure refined from neutron diffraction data collected at 4.8 kbar [61]. The amount of clathrate present in the diffraction profiles was small and only the lattice constants were refined.

No reflections from the TiZr pressure cell were observed and the background was adequately modelled by a simple cosine Fourier series, section 3.6.6.

During refinement, additional peaks were clearly visible at 2.9, 3.1 and 3.5 Å with perhaps smaller peaks at 2.1, 2.3 and 4.0 Å, figures 89 and 97. Fortunately, this phase had also been seen in the ice V data and was not an indication of an incorrect model for ice IV. The phase could not be identified as any ice or clathrate phase and was excluded from the diffraction profiles. It should be noted that only peaks at d-spacings greater than 2 Å could be easily identified. Peaks at shorter d-spacings may have influenced the refinement and the results obtained. The nature of this phase is further discussed in section 7.4.2.

To help the refinement reach the global minimum an initial bond length restraint of O–D = 0.97(1) Å was used and thermal factors were constrained to the same value for each atom type. Both restraints were later removed. The two permitted deuterium occupancies were refined but varied very little from 50%. The values were therefore reset to 50% and kept fixed.

Figures 89 to 94 show the profile fits arising from the refinement of the various data sets. Structural information obtained from the refinement of the data set collected at 5.05 kbar and 260 K are listed in tables 42 to 46.

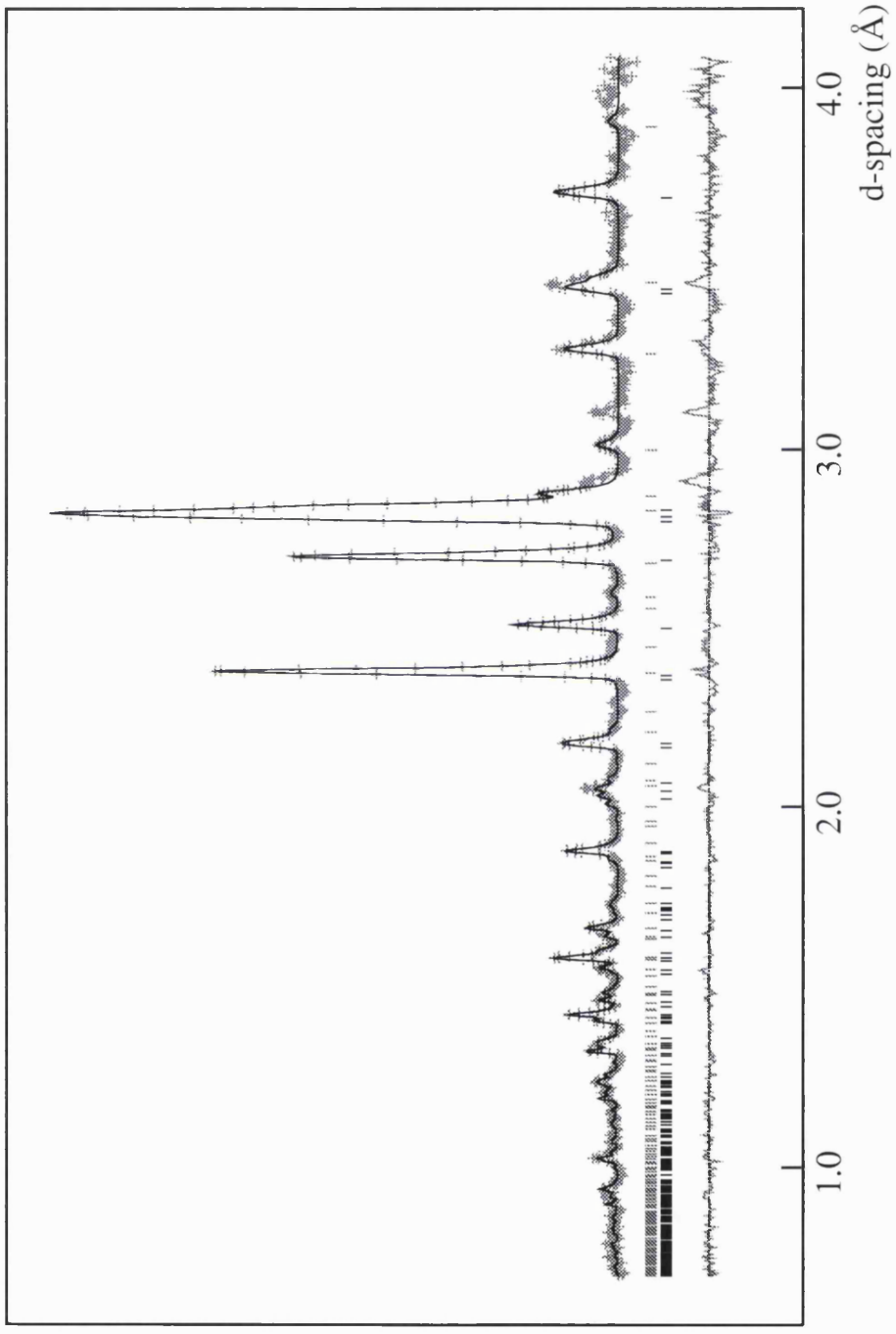

Figure 89: The profile fit for the data collected at 5.05 kbar and 260 K, $R_p = 0.0058$ and $R_{wp} = 0.0055$. The amount of argon clathrate determined by the refinement was 14 wt.%.

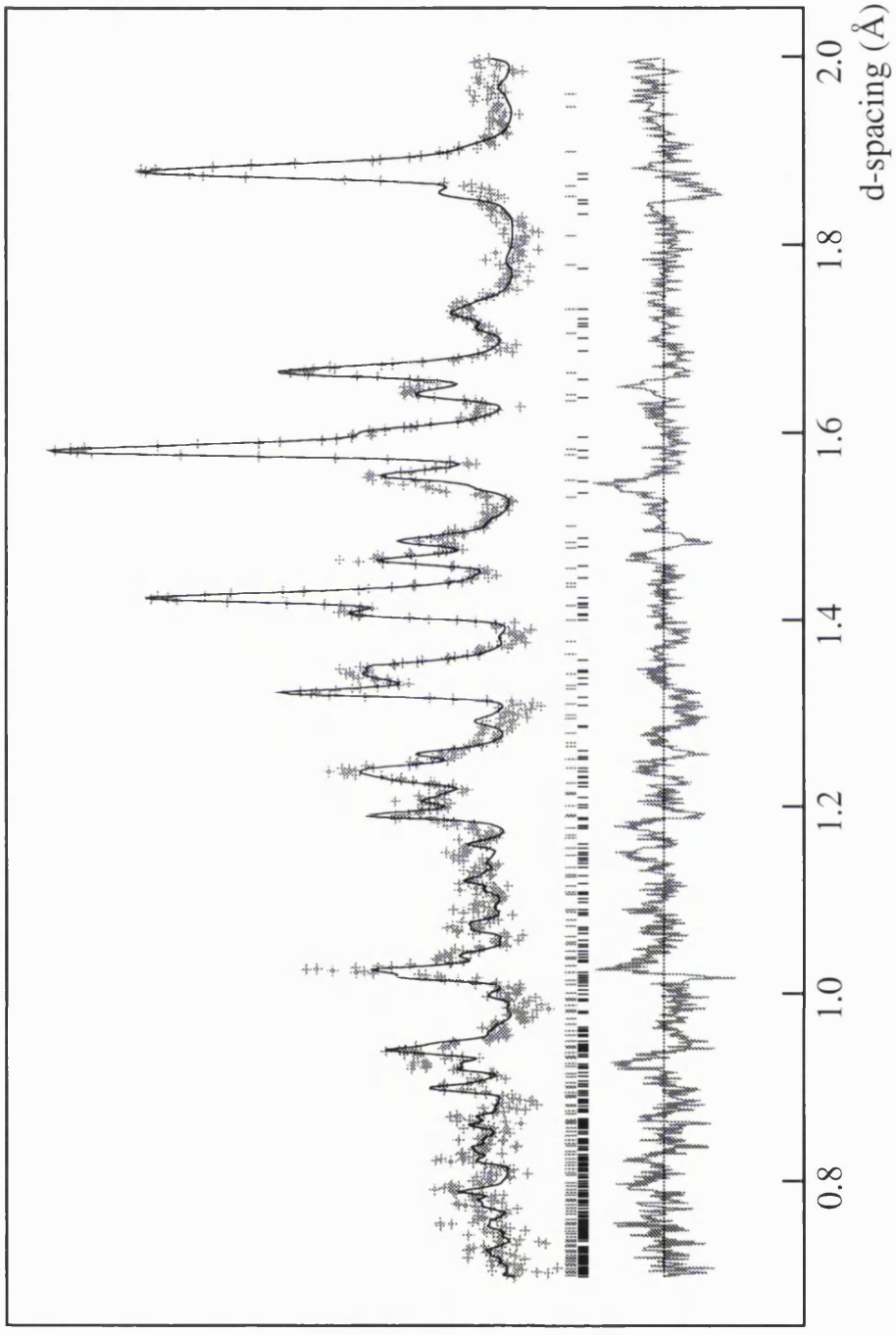

Figure 90: The profile fit for the data collected at 5.05 kbar and 260 K in the 0.7–2.0 Å region.

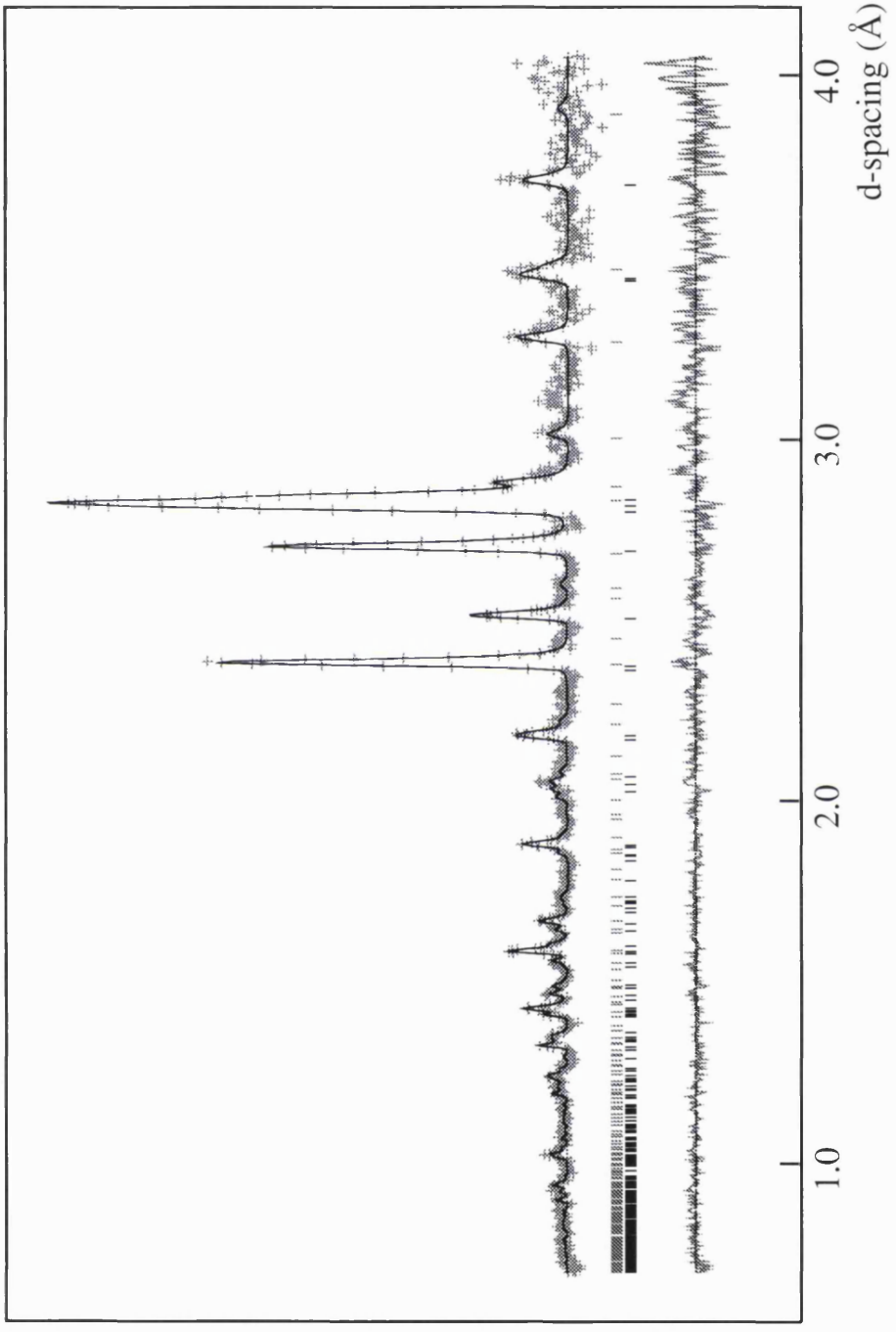

Figure 91: The profile fit for the data collected at 4.80 kbar and 260 K, $R_p = 0.0128$ and $R_{wp} = 0.0094$.

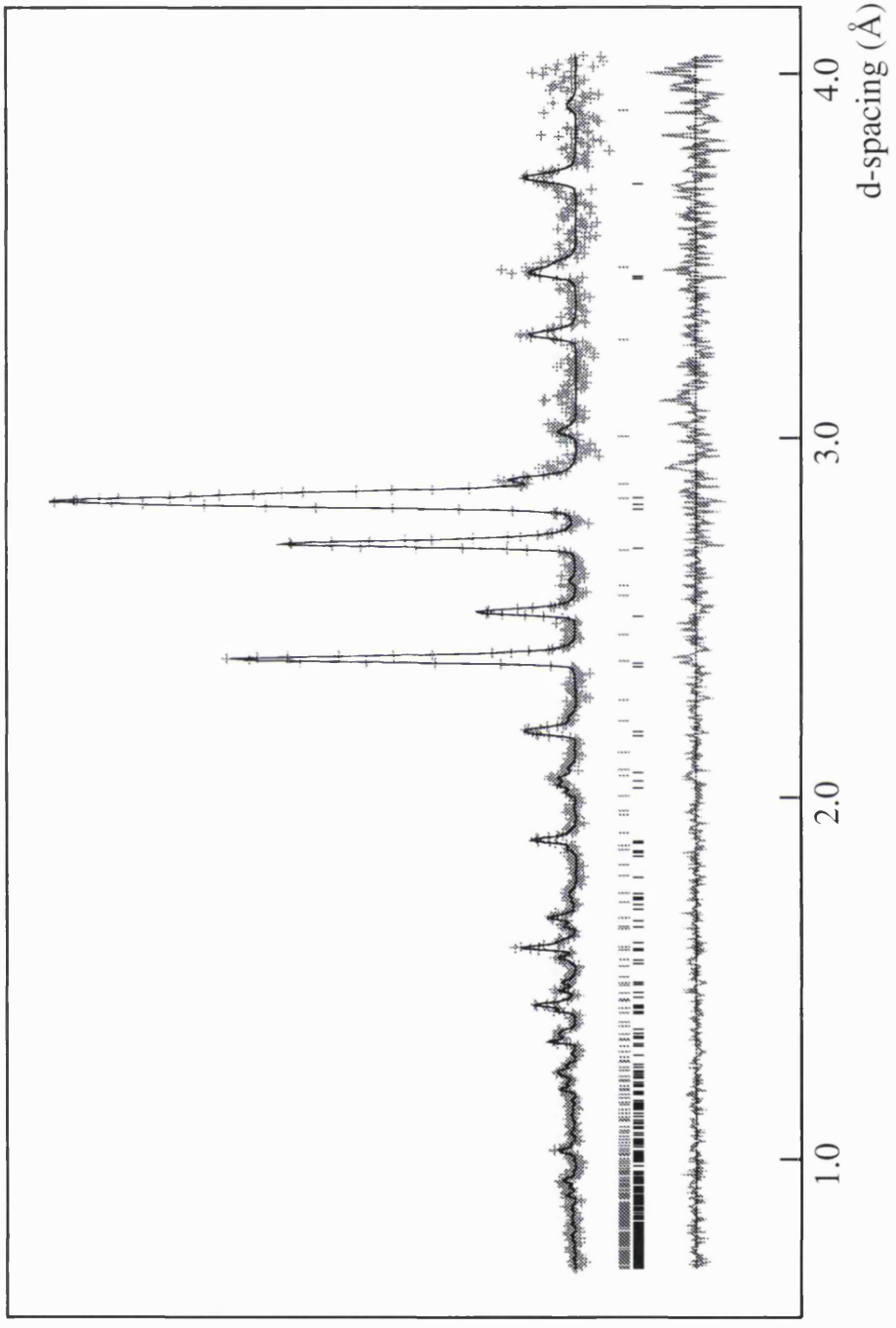

Figure 92: The profile fit for the data collected at 4.51 kbar and 260 K, $R_p = 0.0129$ and $R_{wp} = 0.0096$.

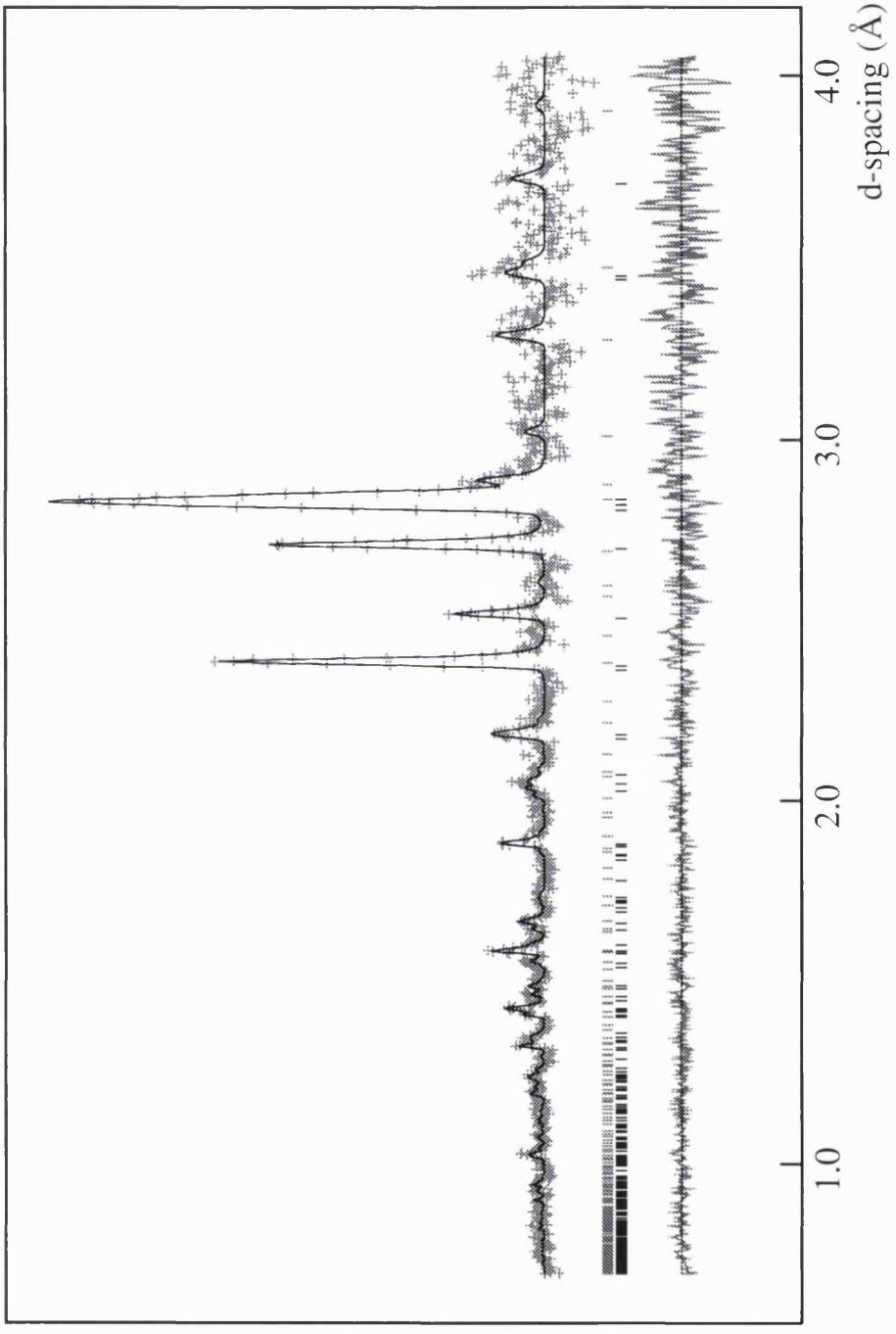

Figure 93: The profile fit for the data collected at 4.21 kbar and 260 K, $R_p = 0.0200$ and $R_{wp} = 0.0134$.

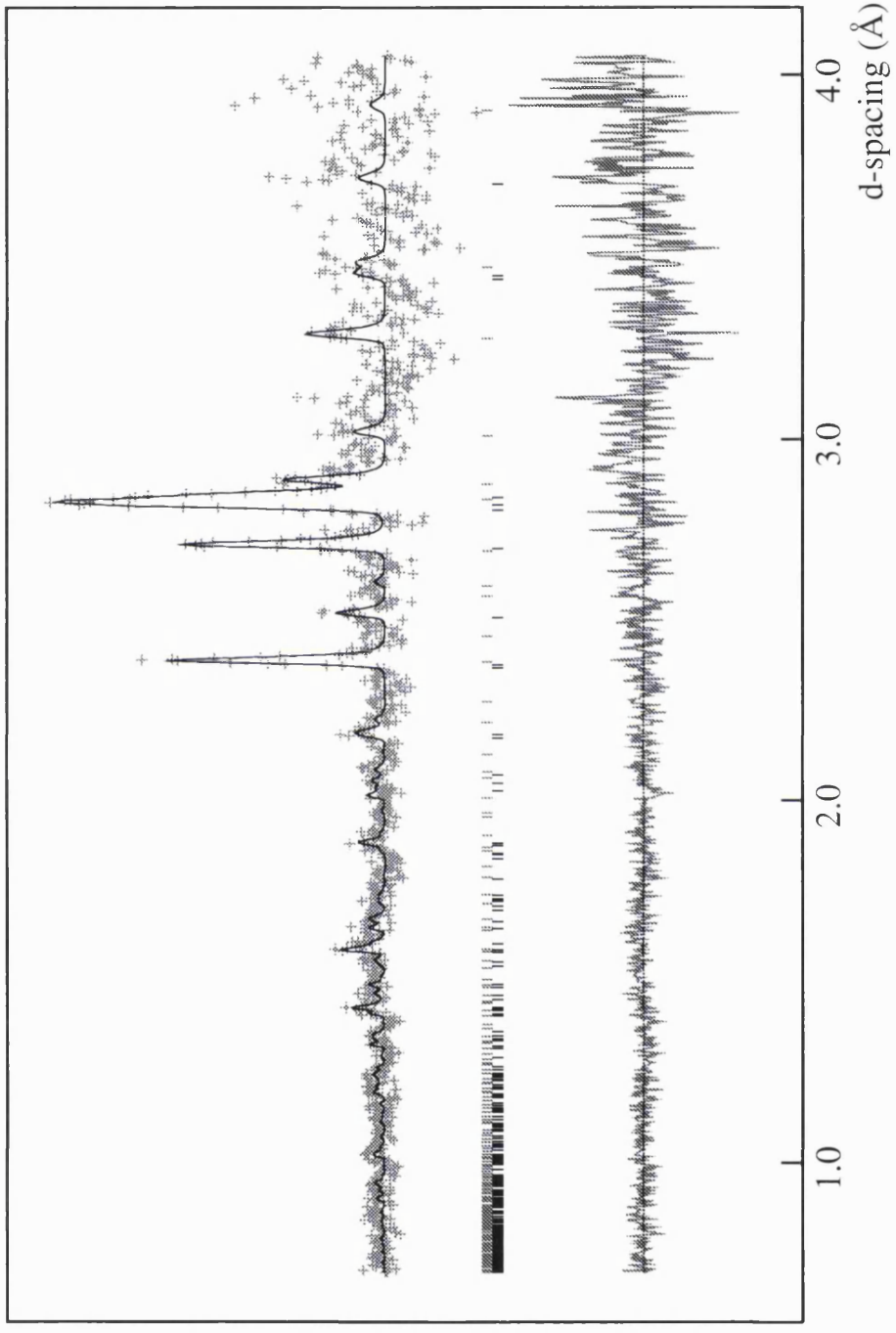

Figure 94: The profile fit for the data collected at the liquid–IV equilibrium curve, 4.16 kbar and 260 K, $R_p = 0.0222$ and $R_{wp} = 0.0146$.

P(kbar)	T(K)	a_H(Å)	c_H(Å)	c_H/a_H	V(Å^3)	ρ(gcm^{-3})
5.05	260	8.67849(14)	17.0181(4)	1.96076(7)	1110.02(4)	1.43614(5)
4.805	260	8.68394(38)	17.0246(10)	1.96049(15)	1111.84(9)	1.43379(12)
4.51	260	8.69185(38)	17.0320(10)	1.95952(15)	1114.35(9)	1.43056(12)
4.21	260	8.69856(53)	17.0417(14)	1.95912(22)	1116.71(13)	1.42754(17)
4.16	260	8.6997(12)	17.0465(31)	1.95947(49)	1117.31(30)	1.42677(38)

Table 42: Ice IV lattice constants and densities

	x	y	z	U_{iso}
O(1)	0.0000(0)	0.0000(0)	0.0903(6)	0.0464(28)
O(2)	0.3625(10)	0.2379(19)	0.0080(6)	0.0517(22)
D(3)	0.0000(0)	0.0000(0)	0.0355(8)	0.0699(61)
D(4)	0.0259(9)	0.1157(10)	0.1084(4)	0.0453(31)
D(5)	0.4633(16)	0.2880(15)	-0.0265(6)	0.0566(43)
D(6)	0.2982(21)	0.2973(13)	-0.0027(10)	0.0504(36)
D(7)	0.3217(12)	0.1135(23)	0.0048(8)	0.0404(35)
D(8)	0.4280(18)	0.3348(20)	0.0467(4)	0.0656(49)

Table 43: Ice IV atomic positions and isotropic thermal factors.

O(1)–D(3)	0.933(9)	O(1)···D(3)	2.142(22)
O(1)–D(4)	0.963(8)	O(2)···D(4)	1.823(10)
O(2)–D(5)	0.958(9)	O(1)···D(5)	1.815(13)
O(2)–D(6)	0.948(10)	O(2)···D(6)	1.857(11)
O(2)–D(7)	0.954(8)	O(2)···D(7)	1.829(11)
O(2)–D(8)	0.993(9)	O(2)···D(8)	2.038(19)

Table 44: Ice IV O–D and O···D bond lengths.

O(1)–O(1′)	3.075(22)	O(1)···O(2)	3.235(10)
O(1)–O(2′^{v})	2.743(10)	O(1)···O(2′)	3.103(20)
O(2)–O(2′)	2.782(8)	O(2^{v})···O(2$^{v\prime}$)	3.139(21)
O(2)–O(2″)	2.939(25)		

Table 45: Ice IV O–O bonded and O···O non-bonded distances.

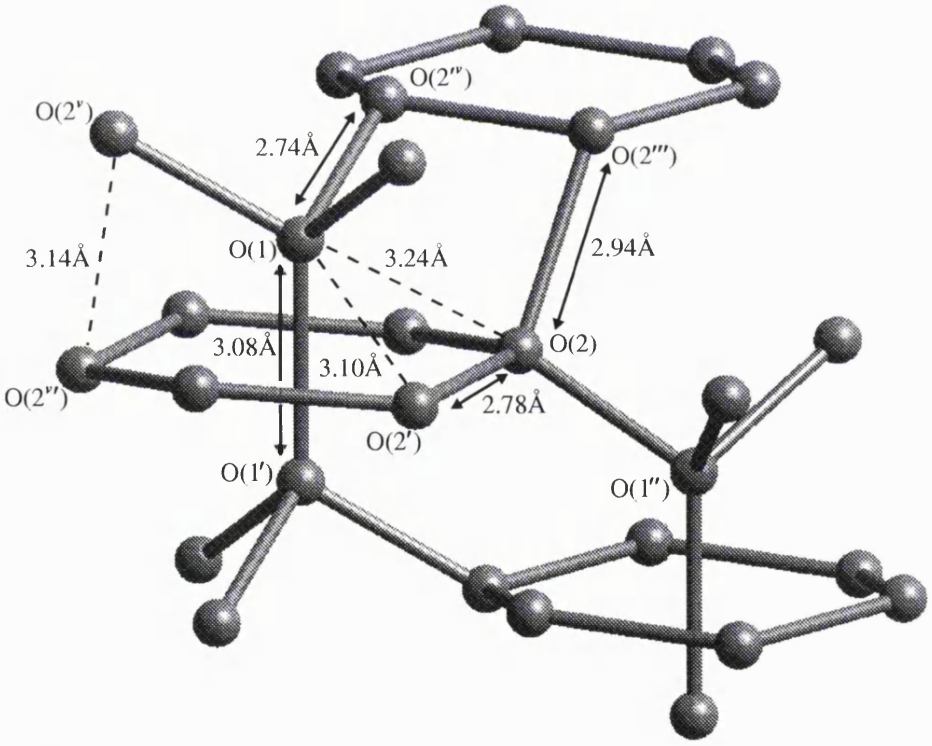

Figure 95: The ice IV O–O bond lengths and short non-bonded O···O distances.

D(3)–O(1)–D(4)	108.6(0.9)	O(1′)–O(1)–O(2^{v})	121.5(0.3)
D(4)–O(1)–D(4)	110.3(0.9)	O(2$'^{v}$)–O(1)–O(2^{v})	95.1(0.4)
D(5)–O(2)–D(6)	106.7(2.1)	O(1″)–O(2)–O(2″)	128.3(0.6)
D(5)–O(2)–D(7)	102.6(2.0)	O(1″)–O(2)–O(2′)	93.6(0.7)
D(5)–O(2)–D(8)	90.9(1.0)	O(1″)–O(2)–O(2‴)	109.2(0.5)
D(6)–O(2)–D(7)	128.2(1.4)	O(2″)–O(2)–O(2′)	119.1(0.1)
D(6)–O(2)–D(8)	84.8(1.9)	O(2″)–O(2)–O(2‴)	124.3(0.7)
D(7)–O(2)–D(8)	136.7(2.0)	O(2′)–O(2)–O(2‴)	85.5(0.5)

Table 46: Ice IV D–O–D and O–O–O bond angles. The entries in each line correspond to the same water molecule orientation.

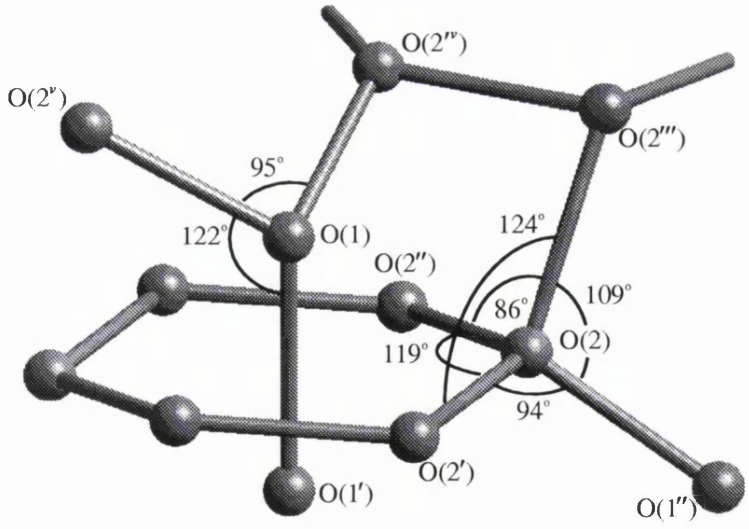

Figure 96: The ice IV O–O–O bond angles.

7.4 Discussion

7.4.1 Preparation

The recipe described in section 7.2 was successful in forming ice IV; its reproducibility however is unknown. In the short time available to explore this region of the phase diagram, three freezings were made at 5.0, 5.5 and 5.8 kbar. At 5.0 kbar, a cooling rate of 6 Khr^{-1} led to the formation of ice V. At 5.5 kbar, a cooling rate less than 3 Khr^{-1} led to the formation of a new ice structure, labelled the "blue phase." Subsequent work has shown that a cooling rate of 6 Khr^{-1} at this pressure results in the formation of ice V rather than the blue phase. In comparison, the cooling rate used in the formation of ice IV was quick, 18 Khr^{-1}. Unfortunately, this is the only time freezing under 5.8 kbar was attempted. It is not, therefore, known whether a high pressure or a fast rate of cooling was the most important factor for the formation of ice IV. However, earlier experiments in which the liquid was frozen at pressures less than 5.5 kbar with variable cooling rates would suggest the former.

Engelhardt and Whalley [43] found that the sample size was important for the successful formation of ice IV. Samples in the range 0.8–1.5 ml failed to form ice IV after some sixty attempts. A more successful rate of one in ten was found for samples of only 0.2 ml. Engelhardt and Whalley believe this is because large samples "are not able to supercool enough." Exactly what is meant by this phrase is unknown. Perhaps the use of a constant cooling rate resulted in temperature gradients across their samples. A large sample cooled at a constant rate may drop into the formation region of ice V before ice IV had a chance to form. Such a finding would be dependent on sample geometry and could easily be resolved by halting the cooling process, a procedure which was found necessary in this work for the formation of the blue phase.

The use of small samples for study with neutron diffraction, however, is impractical. Samples were therefore prepared from 1.5 ml of D_2O, though fortunately the problems found by Engelhardt and Whalley for large samples were not encountered.

7.4.2 Additional phase

Refinement of the data clearly indicates the structure proposed by Engelhardt and Kamb [46] is correct. Other features in the data, which cannot be attributed to any phase of ice or clathrate, were also observed in the ice V data and are not therefore an indication of an incorrect structure.

The origin of this unidentified phase is unknown. The phase content increased in the ice V data as the temperature was brought closer to the melting curve. This would suggest some form of argon hydrate. However, any solid-solid transition would benefit from the additional mobility of the water molecules by temperature increase. Another possibility is a new form of ice which is the more stable phase under these conditions of pressure and temperature. Ices IV and V may be easier to nucleate and with time transform to the more stable form. However, I do not know of any ice transition that once initiated does not occur with great speed at these temperatures. The case for an argon hydrate compound would therefore seem the more valid.

The reflections from the phase, highlighted in figure 97, can be fitted to a cubic cell of unit length 9.72 Å. The highest symmetry to meet these reflection conditions is $Pn\bar{3}m$.

7.4.3 The ice IV structure

The structure proposed by Engelhardt and Kamb [46] is confirmed by this work. Although their data were collected on samples recovered to ambient pressure at 110 K,

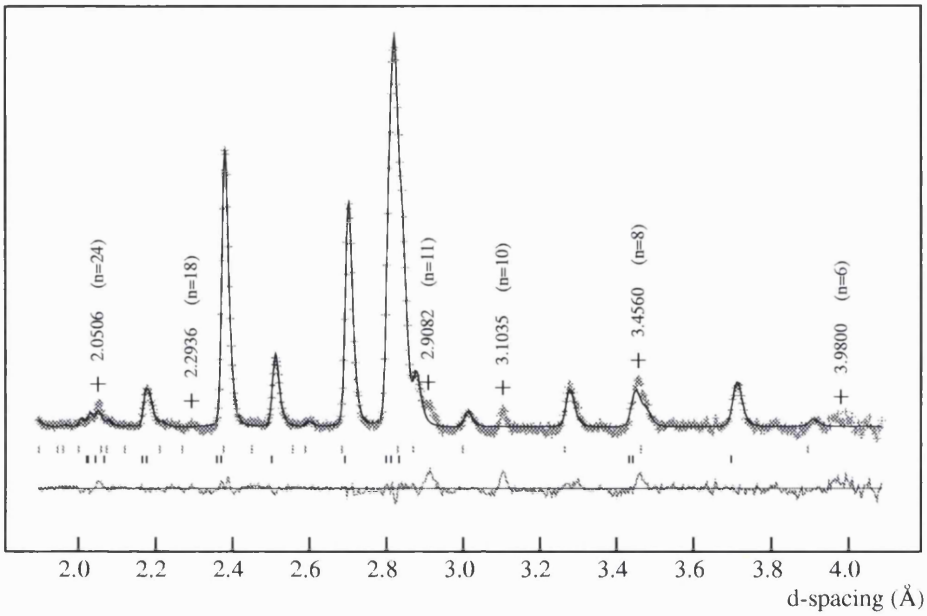

Figure 97: Reflections attributed to an unidentified phase
The reflections $n = h^2 + k^2 + l^2$ have been indexed for a cubic cell of length 9.72 Å.

there appears little difference in the structure at high temperature and pressure.

A general description of the structure of ice IV is given in section 7.1. In short, water molecules of type O(2) form planes of hexagonal rings, figure 86. Each hexagonal ring within a plane bonds to the nearest rings in the planes immediately above and below, figure 87. Water molecules of type O(1) then sit immediately above and below the centre of these rings. These then serve to bond each plane to the second nearest plane.

7.4.4 The O–O distances

Inspection of the O–O bond lengths, table 45, reveals two very large distances. As proposed by Engelhardt and Kamb [46], who found similar if somewhat shorter distances, the long O–O bond lengths must be a consequence of intermolecular repulsion

from non-bonded molecules. There are three particularly short non-bonded O···O distances, table 45 and figure 95. Two of these involve interactions between the water molecules which form the hexagonal rings and the water molecules which sit directly above and below. As a consequence of the short, non-bonded distances, the water molecules above and below each ring are repelled causing the bond which passes through the ring, O(1)–O(1′), to increase in length, figure 98.

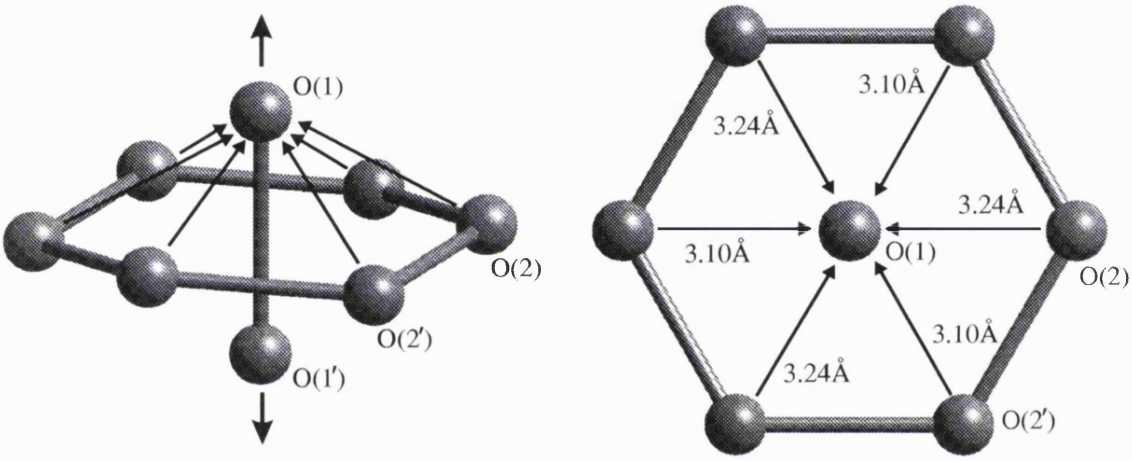

Figure 98: Water molecules which form the hexagonal rings repel the water molecules which sit directly above and below the centre of the ring. This causes the bond which passes through the rings, O(1)–O(1′), to increase in length.

The shortest non-bonded distances, however, are those between neighbouring planes. Each hexagonal ring within a plane bonds to six other rings, three in the plane above and three in the plane below. For each of the six rings that a particular ring bonds to, there is a short non-bonded distance between water molecules, figure 99. This short, non-bonded distance forces the planes further apart, causing the bond between neighbouring rings, O(1)–O($2'^{v}$), to increase, figure 99.

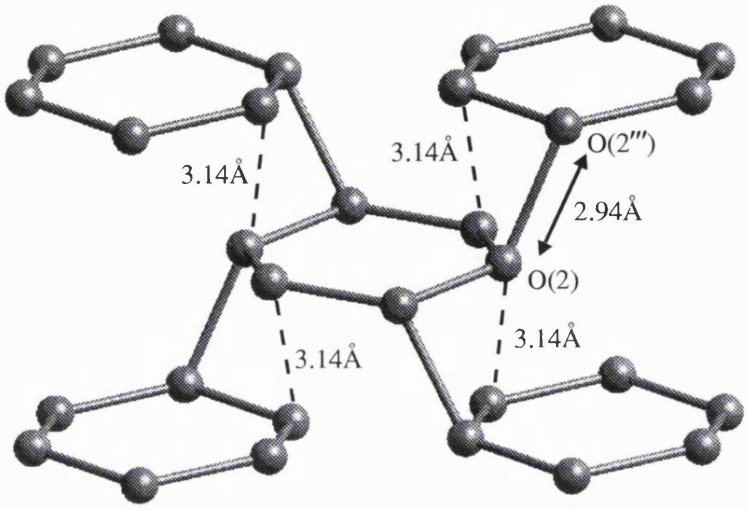

Figure 99: Each hexagonal ring bonds to six other hexagonal rings, three in the plane above and three in the plane below; only four of the rings are shown for clarity. For each of the six rings that a particular ring bonds to, there is a short non-bonded distance of 3.14 Å. The repulsion that arises, forces apart the planes resulting in a long O(2)–O(2‴).

7.4.5 The O–D distances

The O–D distances, table 44, although very different from the vapour value of 0.97 Å, are as expected for an ice in which the water molecules are orientationally, and therefore positionally, disordered (see sections 5.4.4 and 5.4.5).

Water molecules of type O(1) are situated on the $\bar{3}$ axis. Both O(1) and D(3) are therefore constrained to move along this axis only. In addition, an inversion at the centre of the hexagonal rings means the water molecule must bond with its symmetrical equivalent via D(3), figure 100. In the space-time averaged structure, there are two water molecules above and below the centre of each ring. The two are equidistant from the ring and consist of one oxygen atom and four deuterium atoms, each with a 50% probability of occupancy, figure 100. However, in real space and time, the two water molecules each consist of one oxygen atom and two deuterium

atoms, all of which are 100% populated. In addition, the bond which passes through the centre of the hexagonal ring must satisfy the Bernal-Fowler rules. Therefore, one, and only one, deuterium atom must sit along the $\bar{3}$ axis, figure 100.

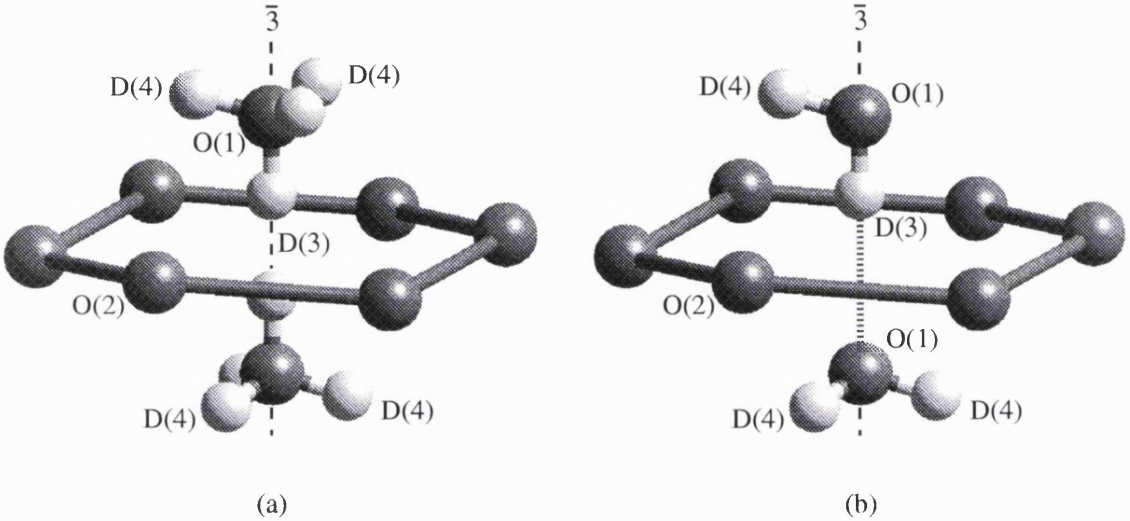

Figure 100: (a) The space-time average structure with each water molecule consisting of one oxygen and four deuterium atoms, each deuterium site being 50% populated. (b) The true local structure with each water molecule consisting of one oxygen and two deuterium atoms, both of which are 100% populated. The deuterium atoms of the hexagonal ring have been omitted for clarity.

The two water molecules experience interatomic repulsion from the hexagonal ring. However, the water molecule with the deuterium atom directed towards the ring will experience greater repulsion. The two water molecules are therefore no longer equidistant from the ring. The net result is shown in figure 101. The positions determined by crystallography are the average of the two water molecule positions and results in shorter bond lengths for both O(1)–D(3) and O(1)–D(4). A difference in position of 0.074 Å for the two water molecule orientations would result in an O(1)–D(3) bond length of 0.933 Å and an O(1)–D(4) bond length of 0.962 Å. The bond lengths determined in this work are 0.933(9) and 0.963(8) Å respectively, table 44.

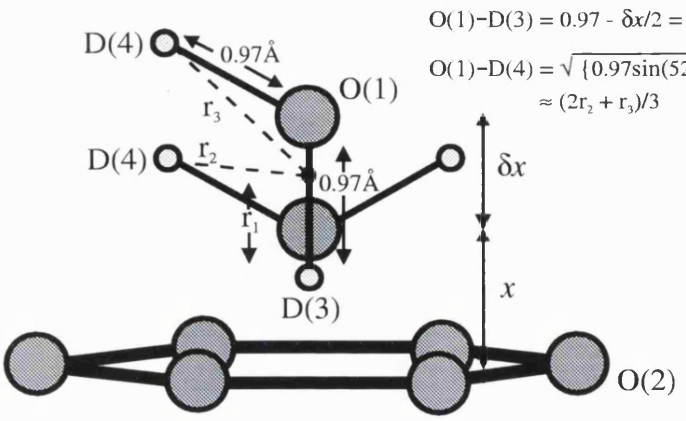

Figure 101: The figure shows a water molecule of type O(1) situated above the hexagonal ring. There are two orientations shown. In the first, the water molecule is oriented such that both deuterium atoms are directed away from the ring. The water molecule experiences interatomic repulsion from the water molecules which form the hexagonal ring, and sits at a distance x from the centre. In the second, the water molecule is oriented such that one of the deuterium atoms is directed towards the hexagonal ring. The interatomic repulsion experienced is greater and the water molecule is repelled further from the centre of the ring, $x + \delta x$. The average of the two orientations, as determined by crystallography, results in both a short O(1)–D(3) and O(1)–D(4) bond length. The black dot represents the mean position of the oxygen atom O(1). With $\delta x = 0.074$ Å, O(1)–D(3) = 0.933 Å and O(1)–D(4) = 0.962 Å.

Other sources may also be responsible for the short O(1)–D(3) and O(1)–D(4) bond lengths. For example, O(1) is constrained to move along the $\bar{3}$ axis only. Locally, however, the oxygen is not so heavily constrained and additional differences in bond lengths may arise from its shift from this axis. Unfortunately, such information cannot be gained from crystallography alone and requires the use of an a complementary technique which can probe the local environment, e.g. diffuse scattering.

Water molecules of type O(2), which form the hexagonal rings, exhibit short and long O–D bond lengths, table 44. The long O(2)–D(8) bond, 0.99 Å, most probably arises from the long O(2)–O(2) bond, responsible for binding each hexagonal ring to six neighbouring rings, figure 95. The length of the O(2)–O(2) bond, along which the

deuterium atom D(8) is located, will cause the water molecule to be pulled from the hexagonal ring to reduce the amount of bond stretching, figure 102. Since the water molecule must bond to planes both above and below, the net result is a O(2)–D(8) bond length greater than 0.97 Å, figure 102.

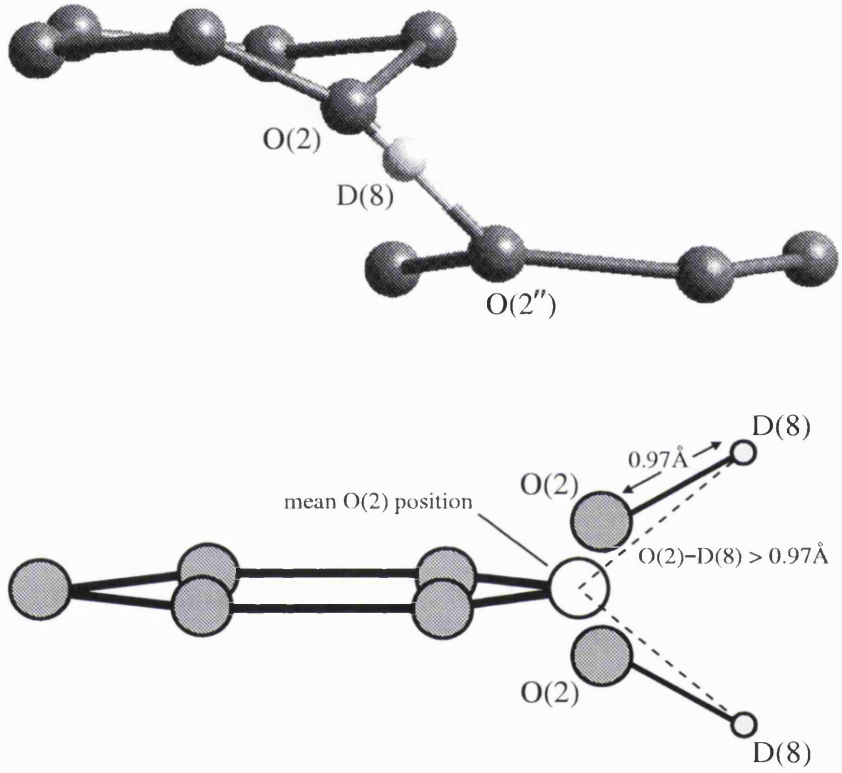

Figure 102: The long O(2)–O(2″) bond, which binds each hexagonal ring to six neighbouring rings, causes the water molecule to be pulled from the hexagonal plane (top). Since each hexagonal ring bonds to three rings in the above plane and three below, the water molecule responsible for binding the rings is displaced in both directions. The mean O(2) position is therefore in the plane of the ring, resulting in an artificially long O(2)–D(8) bond length (bottom).

The factors responsible for the short O(2)–D(5), O(2)–D(6) and O(2)–D(7) are unknown. However, the positional disorder responsible for the long O(2)–D(8) will

be a contributing factor. In addition, the water molecules will move to better accommodate the O–O(2)–O bond angles and therefore alleviate strain on the hydrogen bonds. For example, the hexagonal rings are approximately flat, with an average internal bond angle around the ring, O(2″)–O(2)–O(2′), of 119.1°, table 46. To alleviate strain on the hydrogen bonds the water molecules most probably pucker such that the O–O(2)–O bond angle approaches 104.5°. This will result in positional disorder since the direction of pucker for a particular water molecule will vary depending on the orientation it adopts.

7.4.6 The bond angles

The variation in D–O–D bond angles from the vapour value of 104.5°, table 46, is simply a further indication of local disorder. In particular, the bond angles involving D(8) deviate markedly from 104.5° and must arise from the disordered position of D(8) discussed in the previous section.

Of greater interest are the O–O–O bond angles which provide an indication of the hydrogen-bond bending. The degree of bond bending that occurs in ice IV is smaller than that found for ices V and the newly found "blue phase", table 47, all of which exist within the same region of the ice phase diagram. Although the degree of bond

	$\rho(\mathrm{gcm}^{-3})$	$<(\delta\theta)^2>^{1/2}$
Blue phase	1.4365(1)	18.87
Ice IV	1.4357(1)	15.06
Ice V	1.4021(1)	18.54

Table 47: The density and bond bending found for ices IV, V and the blue phase at 5.0 kbar and 260 K. $<(\delta\theta)^2>^{1/2}$ is the r.m.s. of O–O–O bond angle deviations from the ideal tetrahedral angle of 109.5°.

bending in ice IV is smaller than that of ice V, an increase in density is achieved by virtue of the interpenetrating bond and shorter non-bonded contacts which result.

7.4.7 Orientational disorder

The change in entropy measured by Bridgman [30] for the ice IV–VI transition was small, implying no change in configurational entropy across the transition, i.e. since ice VI is orientationally disordered, so must be ice IV. The broad stretching and rotational bands in the infrared spectra were interpreted as further evidence for orientational disorder. Although Engelhardt and Kamb [46] used X-ray diffraction, which is insensitive to small variations in the occupation of the hydrogen atoms, they found no violations of symmetry to suggest ice IV was ordered. The results of this work confirm that ice IV is disordered at high temperatures. No violations of symmetry were observed and when refined the deuterium atom populations did not differ from the fully disordered values of 50%.

Engelhardt and Kamb [46] suggested complete disorder was probably due to the lack of variation in the O–O–O bond angles. They found all the O–O–O bond angles, although very different, to deviate from 104.5° by similar amounts. There were therefore no favourable or particularly unfavourable orientations which might promote ordering.

The O–O–O bond angles found in this work, table 46, are comparable with those found for orientationally ordered ice II, table 11. The suggestion made by Engelhardt and Kamb does not, therefore, make immediate sense. However, as is demonstrated by example below, their suggestion is correct, but it forms only part of the explanation as to why the water molecules are orientationally disordered. More important is the high degree of local symmetry possessed by the structure, such that orientations which

might prove favourable cannot occur throughout the structure entirely.

Water molecules of type O(1) can adopt one of six possible orientations. Three of these involve the water molecule pointing away from the centre of the hexagonal ring, and three pointing towards the ring, figure 100. If the water molecule points away from the ring, then the deuterium atoms are donated to two, out of a possible three, hexagonal rings. It does not matter to which two rings the atoms are donated since all rings, and therefore the three available O–O–O bond angles, are equivalent. The water molecule therefore adopts all three orientations with equal probability. Similarly, if the water molecule points towards the ring, one deuterium atom is donated through the ring, and the other is donated to one of three rings. Again, all three rings are equivalent and the three orientations occur with equal probability.

Disorder arises because the O–O–O bond angles for the different orientations are identical. It therefore makes no difference, energetically, which orientation the water molecule adopts, and as a result, all are occupied equally.

This statement, however, is not entirely correct. The water molecule has six possible orientations: three involve the deuterium atoms pointing away from the ring and have the same $O(2'^{v})$–O(1)–$O(2^{v})$ bond angle, and three involve one deuterium pointing towards the ring and have the same O(1′)–O(1)–$O(2'^{v})$ bond angle. The two O–O–O bond angles, however, are different, table 46. It is therefore possible that of the six orientations available, the water molecule prefers the three which involve one deuterium atom pointing towards the hexagonal ring. However, there is a water molecule on the opposite side of the ring which is essentially its mirror. It too will wish to point towards the hexagonal ring, yet only one deuterium is permitted per O–O bond. Only one of the water molecules can, therefore, direct a deuterium at the ring. Sometimes it will be the water molecule above the ring and other times

it will be the one below. Even though the water molecule may find pointing at the ring preferential, it can only achieve this 50% of the time. In this sense, it is the high degree of local symmetry possessed by the structure that is responsible for the orientational disorder.

A similar situation is found for water molecules of type O(2). Although different O–O(2)–O bond angles exist, table 46, the symmetry of the structure is such that a favourable orientation can not occur throughout.

Orientational disorder at low temperatures, though not probed by this work, seems likely. As the temperature decreases, the average energy of the water molecules decreases. The water molecules then begin to adopt the orientations of lowest energy. However, in ice IV, either the orientations are of similar energies, or favourable orientations can not occur throughout the structure because of its symmetrical nature. For the same reasons as described above, the orientations of the water molecules at low temperatures are disordered.

This situation is similar to that which occurs for ices Ih and Ic, the only other ice structures to remain disordered at low temperatures. The O–O–O bond angles in ices Ih and Ic are all 109°. All orientations are therefore energetically identical and the water molecules fail to order.

X-ray diffraction [46] and infrared spectroscopy [44] failed to find any evidence of orientational order in samples recovered to ambient pressure at 110 K. The samples were quenched at a rate of 60 $Kmin^{-1}$. The relaxation times for water molecules in ice are typically 1 second at 170 K and 1 minute at 160 K. This would suggest that the water molecules were "frozen-in" at a temperature between 165 and 160 K. Ice IV is therefore orientationally disordered at all temperatures above 160 K.

7.4.8 Metastability

The difference in Gibbs free energy for two systems at constant temperature and pressure is defined by:

$$\Delta G = \Delta E + p\Delta V - T\Delta S \tag{19}$$

where ΔG is the difference in Gibbs free energy at a particular pressure and temperature; ΔE, the difference in internal energy; ΔV, the difference in volume; and ΔS, the difference in entropy.

It may seem surprising, therefore, to find that ice IV is metastable with respect to ice V, yet has a smaller amount of bond bending (lower internal energy) and a higher density (smaller volume), table 47. However, the internal energy of ice IV, with respect to ice V, is increased by additional bond stretching, as evidenced by the two long O–O distances, and by an increase in non-bonded interactions, as evidenced by the short O$\cdots$O distances, table 45. Furthermore, ice V is partially ordered and consequently the O–O–O bond angles with highest bond strain are less occupied, i.e. the amount of bond bending is not as great as that in table 47.

The difference in the Gibbs free energy between ice V and ice IV, as estimated by Engelhardt and Kamb [46], is 95 $Jmol^{-1}$ near 5 kbar and 262 K. This is, as expected, a small figure since if the difference in free energy were much larger, ice IV would immediately transform to ice V and would not be observed as a metastable phase.

Since ice IV is orientationally disordered, and ice V partially ordered as listed in table 31, the difference in configurational entropy is approximately -27 $JK^{-1}mol^{-1}$. The figure is negative and will therefore decrease the difference in free energy. Had ice V been fully disordered, then the difference in free energy would been increased by 27 $Jmol^{-1}$ and might be enough to prevent the formation of ice IV. The existence of metastable phases within the stability region of ice V might therefore be due, in

part, to the partial ordering of water molecules within ice V.

7.4.9 Compressibility

Since data were recorded at several different pressures, a physically more correct model of the compressibility can be obtained, c.f. the linearity assumed for ices II, III and V. Using the universal equation-of-state (EOS) of Vinet *et al.* [122], the variation in volume with pressure is given by:

$$p = 3B_0 x^{-2}(1-x)\exp\left[\frac{3}{2}(B_0' - 1)(1-x)\right] \tag{20}$$

where

$$x = \left(\frac{V}{V_0}\right)^{1/3} \tag{21}$$

and B_0 and B_0' are the bulk modulus and its derivative at zero pressure.

Another commonly used EOS is the Birch-Murnaghan EOS [123], given by:

$$p = \frac{3}{2}B_0 x^{-5}(1-x^{-2})\left[\frac{3}{4}(B_0' - 4)(1-x^{-2}) - 1\right] \tag{22}$$

The EOSs were then fit to the pressure-volume data, figure 103, by least-squares, with the parameters listed in table 48.

	Vinet *et al.*	Birch-Murnaghan
V_0	1160(31)	1160(37)
B_0	90(131)	90(158)
B_0'	11(32)	12(48)

Table 48: The EOS parameters derived from a least-squares fit of the pressure-volume data, figure 103.

The errors associated with the parameters are large and arise from the small number of points spanning a particular small area of parameter space. In comparison,

the EOS for ice VII [124,125] has been determined with parameter errors of around 2%. However, a large number of data points were collected over the large pressure range 50 to 1000 kbar. Furthermore, one of the parameters, B_0 or V_0, was fixed according to estimates based on other work. The fixing of a parameter is particular important in achieving small errors, as demonstrated in table 49 in which V_0 was fixed at 1160 Å^3.

	Vinet *et al.*	Birch-Murnaghan
V_0	1160	1160
B_0	89.4(1.8)	88.6(2.0)
B_0'	11.4(1.0)	12.2(1.3)

Table 49: The EOS parameters derived from a least-squares fit of the pressure-volume data, figure 103, with V_0 fixed at 1160 Å^3.

Using a linear relationship to describe the pressure-volume data, the bulk modulus of ice IV over the pressure range 4.2–5.05 kbar at 260 K is 143(2) kbar, equation 12. At 4.6 kbar and 260 K, the bulk moduli using the Vinet *et al.* and Birch-Murnaghan EOSs, with the parameters listed in table 49, are 142(5) and 145(6) kbar respectively.

A similar description can be used for the individual lattice constants a_H and c_H, with $x = a/a_0$ and $x = c/c_0$. However, with the errors involved, a description of this nature seems meaningless and the compressibilities were therefore estimated using a linear approximation. Again using least-squares, the compressibilities in the a_H- and c_H-axis directions are 2.75(7) and 1.62(7) Mbar^{-1} respectively.

It is not surprising to find a change in the c_H/a_H ratio with pressure changes since the structure along the two axes is very different. While compression in the a_H direction involves squashing the hexagonal rings within a plane, compression in the c_H direction involves collapsing the planes together. With the compressibility in the

c_H-axis direction smaller than that in the a_H-axis direction, collapsing of the planes appears more difficult. This is almost certainly due to the interatomic repulsion, figures 98 and 99, which must be overcome by compressing in this direction.

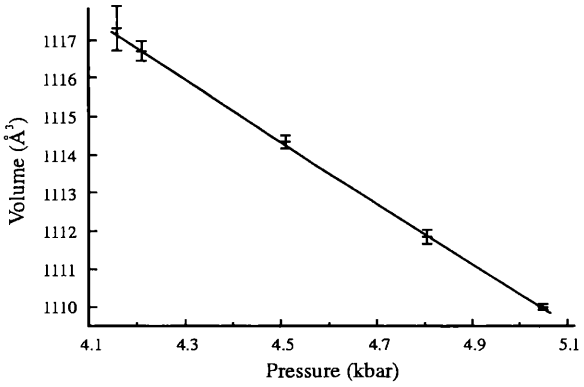

Figure 103: The variation in volume of ice IV with pressure at 260 K. The line represents a least-squares fit to a Vinet *et al.* EOS, table 48. The errors on each point represent two e.s.ds.

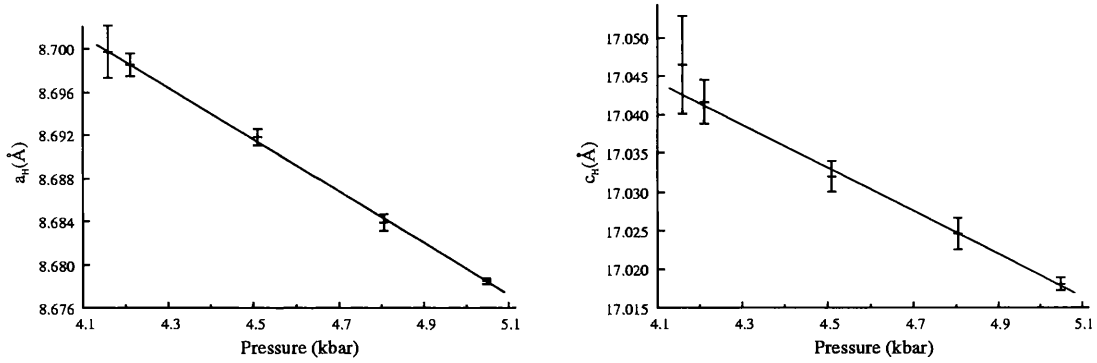

Figure 104: The variation in ice IV lattice constants, a_H and c_H, with pressure at 260 K. The line represents a linear least-squares fit. The errors on each point represent two e.s.ds.

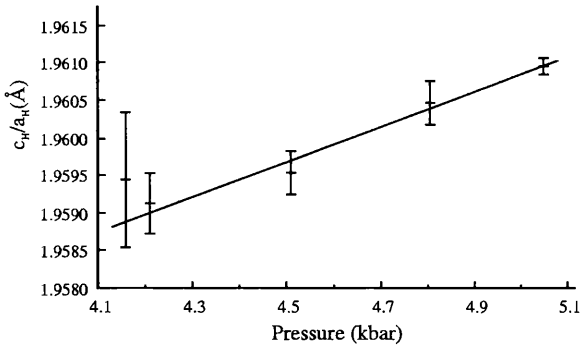

Figure 105: The variation in the ice IV lattice constant ratio, c_H/a_H, with pressure at 260 K. The line represents a linear least-squares fit. The errors on each point represent two e.s.ds.

7.4.10 The melting curve

This work found D_2O ice IV in equilibrium with the liquid at 4.16 kbar and 260 K. This is very different to the liquid–IV equilibrium curve determined by Engelhardt and Whalley [43], figure 106. At 260 K, D_2O ice IV is expected to melt at 4.50 kbar. Organic nucleants may be responsible for influencing phase stability, thereby creating artificial melting curves. Unfortunately, the work of both Bridgman [30] and Nishibata [45] predict a melting pressure of 4.6 kbar at 260 K. The cause of this discrepancy is unknown.

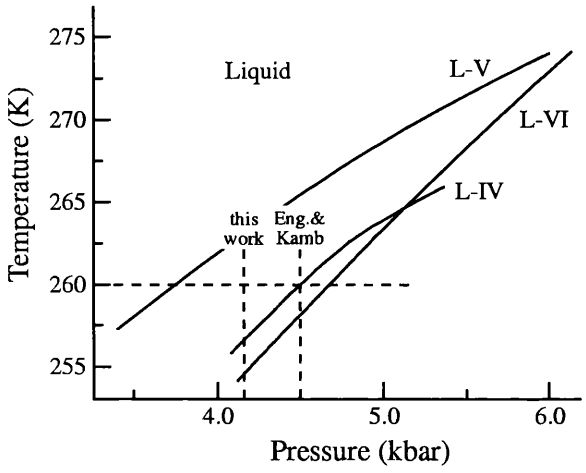

Figure 106: The D_2O ice melting curves determined by Engelhardt and Whalley [43]. At 260 K, Engelhardt and Whalley found ice IV to melt at 4.5 kbar, while this work found ice IV to melt at 4.16 kbar.

There were no indications to suggest that the ice and liquid were not in equilibrium at 4.16 kbar and 260 K. When the pressure was decreased to 3.9 kbar, the ice began to melt and the pressure rose quickly to 4.10 kbar. After a few minutes, the increase in pressure slowly came to a stop at 4.16 kbar. After an hour, the pressure failed to change and was again decreased to 4.0 kbar. After a several minutes, the pressure rose again to 4.16 kbar. From these observations, it appeared that pressure equilibration had been reached.

There is nothing in literature to suggest that the ice IV structure formed by

Bridgman [30] and Nishibata [45] is the same as that formed by Engelhardt and Whalley [43]. This statement is particularly important in view of the new ice structures that have been observed in this region of the phase diagram, chapters 8 and 9. Perhaps then, the melting curve determined by Engelhardt and Whalley is influenced by the use of nucleants, while the melting curve determined by Nishibata and Bridgman is for another ice structure. However, with the location of the ice IV melting curve determined by Engelhardt and Whalley in good agreement with those found by Bridgman and Nishibata, such a hypothesis, although possible, seems unlikely.

7.5 Conclusions

Engelhardt and Kamb [46] proposed the structure of ice IV based on samples quenched to 110 K and recovered to ambient pressure. Furthermore, the samples on which the diffraction data were collected were formed with the use of organic nucleants. This work confirms for the first time that the structure formed at high temperature and pressure, and without the use of nucleants, is the same.

The density of ice IV is greater than that of ice V, yet has a smaller amount of hydrogen-bond bending. This is achieved through a form of interpenetration, in which a hydrogen bond passes through a hexagonal ring of water molecules. The short, non-bonded interactions that arise from the interpenetration cause the water molecules which sit directly above and below the centre of the ring to be repelled. This in turn leads to the longest O–O bond length found in any ice structure.

Although the degree of bond bending in ice IV is smaller than that for ice V, the internal energy is actually increased. This is brought about by an increase in bond stretching and an increase in non-bonded interactions. The increase in internal energy

is offset by a higher density such that the difference in Gibbs free energy between ices IV and V is small.

The water molecules in ice IV are orientationally disordered at high temperatures. The work by Engelhardt and Whalley [44], and Engelhardt and Kamb [46], found the same disorder at 110 K. Orientational disorder at this temperature is uncommon, with ices Ih and Ic the only other structures to exhibit such behaviour. There are two factors which appear to be responsible for the observed disorder. First, most of the orientations are energetically similar and therefore occur with equal probability. Second, the structure exhibits high local symmetry such that any orientations that might prove energetically favourable can not occur entirely throughout the structure.

The stability region of metastable ice IV is incomplete and the effect of organic nucleants on phase stability is unknown. The preparations used in this work were successful in the formation of ice IV without the use of such nucleants. Although the procedures have never been retried, this form of preparation may offer a reproducible way of forming uncontaminated ice IV.

It still remains uncertain whether the ice structure formed by Bridgman [30] and Nishibata [45], by releasing the pressure on ice VI, is the same as that formed by Engelhardt and Whalley [43], by freezing the liquid with the use of nucleants. With the finding of new ice structures in this region of the phase diagram, further work is needed to address this question. Since the path followed by Engelhardt and Whalley was employed in this work, diffraction experiments following the path of Bridgman and Nishibata are needed. This should be possible with X-rays or neutrons, and anvil cells.

Chapter 8

The yellow phase

8.1 Introduction

During experiments in which liquid water was frozen under pressures in excess of 5 kbar, two unidentified phases were formed. The first, labelled the "yellow" phase, has subsequently never been found even upon following the same experimental conditions. However, in searching for the yellow phase a further new phase was formed, labelled the "blue" phase. This is discussed in chapter 9.

The possible existence of other forms of ice within stability region of ice V does not appear to be new. Engelhardt and Whalley [43] during their work on ice IV found evidence for the existence of other metastable phases. Unfortunately, the phases proved very difficult to form and could not be retained sufficiently long for useful study.

8.2 Experimental procedure

The yellow phase was prepared only once during an experiment on the IRIS diffractometer. A TiZr gas pressure cell was loosely filled with silica wool into which ~1.5 ml of D_2O was distributed by use of a syringe and needle. Argon pressure was increased to 5.5 kbar at room temperature and the cell lowered into a cryostat located on the diffractometer. The temperature was then decreased at a rate of 10 Khr^{-1}. At 263 K, a liquid–solid transition occurred, immediately identified by a drop in pressure from 5.4 to 4.6 kbar. Inspection of the diffraction profiles revealed reflections which could not be identified as any known phase of ice or argon clathrate. Data were subsequently collected, over a period of 11 hours, at 4.57 kbar and 260 K. Afterwards, the pressure was decreased to 4.3 kbar without any change of phase, and then, accidentally, to 3.0 kbar which caused the sample to melt. Recovery of the phase proved unsuccessful.

8.3 Indexing

The formation of the yellow phase was accomplished only once with data collected in the range 1 to 11 Å, figure 107. Only eight reflections in this range makes the task of indexing difficult and inconclusive. Yet the fact that only eight reflections were observed, all of which were strong compared to the reflections observed later for ices III and V, suggests that the structure formed was simple. Considering then only cubic systems, the reflections can be indexed by a cell of length 10.82 Å, with the corresponding hkl values listed in table 50. The highest symmetry space group to meet these reflection conditions is $Ia\bar{3}d$.

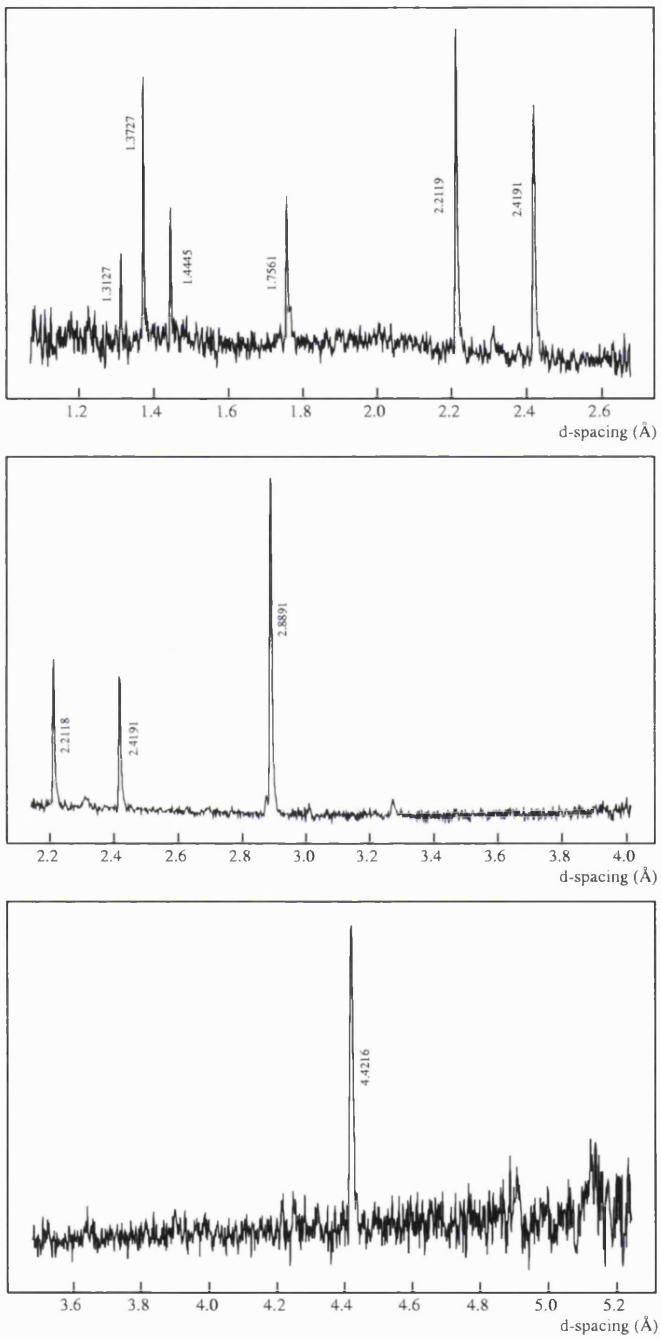

Figure 107: Raw data profiles of the yellow phase at 4.57 kbar and 260 K collected on IRIS. Only reflections attributed to the yellow phase are indexed, other non-indexed reflections can be attributed to the pressure cell and argon clathrate. No reflections, which could be attributed to the yellow phase, were observed at d-spacings greater than 4.6 Å.

d-spacing (Å)		$h^2 + k^2 + l^2$
observed	calculated	
4.4216	4.4172	6
2.8891	2.8918	14
2.4191	2.4194	20
2.2118	2.2086	24
1.7561	1.7552	38
1.4445	1.4459	56
1.3727	1.3741	62
1.3127	1.3121	68

The sole occurrence of reflections with h=k=l=$2n$ suggests a body centred structure.

Table 50: Assignment of reflections corresponding to a cubic cell of length 10.82 Å.

8.4 Density

Unfortunately, the density of the sample cannot be estimated reliably from the experiment. After data collection, the pressure was released, resulting in the unfortunate loss of the phase: there were no transitions to other forms of ice of know density, and although a pressure drop upon formation of the phase was recorded, indicative of a volume change, no other ice phase was formed following the same route which could be used as a reference. Using the cell length of 10.82 Å and the densities of other ices under similar conditions of pressure and temperature, the expected number of water molecules per unit cell for each corresponding density are listed in table 51.

Ice V		Ice IV	Blue Phase
4.0 kbar 254 K	5.0 kbar 254 K	4.5 kbar 260 K	5.0 kbar 260 K
53.14	53.55	54.39	54.69

Table 51: Number of water molecules per unit cell if the yellow phase has a density similar to that of ices IV, V and the blue phase. The densities were determined from data collected in this work.

8.5 Structure determination

For the space group $Ia\bar{3}d$, site multiplicity makes it impossible to arrange 54 water molecules within the unit cell; however, the symmetry does permit 56. Unfortunately, every configuration tried led to unphysical O–O bond distances and angles. The next nearest number of water molecules permitted are 48 and 64 which again could not be arranged to make physical sense.

The next space group to best meet the reflections conditions is $I\bar{4}3d$. The multiplicity of this space group allows the arrangement of 48, 52 and 60 water molecules within the unit cell, all of which were tried without success.

At this stage, attempts to identify the structure were abandoned. With an uncertain indexing scheme, space group and density, further efforts seemed pointless.

8.6 Conclusions

The structure of the yellow phase remains undetermined. Whether the phase is a form of ice or argon hydrate is similarly unknown. The drop in pressure due to formation is of the order of that observed for ices IV and the blue phase, sections 7.2 and 9.2. For the ices, the drop in pressure arises from a decrease in sample volume, the ice being more dense than the liquid. However, a drop in pressure would also be expected for an argon compound which consumes gas during formation yet has a comparable, or even lower, density than that of the liquid. Nevertheless, it is doubtful that the phase is a form of argon clathrate. Clathrate-like structures form slowly, often taking days or weeks for complete formation. The liquid–solid transition, however, occurred over a period of seconds.

Further experiments following the same recipe have proven fruitless. Other than

continued trial and error, perhaps with the use of organic nucleants as described by Evans [42], nothing can be suggested as a possible approach for the successful formation of the yellow phase.

Further efforts at solving the structure with the data already collected are possible, although difficult. The indexing scheme is uncertain, only cubic symmetry was attempted, and the density is unknown. Even assuming the unit cell dimensions are correct and the number of water molecules per unit cell lie in the range 52–56, the possibilities of arranging the water molecules under all the cubic space groups are enormous.

A rather more shrewd approach would be to tackle the problem with some form of computer algorithm. Its task: to arrange 54 water molecules in a box of length 10.82 Å such that an ice structure, with physical bond distances and angles, is formed. There are many restraints that could be imposed on such a system to help find the solution. It is uncertain whether such an approach would be successful, but with more time it would have been an interesting idea to pursue.

Chapter 9

The blue phase

9.1 Introduction

In attempting to reproduce the yellow phase, chapter 8, a further unidentified phase was formed. Unlike the yellow phase, the phase proved to be reproducible and data sufficient for structure determination were collected. The phase is a new form of ice, topologically different to all other known water structures. It appears to exist within the established stability region of ice V making it the second metastable phase to be found in this region of the ice phase diagram.

9.2 Experimental procedure

TEB

The blue phase was first formed during an experiment on the TEB diffractometer. Primarily aimed at forming the yellow phase, a rather complicated route was followed that led to the eventual formation of the phase. As in the IRIS experiment, during

which the yellow phase was formed, the pressure cell was loaded with liquid D_2O and silica wool, the argon pressure increased to 5.5 kbar, and the whole assembly cooled at a rate of 10 Khr^{-1}. However, rather than forming the yellow phase, ice V formed at 262 K with a drop in pressure from 5.3 to 4.5 kbar. This unwanted phase was melted by releasing the pressure to 3 kbar, the release of pressure being much quicker in melting the sample than warming. However, problems with the compressor meant pressure increase could not be attempted until the following morning and the sample was left overnight under 3 kbar argon pressure and at 262 K. Once the compressor had been repaired the pressure was increased to 5.6 kbar and after an hour there was a transition to the blue phase. The pressure dropped from 5.6 to 5.1 kbar, and data were eventually collected at 5.1 kbar and 260 K. Unfortunately, this all happened towards the end of the beam time allocation and only 8 hours were spent on data collection. The quality of the data was sufficient for phase identification only.

PEARL

The experiment on PEARL was very similar to that carried out on TEB in that the work was of an exploratory nature. The hopes were that any of the phases: yellow, blue or ice IV, could be reproducibly formed for further study on another instrument. The experiment proved very successful with the formation of both the blue phase and ice IV. The conditions that led to the formation of ice IV are detailed in chapter 7. For the blue phase, liquid D_2O and silica wool were loaded into a TiZr gas pressure cell. Argon pressure was increased to 5.5 kbar and the assembly lowered into a cryostat at 270 K. Once at 270 K, the pressure, which had decreased due to cooling, was topped up to 5.5 kbar. The sample was then cooled at a rate of 2.5 Khr^{-1} with a phase transition at 261 K, noticeable by the sudden drop in pressure from 5.46 to

4.89 kbar. Inspection of the data revealed that the phase formed was the same as that formed on TEB, with the individual detectors indicating a good powder. Data were then collected, over a period of 11 hours, at 4.82 kbar and 261 K.

After data collection, the sample was cooled with a transition to ice V occurring in the temperature range 245–250 K. This transition, which resulted in a pressure increase from 4.65 to 4.81 kbar, provided an indication of the density for the blue phase which proved useful in later structure determination.

D2B

The data collected on PEARL were sufficient for initial structure solution. However, unrealistic thermal factors for the deuterium atoms cast some doubt on the detailed model. Further data were therefore collected on D2B which would provide better quality data on the short d-spacings necessary to determine accurate thermal factors. In addition, the use of a fixed-wavelength instrument would highlight any reflections at d-spacings not covered by PEARL (> 4 Å).

Liquid D_2O and silica wool were loaded into a TiZr cell and the argon pressure increased to 5.5 kbar at room temperature. The sample was cooled quickly to 270 K and the pressure topped up to 5.5 kbar. The sample was then cooled further at a rate of 2.5 Khr^{-1} from 270 to 260 K. Although the phase had not formed upon reaching 260 K, further cooling was abandoned for fear that lower temperatures may favour the formation of ice V. After a wait of 3 hours the blue phase finally formed. Data were then collected at 5.0 kbar and 260 K over six different omega positions, with a total of 12 hours data collection time.

HRPD

With the structure of the blue phase determined (PEARL) and confirmed (D2B), the time on HRPD was spent collecting data at various pressure and temperature conditions to obtain information on the compressibility and expansivity of the new phase. In addition, points on the melting curve of the blue phase were also recorded.

The preparation of the blue phase was similar to previous preparations: liquid D_2O and silica wool were loaded into a TiZr gas pressure cell, the argon pressure increased to 5.5 kbar at room temperature, the sample cooled quickly to 270 K, and the pressure topped back up to 5.5 kbar at 270 K. However, in an attempt to identify the importance of cooling rates for the successful formation of the blue phase, the first attempt continued by cooling from 270 K at a rate of 5 Khr^{-1}. This slightly faster rate of cooling led to the formation of ice V at 261 K. A new sample was prepared and cooled using the previously successful rate of 2.5 Khr^{-1}. Upon reaching 260 K, the blue phase had yet to form. After a period of two hours at this condition, the blue phase formed with a drop in pressure from 5.49 to 5.12 kbar. Data were then collected at the following points for lattice constants only: 5.5 kbar and 260 K, 5.4 kbar and 260 K, 5.3 kbar and 260 K, 5.2 kbar and 260 K, 5.1 kbar and 260 K, 5.0 kbar and 260 K, 5.0 kbar and 255 K, and 5.0 kbar and 264 K.

Afterwards, the sample was warmed gradually in an attempt to locate the melting curve. At $\sim$266 K, the sample began to melt, noticeable by changes in pressure. As the sample melted, the pressure increased due to changes in sample volume, the blue phase being more dense than the liquid. At 266.5 K, the pressure eventually equilibrated at 5.22 kbar. Data were then collected at this point on the liquid–blue curve; the pressures at the beginning and end of data collection were 5.200 and 5.215 kbar respectively. A further point on the melting curve was established, using

the same approach, at 265 K and 5.05 kbar. Unfortunately, there was insufficient time for further neutron data to be collected.

9.3 Structure solution

9.3.1 Indexing

The structure of the blue phase was solved from the data collected on PEARL. Although data had previously been collected on TEB, the quality was insufficient for structure solution, figure 108. The PEARL data spanned the range 0.8 to 4.1 Å, with reflections attributed to the blue phase listed in table 52. Using these reflections, many indexing schemes were suggested by the software routines: FZON [126], TREOR [127] and DICVOL [128]. However, among the various schemes being suggested, the lattice constant 8.33 Å was found to frequently occur. Working manually, this figure was kept fixed and the reflections indexed on the basis of a cubic, hexagonal and tetragonal cell. The most likely scheme was tetragonal with $a = 8.33$ and $c = 4.04$ Å, which also accounted for some smaller peaks which were omitted from the original indexing list. The reflections were then assigned their hkl values, table 52, with $I\bar{4}2d$ the highest symmetry space group to meet the reflection conditions.

9.3.2 Density

Once data on the blue phase had been collected, the sample was cooled with a transition to ice V observed at 4.65 kbar and 245 K. The increase in pressure resulting from the transition, 4.65 to 4.81 kbar, implied an increase in sample volume, and hence the density of ice V must be less than that of the blue phase. In addition, since the volume of liquid used for each sample was approximately the same, the density

d–spacing (Å)	*hkl*	d–spacing (Å)	*hkl*
2.945	2 2 0	1.429	4 1 2
2.739	2 1 1		5 3 0
2.635	3 1 0	1.408	3 3 2
2.289	3 0 1	1.370	6 1 0
2.085	4 0 0		4 2 2
2.008	3 2 1	1.271	5 1 2
1.819	2 0 2		2 1 3
1.604	3 1 2	1.017	5 5 2
1.449	4 0 2		7 1 2
			5 2 3

From the assignment of *hkl*'s, the following reflection conditions are observed:

$$hk0 \;:\; h + k = 2n$$
$$h0l \;:\; h + l = 2n$$

and possibly:

$$hh0 \;:\; h = 2n$$
$$hkl \;:\; h + k + l = 2n$$

Table 52: Assignment of reflections corresponding to a tetragonal cell, $a = 8.33$ and $c = 4.03$ Å.

can also be estimated from the abrupt drops in pressure associated with the sample freezing. For the blue phase the pressure dropped by 640 bar upon formation; for ice V the drop was only 370 bar; whilst a drop of 700 bar was recorded for ice IV. It would therefore appear that the density of the blue phase was greater than that of ice V and slightly less than, if not comparable to, that of ice IV. If the density of the blue phase were that of ice V then the unit cell would consist of 11.79 water molecules; a density equivalent to that of ice IV would result in 12.02 water molecules. A unit cell comprising twelve water molecules therefore seemed likely.

9.3.3 Structure determination

Fortunately, twelve water molecules per unit cell were permitted under the space group $I\bar{4}2d$ by occupying two of the four special positions: 4(0, 0, 0), 4(0, 0, 1/2), 8(x, 1/4, 1/8) and 8(0 0 z). All permutations of these sites were tried for all x and

z with only one configuration leading to a sensible structure. An oxygen atom at (0, 0, 0) and another at (3/8, 1/4, 1/8) resulted in a structure in which the O–O bond distances were in the range 2.77–2.89 Å, the O–O–O bond angles in the range 83.6–130.5°, and there were no O···O non-bonded distances less than 3.4 Å. The deuterium atoms were then placed along the O–O bonds at a distance of 0.97 Å from each oxygen.

9.4 Refinement

PEARL

The initial model used in the refinement, as determined in section 9.3.3, is detailed in table 53. The asymmetric unit comprises only five atoms, two oxygen and three deuterium. Orientational ordering of the water molecules is not permitted under the space group $I\bar{4}2d$; the occupancies of the deuterium atoms were therefore fixed at 50%.

	x	y	z	U_{iso}
O(1)	0	0	0	0.040
O(2)	0.37500	0.25	0.125	0.040
D(3)	0.04216	0.09054	-0.12138	0.050
D(4)	0.28855	0.25000	0.28629	0.050
D(5)	0.42236	0.33164	0.26592	0.050

Table 53: Initial model used in the refinement of the blue phase.

The argon clathrate that formed during data collection was modelled on the structure refined from neutron diffraction data collected at 4.8 kbar and 273 K [61]. The

amount of clathrate present was small and only the lattice constants were refined.

Although a sample collimator (section 3.5) was not used due to the slightly different geometry of PEARL, no reflections from the TiZr pressure cell were observed. The background, which was very high due to poor incident and scattered beam collimation, was modelled by a simple cosine Fourier series, section 3.6.6. The high background in turn resulted in artificially low R-factors (see section 2.7.1).

The structure was refined free of any O–D bond-length restraints and the thermal factors were refined isotropically. After refinement, small differences in the data profiles could be seen, figure 109. The thermal factors were then refined anisotropically with a much improved fit, figure 110. However, the resulting deuterium thermal factors were unrealistically high. It is uncertain whether this is due to poor data statistics at short d-spacings, figure 111, or a small amount of texture which had gone unnoticed through inspection of the individual detectors.

D2B

The D2B data were refined in a manner similar to that used in refining the PEARL data. The same initial models for the blue phase and argon clathrate were used. Again, no reflections from the TiZr cell were observed and hence no regions of data were excluded. A feature in the background at 38° could not be modelled mathematically and required a few fixed points. The structure was again refined free of any bond-length restraints with anisotropic thermal factors.

HRPD

The quality of the data was such that the atomic parameters could not be refined. The purpose of the HRPD experiment was to obtain lattice constant information only.

The positional model used in refining the data was that obtained from the refinement of the D2B data, table 55.

9.5 Results

The profile fits from the refinement of the various data sets are shown in figures 108 to 115. All data on HRPD were collected over the same period of time, hence the difference profiles for the different data sets were all very similar. Only two of the nine HRPD data sets are therefore shown.

The lattice constants are listed in table 54. There is a small difference in lattice constants for data collected on different instruments. Only during the D2B experiment were silicon data collected for instrument calibration. Although the HRPD instrument parameters should not have changed since previous experiments, the poor data quality meant it was impossible to fully refine the profile parameters. Differences in lattice constants can be attributed to subtle changes in the profile parameters for these data.

The atomic positions and thermal factors resulting from the refinement of data collected on PEARL and D2B are listed in tables 55 and 56. With doubts surrounding the quality of the PEARL data, section 9.4, only the D2B data were used to determine the bond lengths and angles, tables 57 to 59.

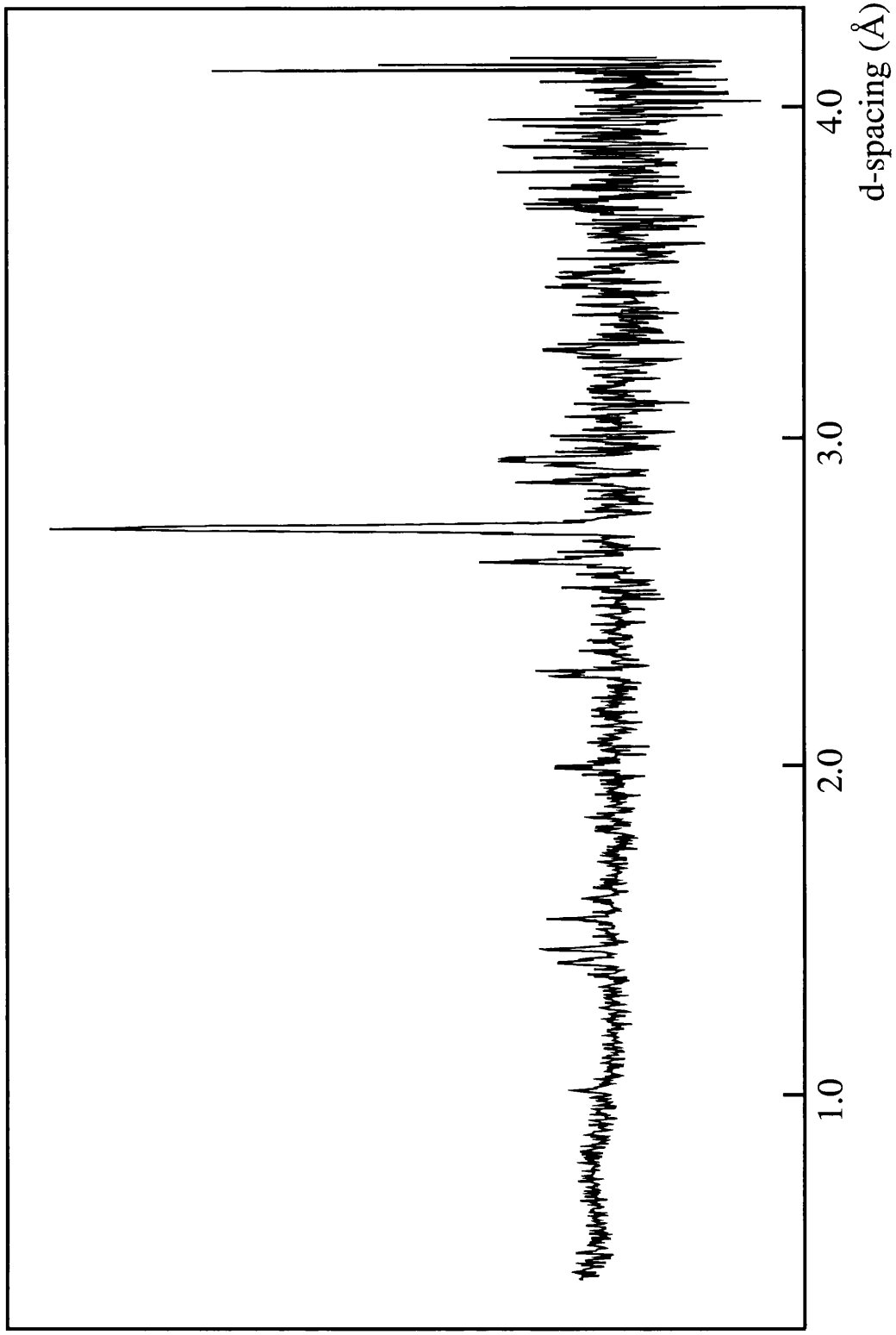

Figure 108: The raw profile of the blue phase data collected on TEB at 5.1 kbar and 260 K.

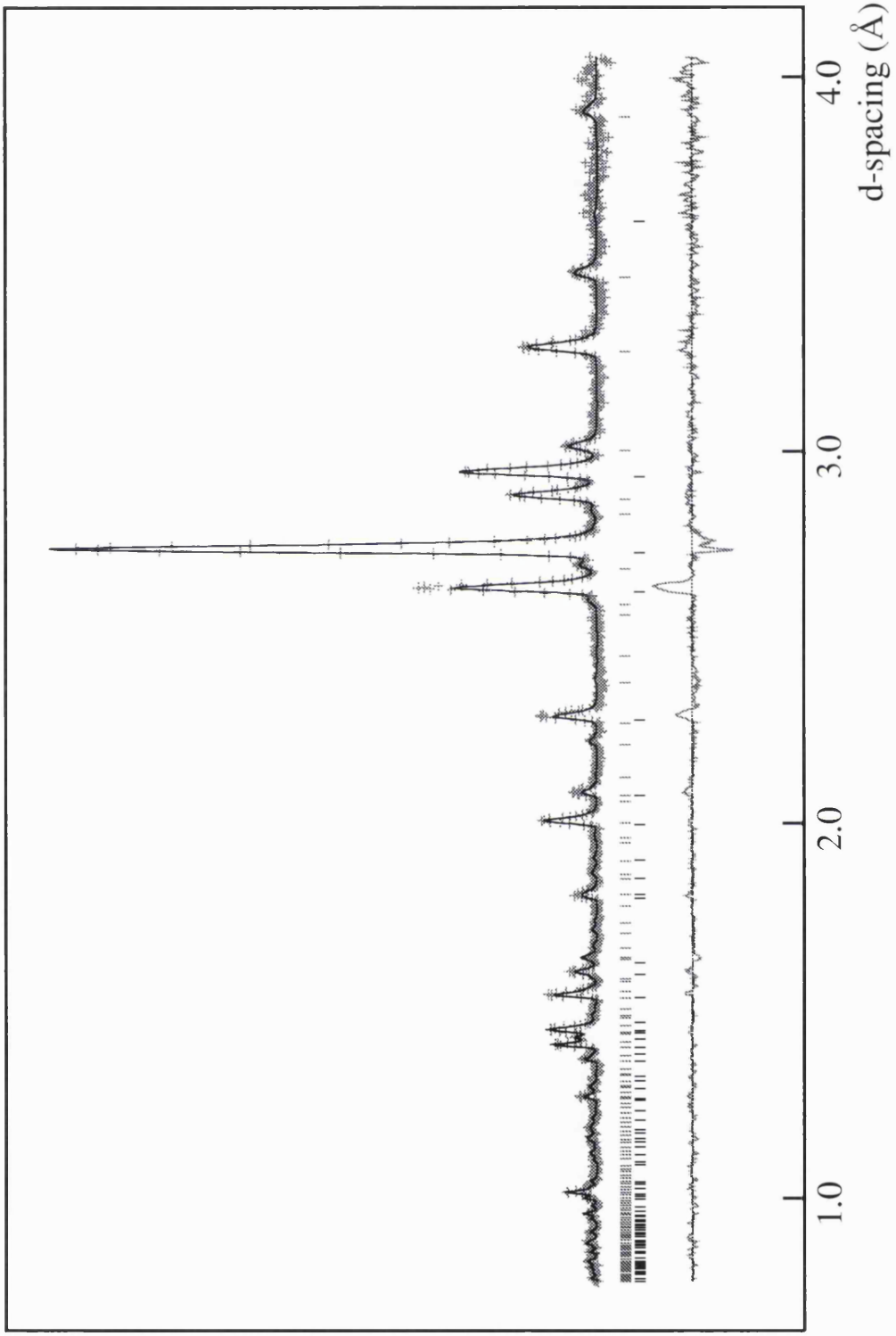

Figure 109: The profile fit for the blue phase data collected on PEARL at 4.82 kbar and 261 K, $R_p = 0.0069$ and $R_{wp} = 0.0065$. The amount of argon clathrate determined by the refinement was 20 wt.%. The thermal factors were refined isotropically.

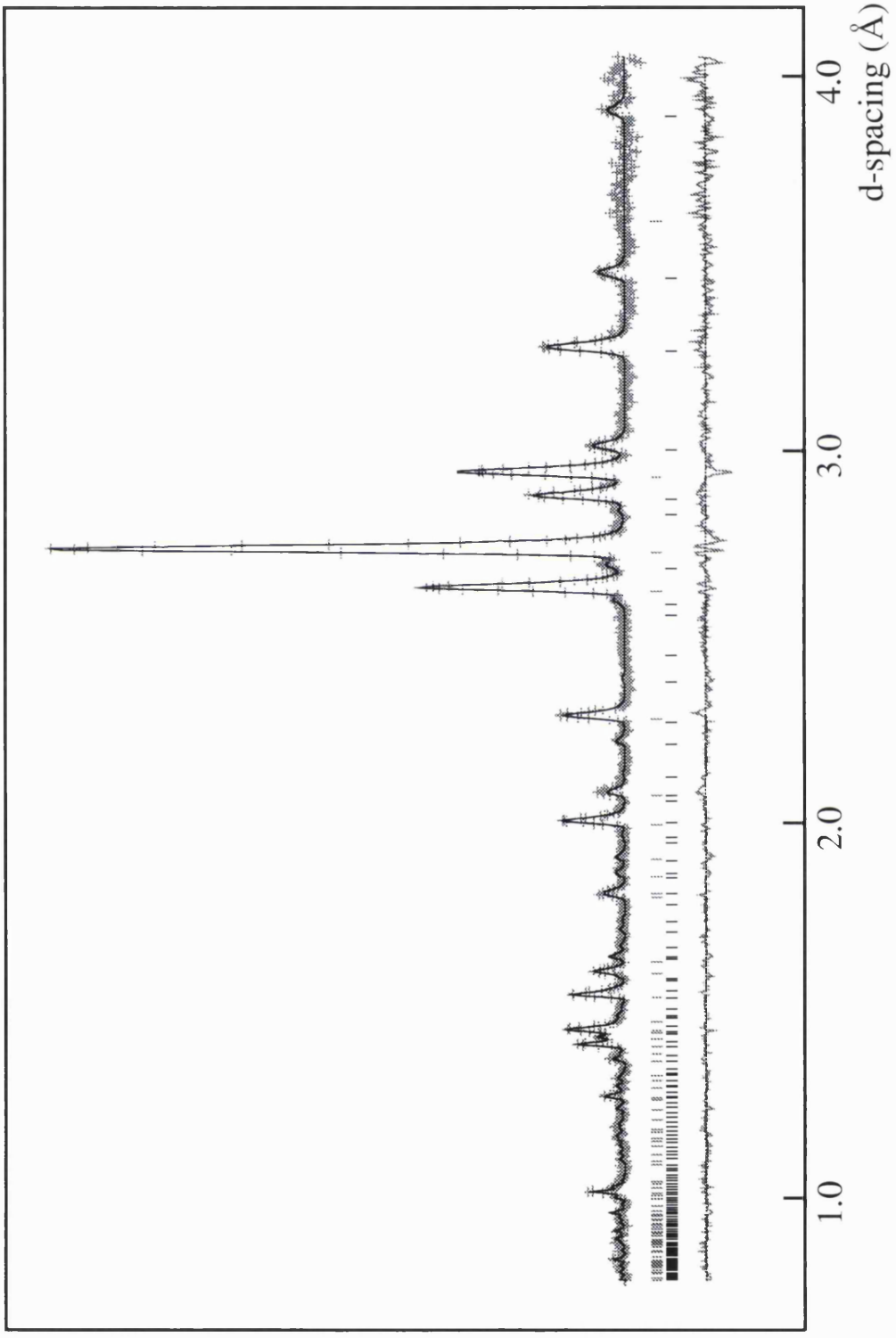

Figure 110: The profile fit for the blue phase data collected on PEARL at 4.82 kbar and 261 K, $R_p = 0.0057$ and $R_{wp} = 0.0048$. The thermal factors were refined anisotropically.

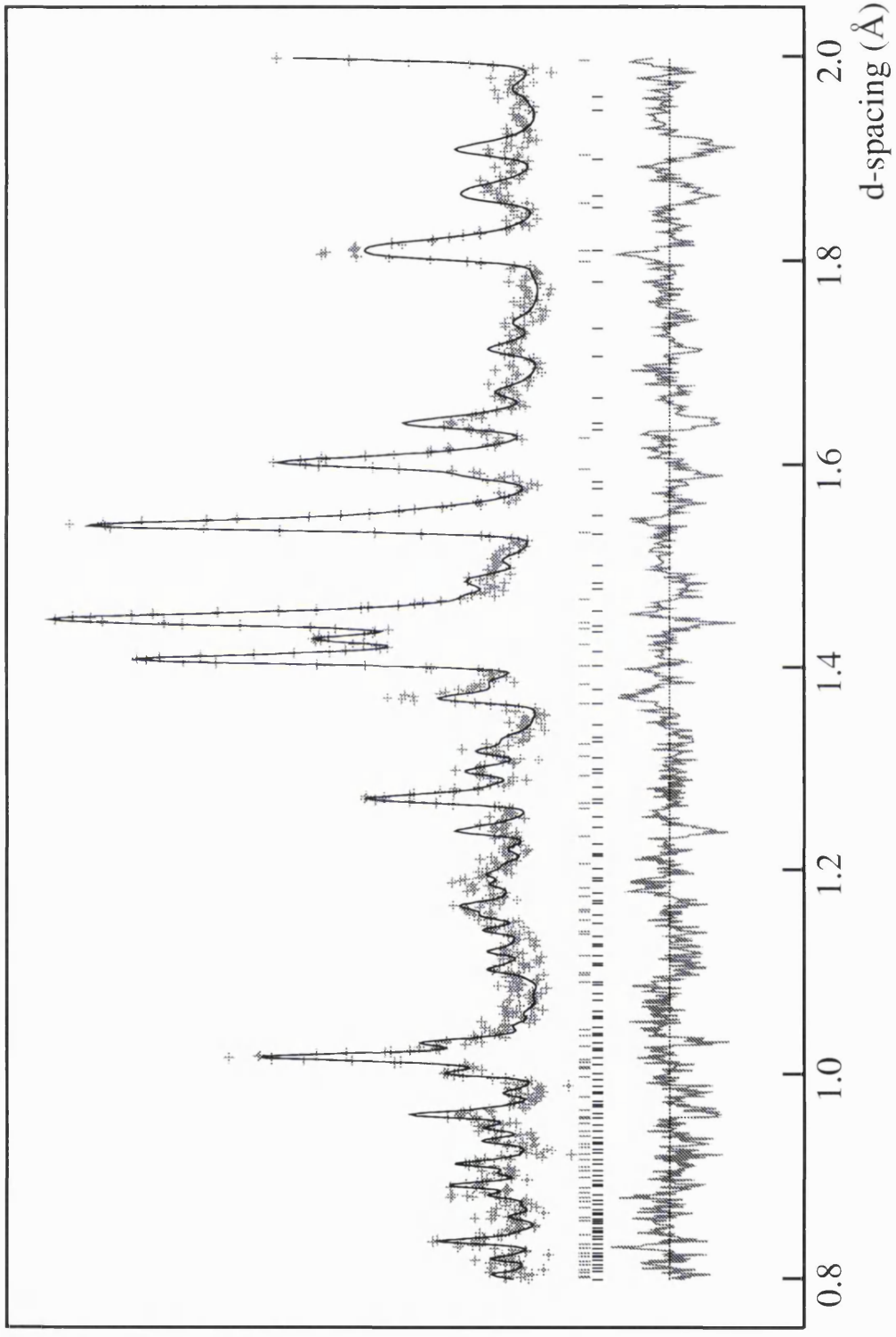

Figure 111: The profile fit for the blue phase data collected on PEARL at 4.82 kbar and 261 K in the 0.8–2.0 Å region.

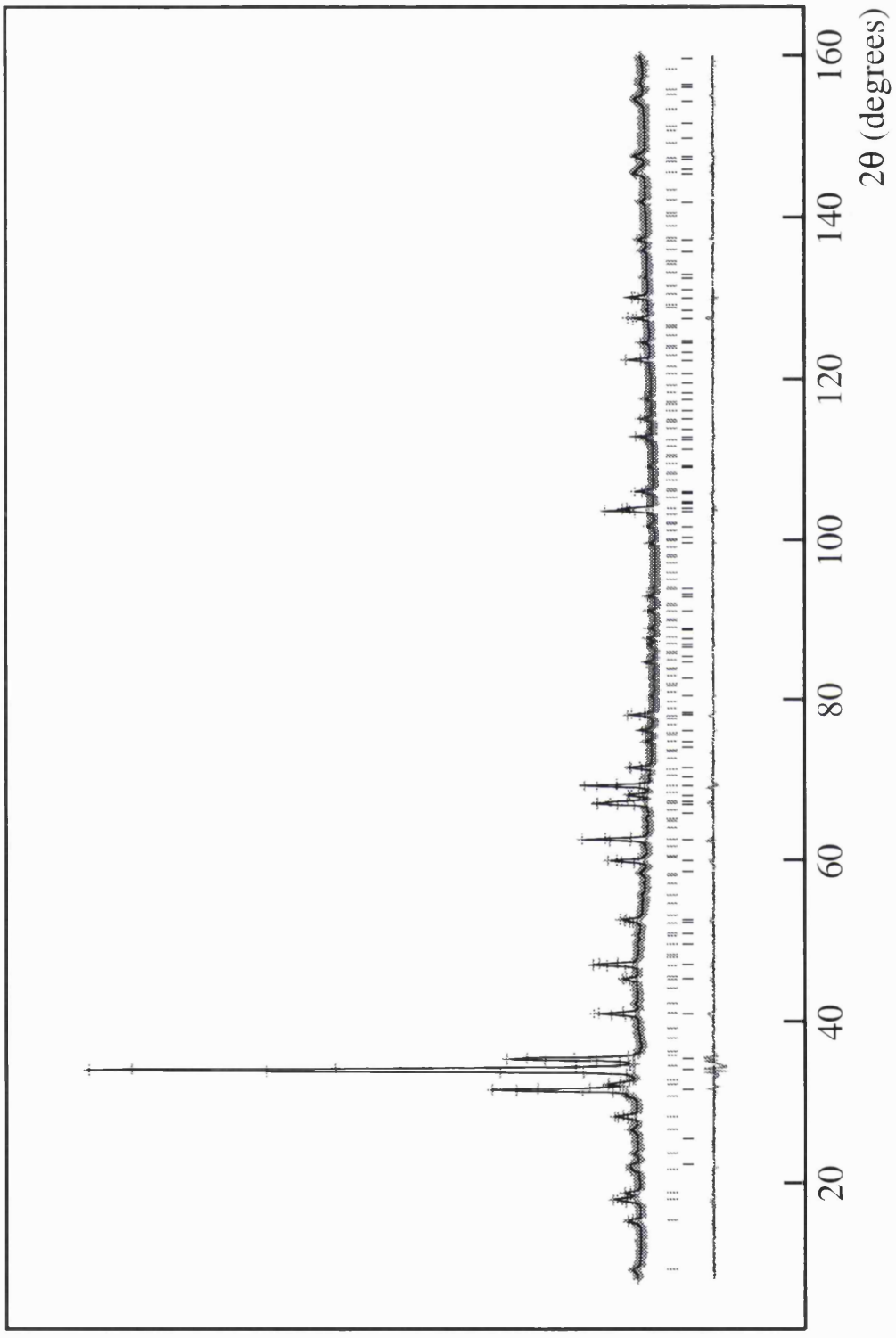

Figure 112: The profile fit for the blue phase data collected on D2B at 5.00 kbar and 260 K, $R_p = 0.0098$ and $R_{wp} = 0.0139$. The amount of argon clathrate determined by the refinement was 14 wt.%.

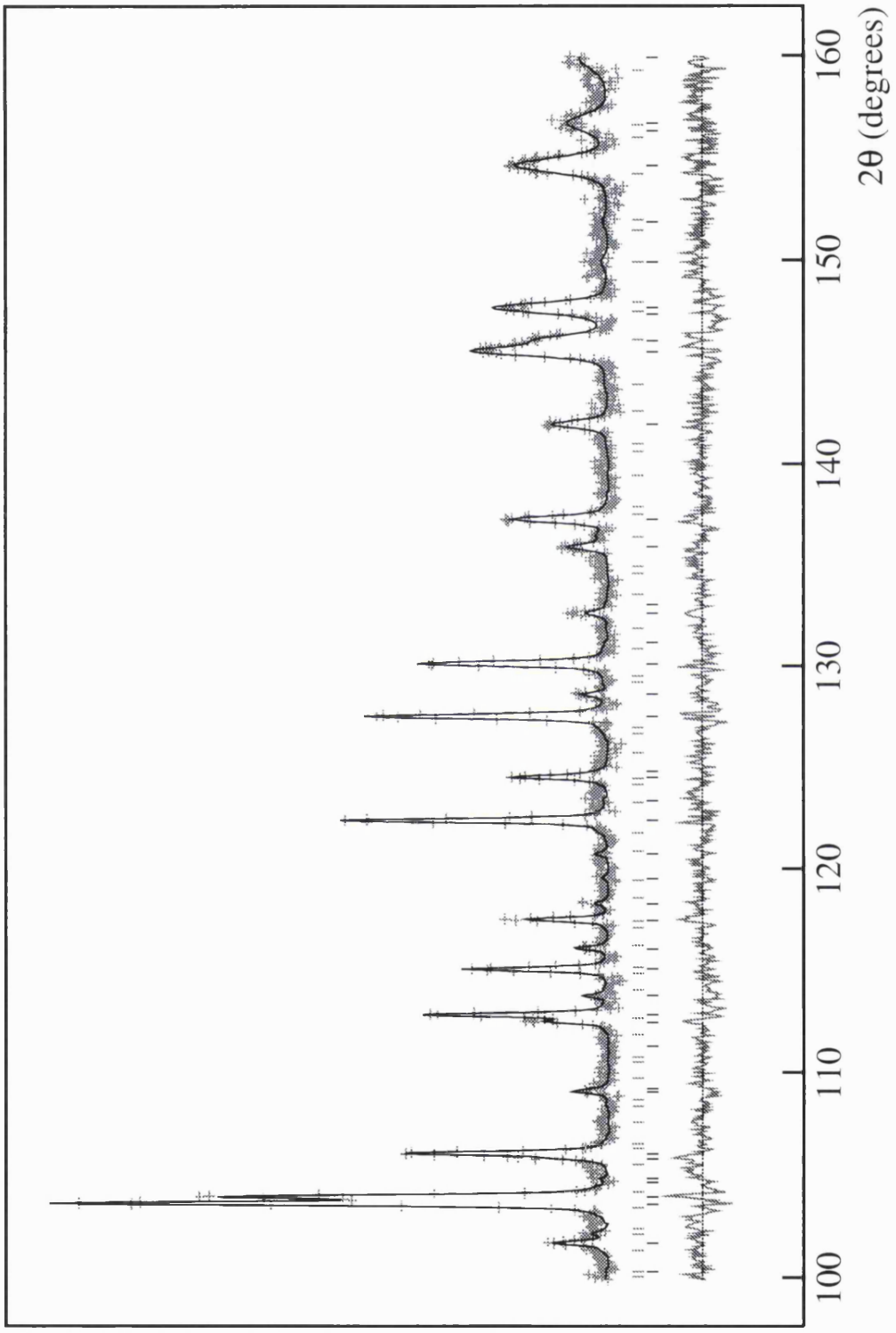

Figure 113: The profile fit for the blue phase data collected on D2B data at 5.00 kbar and 260 K in the 100°–160° region.

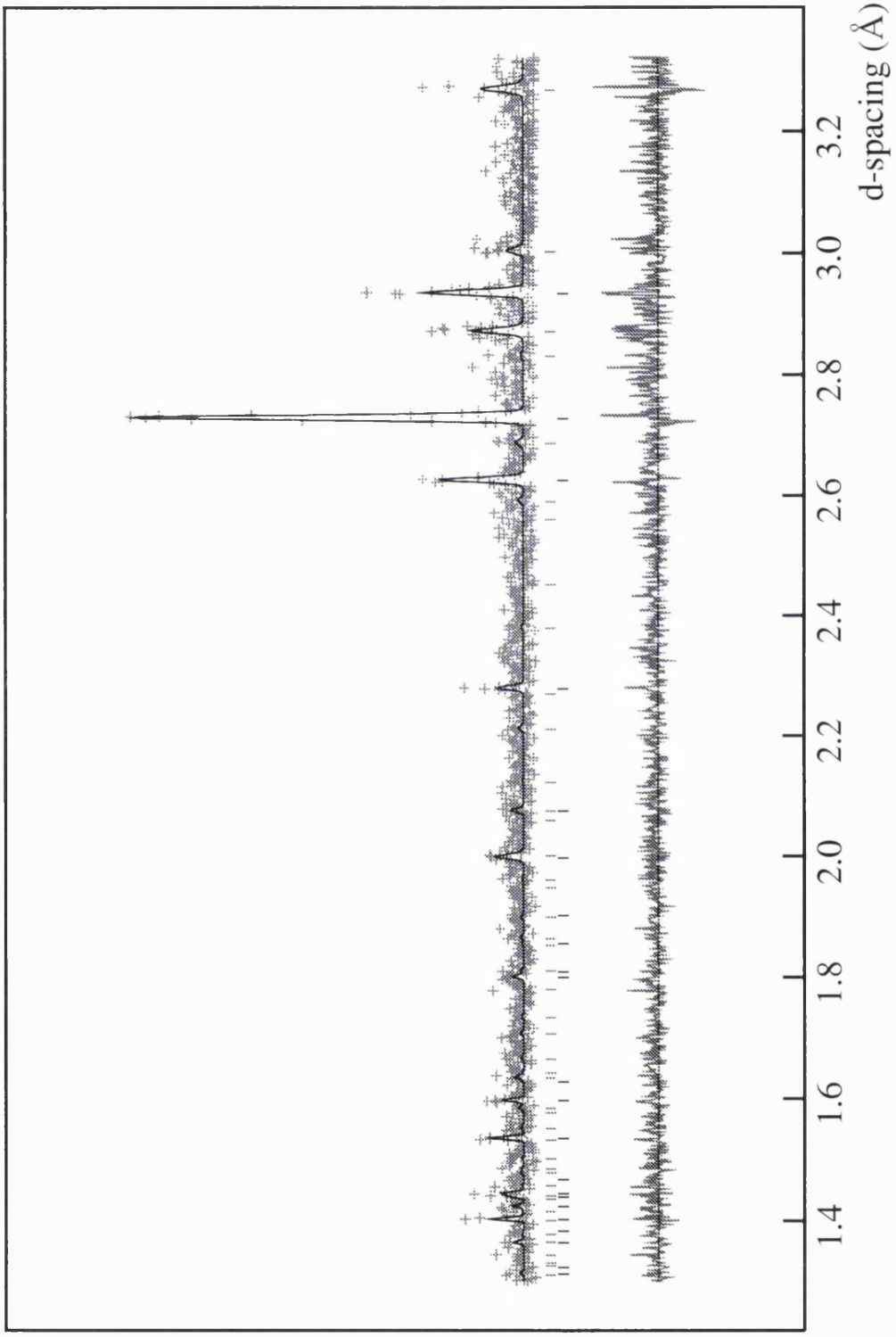

Figure 114: The profile fit for the blue phase data collected on HRPD at 5.01 kbar and 260 K, $R_p = 0.4063$ and $R_{wp} = 0.4547$. The amount of argon clathrate determined by the refinement was 10 wt.%.

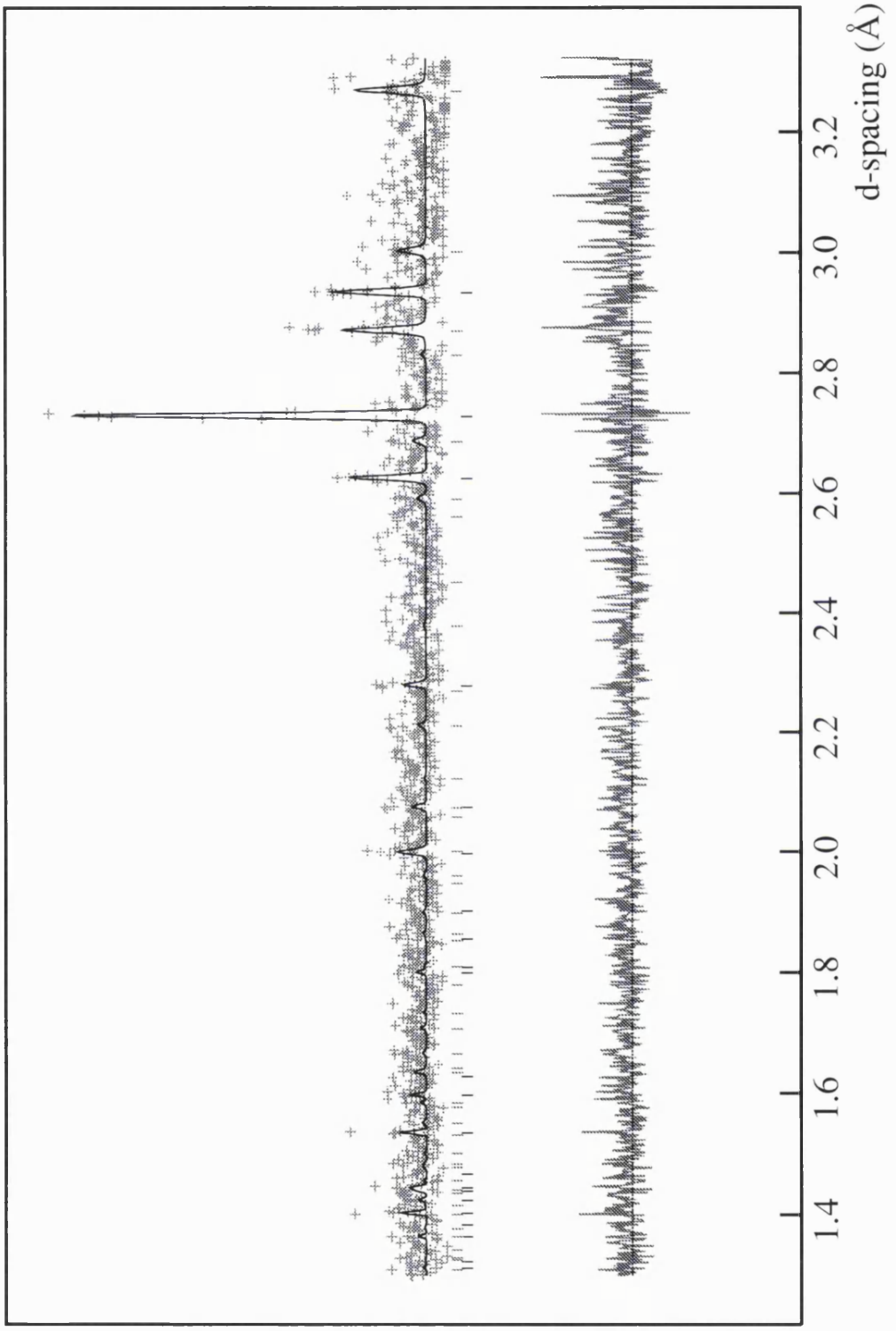

Figure 115: The profile fit for the blue phase data collected on HRPD at 5.22 kbar and 266.5 K — on the liquid–blue melting curve, $R_p = 0.4512$ and $R_{wp} = 0.4943$.

P(kbar)	T(K)	a(Å)	c(Å)	c/a	V(Å^3)	ρ(gcm^{-3})	Inst.
4.82	261.0	8.3076(5)	4.0273(3)	0.48477(5)	277.95(3)	1.4339(2)	PEARL
5.00	260.0	8.30373(9)	4.02373(8)	0.484569(11)	277.444(7)	1.43646(4)	D2B
5.00	255.0	8.2952(5)	4.0203(4)	0.48465(6)	276.64(4)	1.4406(2)	HRPD
5.01	260.0	8.2998(4)	4.0211(4)	0.48448(5)	277.00(3)	1.4387(2)	HRPD
4.99	264.0	8.3016(5)	4.0236(4)	0.48468(6)	277.29(4)	1.4372(2)	HRPD
5.10	260.0	8.2974(5)	4.0205(4)	0.48455(6)	276.80(3)	1.4398(2)	HRPD
5.20	260.0	8.2957(5)	4.0199(4)	0.48458(6)	276.65(4)	1.4406(2)	HRPD
5.21	266.5	8.2991(7)	4.0217(5)	0.48459(7)	276.99(5)	1.4388(3)	HRPD
5.30	260.0	8.2938(5)	4.0195(4)	0.48464(6)	276.49(4)	1.4414(2)	HRPD
5.40	260.0	8.2915(4)	4.0192(4)	0.48474(5)	276.32(3)	1.4423(2)	HRPD
5.50	260.0	8.2899(4)	4.0189(4)	0.48479(5)	276.19(3)	1.4430(2)	HRPD

Table 54: Blue phase lattice constants and densities.

	x	y	z	U_{iso}
O(1)	0	0	0	0.0336(9)
	0	0	0	0.0272(24)
O(2)	0.3643(4)	0.25	0.125	0.0349(6)
	0.3495(10)	0.25	0.125	0.0295(19)
D(3)	0.0419(6)	0.0871(4)	-0.1340(13)	0.0452(8)
	0.0455(11)	0.0936(8)	-0.1601(21)	0.0300(20)
D(4)	0.2922(5)	0.2181(4)	0.3090(12)	0.0433(9)
	0.3019(8)	0.2862(9)	-0.0881(21)	0.0378(23)
D(5)	0.4202(6)	0.3327(6)	0.2226(15)	0.0413(6)
	0.4141(10)	0.1826(12)	0.0566(26)	0.0352(26)

Table 55: The blue phase atomic positions and isotropic thermal factors from refinement of the data collected on D2B (top) and PEARL (bottom).

	U_{11}	U_{22}	U_{33}	U_{12}	U_{13}	U_{23}
O(1)	0.0446(30)	0.0446(30)	0.0337(51)	0	0	0
	0.046(6)	0.046(6)	0.053(16)	0	0	0
O(2)	0.0548(28)	0.0234(21)	0.0234(18)	0	0	-0.0106(13)
	0.026(7)	0.034(6)	0.026(7)	0	0	-0.027(4)
D(3)	0.0382(24)	0.0580(48)	0.0433(36)	0.0126(23)	-0.0234(25)	-0.0083(24)
	0.013(7)	0.098(14)	0.024(9)	0.003(6)	-0.028(7)	-0.018(6)
D(4)	0.0599(44)	0.0463(25)	0.0252(40)	-0.0011(19)	-0.0028(15)	-0.0025(14)
	0.094(15)	0.047(7)	-0.008(9)	0.001(6)	-0.023(6)	-0.013(4)
D(5)	0.0450(28)	0.0575(28)	0.0353(34)	0.0156(21)	-0.0038(19)	-0.0190(19)
	0.018(7)	0.071(10)	0.030(8)	-0.040(7)	0.015(6)	-0.024(6)

Table 56: Anisotropic thermal factors from refinement of the data collected on D2B (top) and PEARL (bottom).

O(1)–D(3)	0.967(4)	O(1)···D(5)	1.901(5)
O(2)–D(4)	0.988(4)	O(2)···D(4)	1.837(4)
O(2)–D(5)	0.918(5)	O(2)···D(3)	1.838(4)

Table 57: Blue phase O–D and O···D bond lengths.

O(1)–O(2)	2.803(1)	O(1)···O(1′)	4.0237(1)
O(2)–O(2′)	2.766(4)	O(1′)···O(2)	3.450(1)
		O(1′)···O(2′)	3.703(3)
		O(2)···O(2″)	4.0237(1)
		O(2)···O(2‴)	3.489(2)

Table 58: Blue phase O–O bonded and O···O non-bonded distances.

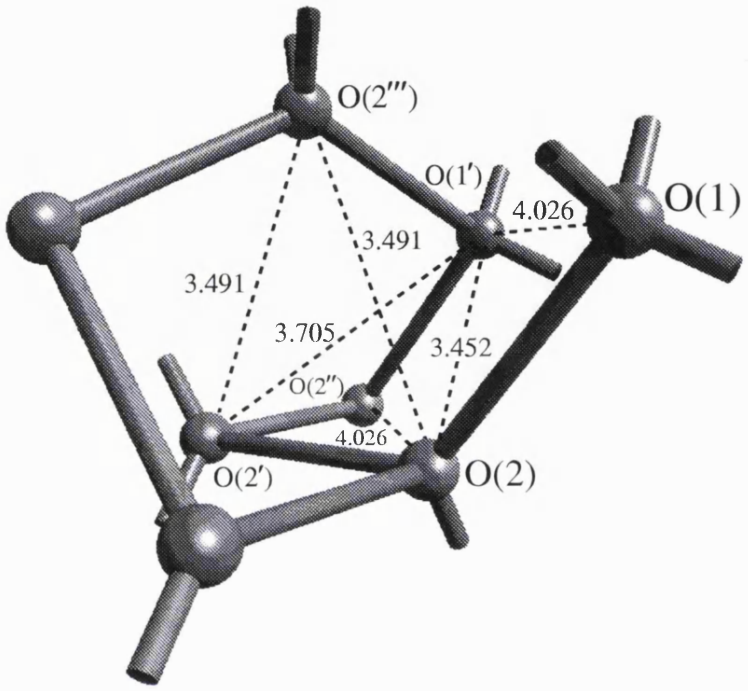

Figure 116: The blue phase short non-bonded O···O distances.

D(3)–O(1)–D(3)	108.1(3)	O(2)–O(1)–O(2‴)	106.85(2)
D(3)–O(1)–D(3)	112.2(6)	O(2)–O(1)–O(2′′′)	114.86(3)
D(4)–O(2)–D(4)	105.4(8)	O(2′)–O(2)–O(2″)	93.34(2)
D(4)–O(2)–D(5)	100.7(5)	O(2′)–O(2)–O(1)	83.36(2)
D(4)–O(2)–D(5)	115.3(3)	O(2″)–O(2)–O(1)	131.87(5)
D(5)–O(2)–D(5)	119.2(7)	O(1)–O(2)–O(1′)	132.58(1)

Table 59: Blue phase D–O–D and O–O–O bond angles.

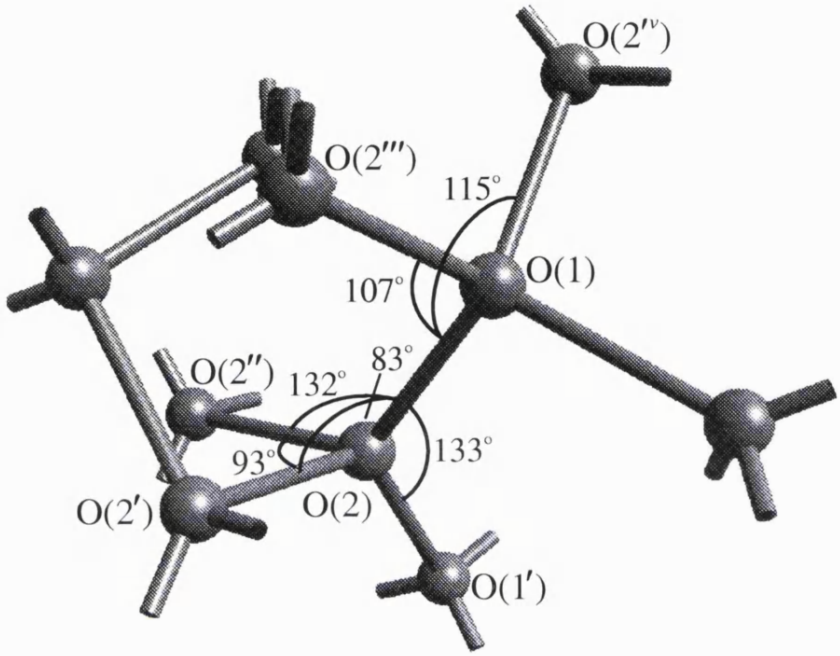

Figure 117: The blue phase O–O–O bond angles.

9.6 Discussion

9.6.1 Phase identification

Although refinement of the PEARL data suggested the blue phase had been correctly identified, there were some doubts surrounding the detailed model. When refined isotropically, the thermal factors were reasonable, table 55, but significant differences could be seen in the difference profile, figure 109. When refined anisotropically, the agreement between calculated and observed intensities improved, figure 110, but the thermals factors were unphysical, table 56. The PEARL diffractometer was set up at that time for work with the Paris–Edinburgh anvil cell and was not sufficiently collimated for our experiment. This resulted in poor data quality at short (< 1.5 Å)

d-spacings which may have lead to the refinement of erroneous thermal factors. Alternatively, the cause of error may be related to the powder quality. Although inspection of the individual detectors failed to find any strong texture within the sample, a small amount of texture may have gone unnoticed.

Fortunately, the phase was reproduced on D2B which provided better quality data at short d-spacings necessary for the determination of accurate thermal factors. D-spacings out to 20 Å were also covered by the diffractometer which would highlight any reflections not covered by PEARL. Furthermore, the sample could be rotated about the omega axis which would eliminate any small texture that might be present in the sample.

The results of the D2B refinement, figure 111, indicated the structure proposed was indeed correct. There were no reflections omitted by the refinement and sensible values for thermal factors, interatomic distances and angles were obtained.

9.6.2 Reproducibility

During the early stages of this work, the high-pressure ices were formed from the liquid with the use of silica wool. Unfortunately, the quality of the powder formed on freezing was rarely ideal. Work on the argon hydrate system, however, had shown that the high-pressure ices could be formed from good powdered ice by using argon gas as the pressure medium. It was during the initial work, when the ices were prepared from the liquid, that the yellow and blue phases were formed. Only after data on ices III and V had been collected, i.e. towards the end of this work, did attention return to these unknown phases. The experiment on PEARL proved highly successful with the formation of two metastable phases: ice IV and the blue phase. Since then, the blue phase has only been attempted on three occasions, and when the same methodology

was adopted, all attempts were successful.

The blue phase was formed by cooling at a rate of 2.5 Khr^{-1} from 270 to 260 K at 5.5 kbar, and on no occasion has the formation of the phase been unsuccessful when following this recipe. The rate of cooling appears important for nucleation of the phase since a slightly faster cooling rate of 5 Khr^{-1} resulted in the formation of ice V. The importance of the precise pressure is, however, unknown.

9.6.3 Description of structure

As in all other ices, the water molecules of the blue phase bond together tetrahedrally to form a single network. Water molecules of the type O(2) bond to one another to form zigzag chains which run parallel to the *c*-axis and oscillate in either the *a*- or *b*-axis plane, figure 118. The chains are then linked together by water molecules of the type O(1), figure 119, to form spiralling channels approximately pentagonal in shape. These channels run parallel to the *c*-axis and exhibit four-fold symmetry about the O(1) atoms.

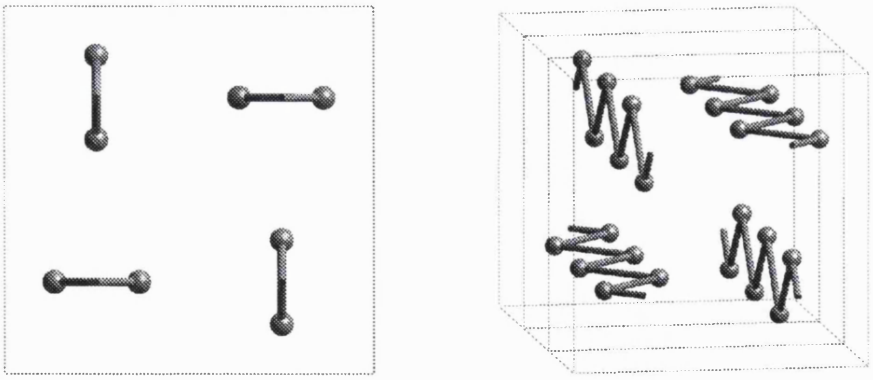

Figure 118: The zigzag chains formed by O(2) atoms, viewed down the *c*-axis.

The location of the O(1) water molecules with respect to the zigzag chains creates a torque on the O(2) water molecules, figure 120. This torque causes the water

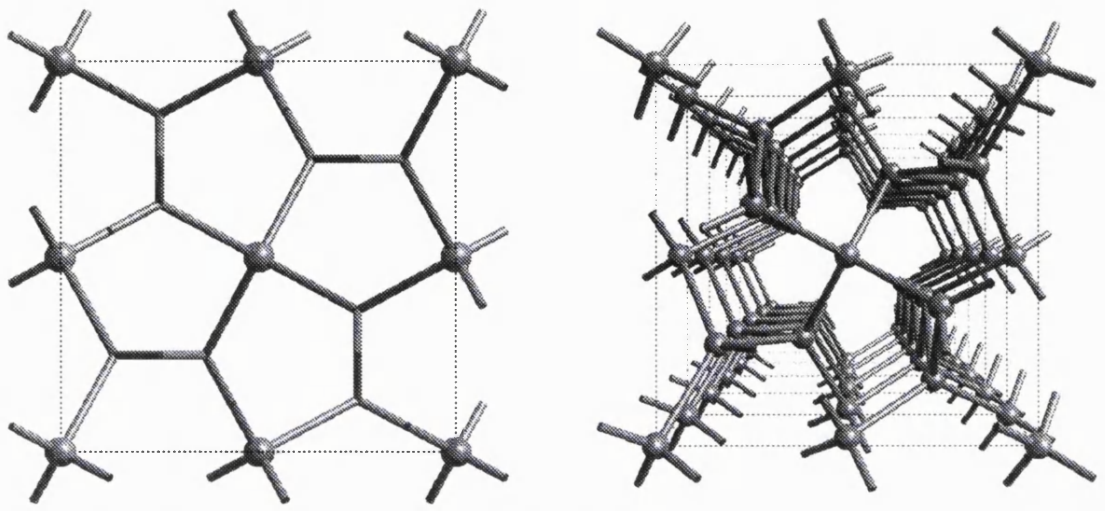

Figure 119: The zigzag chains are linked by O(1) atoms, forming pentagonal channels which spiral parallel to the *c*-axis. The O(1) atoms are shown as spheres in the figure left, whilst a perspective view of the structure is shown right.

molecules to rotate, pulling the deuterium atoms off the plane of the chain, figure 120.

The structure consists of only seven- and eight-membered rings and provides a counter-example to the generally held belief that tetrahedral frameworks, such as ices, clathrates, aluminosilicates and zeolites, must contain some rings smaller than seven-membered rings [129]. This was not based on physical limitations but purely on the occurrence of rings found in some 130 other such structures [130]. The blue phase represents the only known four co-ordinated network which has such an arrangement of rings.

The O–O bond distances, with a mean of 2.794 Å, are of the order seen in other ice structures at lower pressures, e.g. ices Ih [59], II (table 10), III (table 22). There is no evidence of bond strain or non-bonded interactions influencing the detailed oxygen framework, such as that seen in ices IV (chapter 7) and V (chapter 6).

The O–O–O bond angles show substantial deviations from the ideal tetrahedral

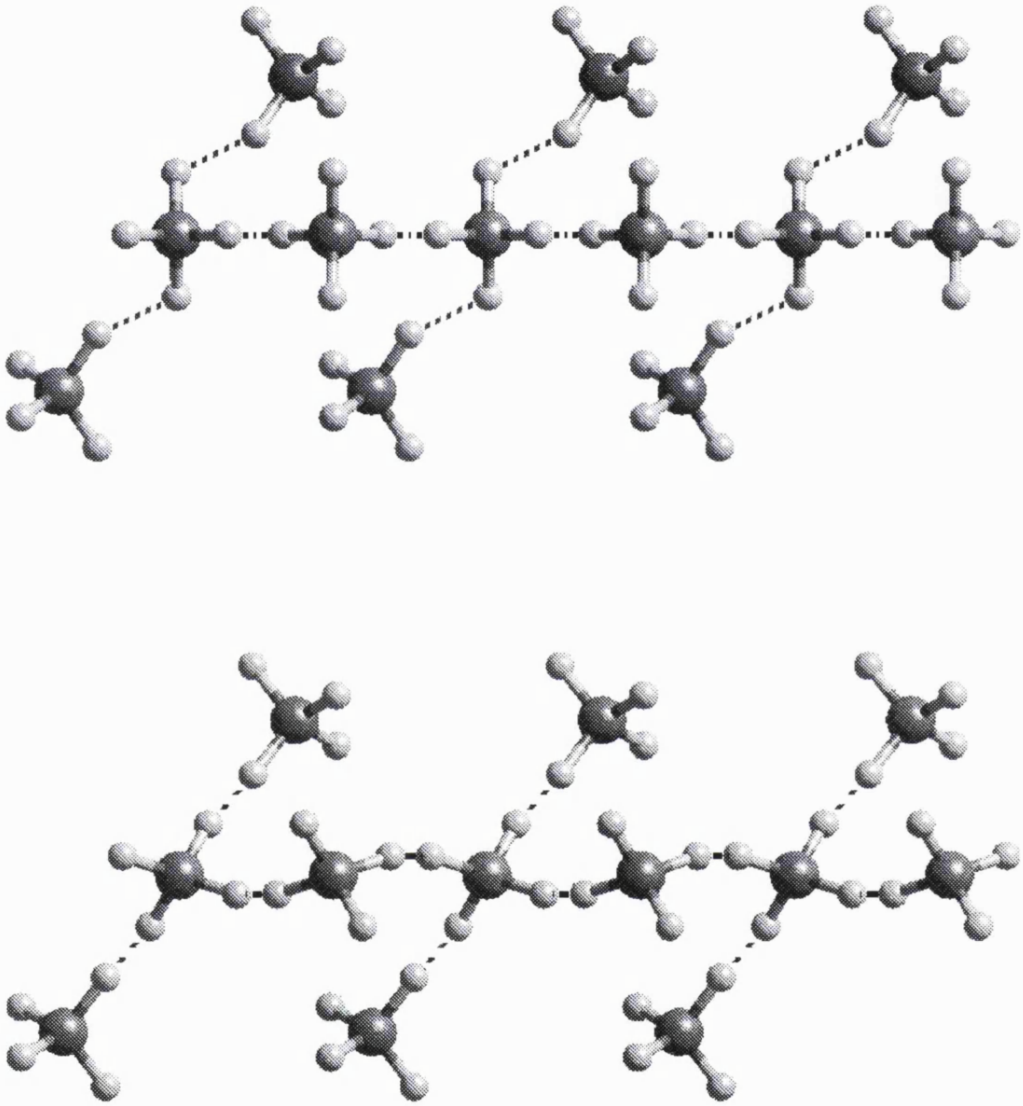

Figure 120: Water molecules of type O(2) which form zigzag chains experience a torque due to the position of O(1) (top). The torque causes the O(2) water molecules to rotate, thereby pulling the deuterium atoms off the plane of the chain (bottom).

angle of 109.5°. The total magnitude of these deviations is the largest of all the ice structures, with the exception of ice VI. This high degree of bond bending accounts for the increase in density of the blue phase over ice V. The density of the blue phase at 5 kbar and 260 K is 1.4365(1) gcm^{-3}, table 47. This is greater than the density of ice V under similar conditions, 1.4021(1) gcm^{-3}, yet comparable to that of ice IV, 1.4357(1) gcm^{-3}. For ice IV, the degree of bond bending is actually smaller than both ice V and the blue phase. Instead, the increase in density over ice V is achieved through a form of interpenetration, in which a hydrogen bond passes through a hexagonal ring of water molecules, figure 88.

9.6.4 Positional disorder

As mentioned in sections 5.4.4, 5.4.5 and 7.4.5, positional disorder arises from water molecules which move locally from their crystallographically mean positions. This is often to alleviate bond bending, bond stretching, and because of repulsive forces from short, non-bonded interactions. For the blue phase, the most obvious indication of local disorder is the short O(2)–D(5) bond length, table 57.

Water molecules of type O(2) occupy sites in which the O–O–O bond angles differ greatly from the D–O–D bond angle of 104.5°, table 59. The resulting strain on the hydrogen bonds is most probably relieved locally by water molecules moving from their crystallographic positions.

Four of the orientations occupied by water molecules of type O(2) involve both D(4) and D(5) deuterium atoms. Two of the four orientations involve occupation of the O(1)–O(2)–O(2′) bond angle and the other two involve occupation of O(1)–O(2)–O(2″). The O(1)–O(2)–O(2′) bond angle is smaller than 104.5°. The water molecule will therefore move to increase the bond angle and thereby decrease the strain on

the hydrogen bond. This movement will result in shorter O(2)–D(4) and O(2)–D(5) bond lengths, figure 121. In contrast, the O(1)–O(2)–O(2″) bond angle is greater

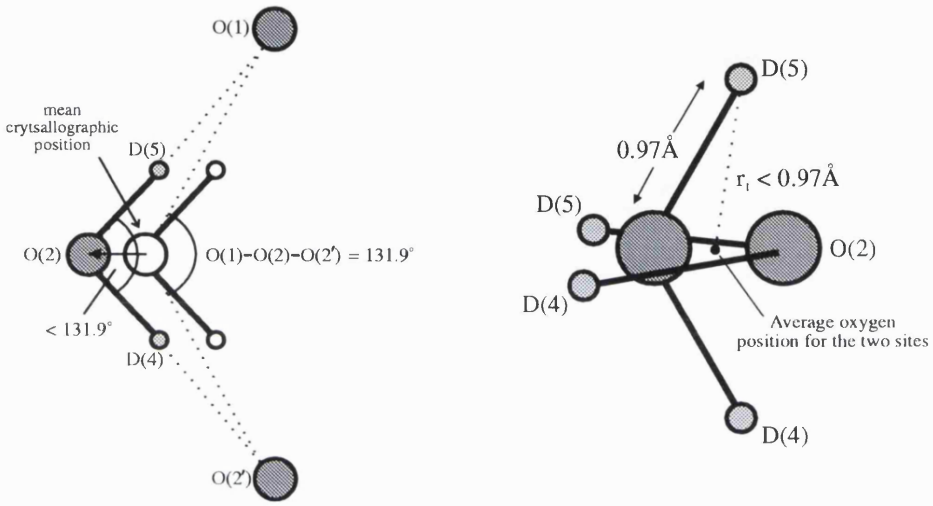

Figure 121: The water molecule moves from the crystallographic site in a direction which serves to decrease the O(1)–O(2)–O(2′) angle (left). The net result of this shift, which by symmetry occurs twice, is an O–D bond length less than 0.97 Å (right).

than 104.5°. The water molecule will therefore move in a direction which serves to decrease the angle, resulting in longer O(2)–D(4) and O(2)–D(5) bond lengths. The four orientations collectively counteract one another, resulting in O(2)–D(4) and O(2)–D(5) bond lengths of 0.97 Å.

The two remaining orientations occupied by water molecules of type O(2), O(1)–O(2)–O(1′) and O(2′)–O(2)–O(2″), must therefore be responsible for the long O(2)–D(4) and short O(2)–D(5) bond lengths.

The O(1)–O(2)–O(1′) bond angle is greater than 104.5° and will cause the water molecule to move in a direction similar to that in figure 121. The O(2′)–O(2)–O(2″) bond angle is smaller than 104.5° and will cause the water molecule will move in a similar fashion to that demonstrated in figure 122. Unlike the pairing of orientations

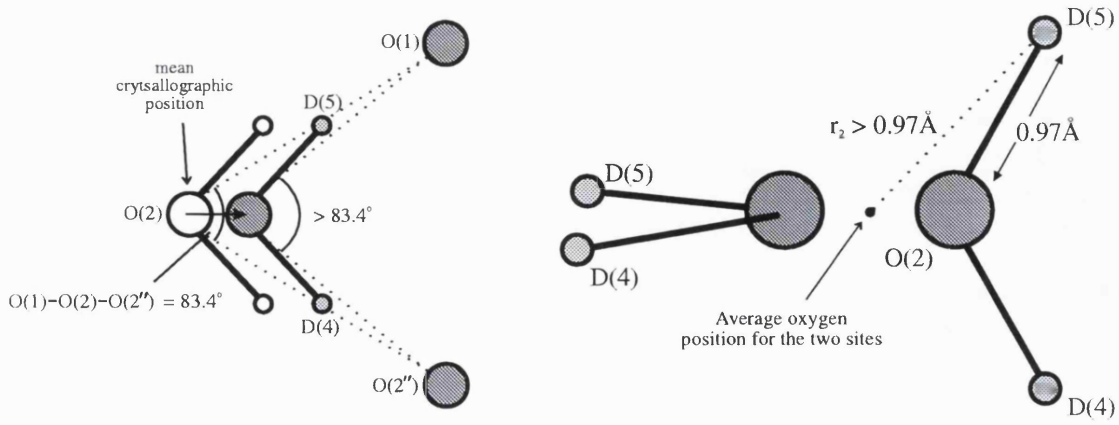

Figure 122: The water molecule moves from the crystallographic site in a direction which serves to increase the O(1)–O(2)–O(2″) angle (left). The net result of this shift is an average O–D bond length greater than 0.97 Å (right).

shown in figures 121 and 122, in which the directions of the shift are directly opposite, the directions of the shifts for the two orientations are approximately the same, figure 123. If the directions of the shifts for both orientations were exactly the same, then identical bond lengths for O(2)–D(4) and O(2)–D(5) would be expected, regardless if one of the orientations was shifted more. However, the torque on the water molecule, figure 120, means that the direction of the shift for the two orientations is slightly different, and can account for the measured bond lengths.

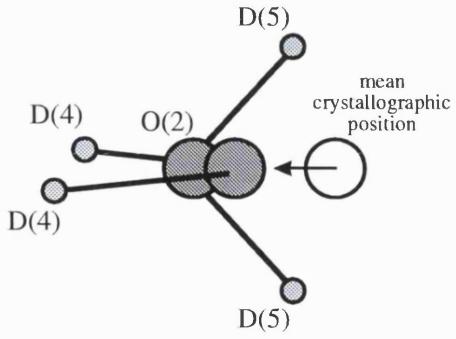

Figure 123: The water molecule moves from the crystallographic mean in a direction which serves to decrease the O(1)–O(2)–O(1′) bond angle, occupied by D(5)–O(2)–D(5), and increase the O(2′)–O(2)–O(2″) bond angle, occupied by D(4)–O(2)–D(4).

Of course, the above description is merely informed guesswork and the exact nature of the local disorder cannot be easily interpreted by crystallography. It is however

reasonable to suggest that the water molecules move from their crystallographic positions to relieve strains.

9.6.5 Orientational disorder

Full orientational order of the water molecules within the blue phase is not possible without a large change in space group symmetry. The four-fold symmetry about O(1) constrains D(3), and hence D(5) which shares O–O bonds with D(3), to a population of 50%. The two-fold symmetry found within the chains similarly constrains D(4) to 50% population. Full orientational order is not therefore permitted.

It is somewhat surprising that with such large bending strains across the bonds, that no form of orientational order is observed. Partial order, strong across some bonds, is observed for ices III and V in which the degree of bond bending is smaller than that found for the blue phase. However, in ices III and V, the degree of bond bending is variable, making the occupation of some bonds more favourable than others. The bond angles in the blue phase, although very different from the ideal tetrahedral angle, all exhibit similar amounts of bond bending. In this way, there is no favouritism over occupation, a situation similarly found in ice IV. However, as is now demonstrated, partial ordering of the water molecules is possible under the current space group symmetry.

It initially appears that full orientational order along the zigzag chains could occur and yet go undetected by crystallography by nature of their four-fold symmetry. For water molecules of type O(2), which make up the chains, the O(2′)–O(2)–O(2″) bond angle is slightly more favourable in terms of bond bending, table 59, than the other five orientations and is therefore the strongest candidate for occupation. In occupying this bond, the water molecules must also occupy the O(1)–O(2)–O(1′) bond angle,

resulting in a chain in which the deuterium atoms form an ordered arrangement as shown in figure 124. Each water molecule of type O(1) bonds together four of these chains with possible arrangements shown in figure 125.

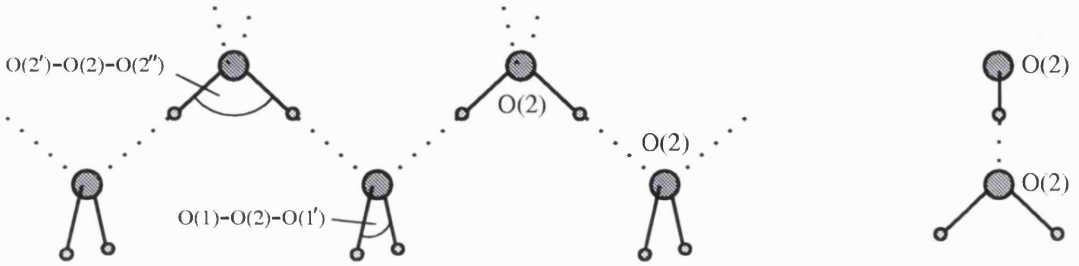

Figure 124: Possible orientational ordering of O(2) water molecules, viewed perpendicular (left) and parallel (right) to the chain.

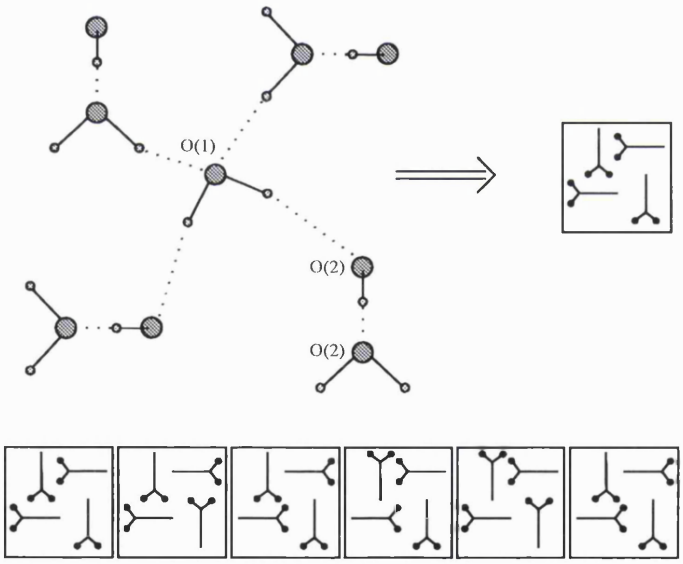

Figure 125: The arrangement of O(2) chains around the central O(1) water molecule. One possible configuration is shown above with all six possibilities shown in abbreviated form below.

If, throughout the entire crystal structure, only one of the arrangements were to occur, then it would certainly be detected by crystallography. But, if the arrangement

of chains was found to change, then by averaging, the water molecule orientations would appear random, i.e. complete orientational disorder detected for a partially ordered structure. Nevertheless, it is not possible to arrange the chains in such a way that the Bernal-Fowler rules are not broken. Figure 126 demonstrates the case for one configuration and a failed attempt at different configurations.

Although full order along the chains is not possible, partial order is still feasible with the occasional change, or kink, in the chain. The example shown in figure 127 is of two chains constructed completely of either O(1)–O(2)–O(2′) or O(1)–O(2)–O(2″) orientations, i.e. completely ordered chains of two different types. Unlike the example shown in figure 124, different configurations can occur throughout the structure without violating the Bernal-Fowler rules, figure 128. Partial ordering of the water molecules is therefore possible.

9.6.6 Metastability

The metastability of ice IV, and the yellow and blue phases must be conditional upon two points. First, ice V must be the more stable; that is to say, the free energy of ice V must be lower than that of the metastable phases. If this were not the case then one would expect the formation of metastable phases from ice V, yet none have been reported. Second, the metastable phases must nucleate more readily than ice V at some pressure and temperature. Without this condition only ice V would form.

Using the workings of Engelhardt and Kamb [46], the difference in free energy between ice V and the blue phase can be determined from the gradient of the blue phase melting curve, $(\partial p/\partial T)_m$, the volume change on melting, ΔV_m, and the temperature

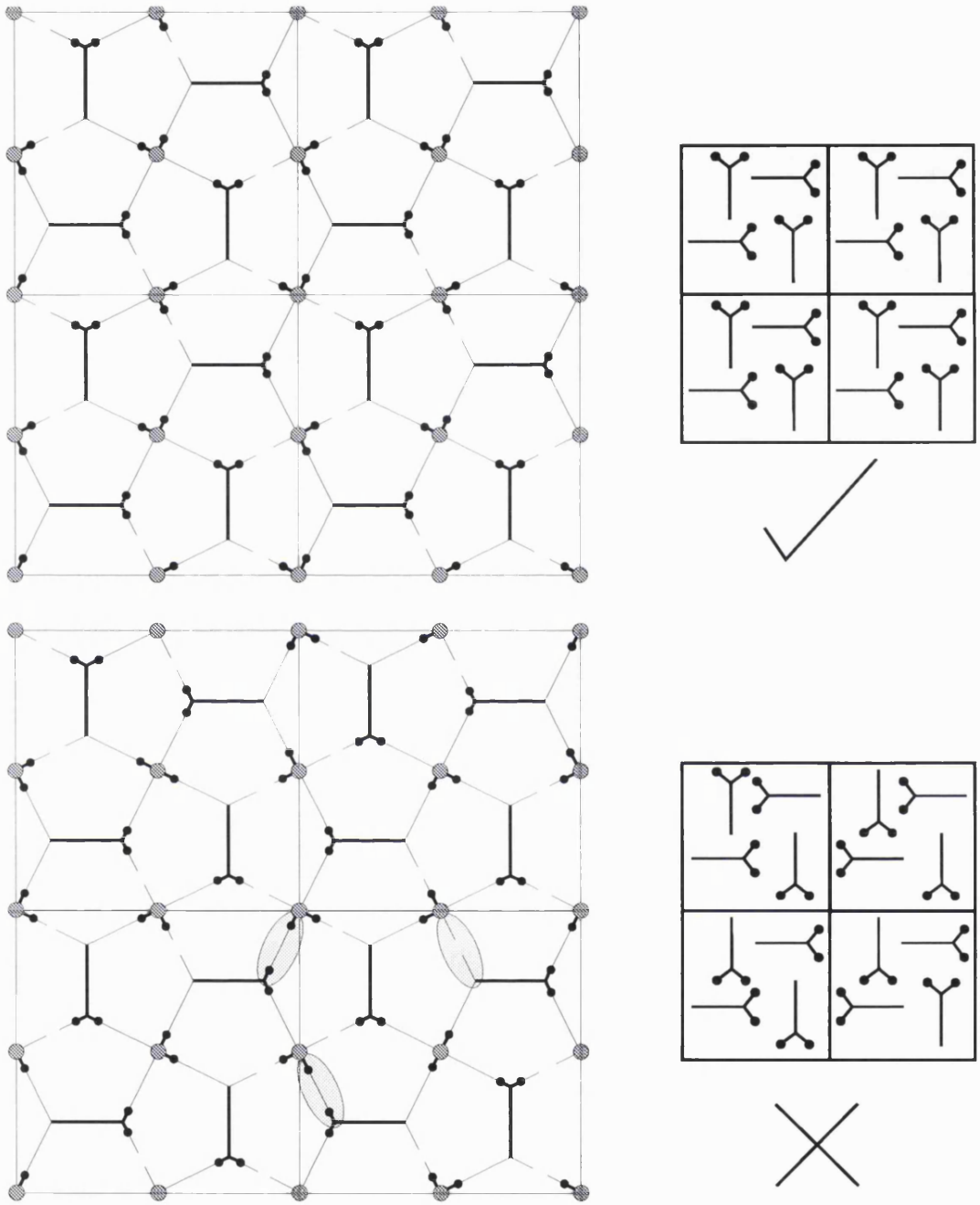

Figure 126: Two possible configurations of orientational order, with each configuration represented by four cells viewed parallel to the c-axis. The top configuration does not violate the Bernal-Fowler rules but would subsequently be detected by crystallography since only one arrangement is occurring. The bottom configuration would not be detected by crystallography since four different arrangements are occurring which would average the occupations. However, the configuration violates the Bernal-Fowler rules across three bonds (shaded regions). Broken lines indicate bonds between water molecules in adjoining cells in the c-axis direction. Since the unit cell naturally repeats, the broken lines can be considered as continuous for this demonstration.

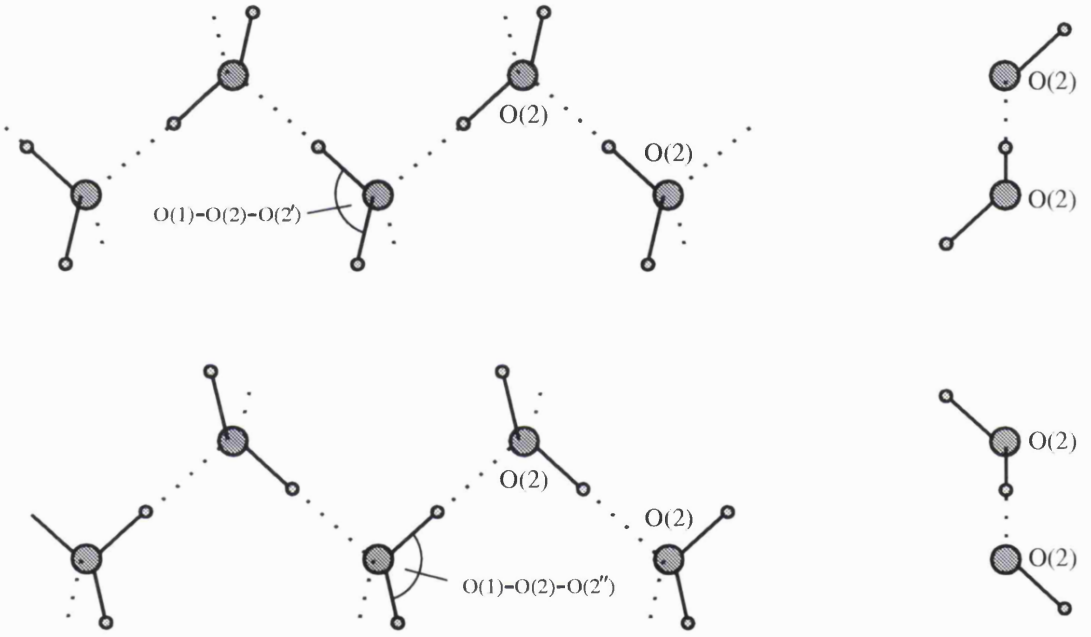

Figure 127: Two ordered chains, one which involves occupation of only O(1)–O(2)–O(2′) bond angles and the other which occupies only O(1)–O(2)–O(2″) bond angles. Each is viewed perpendicular (left) and parallel (right) to the chain.

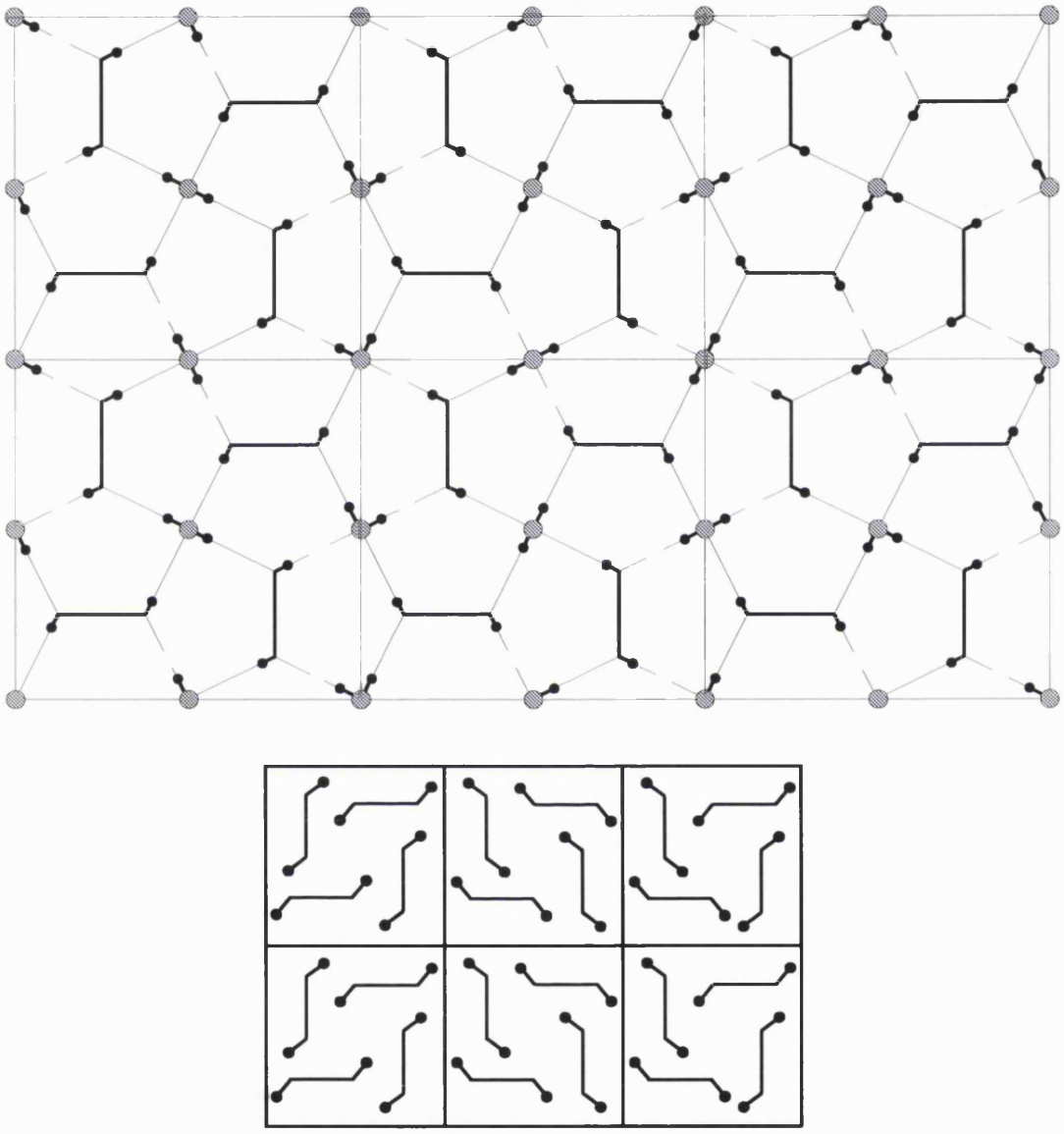

Figure 128: The chains shown in figure 127 can be arranged to form the blue phase without violating the Bernal-Folwer rules. Although, the structure must repeat in one direction (up and down in this example), there is no such constraint on the other direction (left to right). Since any arrangement can occur for each unit cell in this direction, the partial ordering would not be detected by crystallography.

difference in the melting curves for ice V and the blue phase, ΔT_m:

$$\begin{aligned}\Delta G &= \left(\frac{\partial p}{\partial T}\right)_m \Delta V_m \Delta T_m \\ &= (1.133\text{x}10^7\ \text{PaK}^{-1}).(1.629\text{x}10^{-6}\ \text{m}^3\text{mol}^{-1}).(3.63\ \text{K}) \\ &= 67\ \text{Jmol}^{-1}\end{aligned}$$

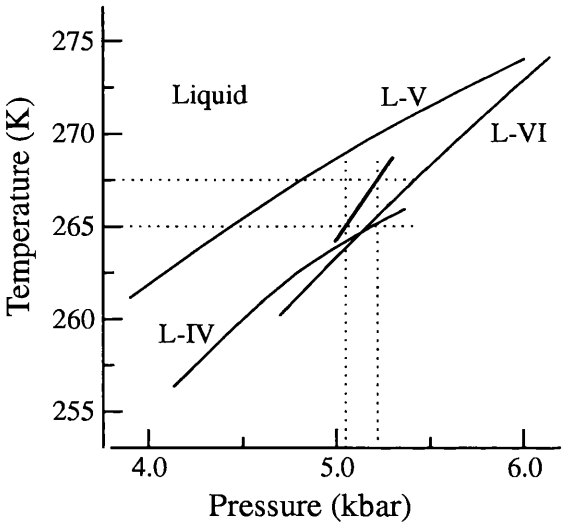

Figure 129: The blue phase melting curve. The two (p,T) points on the melting curve are indicated by dashed lines, with a line between the two representing the liquid-blue melting curve. The ice IV, V and VI melting curves were determined by Engelhardt and Whalley [43].

Using the two data points on the melting curve, figure 129, the difference in free energy between ice V and the blue phase is 67 Jmol^{-1}. This figure is small in comparison to the difference for other ice phases, e.g. the difference for ices V and Ic is ~790 kJmol^{-1} at 148 K [112]. The figure is, however, comparable with the difference in free energy determined by Engelhardt and Kamb [46] for ice V and the other metastable phase, ice IV, 95 Jmol^{-1}. The increase in density of the blue phase, with respect to ice V, must be offset by differences in internal energy and entropy, equation 19.

Although ice V has two shorter, non-bonded O···O distances than the blue phase, they occur infrequently within the structure, table 63. In terms of O···O non-bonded

distance less than 3.5 Å, the blue phase has 5.34 per water molecule while ice V has only 1.43 per water molecule, table 63. There is therefore an increase in non-bonded interactions for the blue phase. The degree of bond stretching in the blue phase is decreased with respect to ice V, tables 58 and 35. However, there is an increase in bond bending, table 47. The higher internal energy of the blue phase, relative to ice V, must therefore arise from increased bond bending and an increase in repulsive, non-bonded contacts.

If it is assumed that the blue phase is orientational disordered, and ice V partially ordered as listed in table 31, then the difference in configurational entropy between ice V and the blue phase is approximately -27 $JK^{-1}mol^{-1}$ The figure is negative and will therefore decrease the free energy. Since the degree of orientational disorder within the blue phase is unknown, the figure is clearly questionable. However, for the entropy contribution to increase the free energy, the ordering within the blue phase would have to be greater than that observed for ice V.

No explanation can be offered on the complex issue of nucleation. Time appears to be an important factor in obtaining the blue phase. It is unknown, however, what the water molecules do given the extra time in cooling from 270 to 260 K.

Ice V is the stable structure, yet it contains four-membered rings, which for a tetrahedral system are inherently highly strained. In contrast, the blue phase is made up of larger rings (seven- and eight-membered). The liquid state can perhaps be viewed as a tetrahedral network in which different ring structures "melt" and "reform" due to local energetic fluctuations. In order to nucleate ice V, it seems reasonable to expect that a critical nucleus containing four-membered rings must occur. However, the high strain involved suggests this may not occur easily, whereas a nucleus of the less strained blue phase perhaps forms more easily. Thus, although

other factors in the extended ice V structure may compensate for the high strain in the four-membered rings, it may be that although, less stable as an extended network, the blue phase nucleates more easily.

There is evidence of a new ice structure which forms from the liquid under conditions at which ice VI is stable [131]. Interestingly, ice VI is the only other ice structure to contain four-membered rings.

9.6.7 Compressibility and expansivity

The lattice constants obtained from the refinement of the HRPD data were fit by least-squares to the Vinet *et al.* [122] and Birch-Murnaghan [123] equation-of-states, equations 20 and 22. The parameters arising from the fit of the pressure-volume data, figure 130, are listed in table 60.

	Vinet *et al.*	Birch-Murnaghan
V_0	288(27)	288(32)
B_0	97(510)	97(684)
B_0'	14(115)	16(214)

Table 60: The EOS parameters derived from a least-squares fit of the pressure-volume data, figure 130.

As explained in section 7.4.9, the large errors associated with the EOS parameters, table 60 arise from the small number of data points spanning a particular small area of parameter space. Table 61 lists the EOS parameters obtained by least-squares if V_0 is fixed at 288 Å^3.

Using a linear relationship to describe the pressure-volume data, the bulk modulus of the blue phase over the pressure range 5.0–5.5 kbar at 260 K is 173(6) kbar, equation

	Vinet *et al.*	Birch-Murnaghan
V_0	288	288
B_0	96.9(4.2)	95.0(5.0)
B_0'	14.5(2.1)	16.6(3.3)

Table 61: The EOS parameters derived from a least-squares fit of the pressure-volume data, figure 130, with V_0 fixed at 288 Å^3.

12. At 5.3 kbar and 260 K, the bulk moduli using the Vinet *et al.* and Birch-Murnaghan EOSs, with the parameters listed in table 61, are 174(5) and 183(6) kbar respectively. This is the highest bulk modulus of all the single network ices [93, 94]; only ices VI and VII(VIII), which comprise of two, interpenetrating sub-lattices, figure 5, can boast higher values [94, 132].

The variations in the individual lattice constants with pressure, again at 260 K, are shown in figures 131 and 132. Using a linear least-squares fit, the compressibilities in the a- and c-axis directions are 2.38(7) and 1.09(10) Mbar^{-1} respectively.

The change in the blue phase volume with temperature at 5 kbar is shown in figure 133. Again using a linear least-squares fit, the expansivity of the blue phase over the temperature range 255–264 K is 274(5) MK^{-1}.

Although the variation in volume with temperature appears linear, the changes in the individual lattice constants do not, figures 134 and 135. In the refinement of both the PEARL and D2B data, anisotropic refinement of the thermal factors was important in obtaining a good profile fit. Different thermal expansivities along the two axes is therefore not unexpected. However, the departure from linearity is particularly strong for the change in the lattice constants over such a small temperature range. The melting temperature of the blue phase at 5.0 kbar is around 264.5 K, figure 129. The behaviour may therefore be the signature of structural changes within the blue

phase as the melting temperature is approached.

If the lattice constants are assumed to vary linearly between 255 and 260 K, then the thermal expansivities in the a- and c—axis directions are 114(17) and 45(28) MK^{-1} respectively.

Although not as severe as that in ice III, the blue phase exhibits anisotropic compressibility and expansivity, with compression and thermal expansion of the structure easiest along the ab-axis. The O(1′)···O(2) non-bonded distance of 3.452 Å is the shortest in the structure, and is most sensitive to changes in the c lattice constant. For example, if the a and c lattice constants are each decreased by 0.1 Å, then the O(1′)···O(2) distance decreases to 3.433 and 3.407 Å respectively. With 2.67 O(1′)···O(2) contacts for every water molecule, it is possible that the small anisotropy arises from this short non-bonded contact.

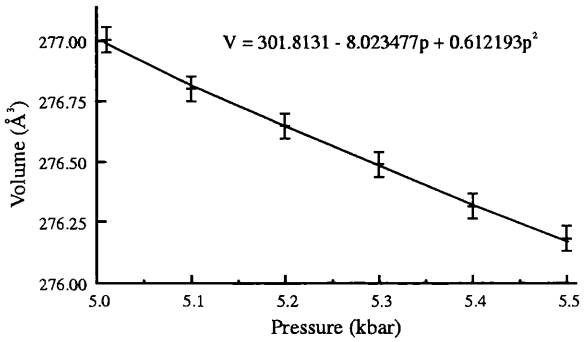

Figure 130: The variation in volume of the blue phase with pressure at 260 K. The line represents a least-squares fit to a Vinet *et al.* EOS, table 60. The errors on each point represent two e.s.ds.

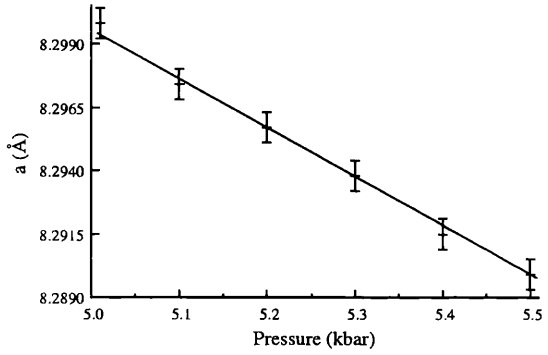

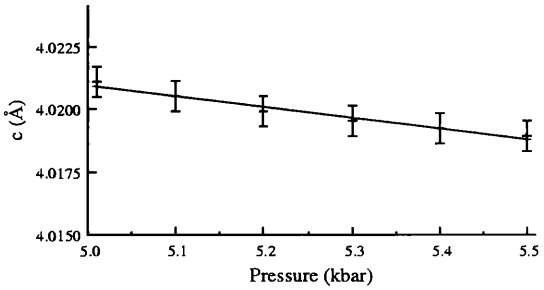

Figure 131: The variation in the lattice constants of the blue phase with pressure at 260 K. The line represents a linear least-squares fit. The errors on each point represent two e.s.ds.

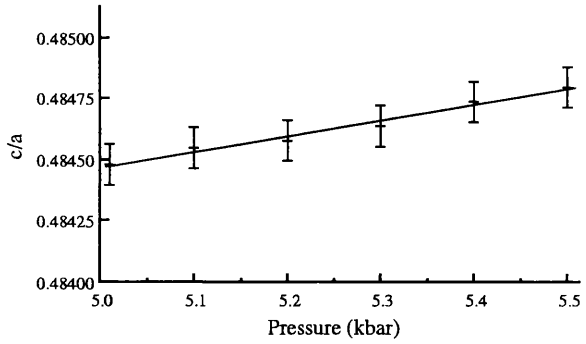

Figure 132: The variation in lattice constant ratio c/a with pressure at 260 K. The line represents a linear least-squares fit. The errors on each point represent two e.s.ds.

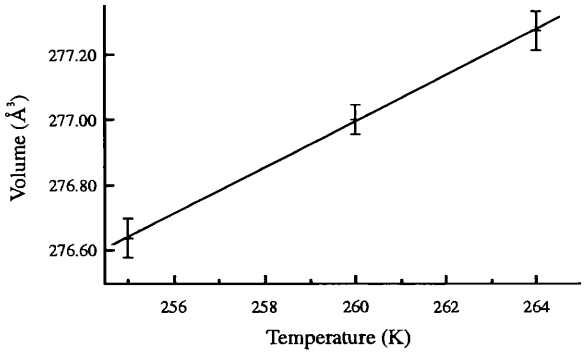

Figure 133: The variation in volume of the blue phase with temperature at 5.0 kbar. The line represents a linear least-squares fit. The errors on each point represent two e.s.ds.

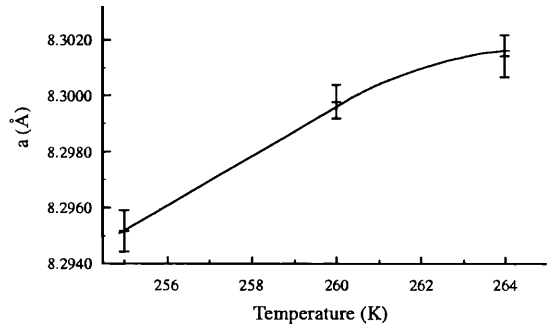

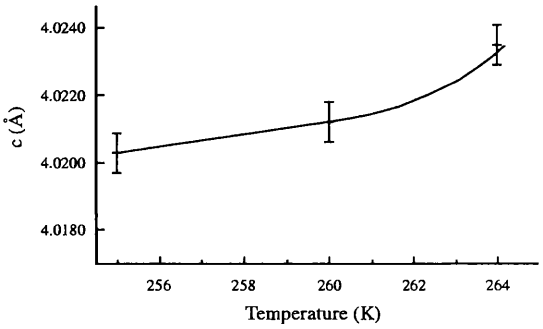

Figure 134: The variation in the lattice constants of the blue phase with temperature at 5.0 kbar. The errors on each point represent two e.s.ds.

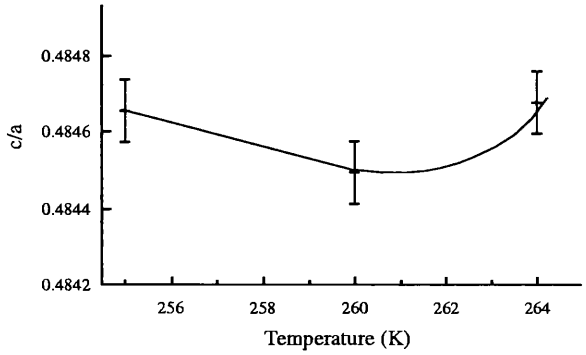

Figure 135: The variation in lattice constant ratio c/a with temperature at 5.0 kbar. The errors on each point represent two e.s.ds.

9.6.8 Comparison of ice structures

The densities, degree of bond bending and bulk moduli for all the ice structures examined in this work are listed in table 62, along with the corresponding temperature and pressure conditions. In addition, ice Ih is included for comparison. The density of D_2O ice Ih was determined from the lattice constant data of Röttger *et al.* [58], and the bulk modulus is that quoted by Gagnon *et al.* [133] for H_2O ice Ih. Although differences in the bulk moduli might be expected for H_2O and D_2O ice, there was good agreement between the bulk moduli found in this work for D_2O ices II, III and V, and those found by others for H_2O [93, 94, 107]. It seems reasonable to assume that the bulk moduli for D_2O will be similar to that quoted here for H_2O.

	p(kbar)	T(K)	ρ(gcm^{-3})	$< (\delta\theta)^2 >^{1/2}$	B^T(kbar)
Ih	0	250	1.01907(5)	0	90
III	2.9	250	1.28889(18)	15.5	88(2)
II	3.8	200	1.33922(5)	17.0	148(1)
V	4.5	254	1.39862(14)	18.3	134(2)
IV	4.63	260	1.43184(17)	15.1	143(2)
Blue	5.25	260	1.4343(3)	18.9	173(6)

Table 62: The density, bond bending and bulk moduli for the various ice phases examined in this work. $< (\delta\theta)^2 >^{1/2}$ is the r.m.s. of O–O–O bond angle deviations from the ideal tetrahedral angle of 109.5°.

Although the figures listed for ice II were determined from data collected at 200 K, the values will not be significantly changed at 250 K as to affect the discussion below. It should also be noted that the bond bending for ices III and V might be smaller than that quoted due to partial ordering.

There are two key elements which determine the strength of the ice structures: the

hydrogen bonds which bind the water molecules together, and the repulsive contacts which exist between the water molecules. As the ice structures are compressed, the hydrogen bonds become strained and eventually break, with the water molecules rearranging to form an ice structure of higher density. The increase in density across a phase transition results in an increase in the number of hydrogen bonds per unit volume, and an increase in the number of short, non-bonded contacts. Therefore, as the density increases, the bulk modulus is expected to increase. However, for many of the ice transitions, the increase in density is brought about by an increase in the bending of the hydrogen bonds. Although it is unknown exactly how the stiffness of the hydrogen bond responds to bending, it is thought that a near-linear bond is stiffer than one which is considerably bent [94, 134]. An increase in bond bending might therefore decrease the bulk modulus.

Gagnon *et al.* [134] classified the ices into three groups based on the strength of the hydrogen bonds: (1) disordered ices with linear hydrogen bonds (Ih and Ic), (2) disordered ices with non-linear hydrogen bonds (III, IV, V and the blue phase), and (3) ordered ices (II and IX). However, the classification was based on bulk moduli data for ices Ih, II, III, V and VI only. From the data collected in this work, which includes for the first time compressibility information on ice IV and the blue phase, it is apparent that this classification is an oversimplification and the task of understanding the strength of the ices in terms of hydrogen bonding is much more complicated.

Ices Ih and III have similar bulk moduli, yet ice III has a much higher density. The hydrogen bonds in ice Ih are linear whilst those in ice III are not. This would suggest that linear hydrogen bonds are stiffer than non-linear hydrogen bonds. However, the stiffness of the bent hydrogen bond must increase as the bending of the bond increases. This is evident from the data on ice IV and the blue phase. The densities for both

phases are very similar, yet the blue phase with its much increased bond-bending has the higher bulk modulus. Since it is ice IV which has the shorter, repulsive contacts, the increase in strength of the blue phase must be attributed to the increased bending of the hydrogen bonds.

Gagnon *et al.* [134] also suggested that the hydrogen bonds in ordered ices were stronger than those in disordered ices. If only the plot of density versus bulk modulus is consulted, figure 136, then there is perhaps evidence of this, with the bulk modulus for ice II rather high considering the density of the structure. However, when the amount of bond-bending is taken into consideration, figure 137, then ice II no longer seems anomalous.

So far, the strength of the ice structures has been considered in terms of the hydrogen bonds only. However, repulsive, non-bonded interactions must also play an important role in determining the strength of a structure. The shortest non-bonded O···O distances for each of the ice structures are listed in table 63.

Ih		II		III		V		IV		Blue	
4.51	6	3.21	2	3.51	0.67	3.27	0.57	3.10	1.5	3.45	2.67
4.52	6	3.50	2	3.65	1.33	3.38	0.57	3.14	0.75	3.49	2.67
		3.56	2			3.48	0.29	3.24	1.5		
		3.58	2			3.51	0.86				
						3.56	0.57				
						3.61	1.14				

Table 63: The O···O non-bonded distances and their multiplicities for the different ice structures. Only distances less than 3.65 Å are listed; no distance shorter than 4.5 Å exists for ice Ih. The first column of each pair are the O···O distances in Å, while the number of such contacts per water molecule are listed in the second column.

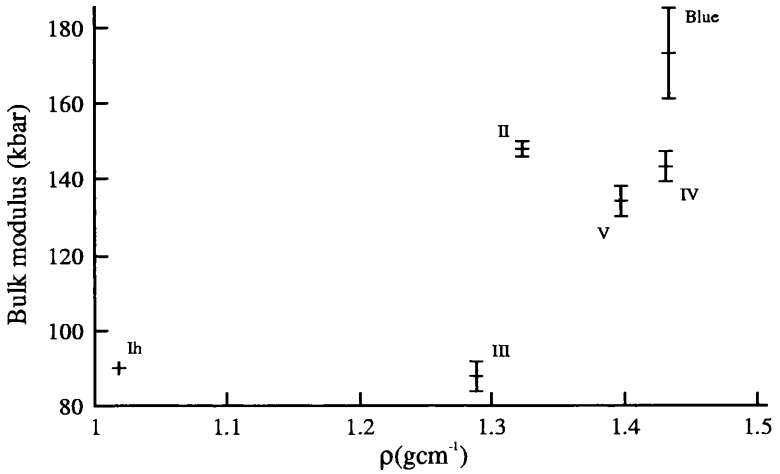

Figure 136: Bulk modulus versus density for the various phases of ice. The errors on each point represent two e.s.ds.

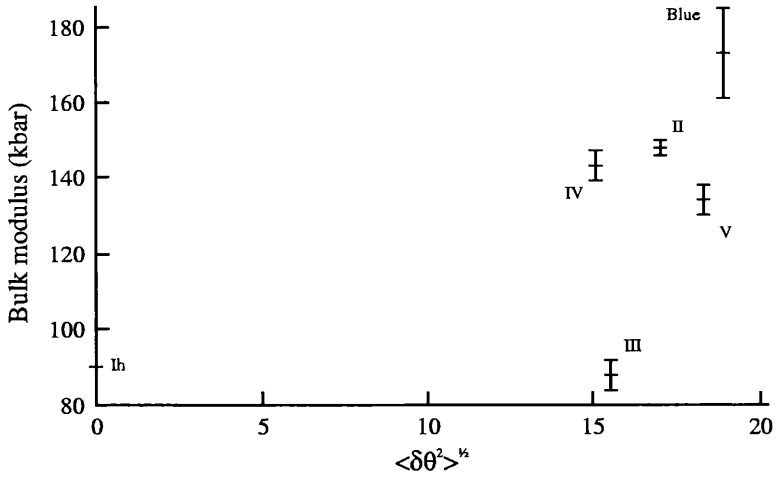

Figure 137: Bulk modulus versus bond-bending for the various phases of ice. The errors on each point represent two e.s.ds.

An inspection of the O···O distances, table 63, suggests that the non-bonded interactions are greater in ice II than they are in ice V. Although the bulk modulus of ice II may seem high when comparing only the densities of the different ice structures, the strength of the structure can perhaps be explained by bond bending, which is greater in ice II that it is in ice IV, and non-bonded interactions, which are greater in ice II than in ice V; both ices IV and V are denser than ice II. There is therefore no strong evidence to support the suggestion that the hydrogen bonds in orientationally ordered ice II are stronger than those in the orientationally disordered ices.

The thermal expansivities for the various ice structures examined in this work are listed in table 64. It should be noted that the values for ice II were obtained by assuming that the density varies linearly over the pressure range 2.8–4.8 kbar. The errors surrounding the values for ice II are therefore an underestimate. The values for D_2O ice Ih were determined from the lattice constant data of Röttger *et al.* [58].

	p(kbar)	T(K)	$\rho(\mathrm{gcm}^{-3})$	$\beta(\mathrm{MK}^{-1})$
Ih	0	242.5	1.02034(17)	173(11)
III	2.5	245	1.28427(14)	239(12)
II	4.2	225	1.33458(11)	261(2)
V	5.0	245.5	1.40675(9)	240(5)
Blue	5.0	257.5	1.4355(3)	274(5)

Table 64: The density, and thermal expansivity for the various ice phases examined in this work.

With the exception of ice Ih, the thermal expansivities of the different ice structures are all of the same magnitude. The lower figure for ice Ih implies less lattice anharmonicity and most likely arises from the linear hydrogen bonds present within the structure. There is therefore further evidence to support the suggestion that

linear hydrogen bonds are stiffer than ones which are bent. Likewise, there is no evidence from the expansivities to suggest that the hydrogen bonds in the orientationally ordered ice II structure are stiffer than those in the disordered structures.

9.7 Conclusions

The blue phase is a new form of ice found metastably within the stability region of ice V. The water molecules bond tetrahedrally to form a structure in which channels, approximately pentagonal in shape, spiral parallel to the *c*-axis. The structure consists of only seven- and eight-membered rings, providing a counter-example to the generally held belief that tetrahedral structures must have rings smaller than seven-membered.

Although full orientational order of the water molecules is not permitted under the current space group symmetry, it is possible that partial order is present.

The density of the blue phase is greater than that of ice V and is achieved through increased bending of the hydrogen bonds. This is unlike ice IV which achieves a similar density to the blue phase through interpenetration of bonds. The degree of bond bending is the largest of all the ice structures, with the exception of ice VI. All the O–O bond lengths are comparable with those found in ices Ih, II, and III at lower pressures. There is therefore no suggestion of bond strain or non-bonded interactions influencing the detailed structure.

Like ice IV, which is another ice structure found metastably within ice V, the difference in free energy between ice V and the blue phase is small. The increase in density is offset by an increase in internal energy, brought about by an increase in bond bending and non-bonded interactions. The uncertainty surrounding the water

molecule orientations means the entropic contribution to the free energy is uncertain.

The blue phase, together with the yellow phase, ice IV and ice V, further demonstrates the versatility of the hydrogen bond in forming different ice structures under the same conditions of temperature and pressure. The fine balance of enthalpic and entropic contributions to the free energy for these systems should prove useful in critically testing the viability of water molecule potentials.

Further work is needed to clarify some outstanding questions surrounding the blue phase. The melting curve is still unknown with any accuracy. The degree of orientational order adopted by the water molecules is also unknown. With only three crystallographically different O–O bonds, further work using Raman or infrared spectroscopy might give some indication of the orientational disorder. In addition, information on the local environment of the water molecule could be obtained from diffuse neutron scattering and might give an indication of the orientational and positional disorder. It is clear that full orientational order is not present; dielectric measurements may prove inconclusive in identifying partial order.

Diffraction and spectroscopic work on samples quenched to liquid nitrogen temperatures will also be of interest to see whether the blue phase achieves full orientational order at low temperatures.

Chapter 10

Summary

Prior to this work, the structures of the ices in the medium-pressure range (2–6 kbar), with the exception of ice III(IX), were known only for samples quenched to liquid nitrogen temperatures and recovered to ambient pressure. However, it is suspected that structural changes within the ices might occur when recovered in this way. In this work, the structures of ices II, III, IV and V were examined under their thermodynamic conditions of stability by the use of neutron, powder diffraction.

Past attempts at studying ice in the medium-pressure range have been made using helium gas as the pressure medium [41, 87, 103]. However, the helium atoms were found to enter the ice II structure [41] making it extremely difficult to form ice III and impossible to form ice V [89].

In this work, argon gas was used as the pressure medium. The size of the argon atom was found to be sufficiently large to prevent its inclusion within the ice II structure. Unfortunately, the argon atom is large enough to stabilise a clathrate hydrate structure [92]. The formation of clathrate from ice was therefore unavoidable using argon. However, experiments had shown that by working at temperatures away

from the ice melting curve, the rate at which argon clathrate forms is greatly reduced.

Initial attempts at preparing the ices followed the same approach as that used by Londono *et al.* [103] with the liquid frozen under pressure. Unfortunately, many of the samples prepared in this way were textured making the results obtained inconclusive. However, an alternative route was found which led to the successful formation of the medium-pressure ices. Rather than increasing the pressure and then decreasing the temperature, the ices could be formed by first decreasing the temperature and then increasing the pressure. In this way, the pressure and temperature conditions can be kept within the boundaries of the solid phase. Samples were thereafter prepared from powdered ice Ih which ensured a good quality powder for the diffraction experiments.

Although the structure of ice II under pressure had been studied before, helium gas was used and was found to be included within the structure [41]. The diffraction data in this work represents the first to be collected on ice II under pressure without the use of helium. The structure of ice II for the helium-free and helium-affected systems are similar, though different in detail. The helium atoms sit at well defined positions within the c_H-axis channels, with the amount of helium increasing as the pressure is increased. The helium atoms repel the water molecules which form the flat, hexagonal rings, and also the deuterium atoms which form the channel vertices. The repulsion causes the channel width to increase and its length to contract; this is reflected in the lattice constants with a_H increasing and c_H decreasing on the inclusion of helium. The expansion in the channel width is not translated directly to the lattice constants. Rather, it is largely accommodated through a decrease in the separation of neighbouring channels.

As the pressure is increased, the distance between neighbouring channels in the helium-free structure decreases. The diameter of the flat ring remains unchanged

whilst the diameter of the puckered ring decreases, thereby alleviating increases in hydrogen-bond strain. In the helium-affected structure, the distance between neighbouring channels is already short by virtue of the channel expansion due to helium inclusion. No significant decrease in channel separation is observed on increasing the helium pressure.

The structure of ice III had been studied once before with the results suggesting that the water molecules adopt partially ordered orientations [103]. This finding was particularly important since the generally held belief until that time was that the water molecules in ice adopt either fully disordered or fully ordered orientations. Unfortunately, the results obtained for ice III were questionable and the partial order remained only a suggestion. This work has examined the structure of ice III and found that the water molecules are indeed partially ordered.

As ice III is cooled through the temperature range 210–165 K, the water molecules orient into an almost fully ordered structure (ice IX) [33]. The driving force thought to be responsible for the ordering process is the desire by the water molecules to occupy orientations in which the hydrogen bonds are least bent. Indeed, the water molecules in ice IX occupy the orientations with the least amount of hydrogen-bond bending [101]. However, the partial order found in this work for ice III cannot be explained purely on the basis of orientations favourable in terms of hydrogen-bond bending. There must therefore be other factors responsible for the ordering of the water molecules, most likely D···D and O···D non-bonded contacts and the O–D···O···D–O acceptor angles. The influence of these other factors on the orientations of the water molecules is evident in the orientationally ordered ices, II and IX. In ice II the water molecules fail to occupy the orientations with the least amount of hydrogen-bond bending [84], whilst the positions of the water molecules in ice IX are

such that the hydrogen-bond bending is unnecessarily increased [101].

During the work on ice III, unexpected phase transitions were observed. In trying to form ice III from ice Ih, there was a transition to a non-crystalline phase at 2.8 kbar and 248 K. Although the transition was most probably the melting of ice Ih, an amorphous solid cannot be ruled out. When ice III was studied at 3.3 kbar and 250 K, the phase transformed to ice II over a period of several hours. The resulting ice II was heavily textured suggesting that the ice III slowly melted, with the melt then forming ice II. Although rather strange, this behaviour has been observed before [87].

Only twice has the structure of ice V been studied by diffraction, once using X-rays [108] and once using neutrons [1]. However, the studies were on samples recovered to ambient pressure at 110 K; the structure of ice V under its thermodynamic conditions of stability remained unknown. This work represents the first diffraction data to be collected on ice V under such conditions. Although the oxygen framework for recovered ice V is similar to that found in this work for ice V under pressure, there are significant differences. For example, the O–O distances in the recovered structure were found to cluster around 2.80 Å with the exception of one "conspicuously long" bond at 2.87 Å [108]. No such behaviour is found in the ice V structure under pressure. The O–O bond lengths all differ greatly, with two distances shorter than 2.7 Å, while the "conspicuously long" bond in this work was found to be 3.01 Å. The short and long O–O bond distances are thought to be caused by the four-membered rings which exist within the ice V structure. The hydrogen-bond bending that must exist within these rings will be relieved by an increase in the bond distance between water molecules. This causes the O–O bond lengths within the rings to increase, and other bond lengths, such as those between neighbouring rings, to decrease. In comparing

the bond lengths with spectroscopic data [115], it is evident that empirical relationships relating the O–D stretching frequency to the O–D and/or O–O bond lengths are inadequate.

Dielectric [85] and spectroscopic [115] measurements on ice V implied the water molecule orientations were disordered at high temperatures. However, the study of ice V at 110 K and ambient pressure by neutron diffraction found that the water molecules adopted partially ordered orientations [1]. The partial order was interpreted as an intermediary to full order with the kinetics at low temperatures responsible for preventing the water molecules from orienting into a fully ordered state. The orientations of the water molecules were still thought to be disordered at high temperatures with a transition corresponding to ordering of the water molecules at around 125 K. This work has shown that the water molecule orientations are not disordered at high temperatures but are partially ordered in a manner similar to that observed at low temperatures. In addition, the amount of ordering was found to increase with increasing pressure and with decreasing temperature.

An endothermic transition, thought to be due to orientational ordering, was observed for ice V over the temperature range 106–132 K [112]. The change in entropy recorded for KOH-doped ice V over the transition was 1.9 $Jmol^{-1}K^{-1}$. If the ordering found in this work is linearly extrapolated to 130 K, then the transition entropy corresponds to a highly ordered (82%) structure. The space group symmetry of ice V at high temperatures does not permit full orientational order and a change in space group at low temperatures seems likely to account for the change in entropy.

Ice IV is a metastable phase that has proven difficult to form, the difficulty arising from the instability of ice IV with respect to ice V. Only once has the structure of ice IV been suggested [46], based on X-ray diffraction data on samples prepared with

the use of organic nucleants, quenched to 110 K and recovered to ambient pressure. In this work, ice IV was successfully prepared without the use of nucleants and its structure determined by neutron diffraction at high temperature and pressure. The results of this work confirm for the first time that the structure proposed is correct.

The density of ice IV is greater than that of ice V, yet ice IV has a smaller amount of hydrogen-bond bending. This is achieved through a form of interpenetration in which a hydrogen bond passes through a hexagonal ring of water molecules. The short, non-bonded interactions that arise from the interpenetration lead to the longest O–O bond length found in any ice structure. Although the degree of bond bending in ice IV is smaller than that for ice V, there is an increase in bond stretching and non-bonded interactions. The internal energy of ice IV is therefore greater that ice V but is offset by a higher density such that the difference in Gibbs free energy between the two ices is small.

The water molecules in ice IV are orientationally disordered at high temperatures and most probably disordered at 110 K [46]. There are two factors which appear to be responsible for the observed disorder. First, most of the orientations are energetically similar and therefore occur with equal probability. Second, the structure exhibits high local symmetry such that any orientations that might prove energetically favourable can not propagate entirely throughout the structure.

During the initial work in which the ices were prepared from the liquid, two unidentified phases were formed at pressures and temperatures under which ice V is expected to form. The first, labelled the "yellow" phase, has subsequently never been formed even upon following the same experimental conditions. Attempts at solving the structure from the data collected proved unsuccessful, this is due mainly to the small number of reflections observed in the data profiles. Although unknown,

the structure is thought to be a new phase of ice which exists metastably within the stability region of ice V.

The second unidentified phase, labelled "blue", has been formed in this work several times, and its structure solved from the data collected. The phase is a new form of ice, again found metastably within the stability region of ice V. The water molecules bond tetrahedrally to form a structure in which channels, approximately pentagonal in shape, spiral parallel to the *c*-axis. The topology of the phase is unlike that of any solid water structure and comprises only seven- and eight-membered rings, providing a counter-example to the generally held belief that tetrahedral structures must have rings smaller than seven-membered [129].

The density of the blue phase is greater than that of ice V and is achieved through increased bending of the hydrogen bonds. This differs from the other metastable phase, ice IV, which achieves an increase in density through interpenetration. The amount of bond bending in the new phase is the largest of all the ice structures, with the exception of ice VI [104]. The increase in bond bending over ice V brings about an increase in internal energy. This is offset by an increase in density resulting in a small difference in Gibbs free energy between the new phase and ice V.

Although full orientational ordering of the water molecules is not permitted under the current space group symmetry, partial order is possible and would not be detected crystallographically.

The blue phase, together with the yellow phase, ice IV and ice V, further demonstrates the versatility of the hydrogen bond in forming different ice structures under the same conditions of temperature and pressure. The fine balance of enthalpic and entropic contributions to the free energy for these systems should prove useful in critically testing the viability of water molecule potentials.

In addition to the two new metastable forms of ice, a further unidentified phase was formed during studies of ices IV and V. The amount of phase gradually increased with time suggesting a new form of argon hydrate compound. The small amount of phase present made structure determination impossible. Nevertheless, the reflections were indexed to a cubic cell of 9.72 Å in length, with $Pn\bar{3}m$ the space group which best satisfies the reflection conditions.

There is evidence from the compressibilities and expansivities of the various ice structures examined in this work, that linear (or near-linear) hydrogen bonds are stiffer than those which are bent. However, the stiffness of the bent hydrogen bond appears to increase with bending. There is no evidence to support the suggestion [134] that the hydrogen bonds in orientationally ordered ice II are stronger than those in the disordered ices.

10.0.1 Further work

The results of this work have highlighted several areas of further study within the medium-pressure range of the ice phase diagram, some of which are possible with the data presented in this thesis.

The discussion on ice II was concerned with changes in the structure upon helium inclusion and pressure increase. However, ice II is orientationally ordered and therefore exhibits no positional disorder. The bond lengths and angles obtained from the diffraction data are therefore representative of the true water molecule geometry within the ice structure. The diffraction data in this work are the first to be collected on helium-free ice II under pressure. Comparisons with the bond lengths and angles determined in this work and those found for recovered ice II [81,84], and also the free water molecule (monomer and dimer), should be made.

It is clear from this work that non-bonded interactions are important in the orientational ordering of the water molecules. A careful examination of the D···D and O···D distances for ices II and III should provide some idea of the contacts responsible for the observed order. Although the picture is much more complicated for ice V, there are two deuterium sites which seem particularly unfavourable. Again, a detailed examination of the structure might indicate why.

The positions of the deuterium atoms in ice III are perhaps questionable. However, by examining the oxygen frameworks of ices III (disordered) and ice IX (ordered), the amount of positional disorder within ice III can be estimated. This can then be used to clarify whether the O–D distances found in this work for ice III can be explained in terms of positional disorder.

Neutron diffraction data have recently been collected on ice V over the temperature range 120–250 K. Initial indications are that no change in space group symmetry occurs at these temperatures. The data will however highlight the variation in orientational order with temperature and may indicate the onset of an ordering transition such as that found for ice III–IX [33]. Since no change in space group was found, further work with the use of KOH is needed to overcome the kinetic restraints placed on the system at low temperatures. The results obtained in this work suggest that a change in space group is needed to account for the entropy change measured by Handa *et al.* [112]. Neutron diffraction studies of KOH-doped ice V should record this change in space group, from which the fully ordered ice V structure can be deduced.

The ice IV sample examined in this work was prepared in a similar way to Engelhardt and Whalley [43]: freezing the liquid under pressure. However, this form of preparation differs from that employed by Bridgman [30] and Nishibata [45], who formed ice IV by decreasing the pressure on ice VI. Further work is needed to confirm

that the ice IV structure formed originally by Bridgman, is the same as that found in this work. This is particularly important in light of the other metastable phases found to exist in this region of the ice phase diagram. X-ray or neutron diffraction data on samples prepared in the same way as Bridgman and Nishibata should resolve this issue. This will require pressures of around 7 kbar [45] which should soon be possible with gas pressure cells, though certainly possible with anvil cells.

The mapping of the stability region of ice IV is important, particularly the ice IV melting curve which can be used to determine the Gibbs free energy of the structure. Large differences in the location of the ice IV melting curve were found between this work and that of Engelhardt and Whalley [43]. The cause of this discrepancy is unknown and further work is required to resolve this.

Engelhardt and Kamb [46] found the water molecules in ice IV were orientationally disordered at low temperatures. However, Engelhardt and Kamb quenched their samples at a rate of 60 $Kmin^{-1}$, which most probably froze the water molecules kinetically at 160 K, preventing them from reorienting into a partially or fully ordered state. Further work on ice IV at low temperatures is needed in which cooling rates are kept in line with the relaxation times of the water molecules. Neutron diffraction appears the best tool for such a study since any change in orientational order would be immediately identified by a change in the space group symmetry. If no change is observed above 150 K, then samples doped with KOH will be of use for studies at lower temperatures.

The blue phase is a new ice structure, and as such necessitates further study. The melting curve is unknown with any accuracy and is required for estimates of the free energy. Local, orientational order, which cannot be detected crystallographically, might be present within the blue phase. With only three crystallographically different

O–O distances, an indication of partial orientational order might be provided by Raman or infrared spectroscopy. It is evident from the space group symmetry that full orientational order does not exist at high temperatures. Diffraction and spectroscopic work on samples cooled to temperatures below 150 K will therefore be of interest in seeing whether the blue phase achieves full or partial orientational order at low temperatures.

The study of ices III, IV, V and the blue phase by diffuse neutron scattering might provide some indication of the magnitude and direction of the positional disorder present within these ice structures. In addition, evidence of local orientational order in ice IV and the blue phase, impossible to detect crystallographically, might also be revealed. Such information will be of use in understanding the mechanisms responsible for the positional and orientational disorder in these ice structures.

The structure of the yellow phase remains undetermined and further work is required to identify the phase. It is unlikely that the structure of the yellow phase will be solved from the data presented in this work. The small number of reflections makes the indexing and space group determination inconclusive and the density is unknown with any accuracy. Further diffraction data are therefore needed to solve the structure. Unfortunately, other than trial and error, no recommendation on how to form the phase can be offered. Attempts using the organic nucleants suggested by Evans [42] may prove to be successful.

Another unidentified phase was formed in this work during data collection on ices IV and V. The phase was observed to increase in quantity with time suggesting some form of argon hydrate structure. Again, further diffraction work is required to identify the phase. Formation of the phase should be possible by first forming ice V (or ice IV) and then leaving under 5.0 kbar argon pressure at around 260 K. The

sample should be left under this condition for at least a week to ensure complete, or almost complete, phase formation.

Appendix

The models used in refining the argon clathrate phase (space group $Fd\bar{3}m$, $a = 17.15$ Å) are listed below.

	x	y	z	occ.	U_{iso}
O	0.875	0.875	0.875	1.0	0.054(4)
O	0.7828(3)	0.7828(3)	0.7828(3)	1.0	0.061(3)
O	0.8189(2)	0.8189(2)	0.6300(3)	1.0	0.058(1)
D	0.8412(4)	0.8412(4)	0.8412(4)	0.5	0.068(7)
D	0.8174(5)	0.8174(5)	0.8174(5)	0.5	0.071(6)
D	0.7946(4)	0.7946(4)	0.7275(4)	0.5	0.050(3)
D	0.8038(4)	0.8038(4)	0.6816(4)	0.5	0.053(3)
D	0.8589(4)	0.8589(4)	0.6292(6)	0.5	0.068(4)
D	0.7302(4)	0.8550(3)	0.5854(4)	0.5	0.058(2)
Ar	0	0	0	0.99(3)	0.082(12)
Ar	0.332	0.332	0.332	0.165(8)	0.25
Ar	0.418	0.418	0.418	0.165(8)	0.25

Table 65: Model of the argon clathrate phase refined from neutron diffraction data collected at 2.5 kbar and 273 K.

	x	y	z	occ.	U_{iso}
O	0.875	0.875	0.875	1.0	0.057(23)
O	0.7855(14)	0.7855(14)	0.7855(14)	1.0	0.052(15)
O	0.8220(9)	0.8220(9)	0.6272(18)	1.0	0.070(8)
D	0.8457(19)	0.8457(19)	0.8457(19)	0.5	0.075(30)
D	0.8138(17)	0.8138(17)	0.8138(17)	0.5	0.058(26)
D	0.7922(15)	0.7922(15)	0.7281(15)	0.5	0.067(20)
D	0.7991(15)	0.7991(15)	0.6778(20)	0.5	0.046(12)
D	0.8568(13)	0.8568(13)	0.6336(16)	0.5	0.048(14)
D	0.7247(15)	0.8578(16)	0.5835(17)	0.5	0.063(10)
Ar	0	0	0	0.66(8)	0.07
Ar	0.332	0.332	0.332	0.10(3)	0.25
Ar	0.418	0.418	0.418	0.10(3)	0.25

Table 66: Model of the argon clathrate phase refined from neutron diffraction data collected at 4.8 kbar and 273 K.

Bibliography

[1] W. C. Hamilton, B. Kamb, S. J. La Placa, and A. Prakash, in *Physics of Ice*, B. B. N. Riehl and H. Engelhardt, eds., (Plenum Press, New York, 1969), pp. 44–58.

[2] J. F. Nagle, in *Physics and Chemistry of Ice*, E. Whalley, S. J. Jones, and L. W. Gold, eds., (Royal Society of Canada, Ottawa, 1973), pp. 70–71.

[3] R. Howe and R. W. Whitworth, *J. Chem. Phys.* **86,** 6443 (1987).

[4] M. J. Tait and F. Franks, *Nature* **230,** 91 (1971).

[5] I. Nezbeda, *J. Mol. Liquids* **73-74,** 317 (1997).

[6] W. Dansgaard *et al.*, *Nature* **364,** 218 (1993).

[7] K. Rozanski, S. J. Johnsen, U. Schotterer, and L. G. Thompson, *Hydrolog. Sci. J.* **42,** 725 (1997).

[8] D. Raynaud *et al.*, *Science* **259,** 926 (1993).

[9] J. Chappellaz *et al.*, *Nature* **366,** 443 (1993).

[10] C. U. Hammer, *J. Glaciol.* **25,** 359 (1980).

[11] C. U. Hammer, H. B. Claussen, and W. Dansgaard, *Nature* **288,** 230 (1980).

[12] M. Legrand and R. J. Delmas, *Nature* **327,** 671 (1987).

[13] S. C. Mossop, *Bull. Amer. Meteor. Soc* **66,** 264 (1985).

[14] P. V. Hobbs and A. L. Rangno, *J. Atmos. Sci.* **42,** 2523 (1985).

[15] J. Aussedat, P. Boutron, P. Coquilhat, J. L. Descotes, and G. Faure, *J. de Phys.* **3,** 515 (1993).

[16] J. F. Peyridieu *et al.*, *Cryobiology* **33,** 436 (1996).

[17] I. A. Ryzhkin and V. F. Petrenko, *J. Phys. Chem. B* **101,** 6267 (1997).

[18] V. K. Croutch and R. A. Hartley, *J. Coatings Technol.* **64,** 41 (1992).

[19] C. B. Pilcher, S. T. Rideway, and T. B. McCord, *Science* **178,** 1087 (1972).

[20] L. A. Lebofsky, *Nature* **269,** 785 (1977).

[21] A. L. Broadfoot *et al.*, *Science* **204,** 979 (1979).

[22] J. Klinger, *J. Phys. Chem.* **87,** 4209 (1983).

[23] G. J. Consolmagno, *J. Phys. Chem.* **87,** 4204 (1983).

[24] W. B. Durham, S. H. Kirby, H. C. Heard, and L. A. Stern, *J. de Phys.* **48,** C1–221 (1987).

[25] C. W. Kern and M. Karplus, in *Water : A Comprehensive Treatise, Volume I,* F. Franks, ed., (Plenum Press, New York, 1973), pp. 21–92.

[26] W. S. Benedict, N. Gailar, and E. K. Plyler, *J. Chem. Phys.* **24,** 1139 (1956).

[27] F. J. Lovas, *J. Chem. Phys. Ref. Data* **7,** 1445 (1978).

[28] G. Tammann, *Ann Phys.* **2,** 1 (1900).

[29] P. W. Bridgman, *Proc. Am. Acad. Arts Sci.* **47,** 441 (1912).

[30] P. W. Bridgman, *J. Chem. Phys.* **3,** 597 (1935).

[31] P. W. Bridgman, *J. Chem. Phys.* **5,** 964 (1937).

[32] E. Whalley, D. W. Davidson, and J. B. R. Heath, *J. Chem. Phys.* **45,** 3076 (1966).

[33] E. Whalley, J. B. R. Heath, and D. W. Davidson, *J. Chem. Phys.* **48,** 2362 (1968).

[34] K. R. Hirsch and W. B. Holzapfel, *Phys. Lett. A* **101,** 142 (1984).

[35] A. Polian and M. S. Grimsditch, *Phys. Rev. Lett.* **52,** 1312 (1984).

[36] T. Matsuo, Y. Tajima, and H. Suga, *J. Phys. Chem. Solids* **47,** 165 (1986).

[37] A. H. Narten, C. G. Venkatesh, and S. A. Rice, *J. Chem. Phys.* **64,** 1106 (1976).

[38] O. Mishima, L. D. Calvert, and E. Whalley, *Nature* **310,** 393 (1984).

[39] W. F. Kuhs, D. V. Bliss, and J. L. Finney, *J. de Phys.* **48,** C1–631 (1987).

[40] J. D. Bernal and R. H. Fowler, *J. Chem. Phys.* **1,** 515 (1933).

[41] J. D. Londono, J. L. Finney, and W. F. Kuhs, *J. Chem. Phys.* **97,** 547 (1992).

[42] L. F. Evans, *J. Appl. Phys.* **38,** 4930 (1967).

[43] H. Engelhardt and E. Whalley, *J. Chem. Phys.* **56,** 2678 (1972).

[44] H. Engelhardt and E. Whalley, *J. Chem. Phys.* **71,** 4050 (1979).

[45] K. Nishibata, *Jap. J. Appl. Phys.* **11,** 1701 (1972).

[46] H. Engelhardt and B. Kamb, *J. Glaciol.* **21,** 51 (1978).

[47] H. Engelhardt and B. Kamb, *J. Chem. Phys.* **75,** 5887 (1981).

[48] H. P. Klug and L. E. Alexander, *X-ray Diffraction Procedures* (Wiley-Interscience, New York, 1974).

[49] J. P. Glusker and K. N. Trueblood, *Crystal Structure Analysis* (Oxford University Press, Oxford, 1985).

[50] C. Giacovazzo, *Fundamentals of Crystallography* (Oxford University Press, Oxford, 1994).

[51] C. Hammond, *The Basics of Crystallography and Diffraction* (Oxford University Press, Oxford, 1997).

[52] M. M. Woolfson, *An introduction to X-ray crystallography* (Cambridge University Press, Cambridge, 1997).

[53] E. Hecht, *Optics* (Addison-Wesley, Reading, Mass., 1987).

[54] M. F. C. Ladd and R. A. Palmer, *Structure Determination by X-ray Crystallography* (Plenum Press, New York, 1993).

[55] H. M. Rietveld, *Acta Cryst.* **22,** 151 (1967).

[56] H. M. Rietveld, *J. Appl. Cryst.* **2,** 65 (1969).

[57] V. F. Sears, *Neutron News* **3,** 26 (1992).

[58] K. Röttger, A. Endriss, J. Ihringer, S. Doyle, and W. F. Kuhs, *Acta Cryst.* **B50,** 644 (1994).

[59] W. F. Kuhs and M. S. Lehmann, in *Water Science Reviews 2*, F. Franks, ed., (Cambridge University Press, Cambridge, 1986), pp. 1–65.

[60] J. Paureau and C. Vettier, *Rev. Sci. Instrum.* **46,** 1484 (1975).

[61] C. Lobban, J. L. Finney, and W. F. Kuhs, unpublished (see Appendix).

[62] P. Radaelli, private communication.

[63] K. Ibel, "The Yellow Book. Guide to Neutron Research Facilities at the ILL," (1994).

[64] A. W. Hewat, *Mat. Sci. Forum* **9,** 69 (1986).

[65] R. M. Ibberson, W. I. F. David, and K. S. Knight, *The High Resolution Powder Diffractometer (HRPD) at ISIS - A User Guide*, 1992, report RAL-92-031.

[66] R. I. Smith and S. Hull, *User Guide for the Polaris Powder Diffractometer at ISIS*, 1994, report RAL-94-115.

[67] C. J. Carlile, *Physica B* **182,** 4 (1992).

[68] A. C. Larson and R. B. Von Dreele, *GSAS - General Structure Analysis System*, 1990, report LAUR 86-748.

[69] J. Rodriguez-Carvajal, *FullProf*, 1994.

[70] W. I. F. David, D. E. Akporiaye, R. M. Ibbserson, and C. C. Wilson, *Profile Analysis of Neutron Powder Diffraction Data*, 1993, report RAL-92-032.

[71] P. J. Brown and J. C. Metthewman, *The Cambridge Crystallography Subroutine Library - Mark 4 Users Manual*, 1993, report RAL-93-009.

[72] J. K. Cockcroft, *PROFIL*, 1994.

[73] A. K. Cheetham, in *The Rietveld Method*, R. A. Young, ed., (Oxford University Press, Oxford, 1993), pp. 277–292.

[74] J. J. W. Richardson, in *The Rietveld Method*, R. A. Young, ed., (Oxford University Press, Oxford, 1993), pp. 102–110.

[75] R. B. Von Dreele, J. D. Jorgensen, and C. G. Windsor, *Acta Cryst.* **15,** 581 (1982).

[76] W. I. F. David and J. C. Matthewman, *Acta Cryst.* **18,** 461 (1985).

[77] W. I. F. David, *Acta Cryst.* **19,** 63 (1986).

[78] C. J. Howard, *J. Appl. Cryst.* **15,** 615 (1982).

[79] P. Thompson, D. E. Cox, and J. B. Hastings, *J. Appl. Cryst.* **20,** 79 (1987).

[80] R. B. Von Dreele (unpublished).

[81] W. B. Kamb, *Acta Cryst.* **17,** 1437 (1964).

[82] J. E. Bertie and E. Whalley, *J. Chem. Phys.* **40,** 1646 (1964).

[83] E. D. Finch, S. W. Rabideau, R. G. Wenzel, and N. G. Nereson, *J. Chem. Phys.* **49,** 4361 (1968).

[84] W. B. Kamb, W. C. Hamilton, S. J. La Placa, and A. Prakash, *J. Chem. Phys.* **55,** 1934 (1971).

[85] G. J. Wilson, R. K. Chan, D. W. Davidson, and E. Whalley, *J. Chem. Phys.* **43,** 2384 (1965).

[86] E. Whalley and D. W. Davidson, *J. Chem. Phys.* **43,** 2148 (1965).

[87] G. P. Arnold, R. G. Wenzel, S. W. Rabideau, N. G. Nereson, and A. L. Bowman, *J. Chem. Phys.* **55,** 589 (1971).

[88] A. Kahane, J. Klinger, and M. Phillipe, *Solid State. Comm.* **7,** 1055 (1969).

[89] J. D. Londono, Ph.D. thesis, University of London, 1989.

[90] E. Sloan, *Clathrate Hydrates of Natural Gases* (Marcel Dekker, Inc., New York, 1990).

[91] A. Bondi, *J. Phys. Chem.* **68,** 441 (1964).

[92] D. W. Davidson, Y. P. Handa, C. I. Ratcliffe, J. S. Tse, and B. M. Powell, *Nature* **311,** 142 (1984).

[93] G. H. Shaw, *J. Chem. Phys.* **84,** 5862 (1986).

[94] R. E. Gagnon, H. Kiefte, M. J. Clouter, and E. Whalley, *J. Chem. Phys.* **92,** 1909 (1990).

[95] R. L. McFarlan, *J. Chem. Phys.* **4,** 253 (1936).

[96] W. B. Kamb and S. K. Datta, *Nature* **187,** 140 (1960).

[97] J. E. Bertie, L. D. Calvert, and E. Whalley, *J. Chem. Phys.* **38,** 840 (1963).

[98] G. S. Kell and E. Whalley, *J. Chem. Phys.* **48,** 2359 (1968).

[99] B. Kamb and A. Prakash, *Acta Cryst.* **B24,** 1317 (1968).

[100] S. W. Rabideau, E. D. Finch, G. P. Arnold, and A. L. Bowman, *J. Chem. Phys.* **49,** 2514 (1968).

[101] S. J. La Placa, W. C. Hamilton, B. Kamb, and A. Prakash, *J. Chem. Phys.* **58,** 567 (1973).

[102] K. Nishibata and E. Whalley, *J. Chem. Phys.* **60,** 3189 (1974).

[103] J. D. Londono, W. F. Kuhs, and J. L. Finney, *J. Chem. Phys.* **98,** 4878 (1993).

[104] W. F. Kuhs, J. L. Finney, C. Vettier, and D. V. Bliss, *J. Chem. Phys.* **81,** 3612 (1984).

[105] J. D. Jorgensen and T. G. Worlton, *J. Chem. Phys.* **83,** 329 (1985).

[106] B. Sukarova, W. F. Sherman, and G. R. Wilkinson, *J. Mol. Struct.* **115,** 137 (1984).

[107] C. A. Tulk, H. Kiefte, M. J. Clouter, and R. E. Gagnon, *J. Phys. Chem. B* **101,** 6154 (1997).

[108] B. Kamb, A. Prakash, and C. Knobler, *Acta Cryst.* **22,** 706 (1967).

[109] B. Kamb and B. L. Davis, *Proc. Nat. Acad. Sci. Wash.* **52,** 1433 (1964).

[110] J. E. Bertie, H. J. Labbé, and E. Whalley, *J. Chem. Phys.* **49,** 775 (1968).

[111] B. Kamb and S. J. La Placa, *Trans. Am. Geophys. Union* **56,** V39 1202 (1974).

[112] Y. P. Handa, D. D. Klug, and E. Whalley, *J. de Phys.* **48,** C1–435 (1987).

[113] B. Sukarova, W. F. Sherman, and G. R. Wilkinson, *J. Mol. Struct.* **79,** 289 (1982).

[114] B. Sukarova, G. E. Slark, and W. F. Sherman, *J. Mol. Struct.* **143,** 87 (1986).

[115] B. Sukarova, G. E. Slark, and W. F. Sherman, *J. Mol. Struct.* **175,** 289 (1988).

[116] B. Berglund, J. Lindgren, and J. Tegenfeldt, *J. Mol. Struct.* **43,** 169 (1978).

[117] J. E. Bertie and B. F. Francis, *J. Chem. Phys.* **72,** 2213 (1980).

[118] R. J. Nelmes *et al.*, *Phys. Rev. Lett.* **71,** 1192 (1993).

[119] J. M. Besson *et al.*, *Physical Review B* **49,** 12540 (1994).

[120] J. P. Marckmann and E. Whalley, *J. Chem. Phys.* **41,** 1450 (1964).

[121] J. E. Bertie, H. J. Labbé, and E. Whalley, *J. Chem. Phys.* **49,** 2124 (1968).

[122] P. Vinet, J. Ferrante, J. R. Smith, and J. H. Rose, *J. Phys. C* **19,** L467 (1986).

[123] F. Birch, *J. Geophys. Res.* **83,** 1257 (1978).

[124] J. Hama and K. Suito, *Phys. Lett. A* **187,** 346 (1994).

[125] E. Wolanin *et al.*, *Phys. Rev. B* **56,** 5781 (1997).

[126] J. W. Visser, *J. Appl. Cryst.* **2,** 89 (1969).

[127] P. E. Werner, L. Eriksson, and M. J. Westdahl, *J. Appl. Cryst.* **18,** 367 (1985).

[128] D. Louër and R. Vargas, *J. Appl. Cryst.* **15,** 542 (1982).

[129] G. O. Brunner, *Z. Kristallogr.* **156,** 295 (1981).

[130] M. O'Keeffe and S. T. Hyde, *Zeolites* **19,** 370 (1997).

[131] I-M. Chou and H. T. Haselton, *EOS* **76,** F682 (1995).

[132] Y. Fei, H. Mao, and R. J. Hemley, *J. Chem. Phys.* **99,** 5369 (1993).

[133] R. E. Gagnon, H. Kiefte, M. J. Clouter, and E. Whalley, *J. Chem. Phys.* **89,** 4522 (1988).

[134] R. E. Gagnon, H. Kiefte, M. J. Clouter, and E. Whalley, *J. de Phys.* **48,** C1–29 (1987).